UNIVERSITY OF BERN
FACULTY OF SCIENCE

Department of Chemistry,
Biochemistry and Pharmacy

Professor Natalie Banerji

Conductivity of doped organic semiconductors

Insights from THz time-domain spectroscopy

Inaugural dissertation

presented to the Faculty of Science of the University of Bern to
obtain the PhD of Science in Chemistry and Molecular Sciences

presented by
Eva Gabriela Röck
from Austria

Bern
2025

Acknowledgements

The work of this thesis was realized within the Department of Chemistry, Biochemistry and Pharmaceutical Sciences at the University of Bern under the supervision of Professor Natalie Banerji. I want to express my appreciation and gratitude to the people who have accompanied and supported me during the last four years.

First and foremost, to Professor Natalie Banerji: You welcomed me in your group with great enthusiasm for science. I am very grateful for the opportunity to learn the advanced spectroscopic techniques alongside with the great scientists in the FemtoMat team.

I would also like to thank Dr. Ian Jacobs for being the external examiner of this thesis as well as Prof. Dr. Andrea Cannizzo for chairing the examination.

To the senior scientists Dr. Demetra Tsokkou and Dr. Julien Réhault: Thank you for sharing your experience and knowledge. You both have a way of comprehending complex problems and providing a solution in the most authentic and simple way. Julien, you also have the superpower of fixing a bug on the equipment with your bare presence in a room, that is pretty cool and saved me time trouble-shooting. PD. Dr. Karl Krämer, you always showed up with a smile and an open ear to discuss technical questions. Thanks for giving me the cryostat and the key to a peaceful lab-space to write my thesis. I wish you a joyful retirement.

A big thank you to my former colleagues Dr. Olivier Bardagot and Dr. Gonzague Rebetez that have become friends for a lifetime. Olivier, honestly, I appreciate how dedicated you are to a greater cause: work hard, play hard. You have shown me how playfulness can be an advantage. In science and in life, you always have an open ear and something wise to say. Dear Gonzague, you are one of the few people who contributed constructive criticism when I needed to grow. You inspired me to draw outside the lines in science communication.

To Dr. Kaila Yallum: I have no imagination for who I would be without having you in the picture during this PhD. You and my grandmother are literally the two women

who have inspired me the most to be an unapologetic, ambitious, thoughtful human. I am so thankful to you for being my friend and to the universe, that we have met. Not to mention that you are such a bassist in science as well, not here for the roses on the stage but carrying and translating the deeper meaning.

Thanks to my former students: Maximilian Horn, Basil Hunger, Naomi Ferreira and high school student Liam Jäggi for allowing me to supervise your projects. Doing these projects together with each of you was a huge experience. Maxi, I probably learned more from you than *vice-versa.* Thank you also for contributing the LaTeX guide, the THz conductivity introduction from your Master's and your thoughtful proof-reading of this thesis. I appreciate that you stayed in office N530 with me, because having a high-performance desk neighbour increases your own performance too.

My gratitude goes to the international experts who have given me the chance to learn techniques outside of the FemtoMat expertise. To Professor Christian Müller who has welcomed me in his group at Chalmers Technical University, Sweden, to utilize his temperature dependent electrical conductivity setup. Thanks for being an impactful collaborator during this research stay and throughout. To Professor Benjamin Schwartz and Professor Sarah Tolbert who created an encouraging, focused environment for my research stay in University of California, Los Angeles, USA. You have both shared deep scientific insight in such positive ways. During this research stay I had the priviledge to work with Diego Garcia Vidales, who no doubt is the spin-coating king! Thank you Diego, for being fully committed to the project that I pitched, and hence contributing so positively to this thesis.

I have been fortunate to be fully funded by the Swiss National Science Foundation which enabled the work of this thesis and its wide reach. The SNSF funding fascilitated me to contribute to international conferences. Securing a *UniBe Short Travel Grant* allowed me to solidify my international cutting-edge training. I am extremely thankful for these opportunities.

My final words of appreciation go to my family and friends outside of academia: Especially, to my core family Carmen, Burkhard, Sophia and Raphael who welcome life in distinct, wise ways and who supported me to go my own. To my friends Adina and Valentina: thanks to each of you for giving me some sense of belonging. Thank you, family and friends, for grounding me!

Cheers to everyone, E.

Abstract

Organic semiconductors have emerged as materials that combine the properties of organic molecules and electronics. They are easy to process in solution, provide chemical tunability, are flexible, lightweight, semi-transparent, and bio-compatible, which opens the door to electronics with those properties. Doping is a pivotal method to modulate the conductivity of these materials by inducing charge carriers. Yet, a comprehensive understanding of the conductivity, its origin, potential and limits, remains elusive. This thesis explores the conductivity in doped organic semiconductors, providing innovative and original insights through the application of ultrafast spectroscopy. By employing terahertz (THz) time-domain spectroscopy and optical pump–THz probe spectroscopy, this work investigates the frequency dependent complex conductivity of organic semiconductor and organic–inorganic hybrid semiconductor films. Three recent achievements in enhanced conductivity are highlighted in the chapters. The incorporation of glycolated side-chains in conjugated polymers leads to enhanced conductivity which originates from an increased mobility of charges. The use of the strong oxidant Magic Blue and anion exchange doping leads to a higher number of charges, while also enabling higher mobility *via* recrystallisation. And lastly, the development of non-fullerene acceptor molecules for efficient charge transfer in hybrid materials and generation of mobile charges in optoelectronics. Hence, this thesis presents relevant and novel investigations that aim to ultimately advance the conductivity of organic electronics.

Contents

1 Introduction

Organic semiconductors (OSCs) are relevant in the development of modern technologies ranging from flexible electronics to photovoltaics and bioelectronics. A deep understanding of how these materials conduct charges at the nanoscale, and the origin and limit of their conductivity, remains essential to improve their performance. This thesis explores the intricate relationship between material design, microstructure, doping mechanisms, and the resulting charge transport properties of OSCs. The primary focus is on doped conjugated polymers but is extended to organic–inorganic hybrid materials in the final chapter.

Chapter 2 motivates the organic semiconductor research with applied and fundamental incentives. Starting with an overview of the state-of-the-art, this chapter introduces the context for the development of organic semiconductors and their applications. The aim hereby is to first understand the connection between property and application before the connection between molecular structure and property is elaborated in the thesis. Then, this chapter links the key developments, controversial topics and open questions in the field with the scientific approach of this thesis.

Chapter 3 lays the foundation for this exploration by discussing the materials that form the basis of organic semiconductors. While the chapter is didactic on the background, I limit the extent to materials and concepts directly used in the experimental part. Once the context which shaped the research is clarified, the thesis moves forward to molecular structure of organic semiconductors. First, it explains the molecular building blocks. Among them, conjugated polymers (CPs) gain special attention due to their flexibility, ease of processing, and wide-ranging applicability. A comparison between CPs and molecular OSCs is presented, along with an explanation of backbones and side-chains. Next, hybrid materials are introduced with a focus on bilayer composites. This explains the hybrid materials used later in the thesis, combining an organic small molecule and an inorganic charge transport layer. When these key points together have formed an understanding of the OSCs matrix, the chapter will discuss doping. The doping section introduces the different classifications and methods, also in relation to the concepts of microstructure. While mainly molecular doping is investigated in this thesis, the similarities and differences of electrochemical doping and photo-induced doping are relevant for the thesis and outlined as well. Finally, we have the terminology and background to understand the major material-related concepts in this thesis. This Materials chapter is essential for the interpretation of the experimental results presented later in the thesis. Particularly, the role of side-chains is revisited in Chapter 6, where the properties of conjugated polymers with glycolated side-chains are discussed in relation to their enhanced conductivity. Similarly, the microstructural properties and doping methods play a critical role in the charge transport which is investigated in Chapter 7.

Chapter 4 provides an in-depth examination of charge transport in OSCs. The concept of the density of states, which quantifies how charge carriers populate energy levels, is essential to understand the origin and limit of conductivity in doped OSCs. The chapter also delves into the nature of the doping-induced charge carriers. The so-called polarons are charged quasi-particles that occur with a deformation of a solid-state matrix. This leads to a discussion on charge localization, screening effects, and how charge transport occurs on various length scales—from intramolecular to intermolecular and macroscopic levels. A literature review on charge transport models is presented, with a focus on the semi-localized transport model. The temperature dependence of the conductivity is presented, as an important indicator for the origin of the charge transport. Chapter 4 ties directly into the project performed in Chapter 7, but also deepens the understanding for effects of microstructure and doping from an energetic viewpoint.

In Chapter 5 the methodology is presented with a focus on spectroscopy. Spectroscopy serves as a critical tool for characterising the optoelectronic properties of OSCs. The first section will explain the interpretation of the absorbance of OSCs. Neat and doped films absorb in the ultraviolet to infrared range and the spectra can be read and deconvoluted appropriately. Hence, steady-state absorbance reveals important information about the material's bandgap and doping levels. After the doping-induced charge carriers were introduced in the previous chapter, the corresponding transitions and the band filling is discussed. Subsequently, we will move to THz time-domain spectroscopy, which is used to probe the complex conductivity of materials. Therefore, it is clarified where terahertz frequencies fall on the electromagnetic spectrum. The translation from a terahertz pulse trespassing a material to the complex conductivity is explained in detail. Furthermore, it forms the basis for optical pump–THz probe spectroscopy, which offers insights into photo-induced charge carriers instead of molecular doping-induced charge carriers. Similar to regular THz spectroscopy, the technique can yield the complex conductivity spectra of photo-induced charge carriers. Since it is a pump–probe experiment, it can also yield the dynamics of photo-induced charge carriers over time. Spectroscopy is the core of my experimental expertise and it delivers novel results discussed in this thesis. Especially the frequency-dependent complex conductivity represents a key result in every single results chapter of this thesis. Following the spectroscopic methods, there is a complete list of all methods that I am able to conduct independently.

Chapter 6 investigates the conductivity in conjugated polymers with glycolated side-chains. The introduction of glycolated side-chains can enhance the conductivity of doped conjugated polymers substantially. This chapter presents a project using ultrafast spectroscopy and kinetic Monte Carlo simulations to identify the origin of the enhanced conductivity. The complex conductivity of a well-studied model system is analysed and compared to simulated complex conductivity spectra. This project aims to investigate the effect of the parameters: energetic disorder, dielectric constant, spatial confinement on the nanoscale and structural effects on the macroscopic scale separately.

The topic of Chapter 7 is charge transport in doped polymers. I utilize structural characterization, steady-state absorbance and cryogenic THz time-domain spectroscopy to observe doping-induced disorder and its effect on charge transport in state-of-the-art polymers. Doping has a delicate relationship with charge transport and effects the energetic landscape a charge carrier trespasses. The doping-induced disorder can be estimated by comparing the activation energy to transport and the variations in energy of electronic states resulting from different doping methods. This chapter systematically investigates the effect of backbone, side-chain and doping method on the conductivity and charge transport. Polymers forming anisotropic edge-on networks like PBTTT perform particularly well and have no activation to transport at room temperature. The polymer Pg_3BTTT shows a high conductivity of $4800\,S\,cm^{-1}$ and thermoelectric power factor of $230\,mW\,cm^{-1}\,K^{-1}$. These materials are particularly resilient to doping-induced disorder, the paracrystallinity and lamellar stacking is comparable between doping methods. Contrarily, simple polythiophenes like $Pg_3$2T-T show a drop in conductivity and charge localization due to doping-induced structural changes when doping with Magic Blue. My findings indicate that particularly the formation of doubly-charged species [++] correlate with doping-induced disorder in polythiophenes. Anion exchange doping (AED) almost always mitigates doping-induced disorder. Anion exchange doping and resilient backbone engineering are identified as promising strategies to yield high conductivity and low charge localization in conductive polymers.

Photoconductivity is the topic of Chapter 8. In particular, this chapter presents a project on an organic–inorganic hybrid bilayer that finds application in optoelectronics. The hybrid system takes advantage of the processability of organic materials while benefiting from the high charge mobility of inorganic materials. In organic hybrid photovoltaics, light from the solar spectrum is absorbed forming an exciton, followed by a charge transfer at the interface of the bilayer, followed by the charge transport in an inorganic layer. Each step can contribute to losses that have a negative effect on the performance of the photovoltaics. Optical pump–THz probe spectroscopy is a specialised technique that can elucidate the nature and lifetime of photo-generated charge carriers. This chapter requires a broader background on materials beyond conjugated polymers, extending into the domain of molecular OSCs, non-fullerene acceptor molecules and inorganic transition-metal dichalcogenides. As such, this chapter broadens the scope of this thesis in regards to materials and technique. The aim is to identify the efficiency of charge generation, lifetime of charges after light absorption and the mobility of charges, to contribute to the improvement of organic–inorganic hybrid optoelectronics.

Following the results chapters, the thesis outlines general conclusions. The main take-aways of this thesis and their contribution to the research field is summarized. In conclusion, this thesis weaves together relevant fundamental concepts of >materials, charge transport, and spectroscopy< to set the appropriate terminology and background to discuss experimental results presented in Chapter 6, 7 and 8. The results chapters are adapted and extended versions from manuscripts for publication, so there is detailed information about the contributions of all involved colleagues and collaborators in the appendix. Moreover, the Chapters 3 and 4 represent a well-rounded literature review on the investigated materials and the reported transport models. They include controversial discussions, developments, and open questions in the field of doped organic semiconductors. Chapter 5 is a technical one to explain the advanced spectroscopic methods used in the experimental part. The relevant steps from raw data acquisition to result are presented there. Through this structure, the thesis deepens our understanding of doped conjugated polymers, contributes relevant and novel insights from ultrafast spectroscopy and also presents avenues for exploring material systems relevant to hybrid organic electronics.

2 Context and motivation

> *Look around you. How long does it take you to touch three items made of polymers and three electronic items?*
>
> Entry-level experiment.

Organic semiconductors (OSCs) combine the chemical properties of organic compounds with the electronic properties of a semiconductor. This chapter looks at the distinct chemical and electronic properties of OSCs and how these properties are used in state-of-the-art applications. The understanding of the connection between property and application will feed the context of research in this rapidly evolving field. There will be a snapshot of the market value of commercial applications of organic electronics to date. Then, the recent developments, challenges and open questions in the research field are presented. Each results chapter picks up on one or more of those open question in the research field later on. As such, the links between the research field and the scientific approach of this thesis are presented.

Applied incentives

The chemical and electronic properties of OSC are commercially used today with a global market value of around $80 billion. Moreover, it is projected to keep expanding by 20% in the next ten years[1, 2, 3, 4, 5]. Based on these 5 cited reports, this snapshot of the market value will clarify why *organic electronics* are becoming omni-present in our lives; likely as omni-present as polymers and electronics are independently. The organic electronics expansion is driven by increasing demand for energy-efficient, flexible, and lightweight electronic devices, particularly in consumer electronics, healthcare, and energy sectors. To advance these technologies, a deeper understanding of chemical and electronic properties of OSC is required.

The display sector is the largest and fastest-growing application, accounting for 55% share of the market. OLED technology is extensively used in smartphones, televisions and other displays due to its superior colour accuracy, energy efficiency, and flexibility. The colour accuracy is stemming from the chemical tunability or organic compounds. The energy efficiency is stemming from close-to-unity electroluminescence quantum yields. The flexibility is stemming from the lack of rigid crystallinity in comparison to inorganic semiconductors. This segment is expected to see continued growth, particularly with advancements in transparent, flexible and foldable displays. For example, the companies Samsung and LG have widely adopted OLED technology in their consumer products. Likewise, the OLED lighting sector is also seeing substantial growth with another 20% of the mentioned market share. OLED lighting offers the same advantageous properties as mentioned for displays. OLED displays and lighting are closely related, so the two sectors are feeding from similar research fields and will likely grow in parallel.

It is worth highlighting the first property mentioned: *chemical tunability*. Organic chemistry provides a broad toolbox for the synthesis of new materials, allowing researchers to design and produce an almost limitless variety of organic molecules with different properties. In fact, researchers apply machine learning tools to explore the "unlimited search space" of organic semiconductors that are considered for electronic applications[6].

Flexible and wearable electronics also have a significant share of the global market with 15%. The flexible and wearable properties of OSCs are stemming from their molecular structure. Organic semiconductors are made from carbon-based molecules or polymers that form flexible, π-conjugated structures. These materials have relatively weak van der Waals interactions between molecules or polymer chains, allowing them to bend or stretch without breaking. Particularly devices which consist of polymer chains, flexibility is a prominent property. Such materials I like to visualize as pearl necklaces. These polymers can be formulated to have a high degree of mechanical flexibility, which makes the resulting films resilient under bending, twisting, or stretching. In contrary, traditional inorganic semiconductors are typically rigid and brittle crystals based on the stronger covalent interactions[7].

When adding up these percentages, the mentioned applications represent 90% of today's global market value. That does not reflect any potential of the presented applications. Another highly interesting and relevant sector are bioelectronics and medical sensors. Bioelectronics and medical sensors have about 5% of market share.

These applications leverage the biocompatible and flexible properties of OSCs, for example in biosensors. In biosensing, they offer high sensitivity and low detection limits for biomolecules like glucose. As such, OSCs are also highly relevant in modern healthcare[8, 9].

In the context of bioelectronics, *biocompatible* means to be non-toxic and able to interface biological matter. Materials that are able to conduct ions and electrons are of particular interest. This class of OSCs is called organic mixed ionic electronic conductors (OMIECs) and is used to interface biology and electronics. The biocompatibility of OSCs stems from several intrinsic material properties and structural characteristics that align with biological environments. First, they are primarily composed of carbon-based materials which makes them less reactive with biological tissues compared to traditional inorganic materials. Many OMIECs are specifically designed to be inert or minimally reactive in physiological environments, thereby minimizing interactions that could harm cells or tissues. Second, they can be functionalized with biomolecules, peptides, or other targeting groups to promote selective interactions with specific targets like the before-mentioned glucose. This functionalization allows OSCs to integrate more closely with biological systems, creating more effective interfaces. Third, they can be modified to include hydrophilic side-chains, such as glycolated side-chains, which improve water uptake and enable better ion exchange. This hydrophilicity enhances compatibility with aqueous biological environments and helps with signal transduction in bioelectronic applications. Hydrophilic side-chains also improve material-processability in wet environments, allowing OSCs to function stably in bodily fluids, making them suitable for organic electrochemical transistors (OECTs) in *in-vivo* applications[10].

The last sector of organic electronics that is presented here is organic photovoltaics (OPVs). OPVs are gaining attention to complement traditional inorganic silicon-based photovoltaics in the energy sector. They are known for their flexible, semi-transparent and lightweight nature, which makes them suitable for integration into buildings and portable energy devices. Since the 2000s, polymeric OSC found application in OPVs as effective light-absorbing and charge-transporting material. The development of molecular OSCs as complementary electron-accepting materials created big improvements and hence attention. In particular small molecules called non-fullerene acceptors (NFAs) enhanced the power conversion efficiency. OPVs has only around 0.3% of the mentioned market share, but given the high total that still translates to $210 million. It remains a critical segment with growth driven by sustainability efforts and architectural freedom.

One property of OSCs that stands out and is utilized in OPVs is *semi-transparency*. This property stems from the molecular structure. Particularly π-conjugated systems absorb specific portions of the light spectrum, primarily in the visible or near-infrared (NIR) range. By carefully designing the molecular structure, researchers can tune the absorption spectrum to avoid or minimize certain wavelengths, allowing other portions of visible light to pass through. This selective absorption means that OPVs can be designed to absorb only the wavelengths necessary for energy conversion while letting others through[11, 12].

In conclusion, OSCs offer several properties such as chemical tunability, flexibility, biocompatibility, and semi-transparency. All organic electronic applications rely on charge transport in organic molecules and polymers. The ongoing motivation to investigate these materials is driven by potential applications in a wide range of state-of-the-art technologies, from OLED to wearables, biosensors and photovoltaics. The discussed connection between property and application fuels the understanding of research topics in this rapidly evolving field.

Fundamental incentives

A microscopic understanding of charge transport and conductivity in organic semiconductors has been a key objective of organic electronics research for several decades[13]. There are two quantities that define the conductivity in any material: the number of charge carriers (n) and the mobility of charge carriers μ. The mobility of charge carriers in organic semiconductors is typically $< 1\ \mathrm{cm^2\,V^{-1}\,s^{-1}}$, and high-mobility materials yield around $1–20\,\mathrm{cm^2\,V^{-1}\,s^{-1}}$[14, 15]. The highest mobility measured to date (and to my best knowledge), is $34\,\mathrm{cm^2\,V^{-1}\,s^{-1}}$ by a custom-made organic crystal for OLED applications[16]. While conjugated polymers (CPs) are most promising for printable, flexible and biocompatible applications, their mobility is lower than of organic crystals. CPs have many degrees of conformational freedom and interact with each other by weak van der Waals forces, which results in a complex microstructure in the solid-state[14]. This complex microstructure consists of ordered and disordered regions with distinct charge transport properties. Therefore, high-mobility polymers are tailored to facilitate charge transport by **engineering chemical structures for enhanced chain alignment and crystallinity**[15, 14]. As such, co-polymers with planar donor–acceptor–donor structure and improved chain alignment reach a mobility of $10\,\mathrm{cm^2\,V^{-1}\,s^{-1}}$[17]. Chain alignment and paracrystallinity have been identified the key parameters to promote the conductivity in CPs[15, 14, 18]. The dominant role of ordered regions in charge transport was highlighted through an electroluminescence study of a polymer with varying degrees of regioregularity, whereby the electroluminescence signals originated from the aggregated regions[14]. The correlation between aggregation, paracrystallinity and charge transport showcases how **electronic processes at different length scales** need to be considered to understand charge transport in CPs. It has been shown that in high-molecular-weight CPs, the limiting charge transport process is trapping by lattice disorder. Disorder-induced charge localization is well known in condensed matter. However, only short-range intermolecular aggregation is necessary to yield long-range charge transport, due to interconnectivity of ordered regions[14]. Interconnectivity of ordered regions occurs *via* different phenomena, whereby so-called tie chains, individual long polymer chains bridging regions, on multi-scale transport is reported repeatedly[14, 19, 20]. A second important phenomenon that interconnects ordered regions, even in ultra-dilute blends of CPs, is tunneling[21]. This paragraph can be summarized by two distinct research goals: (i) mitigating disorder-induced charge localization and (ii) understanding multi-scale charge transport in CPs.

Disorder in CPs is best classifying types of disorder such as conformational, structural, energetic and dynamic disorder, and putting them into relation. Conformational disorder stems from deviations in the torsional angles between monomer units and limits the conjugation length[22]. Structural disorder arises from irregular chain packing, point defects, and boundaries between ordered and disordered regions, all of which reduce the intermolecular overlap of π-orbitals and hinder charge transport[14, 19, 20]. As such, conformational and structural disorder lead to energetic disorder. Energetic disorder is defined by variations in energy levels of electronic states[22]. The larger the variations in energy levels of electronic states, the more localized are the charge carriers that occupy these electronic states[23, 24]. Dynamic disorder is defined by time-dependent fluctuations in molecular positions and electronic states due to vibrations or temperature changes. Dynamic disorder, also called transient disorder, is non-neglectable in soft materials like CPs and can localize charge carriers at a given point in time[15]. Disorder leads to charge localization by generating deep, isolated localized states that restrict charge movement. In materials with low dielectric constants, disorder-induced fluctuations are poorly screened. Therefore, polymers with high-dielectric constant and their potential in mitigating electrostatic fluctuation are investigated. Increasing the dielectric constant helps to mitigate these fluctuations, smoothing the energy landscape and enabling charges to escape deep, isolated localized states[25, 26].

Side-chain engineering is a great strategy to tailor polymer properties while preserving a known backbone structure[27, 28]. Glycolated side-chains, in particular, have gained a lot of attention for their enhanced solubility, dielectric constant ($\varepsilon = 5$[26]) and mixed electronic and ionic conductivity, making them ideal for OECTs[29, 30, 31]. By fine-tuning the length, regiochemistry and glycol content of these side-chains, researchers have optimized performance, achieving a balance between hydrophilicity and electronic properties to facilitate charge transport[27, 29, 30, 31, 32, 33]. The **enhanced conductivity with glycolated side-chains** is connected to a higher mobility rather than a higher number of charge carriers[34], which aligns with an improved paracrystallinity[30]. The polar polythiophene derivative P($g_4$2T-T) interestingly has enhanced conductivity upon co-processing with dopants in comparison to sequential solution-processing of the polymer and dopants[35]. The inverse preference is reported for other polymers, where co-processing with dopants can lead to doping-induced disorder[36, 37].

Molecular doping of polymers generates charge carriers *via* a redox reaction[38, 39, 40]. The ionized dopant remains in the film to stabilize the doping-induced charge carriers. Achieving high doping levels and high conductivities is not a straightforward aim. Doping can lead to a disruption of the polymer packing and thereby lead to doping-induced disorder, for example observed in the workhorse model system of poly(3-hexylthiophene) (P3HT) and dopant 2,3,5,6-tetrafluoro-7,7,8,8-tetracyanoquinodimethane (F_4TCNQ)[36, 41, 42]. The effect can be delegated using vapour deposition[43] or incremental doping concentrations[42]. The driving force for p-doping, given by the energy difference between the HOMO of the polymer and the LUMO of the dopant, with F_4TCNQ is limited by its LUMO energy level of −5.2 eV. Hence, many common polymers are not efficiently p-doped by F_4TCNQ and require stronger oxidants to reach high doping levels. To name examples, the donor-acceptor polymers based on diketopyrrolopyrrole like PDPP3T (HOMO≈ -5.2 eV) or the conjugated polymer F8T2 (HOMO≈ -5.5 eV) are widely used in organic electronic research but cannot be molecularly doped well using F_4TCNQ[44, 45, 46, 47]. Stronger oxidants for p-doping thereby aid the understanding of dopant–polymer interactions. For the glycolated polythiophene P($g_4$2T-T) double doping; i.e. the reduced dopant F_6TCNNQ^- undergoing another redox reaction to F_6TCNNQ^{2-} yielding two doping-induced carriers has been reported[48]. The development of the strong oxidant tris(4- bromophenyl)ammoniumyl hexachloroantimonate (Magic Blue or MB) proved to effectively dope polymers with HOMO energy beyond −5.2 eV[44]. Magic Blue also shows spontaneous modulation doping in aligned polymer films, which improves the charge carrier mobility by selective integration of the dopant into more disordered regions[49, 50]. In spontaneous modulation doping, selective integration of the dopant hence reduces packing disruptions in the ordered regions which are essential for charge transport. Moreover, ion exchange doping is a powerful tool to exchange the radical dopant counterions after they served the redox reaction with a polymer chain[45, 51, 52, 53]. Already the first letter by Yamashita *et al.* showed an improved conductivity and coherent transport of PBTTT upon anion exchange between $F_4TCNQ^{\cdot -}$ and $TFSI^-$ from the electrolyte LiTFSI[51]. The role of the counterion size and location have been investigated since with the observation that counterion size plays a minor role, while conductivity increases together with a reduction in structural and dynamic disorder[18, 53]. Recently in 2024, Lu *et al.* pointed out $FeCl_3$-doping leads to structural changes and an increase in face-on orientation in Pg_32T-T films[54], which showcases the severity of doping-induced structural and energetic changes for this material. Anion exchange doping is considered a two-step process of doping (driven by ΔE) and subsequent exchange of ions (driven entropically by grand excess of stable ions)[45, 51, 52, 53]. Yet, the electrolyte might affect the polarity of the doping solution, doping rate, and hence the resulting degree of disorder. As such, AED could become a controllable doping method to mitigate doping-induced disorder.

Besides molecular doping, photo-doping is highly interesting for novel optoelectronics. Following the prominent organic donor–acceptor molecule optoelectronics, hybrid organic–inorganic optoelectronics are investigated intensively[7, 55, 56, 57, 58, 59]. Particularly, combining transition-metal dichalcogenides (TMDs) with organic small molecules gained significant attention since Shastry *et al.* reported the photovoltaic effect in such a hybrid material (MoS_2:PTB7) in 2016[60]. To date, a major limitation for efficient charge generation in TMD:organic hybrid materials is defect-assisted electron–hole recombination across the hybrid interface being a key limiting factor[61] together with defects mediated[62]. WSe_2 is an ultrathin, flexible and semi-transparent transport layer. It has a direct bandgap in the visible (1.6 eV) and strong Coulomb binding energies (100–500 meV) which allows the effective formation of stable excitons[62, 63, 64].

Exciton dissociation at an interface with matching energy alignment can create highly mobile holes (50–200 $\mathrm{cm^2\,V^{-1}\,s^{-1}}$) in WSe_2[65, 66]. This motivates the combination of WSe_2 with electron-accepting small molecules for optoelectronics with highly mobile charge carriers. A famous class of organic small molecules are non-fullerene acceptors (NFAs), which led to major improvements in the organic photovoltaics field[67, 68, 69]. Among the high-efficiency NFAs, the ITIC family gained a lot of attraction since its first synthesis in 2015[70]. IT-4F is such a non-fullerene acceptor molecule that has shown efficient charge generation in combination with different donor molecules[71].

This thesis explores the mechanisms underlying the enhanced conductivity in conjugated polymers (CPs) with glycolated side-chains. Using THz spectroscopy, the work provides novel insights into the conductivity, multi-scale interconnectivity, and charge transport processes of doped CPs. Anion exchange doping is employed to investigate its impact on overall charge transport and doping-induced disorder in organic semiconductors (OSCs). Experiments on electrolyte concentration and resulting paracrystallinity demonstrate that anion exchange doping reduces doping-induced disorder and optimizes conductivity. The findings reveal that this doping approach overcomes various ceilings in conductivity of other doping methods, it allows for high charge carrier density while mitigating doping-induced disorder. Additionally, this thesis details the design, setup, and calibration of a custom cryogenic system for cryogenic THz time-domain spectroscopy. This system enables highly sensitive measurements of charge transport and charge localization as a function of temperature between 300 and 10 K. This technique provides novel and relevant insights into charge transport in doped CPs on short distances of few nanometers and cryogenic temperatures. Together, these contributions advance the understanding of doping methods and the role of glycolated side-chains in improving the performance of conjugated polymers. Moreover, the thesis investigates photoconductivity in a hybrid organic–inorganic bilayer (WSe_2–IT-4F), using optical pump–THz probe time-domain spectroscopy to investigate the number, mobility and lifetime of photo-generated charges in this material class. The insights contribute to understanding how hybrid organic–inorganic systems can be used and improved for optoelectronics.

References for Chapter 2

[1] Expert Market Research. Global organic electronics market report (2023). URL https://www.expertmarketresearch.com/reports/organic-electronics-market. Accessed: 2024-11-14.

[2] Precedence Research. Organic electronics market size, share, growth (2023). URL https://www.precedenceresearch.com/organic-electronics-market. Accessed: 2024-11-14.

[3] Zion Market Research. Organic electronics market by application (2023). URL https://www.zionmarketresearch.com/report/organic-electronics-market. Accessed: 2024-11-14.

[4] MarketsandMarkets. Organic electronics market - global forecast to 2028 (2023). URL https://www.marketsandmarkets.com/Market-Reports/organic-electronics-market-144113962.html. Accessed: 2024-11-14.

[5] IDTechEx. Flexible & printed electronics 2023-2033: Technologies, markets, forecasts (2023). URL https://www.idtechex.com/en/research-report/flexible-printed-electronics-2023-2033-technologies-markets-forecasts/. Accessed: 2024-11-14.

[6] Kunkel, C., Margraf, J. T., Chen, K., Oberhofer, H. & Reuter, K. Active discovery of organic semiconductors. Nature Communications **12** (1), 2422 (2021).

[7] Zhang, W., Li, X., Chen, Y. & Wang, L. Applications of organic solar cells in wearable electronics. Wearable Electronics **15** (2), 123–145 (2024).

[8] Hopkins, J., Fidanovski, K., Lauto, A. & Mawad, D. All-organic semiconductors for electrochemical biosensors: An overview of recent progress in material design. Frontiers in Bioengineering and Biotechnology **7**, 237 (2019).

[9] Gonzalez, M., Smith, J. & Lee, A. Organic electronics in biosensing: A promising frontier for medical and environmental applications. Biosensors **13** (11), 976 (2023).

[10] Rivnay, J. et al. Organic electrochemical transistors. Nature Reviews Materials **3**, 17086 (2018).

[11] Sekine, C., Tsubata, Y., Yamada, N., Kitano, M. & Doi, S. Recent progress of high performance polymer oled and opv materials for organic printed electronics. Science and Technology of Advanced Materials **15** (3), 034203 (2014).

[12] Solak, E. K. & Irmak, E. Advances in organic photovoltaic cells: a comprehensive review of materials, technologies, and performance. RSC Advances **13** (18), 12244–12269 (2023).

[13] Sirringhaus, H. Device physics of solution-processed organic field-effect transistors. Advanced Materials **17** (20), 2411–2425 (2005).

[14] Noriega, R. et al. A general relationship between disorder, aggregation and charge transport in conjugated polymers. Nature Materials **12**, 1038–1044 (2013).

[15] Fratini, S. et al. Charge transport in high-mobility conjugated polymers and molecular semiconductors. Nature Materials **19**, 491–502 (2020).

[16] Liu, J. et al. High mobility emissive organic semiconductor. Nature Communications **6**, 10032 (2015).

[17] Li, J. et al. A stable solution-processed polymer semiconductor with record high-mobility for printed transistors. Scientific Reports **2**, 754 (2012).

[18] Jacobs, I. E. et al. Structural and dynamic disorder, not ionic trapping, controls charge transport in highly doped conducting polymers. Journal of the American Chemical Society **144** (7), 3005–3019 (2022).

[19] Gu, K., Onorato, J. W., Luscombe, C. K. & Loo, Y.-L. The role of tie chains on the mechano-electrical properties of semiconducting polymer films. Advanced Electronic Materials **6** (5), 1901070 (2020).

[20] Lin, S., Onorato, J. & Luscombe, C. K. Impact of side chain engineering on the mechanical and electrical properties of conjugated polymers. Macromolecules **53** (13), 5614–5626 (2020).

[21] Keene, S. T. & Salleo, A. Efficient electronic tunneling governs transport in conducting polymer-insulator blends. Journal of the American Chemical Society **144** (23), 10368–10376 (2022).

[22] Lemaur, V. et al. Resilience to conformational fluctuations controls energetic disorder in conjugated polymer materials: Insights from atomistic simulations. Chemistry of Materials **31** (17), 6889–6899 (2019).

[23] Hoffmann, S. T., Bässler, H. & Köhler, A. What determines the inhomogeneous broadening of electronic transitions in conjugated polymers? The Journal of Physical Chemistry B **114** (51), 17037–17048 (2010).

[24] Venkateshvaran, D. et al. Approaching disorder-free transport in high-mobility conjugated polymers. Nature **515**, 384–388 (2014).

[25] Armin, A. et al. Engineering dielectric constants in organic semiconductors. Journal of Materials Chemistry C **5** (15), 3736–3747 (2017).

[26] Sami, S. et al. How ethylene glycol chains enhance the dielectric constant of organic semiconductors: Molecular origin and frequency dependence. ACS Appl Mater Interfaces **12** (15), 17783–17789 (2020).

[27] Giovannitti, A. et al. Controlling the mode of operation of organic transistors through side-chain engineering. Proc Natl Acad Sci U S A **113** (43), 12017–12022 (2016).

[28] Nielsen, C. et al. Molecular design of semiconducting polymers for high-performance organic electrochemical transistors. J Am Chem Soc **138** (32), 10252–10259 (2016).

[29] Moser, M. et al. Ethylene glycol-based side chain length engineering in polythiophenes and its impact on organic electrochemical transistor performance. Chem. Mater. **32** (15), 6618–6628 (2020).

[30] Hallani, R. et al. Regiochemistry-driven organic electrochemical transistor performance enhancement in ethylene glycol-functionalized polythiophenes. Journal of the American Chemical Society **143** (29), 11007–11018 (2021).

[31] Moro, S. et al. The effect of glycol side chains on the assembly and microstructure of conjugated polymers. ACS Nano **16** (12), 21303–21314 (2022).

[32] Tropp, J. et al. Revealing the impact of molecular weight on mixed conduction in glycolated polythiophenes through electrolyte choice. ACS Materials Letters **5** (5), 1367–1375 (2023).

[33] Siemons, N. et al. Impact of side-chain hydrophilicity on packing, swelling, and ion interactions in oxy-bithiophene semiconductors. Advanced Materials **34** (39), e2204258 (2022).

[34] Kroon, R. et al. Polar side chains enhance processability, electrical conductivity, and thermal stability of a molecularly p-doped polythiophene. Adv. Mater. **29** (24), 1700930 (2017).

[35] Hofmann, A. et al. Highly stable doping of a polar polythiophene through co-processing with sulfonic acids and bistriflimide. J Mater Chem C Mater **6** (26), 6905–6910 (2018).

[36] Jacobs, I. E. et al. Comparison of solution-mixed and sequentially processed P3HT:F_4TCNQ films: effect of doping-induced aggregation on film morphology. J. Mater. Chem. C **4**, 3454–3466 (2016).

[37] Chew, A. R., Ghosh, R., Shang, Z., Spano, F. C. & Salleo, A. Sequential doping reveals the importance of amorphous chain rigidity in charge transport of semi-crystalline polymers. The Journal of Physical Chemistry Letters **8** (20), 4974–4980 (2017).

[38] Lüssem, B., Riede, M. & Leo, K. Doping of organic semiconductors. physica status solidi (a) **210** (1), 9–43 (2013).

[39] Tietze, M. L. et al. Elementary steps in electrical doping of organic semiconductors. Nature Communications **9** (1), 1182 (2018).

[40] Moulé, A. J. et al. Quantifying polaron mole fractions and interpreting spectral changes in molecularly doped conjugated polymers. Advanced Electronic Materials **8** (4), 2100888 (2022).

[41] Duong, D. T., Wang, C., Antono, E., Toney, M. F. & Salleo, A. The chemical and structural origin of efficient p-type doping in P3HT. Organic Electronics **14** (5), 1330–1336 (2013).

[42] Untilova, V. et al. Intercalation and ordering of F_6TCNNQ and F_4TCNQ dopants in regioregular poly(3-hexylthiophene) crystals: Impact on anisotropic thermoelectric properties of oriented thin films. Macromolecules **54** (13), 6073–6084 (2021).

[43] Pingel, P. & Neher, D. Comprehensive picture of p-type doping of P3HT with the molecular acceptor F_4TCNQ. Physical Review B **87** (11), 115209 (2013).

[44] Hofmann, A. I. et al. Chemical doping of conjugated polymers with the strong oxidant Magic Blue. Adv. Electron. Mater. **6** (8), 2000249 (2020).

[45] Murrey, T. L. et al. Anion exchange doping: Tuning equilibrium to increase doping efficiency in semiconducting polymers. J. Phys. Chem. Lett. **12** (4), 1284–1289 (2021).

[46] Kim, N. Y. et al. Enhanced doping efficiency and thermoelectric performance of diketopyrrolopyrrole-based conjugated polymers with extended thiophene donors. Journal of Materials Chemistry C **9** (1), 340–347 (2021).

[47] Karpov, Y. et al. High conductivity in molecularly p-doped diketopyrrolopyrrole-based polymer: The impact of a high dopant strength and good structural order. Advanced Materials **28** (28), 6003–6010 (2016).

[48] Kiefer, D. et al. Double doping of conjugated polymers with monomer molecular dopants. Nat. Mater. **18** (2), 149–155 (2019).

[49] Dash, A. et al. Spontaneous modulation doping in semi-crystalline conjugated polymers leads to high conductivity at low doping concentration. Advanced Materials **36** (13), 2311303 (2024).

[50] Guchait, S. et al. Phase-selective doping of oriented regioregular poly(3-hexylthiophene-2,5-diyl) controls stability of thermoelectric properties. Advanced Functional Materials **34** (39), 2304411 (2024).

[51] Yamashita, Y. et al. Efficient molecular doping of polymeric semiconductors driven by anion exchange. Nature **572** (7771), 634–638 (2019).

[52] Jacobs, I. E. et al. High-efficiency ion-exchange doping of conducting polymers. Adv. Mater. **34** (22), 2102988 (2021).

[53] Xiong, M. et al. Counterion docking: a general approach to reducing energetic disorder in doped polymeric semiconductors. Nature Communications **15** (1), 4972 (2024).

[54] Lu, K. et al. Molecular doping-driven modulation of domain charge transport elevates thermoelectric performance in polar polythiophene. ACS Materials Letters **6** (9), 4351–4359 (2024).

[55] Han, J. et al. Recent progress in 2d inorganic/organic charge transfer heterojunction photodetectors. Advanced Functional Materials **32** (34), 2205150 (2022).

[56] Takada, J. & Saito, S. Progress in electroluminescent devices using molecular thin films. Japanese Journal of Applied Physics **34** (Part 1, No. 7A), 3864–3870 (1995).

[57] Gobbi, M., Orgiu, E. & Samorì, P. When 2d materials meet molecules: Opportunities and challenges of hybrid organic/inorganic van der waals heterostructures. Advanced Materials **30** (18), 1706103 (2018).

[58] Pandey, R. K. et al. Interface engineering for enhancement in performance of organic/inorganic hybrid heterojunction diode. Organic Electronics **45**, 26–32 (2017).

[59] Azadmanjiri, J. et al. 2d layered organic–inorganic heterostructures for clean energy applications. Journal of Materials Chemistry A **6** (9), 3824–3849 (2018).

[60] Shastry, T. A. et al. Mutual photoluminescence quenching and photovoltaic effect in large-area single-layer MoS_2–polymer heterojunctions. ACS Nano **10** (11), 10573–10579 (2016).

[61] Wang, H., Zhang, C. & Rana, F. Ultrafast dynamics of defect-assisted electron–hole recombination in monolayer MoS_2. Nano Letters **15** (1), 339–345 (2015).

[62] Yang, Y., Wang, Z., Zhang, Y., Zhang, Y. & Ni, Z. Substrate mediated electronic and excitonic reconstruction in a MoS_2 monolayer. Journal of Materials Chemistry C **8** (34), 11778–11785 (2020).

[63] Park, S. et al. Direct determination of monolayer MoS_2 and WSe_2 exciton binding energies on insulating and metallic substrates. 2D Materials **5** (2), 025003 (2018).

[64] Obaidulla, S. M., Supina, A., Kamal, S., Khan, Y. & Kralj, M. Van der Waals 2d transition metal dichalcogenide/organic hybridized heterostructures: Recent breakthroughs and emerging prospects of the device. Nanoscale Horizons **9** (1), 44–92 (2023).

[65] Allain, A. & Kis, A. Electron and hole mobilities in single-layer WSe_2. ACS Nano **8** (7), 7180–7185 (2014).

[66] Wu, Z. et al. Defects as a factor limiting carrier mobility in WSe_2: A spectroscopic investigation. Nano Research **9** (12), 3622–3631 (2016).

[67] Lin, Y. & Zhan, X. Non-fullerene acceptors for organic photovoltaics: an emerging horizon. Materials Horizons **1** (5), 470–488 (2014).

[68] Cheng, P., Li, G., Zhan, X. & Yang, Y. Next-generation organic photovoltaics based on non-fullerene acceptors. Nature Photonics **12** (3), 131–142 (2018).

[69] Hou, J., Inganäs, O., Friend, R. H. & Gao, F. Organic solar cells based on non-fullerene acceptors. Nature Materials **17** (2), 119–128 (2018).

[70] Lin, Y. et al. An electron acceptor challenging fullerenes for efficient polymer solar cells. Advanced Materials **27** (7), 1170–1174 (2015).

[71] Forti, G. et al. Recent advances in non-fullerene acceptors of the IDIC/ITIC families for bulk-heterojunction organic solar cells. International Journal of Molecular Sciences **21** (21), 8085 (2020).

3 Materials

> *"Make sure to build your home brick by boring brick, or the wolf's gonna blow it down."*
>
> Hayley Williams.

In this chapter, the necessary terminology for this thesis is established and the materials are defined. While the concepts are presented in a didactic fashion, it focuses on the materials relevant for the experimental part of this thesis. The chapter reviews key discussions on polymer processing, novel developments like anion exchange doping, and open questions like the role of charge spatial confinement and tie chains. Thereby, the relevance and innovation of the used materials is displayed.

3.1 Building blocks for organic semiconductors

In chemistry it can be useful to visualize a material in building blocks. Imagine blocks of π-bonded atoms, mostly carbon (C) and hydrogen (H), occasionally heteroatoms such as sulfur (S) or oxygen (O)[1]. Their electrical properties are determined by π-bonding of orbitals that constitute aromatic rings. When these rings align in the same plane, the orbital overlap extends across multiple rings. The spatial orbital overlap is commonly referred to as conjugation length. Any deviation from coplanarity, such as twisting of the backbone, reduces the conjugation length. Such twisting can arise from various chemical or physical factors[2]. The conjugated structure provides the pathway for charge transport. Polymer side-chains are functional groups attached to the main backbone of a polymer. They are typically pendant groups that extend outward from the repeating units in the polymer chain. Side-chains can significantly influence the physical, chemical, and electronic properties of the polymer by affecting factors such as the solubility, processability, and crystallinity[3]. The building blocks of organic semiconductors can be categorized into two major types: conjugated polymers and small molecules. Figure 3.1 shows the chemical structure of two examplary benchmark materials to visualize the concepts.

3.1.1 Conjugated polymers *versus* molecular OSCs

Conjugated polymers (CPs) are a special type of organic semiconductors which consist of long chains of repeating monomer units, making them highly flexible and easily processable. A common CP is the polythiophene with hexyl side-chains called poly(3-hexylthiophene) (P3HT). The key advantage of polymeric semiconductors is their mechanical flexibility and ease of solution-processing, which enables scalable techniques like inkjet printing and roll-to-roll fabrication[4]. However, their electronic properties can be more indeterminate than for small molecules due to variations in chain length and structural defects[5].

Molecular OSCs consist of discrete low-molecular-weight organic molecules such as pentacene, rubrene, or fullerenes[6]. These materials are more crystalline compared to polymers. However, they can be more difficult to process over large areas due to their tendency to solidify quickly and brittleness. Therefore, controlled processing of molecular OSCs more often requires vacuum deposition methods, but it allows for high-purity and minimal batch-to-batch variation[4]. An example of molecular OSCs which are used in optoelectronic applications are the derivatives in the so-called ITIC-family of indacenodithieno[3,2-b]thiophene-based materials[7]. Molecular OSCs from the ITIC-family serve as an electron-accepting material, pairing with electron-donor materials to form efficient heterojunctions for charge generation upon photo-excitation[7]. From the ITIC-family, IT-4F is a prominent derivative that performs well in terms of heterojunction efficiency[8, 9, 7].

The choice between polymers and small molecules is often dictated by the desired application. For instance, molecular OSCs are typically used in high-efficiency devices, while polymer-based OSCs are preferred for flexible and large-area applications. Figure 3.1 shows a schematic representation and the chemical structure of P3HT and IT-4F representing (a) polymeric and (b) molecular OSCs respectively. Thereby, the single white pearl represents the monomer unit of P3HT which is a thiophene. The chain of white pearls represents the polymer chain of P3HT which is a polythiophene. The IT-4F molecule is composed of distinct donor and acceptor units arranged in an s-shape within the structure. The individual end-capped grey pearls represent are the acceptor units

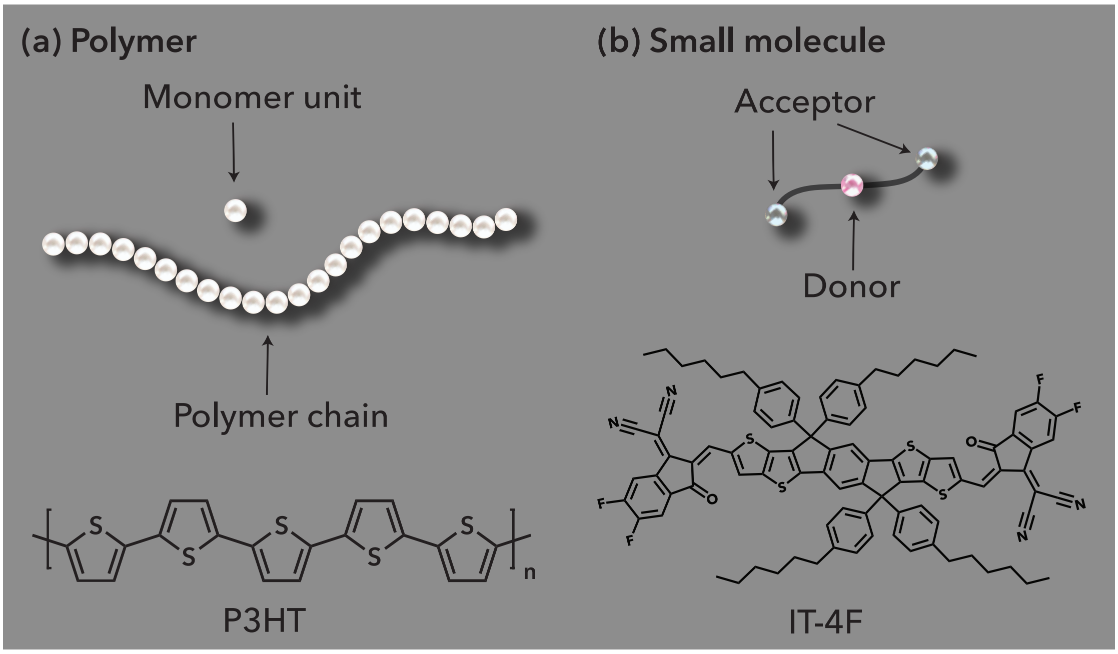

Figure 3.1: The building blocks of (a) polymeric OSCs with P3HT as example and (b) small molecule OSCs with IT-4F as an example.

containing fluorinated groups (-F) and cyano groups (-CN). These strongly electron-withdrawing groups enhance the molecule's electron affinity, promoting efficient charge transport. Lastly, the pink pearl represents the central fused-ring system consisting of benzothiadiazole and thiophene units, which acts as a donor unit in IT-4F.

3.1.2 Polymer backbones and side-chains

The backbone of an organic semiconducting polymer refers to the repeating core structure that forms the primary path for charge transport. OSCs possess conjugated backbones with alternating single and double bonds, enabling delocalized π-electrons and efficient charge transport. The Figure 3.2 showcases the range of conjugated polymer structures used in this thesis, emphasizing their diversity and the impact on electronic properties.

Polythiophenes such as P3HT are among the most studied conjugated polymers due to their relative ease of synthesis, ease of processing and good thermal and oxidative stability[10, 11]. P3HT is known for its practical solubility and moderate charge transport properties, with mobilities typically in the order of $0.1\,\mathrm{cm^2\,V^{-1}\,s^{-1}}$[12]. The incorporation of a thienothiophene unit in the backbone leads to increased planarity and stronger π–π stacking[13]. Hence, the polymer poly[2,5-bis(3-alkylthiophen-2-yl)thieno[3,2-b]thiophene] (PBTTT) exhibits higher mobilities on the order of 0.6–1 $\mathrm{cm^2\,V^{-1}\,s^{-1}}$[13].

Another benchmark material family other than polythiophenes are diketopyrrolopyrrole (DPP)-based polymers, such as PDPP3T and PDPP4T shown in Figure 3.2. The DPP-based materials have alternating electron donor–acceptor (D–A) type backbones. These backbones combine electron-rich (donor, D) and electron-deficient (acceptor, A) units, which enables a ground-state partial charge-transfer state. This in turn facilitates both intrachain and interchain charge transport[14]. The DPP core enhances charge delocalization along the backbone, while the side-chains influence packing and morphology. DPP polymers demonstrate mobilities exceeding 1 $\mathrm{cm^2\,V^{-1}\,s^{-1}}$[14].

The functional groups attached to the backbone further modulate the semiconductor's properties. For example, electron-withdrawing groups (e.g., fluorine) lower the material's energy levels, enabling n-type transport, while electron-donating groups enhance p-type behavior. Backbone planarity and rigidity, as illustrated in PBTTT and DPP backbones, are considered a route towards achieving high mobility. Planar backbones enable an increased conjugation length, intrachain transport, as well as π–π stacking and interchain overlap. Twisted or non-planar structures on the other hand reduce orbital overlap and hinder mobility. The resilience towards conformational fluctuations is relevant to optimize charge transport as shown by atomistic simulations[15].

While the backbone is essential for charge transport, side-chains attached to the backbone play an equally important role in determining solubility, processing behavior, and self-assembly of the material[3, 4, 12]. Many conjugated polymers, such as P3HT, include alkyl side-chains (e.g., hexyl groups) attached to the backbone. Additionally, side-chains can effect the morphology and electronic properties of the semiconductor thin films[3, 12, 16]. The length and structure of the side-chains can significantly influence the packing of organic semiconductor molecules in the solid state. Longer or branched side-chains can hinder π–π stacking interactions. Conversely, shorter or more linear side-chains may enhance packing and improve charge transport. Polar side-chains, such as glycolated side-chains, play a pivotal role in tuning the solubility, ion intercalation, and conductivity of conjugated polymers. By introducing polar functional groups into the side-chains, the polymer's solubility in polar solvents is significantly enhanced, facilitating solution processing and enabling uniform film formation. These side-chains also provide sites for ion intercalation, promoting better interactions with dopants or electrolyte ions during chemical or electrochemical doping. Literature highlights that polar side-chains can improve the ionic conductivity of mixed ionic-electronic conductors (OMIECs) by facilitating ion mobility and creating pathways for charge transport[17, 18]. Studies have further shown that the side-chain length and polarity must be carefully optimized, as excessive polarity or steric hindrance can disrupt molecular packing and reduce charge transport[19]. The comparison of the structures in 3.2 shows how backbone composition and side-chains govern chain planarity, mobility, processing and energetics relevant for doping and the resulting conductivity.

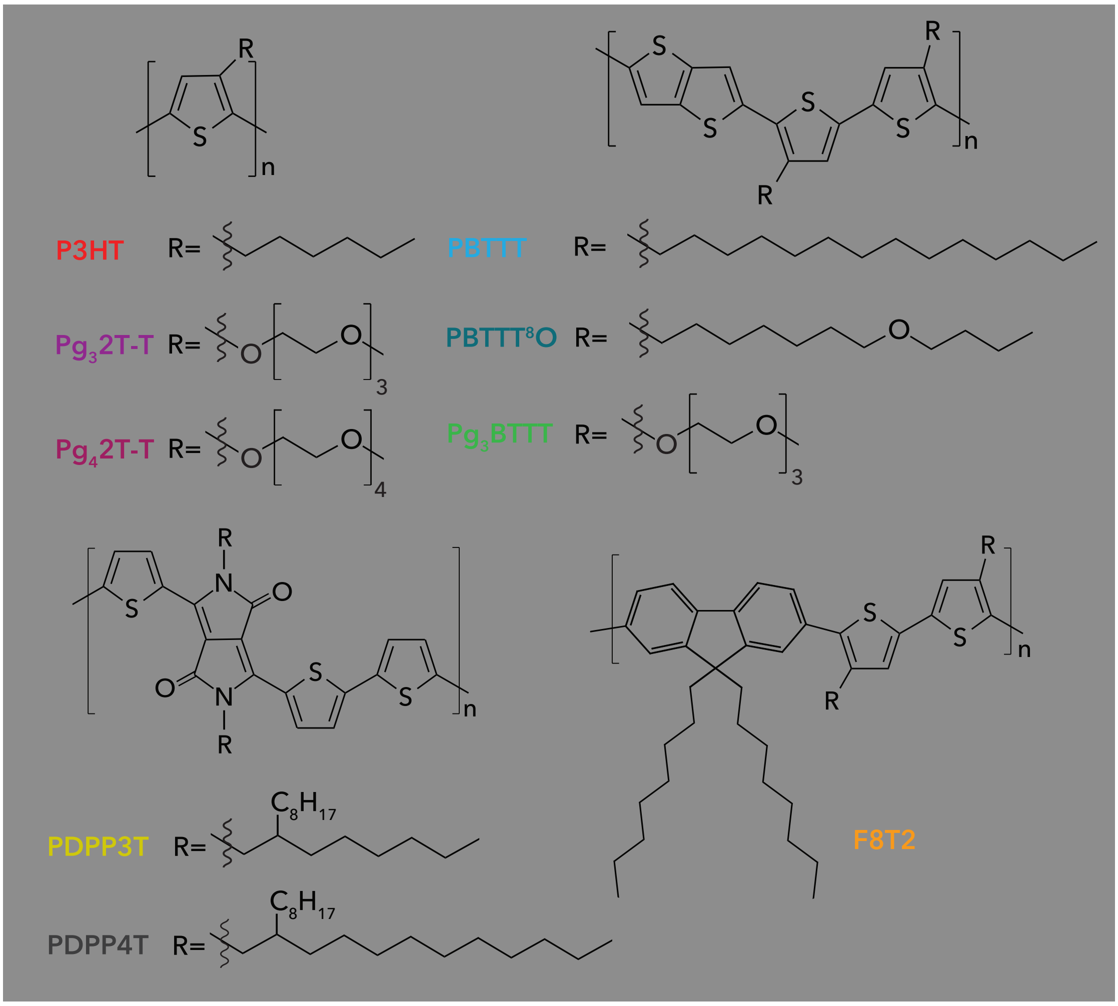

Figure 3.2: The backbones and side-chains of investigated polymers.

3.1.3 Hybrid organic–inorganic materials

Hybrid organic–inorganic materials represent a class of compounds that combine the flexibility, processability, and tunability of organic materials with the robustness, stability, and electronic properties of inorganic materials[20]. These hybrids are particularly attractive for applications in optoelectronics[21, 22, 23]. Beyond optoelectronics, hybrid materials can find applications in bioelectronics, energy storage or catalysis[24]. For the different applications, the architecture of the hybrid materials plays a crucial role. Porous architectures, for example, are a hot topic in bioelectronics and energy storage due to their high surface area for mixed ionic and electronic conduction. For optoelectronics, bilayer architectures, where an organic and inorganic material are layered atop one another, are particularly interesting[22, 25]. In strong contrary to porous architectures, they enable controlled interfaces and directed charge transport.

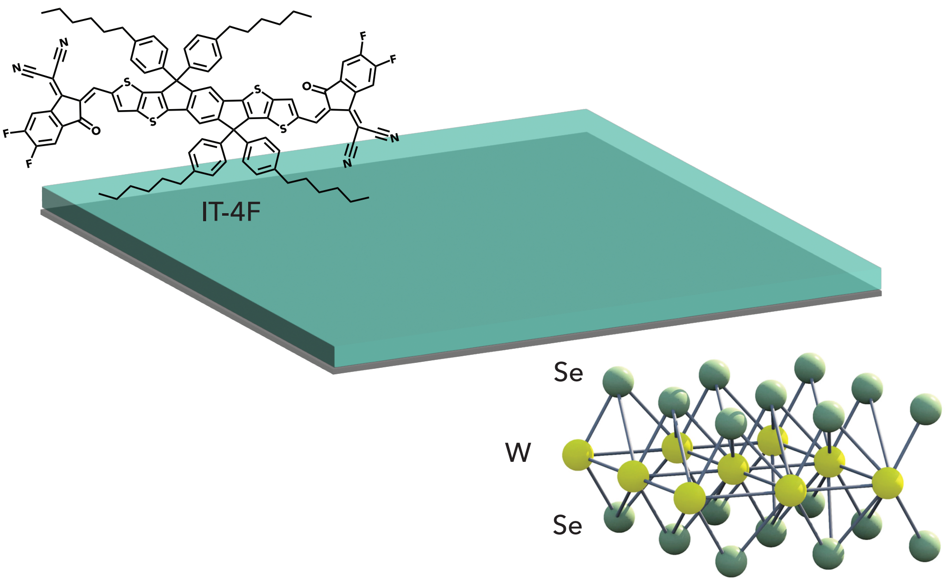

Figure 3.3: Structures of a IT-4F and WSe$_2$ hybrid bilayer. Atomic structure adopted[26].

While the bilayer architecture provides these distinct advantages, they also come with persisting challenges. The interface between the organic and inorganic materials can lead to issues with charge recombination, or exciton diffusion length, potentially reducing device efficiency[20, 27]. Furthermore, achieving a uniform and stable interface can be difficult due to differences in lattice structures, thermal expansion, and chemical compatibility between organic and inorganic layers[22, 28]. To address these challenges, relevant concepts such as energy level alignment, exciton dissociation, and interfacial dipoles must be considered, as they significantly impact the efficiency of charge transfer and the stability of the bilayer architecture.

A promising combination in hybrid materials is that of organic small molecules with transition-metal dichalcogenides (TMDs) and shown in Figure 3.3. As introduced for small molecule OSCs in section 3.1.1, IT-4F is a non-fullerence acceptor molecule used in organic photovoltaics. On the other hand, TMDs like tungsten diselenide (WSe_2) offer direct bandgaps in monolayer form, and stable electronic characteristics[29, 30].

3.2 Microstructure

3.2.1 Packing and vibrational modes

The packing of molecular building blocks in conjugated polymers is governed by non-covalent interactions such as π–π stacking, hydrogen bonding, and van der Waals forces, which are central to self-assembly and microstructure formation. These non-covalent interactions allow for dynamic fluctuations of the structure. In conjugated polymers, vibrational modes are relatively strong due to the flexibility of polymer chains and the coupling between electronic and vibrational states. This vibrational coupling is less pronounced in molecular organic semiconductors (OSCs) where the molecular rigidity suppresses some vibrational degrees of freedom, leading to stronger π–π interactions[31, 32]. The HJ model provides a useful framework for understanding this behavior[31]. Chain planarity and straightness enhance J-type intramolecular aggregation of monomers (head-to-tail coupling). On the other hand, strong vibrational modes in polymers can hinder intermolecular order transiently, leading to a competition between vibrational and electronic coupling. Studies on isolated polymer chains confined in DNA scaffolds[33] or side-chain alignment[34, 35], illustrate that straightened chains exhibit enhanced J-type intramolecular aggregation and improved electronic coupling. Moreover, Lemaur *et al.* show that the resilience to conformational fluctuations controls the energetic disorder and hence the electronic coupling[15].

3.2.2 Ordered and disordered regions

The microstructure of conjugated polymers is a heterogeneous combination of ordered and disordered regions, with significant implications for charge transport. Ordered regions, formed through robust π–π stacking and molecular alignment, facilitate charge transport. Disordered regions, in contrast, can interrupt long-range order and limit charge transport. The interplay between these regions directly influences charge carrier dynamics[12]. As highlighted by Raman spectroscopy studies, doubly charged bipolarons preferentially form in disordered domains[36]. This occurs because these regions lack tight packing and host more counterions, making them energetically favorable for polaron and bipolaron formation[37]. Tie chains, polymer segments that connect crystalline domains, play a critical role in maintaining electrical connectivity by bridging these ordered and disordered regions[12, 38]. As such tie chains improve charge transport across longer distances. While the interconnectivity of ordered regions is an identified key route towards high-mobility, charge transport in disordered regions or amorphous materials occurs as well. As such, ultra dilute polymer–insulator blends maintain effective charge transport with a low mobility[39]. Thereby, charge carriers can traverse disordered regions through quantum tunneling, maintaining overall conductivity despite microstructural disruptions[39]. The importance of fluctuation-induced mechanisms such as tunneling for charge transport in disordered materials is reported since decades[40, 41]. Together, the structural characterization is a decisive factor in understanding charge transport in OSCs.

3.3 Doping

3.3.1 Classification of doping

It is fascinating to consider the versatility of a polymer host capable of being doped through distinct methods: chemical, electrochemical, and photo-induced doping. Each doping approach interacts with the polymer differently, generating charge carriers *via* a different doping mechanism, yet one can learn a lot by comparing the material's doping properties and doping-induced charge carrier properties.

This section explains the classification of doping. The thesis will include three different types of doping, which are shown in figure 3.4. The visualization is organized from left to right, showing three types of doping: (a) chemical doping, (b) electrochemical doping, and (c) photo-induced doping. Each section depicts energy levels and how the doping mechanism creates charge carriers in the polymer film.

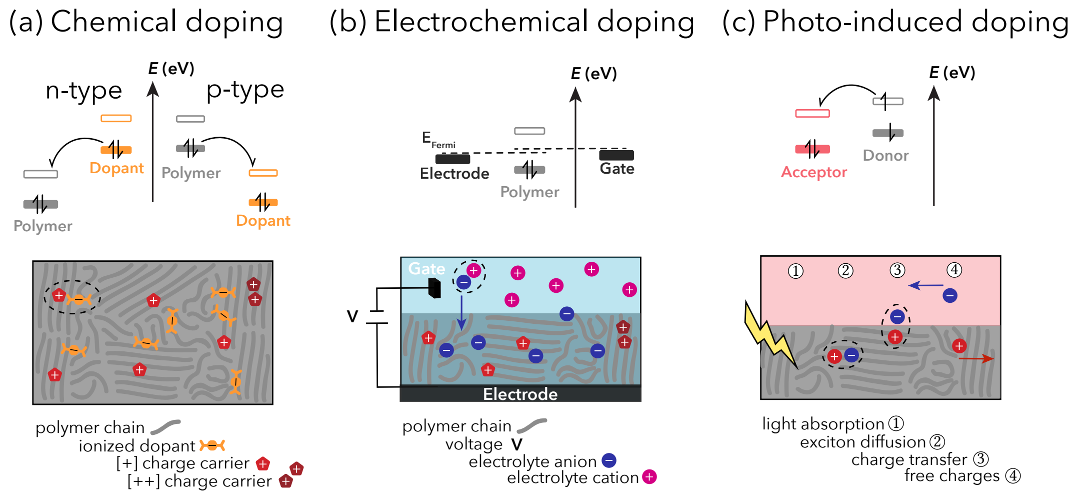

Figure 3.4: Simple scheme on the classification of doping. Energy levels and film with different doping-induced charge carriers. From left to right (a) chemical doping (b) electrochemical doping and (c) photo-induced doping.

Chemical doping

In chemical doping, the polymer interacts with external molecular dopant, by either accepting or donating electrons, leading to the creation of negative charge carriers like electrons in **n-type doping** or positive charge carriers like holes in **p-type doping**, respectively. This process embeds ionized dopants within the polymer matrix, which has an influence on the doping-induced charge carriers on the polymer chain.

Regarding the **energy levels**, as seen in Figure 3.4 (a), there are specific energy levels that allow chemical doping of a polymer with a molecular dopant. The energy levels in (a) illustrate the relevant HOMO (filled bar) and LUMO (unfilled bar) levels of polymer and molecular dopant. In the case of n-type doping, the molecular dopant, called reductant or donor, donates electrons to the polymer's LUMO level, resulting in negative charge carriers in the polymer. This n-type doping creates a partial filling of the molecular orbital which allows for effective electron transport; then the molecular orbital is called singly-occupied molecular orbital (SOMO). In the case of p-type doping, the dopant, called oxidant or acceptor, accepts electrons from the polymer's HOMO level, creating positive charge carriers (holes) in the polymer. This p-type doping enhances conductivity through the introduction of vacant energy states in the HOMO. The manipulation of HOMO and LUMO energy levels through variation of the host or the molecular dopant is therefore essential in tuning the electronic properties of chemically doped materials[42, 43, 44, 45].

The doping-induced **charge carriers** are quasiparticles consisting of charges that propagate along the polymer matrix. Since this thesis includes exclusively examples and results of p-type doping, the scheme also depicts p-type doping and hence positive charge carriers. The bottom part of Figure 3.4 (a) is a scheme of a polymer film including polymer chains, the ionized dopant and doping induced charge carriers. In the shown example of p-type doping, the dopant anion is embedded in the film complementing the positive doping induced charge carriers. There can be singly charged quasiparticles, called **polarons** or shortened by **[+]**, and doubly charged quasiparticles shortened by **[++]**. The charge carriers and their characteristics deserve their own section in this thesis, which can be found in Subsection 5.1.2.

Electrochemical doping

In this thesis, electrochemical doping is only a supplementary result. Hence, a rigorous explanation of the theory is published elsewhere[11, 19, 46, 47, 48]. Electrochemical doping, as shown in Figure 3.4 (b), enables dynamic modulation of charge carriers by applying a voltage. The subfigure illustrates a simple electrochemical cell, where a polymer film is coated onto an electrode and immersed in an electrolyte containing both cations and anions. A quasi-reference electrode is typically in contact with the electrolyte. When a voltage is applied, the electrode withdraws electrons from the polymer, oxidizing it, while electrolyte anions migrate into the polymer to maintain overall charge neutrality. This process allows precise control over the doping level and thereby the polymer's charge carrier density.

The interpretation of energy levels in Figure 3.4 (b) should be interpret with caution. Since the electrode material is often an inorganic semiconductor, it is described using band theory rather than molecular orbital terminology. For instance, indium tin oxide (ITO), a commonly used transparent conducting oxide, has a wide bandgap (3.5–4.3 eV), making it transparent in the visible range while maintaining high electrical conductivity. In electrochemical doping, the external voltage induces oxidation of the polymer, drawing an analogy to chemical doping, where charge carriers are introduced and stabilized by electrolyte counterions. In a two-electrode electrochemical cell, talking about the work funtios is more sensical than talking about the electrochemical potentials of individual components, because the electrochemical potential must be constant across the cell at equilibrium.[11, 19, 46, 47, 48].

The lower part of Figure 3.4 (b) schematically represents the polymer film, illustrating polymer chains, the applied electric field (vertically oriented between the gate electrode and the working electrode), and the migration of electrolyte anions and cations. In the case of p-type electrochemical doping, an applied voltage facilitates the oxidation of the polymer, generating positive charge carriers, while electrolyte anions enter the polymer to ensure charge compensation. Although the doping-induced charge carriers in chemical and electrochemical doping are fundamentally similar, the electrolyte environment in electrochemical doping alters their properties. A comparative discussion on charge carriers in chemically and electrochemically doped films is provided in the supplementary information ofChapter 6, where I quantify the relative populations of charged species in molecularly doped films. To achieve this, I use spectroelectrochemistry to identify the spectral signatures of charged species and compare them with the absorbance spectra of molecularly doped films. While spectroscopy itself is not inherently quantitative, it provides valuable insights into the nature and distribution of charge carriers.

Photo-induced doping

Figure 3.4 (c) shows photo-induced doping, which leverages light energy to create excitons within the polymer that subsequently dissociate into free charge carriers. Here, charge carriers are generated without the need for external dopants or ions, but by utilizing an interface between a donor (polymer) and an acceptor (small molecule) for efficient exciton dissociation.

The top part of Figure 3.4 (c) shows the **energy levels** of donor and acceptor materials. In photo-induced doping, light absorption initiates the doping process. Upon light absorption, an electron gets elevated from the HOMO to the LUMO energy level. In other words, an electron–hole pair, called an **exciton**, forms in the polymer. This stage is depicted in the energy level diagram in Figure (c), one can see the stage upon light absorption in the donor. The 4 steps for charge carrier formation upon photo-induced doping are: 1. light absorption, 2. exciton diffusion, when an exciton migrates through the material, 3. charge transfer (CT), when the excitons dissociate at the donor/acceptor interface and 4. free charges, which can move in the respective layer. The schematic illustrates these four steps upon light absorption by the donor layer.

From the intermediate CT state, charges can either separate fully to become mobile or recombine through geminate recombination, a process where the electron and hole recombine before escaping the Coulombic binding. The extent of geminate recombination is a significant limiting factor in achieving a high yield of mobile charges. Furthermore, after full charge separation, non-geminate recombination (or bimolecular recombination) can occur. In non-geminate recombination mobile charges from a different CT state encounter and recombine, reducing the overall population of mobile carriers. To ensure efficient photo-induced doping and charge mobility in such systems, it is crucial to optimize exciton diffusion, minimize geminate recombination by controlling the driving force for charge separation, and suppress non-geminate recombination through improved charge transport properties. These processes collectively determine the efficiency of generating and maintaining mobile charges in bilayer systems[7, 8, 49].

To sum up, the simple Figure 3.4 effectively shows the types of doping which all are relevant to the thesis. In summary, the different mechanisms for doping and generating charge carriers in conjugated polymers are: chemical doping through charge transfer with molecular dopants, electrochemical doping *via* ion-migration, and photo-induced doping initiated by light absorption. Comparing these methods highlights the adaptability of polymers, where the nature and control of doping-induced charge carriers offer diverse pathways to tailor the material's electronic properties for specific technological needs.

3.3.2 Chemical doping methods

From the above classification of doping, chemical (molecular) doping of conjugated polymers gains special attention in this thesis. In chemical doping, the ionized dopant molecule resides in the polymer matrix permanently. Therefore, the relationship between ionized dopant and conductivity is complex and important to understand. While the driving force for doping has been discussed in the previous section, doping-induced charges are not necessarily mobile. The ionized dopant itself creates an electrostatic potential well that might attract and localize induced charges according to the Coulomb force F.

$$F = k_\mathrm{e}\frac{q_1 q_2}{r^2}, \tag{3.1}$$

with the Coulomb's constant expressed by:

$$k_\mathrm{e} = \frac{1}{4\pi\varepsilon_0} \tag{3.2}$$

Here, the Coulomb's constant is denoted by $k_\mathrm{e} \approx 8.9875 \times 10^9\,\mathrm{N\,m^2C^{-2}}$. The magnitude of the two involved charges q_1 and q_2 , in this case ionized dopant and doping-induced charge carrier, are equal to the elementary charge e. The distance between two charges is denoted by r. And lastly, the permittivity $\varepsilon_0 = 8.85 \times 10^{-12}$ is a fundamental physical constant that quantifies how electric fields behave in a vacuum. At high doping levels the distance between ionized dopants gets smaller. Their electrostatic potential wells overlap with each other, smoothening out and lowering their overall depth. Therefore, the negative effect of trapping by dopant potential wells becomes weaker at high doping levels, which is referred to as Coulomb screening.

The applied method for chemical doping has effects on the doping efficiency and the resulting polymer:dopant microstructure[1, 50, 51]. The doping efficiency is governed by the dissociation of charge-transfer complexes and the Coulomb radius between the charge carriers and counterions[52]. The polymer:dopant microstructure is governed by non-covalent interactions as well[53]. Figure 3.5 illustrates three common chemical doping methods: co-processing, sequential spin-coating and immersed doping.

In co-processing (a), the polymer and dopant are mixed into a single solution and deposited simultaneously onto a substrate, such as a glass slide, using spin-coating. This method ensures homogeneous mixing of the polymer and dopant, often leading to uniform distribution of dopant molecules throughout the polymer matrix. However, the resulting microstructure may be limited by the solubility and miscibility of the components. In sequential spin-coating (b), a dopant solution is spin-coated on top of a pre-formed polymer film from an orthogonal solvent. This stepwise approach allows for precise control of the doping process and the dopant concentration, as the dopant diffuses into the polymer film from the surface. In immersed doping (c), the polymer film is dipped into a dopant solution, promoting diffusion of the dopant molecules into the polymer matrix over time. This method is particularly effective for achieving

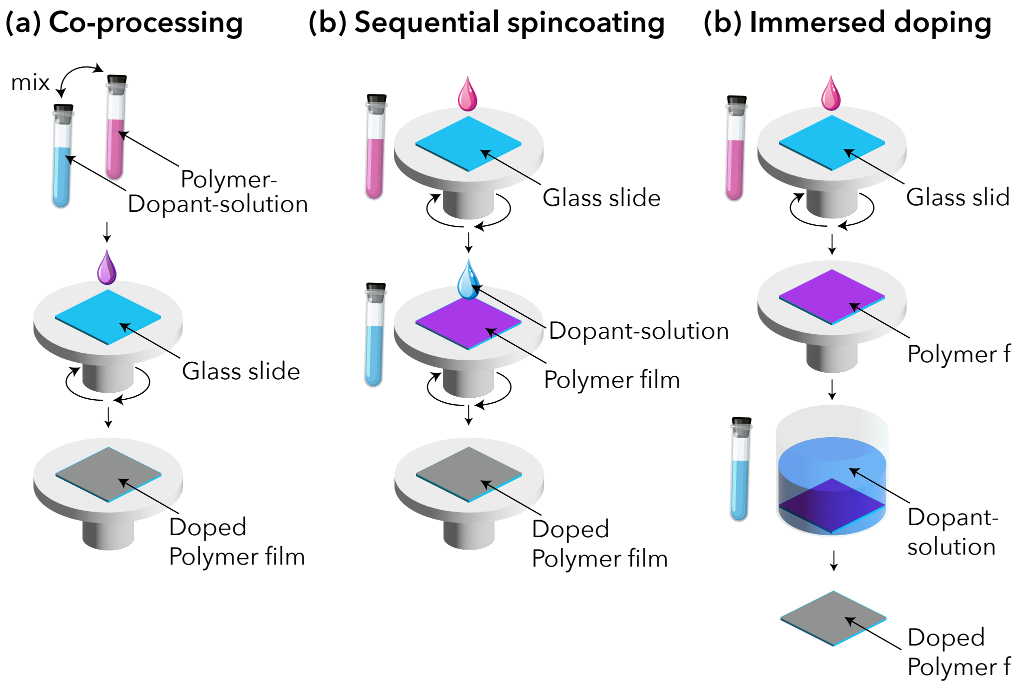

Figure 3.5: Steps of chemical doping by (a) co-processing (b) sequential spin-coating and (c) immersed doping.

deep penetration of dopants, making it suitable for thick films. Immersed doping is diffusion-limited, and the final distribution of dopant molecules depends on the soaking time and the interaction between the polymer and dopant.

These methods provide different degrees of control over the polymer:dopant microstructure, which affects the conductivity, mobility, and charge carrier density. In science, controllable doping methods with reproducible high conductivities are constantly evolving and may include specific incremental steps. In industry, on the other hand, there is a high interest in simple methods that are easily scalable, such as co-processing in one step.

Sequential doping has emerged as a good technique for achieving precise control over doping levels and polymer microstructure. As such, the doping intercalation and doping level can be tuned by adjusting the dopant solution concentration or solvent properties. Immersed doping represents another sequential method with the mentioned advantages. By immersing a polymer film in a dopant solution, the dopant molecules diffuse into the polymer matrix over time. In comparison to sequential spin-coating, the polymer matrix typically has more time to swell in the orthogonal solvent. The immersed doping approach offers high doping control through the duration of immersion, dopant concentration and solvent interactions. Therefore, literature on passive (and active) swelling, including techniques like Quartz Crystal Microbalance with Dissipation (QCM-D), is highly relevant not only for electrochemical doping[54]. A significant advancement in this technique is incremental immersed doping, where the polymer film is sequentially dipped into dopant solutions with progressively higher concentrations or different compositions[55]. This incremental immersed doping also allows phase-selective doping, where the film is dipped in different dopant solutions optimized for different regions of the polymer matrix. Similarly to phase-selective doping, recent studies also highlight the concept of spontaneous modulation doping. In spontaneous modulation doping, the dopants energetically prefer to reside in different regions of the polymer matrix[56, 57]. This occurs due to energetic and microstructural heterogeneities within the film, creating a modulation of doping density. This phenomenon can improve charge carrier mobility by promoting charge delocalization in ordered regions and reducing Coulomb traps[56, 57]. The development of dopants with an affinity to reside in disordered regions has been identified as a route to higher conductivity in chemically doped polymers. In general, the docking of dopants in a polymer matrix is a promising route to increase conductivity and contains an almost limitless number of combinations[53].

Together, these methods demonstrate that the doping process is not merely a means of introducing charges but also a critical tool to control the polymer microstructure and conductivity. The ability to control doping level and intercalation through sequential or immersed doping, as well as the emerging potential of co-crystallization, highlights their importance. A careful consideration of these strategies promises optimized doping methods for highly conductive conjugated polymers.

3.3.3 Anion exchange doping

Anion exchange doping (AED) involves an exchange of the ionized dopant with a stable electrolyte ion. AED is a doping method that builds on the concept of immersed doping by incorporating a second step involving ion exchange. The pioneering work on AED by Yamashita *et al.* demonstrated that replacing radical dopant anions with more stable electrolyte anions enhances the stability of doped polymer systems[58].

The schematic in 3.6 illustrates the AED process compared to ID. In the ID method shown in (a), the polymer film is immersed in a solution containing the dopant. The dopant diffuses into the films and initiates the redox reaction of molecular doping. The ionized dopant resides in the doped polymer film also when the film is dry. In the AED method shown in (b), the polymer film is immersed in a solution containing the dopant and an electrolyte. The dopant (and electrolyte ions) diffuse into the film. The dopant initiates the redox reaction of molecular doping the polymer. The ionized dopant and a more stable electrolyte ions exchange. The electrolyte counterions stay in the dry polymer film. In AED, the driving force of the doping process is still determined by the difference in HOMO and LUMO energy levels between the polymer and dopant respectively. The ion exchange is entropically driven. To assure an efficient exchange between ionized dopant and electrolyte ion, the electrolyte has to be added in high excess[52, 58]. Recent studies report an increase in conductivity, that often comes from a higher paracrystallinity of ordered regions in the polymer[53, 59]. These findings demonstrate the synergistic effect on structural order and charge transport. Notably, studies on ion size dependence suggest that at high doping levels the conductivity enhancement is not significantly correlating with the size of the exchange ion[53, 59, 60]. To sum up, AED combines the benefits of precise doping control, improved stability, improved microstructure and enhanced conductivity, making it a transformative method for chemical doping of conjugated polymers.

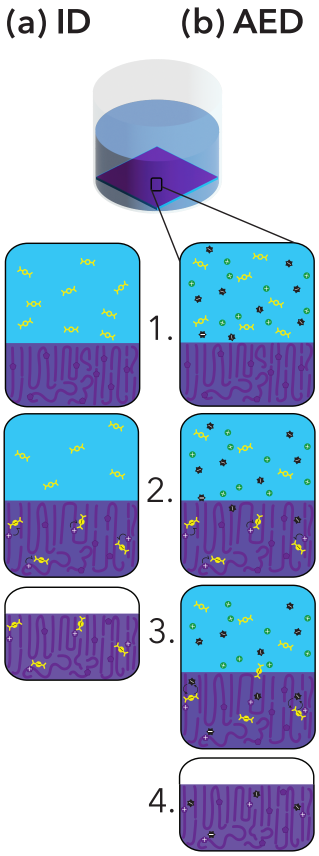

Figure 3.6: Scheme of methods (a) immersed doping (b) anion exchange doping.

References for Chapter 3

[1] Tietze, M. et al. Fermi level shift and doping efficiency in p-doped small molecule organic semiconductors: A photoelectron spectroscopy and theoretical study. Physical Review B **86** (3) (2012).

[2] Bobade, R. S. Polythiophene composites: a review of selected applications. Journal of Polymer Engineering **31** (3), 209–215 (2011).

[3] Meyer, D. L. et al. Side-chain engineering of conjugated polymers: Distinguishing its impact on film morphology and electronic structure. The Journal of Physical Chemistry C **123** (33), 20071–20083 (2019).

[4] Ding, L. et al. Polymer semiconductors: Synthesis, processing, and applications. Chemical Reviews **123**, 7421–7497 (2023).

[5] Fratini, S. et al. Charge transport in high-mobility conjugated polymers and molecular semiconductors. Nature Materials **19**, 491–502 (2020).

[6] Yang, H., Gajdos, F. & Blumberger, J. Intermolecular charge transfer parameters, electron–phonon couplings, and the validity of polaron hopping models in organic semiconducting crystals: Rubrene, pentacene, and c60. The Journal of Physical Chemistry C **121** (14), 7689–7696 (2017).

[7] Forti, G. et al. Recent advances in non-fullerene acceptors of the IDIC/ITIC families for bulk-heterojunction organic solar cells. International Journal of Molecular Sciences **21** (21), 8085 (2020).

[8] Hou, J., Inganäs, O., Friend, R. H. & Gao, F. Organic solar cells based on non-fullerene acceptors. Nature Materials **17** (2), 119–128 (2018).

[9] Cheng, P., Li, G., Zhan, X. & Yang, Y. Next-generation organic photovoltaics based on non-fullerene acceptors. Nature Photonics **12** (3), 131–142 (2018).

[10] Yamamoto, T., Sanechika, K. & Yamamoto, A. Preparation of thermostable and electric-conducting poly(2,5-thienylene). Journal of Polymer Science, Polymer Letters Edition **18**, 9–12 (1980).

[11] Nielsen, C. B. & McCulloch, I. Recent advances in transistor performance of polythiophenes. Progress in Polymer Science **38** (12), 2053–2069 (2013).

[12] Noriega, R. et al. A general relationship between disorder, aggregation and charge transport in conjugated polymers. Nature Materials **12**, 1038–1044 (2013).

[13] Do, K., Huang, D. M., Faller, R. & Moulé, A. J. A comparative md study of the local structure of polymer semiconductors p3ht and pbttt. Physical Chemistry Chemical Physics **12**, 14735–14739 (2010).

[14] Li, J. et al. A stable solution-processed polymer semiconductor with record high-mobility for printed transistors. Scientific Reports **2**, 754 (2012).

[15] Lemaur, V. et al. Resilience to conformational fluctuations controls energetic disorder in conjugated polymer materials: Insights from atomistic simulations. Chemistry of Materials **31** (17), 6889–6899 (2019).

[16] Lin, S., Onorato, J. & Luscombe, C. K. Impact of side chain engineering on the mechanical and electrical properties of conjugated polymers. Macromolecules **53** (13), 5614–5626 (2020).

[17] Kroon, R. et al. Polar side chains enhance processability, electrical conductivity, and thermal stability of a molecularly p-doped polythiophene. Adv. Mater. **29** (24), 1700930 (2017).

[18] Kiefer, D. et al. Double doping of conjugated polymers with monomer molecular dopants. Nat. Mater. **18** (2), 149–155 (2019).

[19] Moser, M. et al. Ethylene glycol-based side chain length engineering in polythiophenes and its impact on organic electrochemical transistor performance. Chem. Mater. **32** (15), 6618–6628 (2020).

[20] Gobbi, M., Orgiu, E. & Samorì, P. When 2d materials meet molecules: Opportunities and challenges of hybrid organic/inorganic van der waals heterostructures. Advanced Materials **30** (18), 1706103 (2018).

[21] Han, J. et al. Recent progress in 2d inorganic/organic charge transfer heterojunction photodetectors. Advanced Functional Materials **32** (34), 2205150 (2022).

[22] Pandey, R. K. et al. Interface engineering for enhancement in performance of organic/inorganic hybrid heterojunction diode. Organic Electronics **45**, 26–32 (2017).

[23] Shastry, T. A. et al. Mutual photoluminescence quenching and photovoltaic effect in large-area single-layer MoS_2–polymer heterojunctions. ACS Nano **10** (11), 10573–10579 (2016).

[24] Zhang, W., Li, X., Chen, Y. & Wang, L. Applications of organic solar cells in wearable electronics. Wearable Electronics **15** (2), 123–145 (2024).

[25] Azadmanjiri, J. et al. 2d layered organic–inorganic heterostructures for clean energy applications. Journal of Materials Chemistry A **6** (9), 3824–3849 (2018).

[26] Vienna, T. Atomically thin solar cells made from tungsten and selenide (2014). URL https://www.laborpraxis.vogel.de/atomar-duenne-solarzellen-aus-wolfram-und-selen-a-437278/. Accessed: 2024-12-29.

[27] Yang, Y., Wang, Z., Zhang, Y., Zhang, Y. & Ni, Z. Substrate mediated electronic and excitonic reconstruction in a MoS_2 monolayer. Journal of Materials Chemistry C **8** (34), 11778–11785 (2020).

[28] Park, S. et al. Direct determination of monolayer MoS_2 and WSe_2 exciton binding energies on insulating and metallic substrates. 2D Materials **5** (2), 025003 (2018).

[29] Allain, A. & Kis, A. Electron and hole mobilities in single-layer WSe_2. ACS Nano **8** (7), 7180–7185 (2014).

[30] Wu, Z. et al. Defects as a factor limiting carrier mobility in WSe_2: A spectroscopic investigation. Nano Research **9** (12), 3622–3631 (2016).

[31] Yamagata, H. & Spano, F. C. Interplay between intrachain and interchain interactions in semiconducting polymer assemblies: The hj-aggregate model. The Journal of Chemical Physics **136** (18), 184901 (2012).

[32] Xu, J. et al. Tuning conjugated polymer chain packing for stretchable semiconductors. Advanced Materials **34** (22), 2104747 (2022).

[33] Peterhans, L. et al. Structural and photophysical templating of conjugated polyelectrolytes with single-stranded dna. Chemistry of Materials **32** (17), 7347–7362 (2020).

[34] Raithel, D. et al. Direct observation of backbone planarization via side-chain alignment in single bulky-substituted polythiophenes. Proceedings of the National Academy of Sciences of the United States of America **115** (11), 2699–2704 (2018).

[35] Jiao, G.-S., Zhang, Y., Cheng, H., Shi, T. & Yan, Z.-C. Role of side chains in the packing structure and dynamics of conjugated polymers. Macromolecules **56** (14), 5248–5258 (2023).

[36] Cavassin, P. et al. Electrochemical doping in ordered and disordered domains of organic mixed ionic–electronic conductors. Adv. Mater. 2300308 (2023).

[37] Voss, M. G. et al. Driving force and optical signatures of bipolaron formation in chemically doped conjugated polymers. Adv. Mater. **33** (3), 2000228 (2021).

[38] Gu, K., Onorato, J. W., Luscombe, C. K. & Loo, Y.-L. The role of tie chains on the mechano-electrical properties of semiconducting polymer films. Advanced Electronic Materials **6** (5), 1901070 (2020).

[39] Keene, S. T. & Salleo, A. Efficient electronic tunneling governs transport in conducting polymer-insulator blends. Journal of the American Chemical Society **144** (23), 10368–10376 (2022).

[40] Asadi, K., Li, M., Blom, P. W. M. & de Leeuw, D. M. Polaron hopping mediated by nuclear tunnelling in semiconducting polymers at high carrier density. Nature Communications **4**, 1710 (2013).

[41] Sheng, P. Fluctuation-induced tunneling conduction in disordered materials. Physical Review B **21** (6), 2180–2195 (1980).

[42] Lüssem, B., Riede, M. & Leo, K. Doping of organic semiconductors. physica status solidi (a) **210** (1), 9–43 (2013).

[43] Tietze, M. L. et al. Elementary steps in electrical doping of organic semiconductors. Nature Communications **9** (1), 1182 (2018).

[44] Duong, D. T., Wang, C., Antono, E., Toney, M. F. & Salleo, A. The chemical and structural origin of efficient p-type doping in P3HT. Organic Electronics **14** (5), 1330–1336 (2013).

[45] Pingel, P. & Neher, D. Comprehensive picture of p-type doping of P3HT with the molecular acceptor F_4TCNQ. Physical Review B **87** (11), 115209 (2013).

[46] Hidalgo Castillo, T. C. et al. Simultaneous performance and stability improvement of a p-type organic electrochemical transistor through additives. Chem. Mater. **34** (15), 6723–6733 (2022).

[47] Sirringhaus, H. 25th anniversary article: Organic field-effect transistors: The path beyond amorphous silicon. Adv. Mater. **26** (9), 1319–1335 (2014).

[48] Giovannitti, A. et al. Controlling the mode of operation of organic transistors through side-chain engineering. Proc Natl Acad Sci U S A **113** (43), 12017–12022 (2016).

[49] Solak, E. K. & Irmak, E. Advances in organic photovoltaic cells: a comprehensive review of materials, technologies, and performance. RSC Advances **13** (18), 12244–12269 (2023).

[50] Hofmann, A. et al. Highly stable doping of a polar polythiophene through co-processing with sulfonic acids and bistriflimide. J Mater Chem C Mater **6** (26), 6905–6910 (2018).

[51] Jacobs, I. E. et al. Comparison of solution-mixed and sequentially processed P3HT:F_4TCNQ films: effect of doping-induced aggregation on film morphology. J. Mater. Chem. C **4**, 3454–3466 (2016).

[52] Murrey, T. L. et al. Anion exchange doping: Tuning equilibrium to increase doping efficiency in semiconducting polymers. J. Phys. Chem. Lett. **12** (4), 1284–1289 (2021).

[53] Xiong, M. et al. Counterion docking: a general approach to reducing energetic disorder in doped polymeric semiconductors. Nature Communications **15** (1), 4972 (2024).

[54] Flagg, L. Q. et al. In situ studies of the swelling by an electrolyte in electrochemical doping of ethylene glycol-substituted polythiophene. ACS Applied Materials & Interfaces **14** (25), 29052–29060 (2022).

[55] Untilova, V. et al. Intercalation and ordering of F_6TCNNQ and F_4TCNQ dopants in regioregular poly(3-hexylthiophene) crystals: Impact on anisotropic thermoelectric properties of oriented thin films. Macromolecules **54** (13), 6073–6084 (2021).

[56] Dash, A. et al. Spontaneous modulation doping in semi-crystalline conjugated polymers leads to high conductivity at low doping concentration. Advanced Materials **36** (13), 2311303 (2024).

[57] Guchait, S. et al. Phase-selective doping of oriented regioregular poly(3-hexylthiophene-2,5-diyl) controls stability of thermoelectric properties. Advanced Functional Materials **34** (39), 2304411 (2024).

[58] Yamashita, Y. et al. Efficient molecular doping of polymeric semiconductors driven by anion exchange. Nature **572** (7771), 634–638 (2019).

[59] Jacobs, I. E. et al. Structural and dynamic disorder, not ionic trapping, controls charge transport in highly doped conducting polymers. Journal of the American Chemical Society **144** (7), 3005–3019 (2022).

[60] Thomas, E. M. et al. Effects of counter-ion size on delocalization of carriers and stability of doped semiconducting polymers. Adv. Electron. Mater. **6** (12), 2000595 (2020).

4 Conductivity and charge transport

> *"All scientific theories are provisional and may be changed, but ... on the whole, they are accepted from Washington to Moscow because of their practical success."*
>
> Sir Nevill Mott [1].

4.1 Conductivity on different length scales

Doped organic semiconductors feature conductivities several orders of magnitude higher than their corresponding conductivity in their pristine state [2]. The conductivity σ is an important measure given by the product of the number of mobile charges N and their mobility μ:

$$\sigma = N\mu e \tag{4.1}$$

Here, e denotes the elementary charge. In case several different charge carriers coexist one would need to sum these species in equation 4.1. Given the mentioned microstructure of polymer films and doping-induced structural changes[3, 4], it is relevant to compare the conductivity of doped polymers on different length scales. Various techniques and geometries to measure conductivity on different length scales exist. The macroscopic conductivity, by linear four-point probe, measures the conductivity over a the long range of millimeters[5]. One way of measuring the conductivity over short distances is by carrying out THz time-domain spectroscopy on the material. An ultrashort THz pulse of approximately 1.5 picosecond trespasses the sample, see Chapter 5 for all details. For now the fact that is important is: Since the THz pulse is ultrashort, the charges do not move very far, usually on the length scale of nanometers. **How far do charges travel during the duration of an ultrafast THz pulse?**

In doped OSCs, the conductivity is constrained by the intrinsic properties of the material[6, 7, 8]. Hereby, the charge carrier mobility μ_{eff} and the effective mass m^* need to be considered. To quantify how far charges in doped OSCs travel during an ultrafast THz pulse, I assume a classical acceleration of charges during the duration of a THz pulse[9]. The calculations uses representative values approximated for the experimental conditions in the laboratory. In doubt, I use the upper limit of a typical range of values. As such, the following calculation yields an upper limit for the distance a charge travels during an ultrashort THz pulse.

The THz pulse has a duration of $t = 1.5\,\text{ps}$, and an electric field strength of below $E = 1\,\text{kV}\,\text{cm}^{-1}$. Doped OSCs have an effective mass m^* of around $m^* = 1.7 \times m_{\text{e}}$, whereby $m_{\text{e}} = 9.11 \times 10^{-31}\,\text{kg}$ is the mass of an electron[11]. Doped OSCs have a mobility on the order of $1\,\text{cm}^2\,\text{V}^{-1}\,\text{s}^{-1}$[6, 7, 8]. Then, the acceleration of a charge carrier is given by:

$$a = \frac{qE}{m^*}, \tag{4.2}$$

whereby $q = 1.602 \times 10^{-19}\,\text{C}$ is the elementary charge. Then, substituting the representative values, the acceleration is calculated as:

$$a = \frac{(1.602 \times 10^{-19}\,\text{C})\,(10^5\,\text{V/m})}{1.7\,(9.11 \times 10^{-31}\,\text{kg})} \approx 1.66 \times 10^{15}\,\frac{\text{m}}{\text{s}^2}.$$

Assuming constant acceleration, the displacement is given by the expression:

$$d = \frac{1}{2}at^2. \tag{4.3}$$

The displacement during the THz pulse duration of $t = 1.5\,\text{ps}$ is calculated to be around $2\,\text{nm}$ when the values are substituted:

$$d = \frac{1}{2}(1.66 \times 10^{15}\,\frac{\text{m}}{\text{s}^2})(1.5 \times 10^{-12}\,\text{s})^2 \approx 2 \times 10^{-9}\,\text{m}.$$

Under typical THz experimental conditions, **charges in doped polymers travel distances of few nanometers**. The average distance is influenced by both the properties of the THz pulse and the properties of the material. This example underscores the unique role of THz spectroscopy in probing short-range transport in doped OSC.

4.2 Charge transport models

4.2.1 Density of states

Charge transport in OSCs is most often described by hopping between localized electronic states[12, 13, 14, 15, 16]. Figure 4.1 shows the filling of electronic states in various types of materials at equilibrium to define the terms (a) band-like transport and (b) localized transport. In elementary quantum mechanics, electrons in a material occupy only discrete energy levels, other energies between these levels are impossible. When many such energy levels are allowed and their corresponding energy difference is small, then these energy levels in combination form a so called ”energy band”. Charges in an energy band can move ballistically, because there is not a significant energy between the states. When the energy difference between states is significant, they are called localized states. The energetic variation of localized states is called energetic disorder. Charges in a material with localized states have to overcome differences in energy and space. Then, charges need thermal energy to ”hop” between localized states. The **density of states (DOS)** describes how many electronic states are available at a given energy level in a material. For OSCs usually the DOS is described by a Gaussian[13], which can broaden inhomogeneously by (doping-induced) disorder[14]. Materials are classified as metals, semiconductors or insulators based on the energy of their energy levels in reference to the Fermi energy as depicted in Figure 4.1. The valence and conduction bands lie below and above the Fermi level respectively. In organic semiconductors, one uses the terminology and framework of molecular orbitals and speaks of HOMO and LUMO energy levels. The valence band is typically associated with the HOMO, while the conduction band is associated with the LUMO.

In semiconductors, the Fermi level lies within the band gap, which means that very few charge carriers are available for conduction. In organics the charge carriers reside in the HOMO or LUMO level. In p-type doping an introduced dopant molecule will oxidize the polymer chain as described in the doping chapter above. This leads to a positive charge carrier (hole) in the HOMO level. The oxidized polymer chain shows different electronic states within the bandgap. The new transitions are associated with states of a quasi-particle consisting of a charge with a corresponding lattice deformation or distortions[17, 18]. These quasi-particles are called **polarons** when they carry one-charge. Two polarons in spatial proximity can lower their energy by sharing the same distortions, which results to an overall attraction between them. If the interaction is sufficiently large, then two polarons can form a bound diamagnetic **bipolarons**, which hence carry two-charges[17, 18, 19, 20, 21, 22]. Initially, low doping concentrations introduce the singly charged polarons. The polaronic states enable charge transport as they allow carriers to hop between localized states. This increases the number of holes in the HOMO level that contribute to conduction. As the doping level rises, more energy states within the gap are filled, which can lead to the formation of bipolarons or possibly other multiply charged species. At very high doping concentrations, the band gap may effectively disappear due to broadening and merging of bipolaron bands with the original conduction or valence band[23]. In this regime, band filling is extensive, and the material may exhibit band-like behavior where charge carriers can move freely across the entire structure, significantly enhancing conductivity[6, 23, 24, 25, 26].

Localized transport models exhibit a characteristic temperature dependence, because since the localized states are separated by a significant energy amount, thermal activation is assisting the hopping between states. At low temperatures, the hopping rate is limited by the energy barrier required for carriers to move between sites, leading to an exponential decrease in conductivity. As temperature increases, more carriers gain sufficient thermal energy to overcome these energy barriers, resulting in a conductivity that monotonously increases with temperature. In contrast, band-like transport models are governed by delocal-

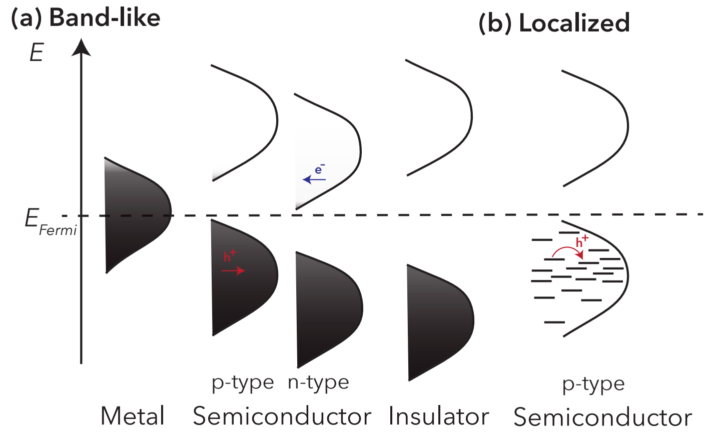

Figure 4.1: Scheme of material classified as (a) metal, semiconductor or insulator with a band-like DOS (b) (p-type) semiconductor with a DOS of localized states.

ized charge carriers in extended states, where conductivity typically decreases with increasing temperature due to enhanced scattering from phonons or lattice vibrations. This inverse relationship distinguishes band-like transport from the thermally activated nature of localized transport. As such, the dominating charge transport mechanism becomes evident when the conductivity is plotted against temperature.

4.2.2 Literature review of charge transport models

This section reviews charge transport models for doped conjugated polymers and molecular OSCs. To do so, it presents and compares the characteristic temperature dependence of the conductivity for various reported models. It explains localized hopping models, delocalized models, heterogeneous models based on perturbation theory, the transient corrections to band-like transport, field-induced carrier heating, the fluctuation-induced tunneling model and the semi-localized transport (SLoT) model.

In a pure **hopping model** the charges are in localized states separated by an energy and separated by a distance. To move to a neighboring state the charges need to hop. Therefore, the conductivity is exponentially decreasing with the temperature T[27].

$$\sigma(T) = \sigma_0 \exp\left(-\frac{W_\mathrm{H}}{k_\mathrm{B}T}\right)^\gamma \tag{4.4}$$

Hereby, σ_0 is a temperature-independent constant pre-factor, the activation energy is denoted by W_H and the Boltzmann constant is denoted by k_B. The exponent $\gamma = 1, \frac{1}{2}, \frac{1}{3}$ is commonly used to phenomenologically assign classical activated, Efros–Shklovskii variable range hopping, or Mott variable range hopping respectively[13, 15, 27]. This exponent influences the slope of the exponential decay. Sir Nevill Mott was aware about the limitations of modelling experimental observations as seen by his quote[1]. Yet, he has contributed significantly to the understanding of charge transport in organic semiconductors by developing the variable range hopping model[28].

Sheng *et al.* introduced the **fluctuation-induced tunneling (FIT) model** which belongs to the category of thermally assisted transport models[29]. It describes electrical transport between conductive regions *via* tunneling through insulating regions. It is particularly useful for heterogeneous systems, such as disordered organic semiconductors or carbon nanotube networks. Tunneling is recognized as the transport mechanism to sustain conductivity in polymers with insulating regions[30, 31]. For example, it sustains electrically conductive channels in organic mixed ionic electronic conductor blends even when the conductive (conjugated polymer) regions only make up for few weight percent (wt%)[31]. It has a similar form to the hopping models, but introduces an additional parameter T_0. The fluctuation-induced tunneling model is expressed as:

$$\sigma(T) = \sigma_{\mathrm{FIT}} \exp\left(-\frac{T_1}{T + T_0}\right) \tag{4.5}$$

Here, the temperature T_0 is marking at which temperature or with which energy the fluctuation-induced tunneling becomes significant. The temperature T_1 is directly related to the minimum energy necessary for the charge carrier to move across the insulating regions formed between conductive regions. The parameters T_1, T_0 allow for a non-zero conductivity at 0 Kelvin based on tunneling. The effective temperature in the denominator of the tunneling model $T + T_0$ has a similar form to hopping transport in an electric field[32]. The **effective temperature correction** to charge transport by Marianer and Shklovskii is based on localized hopping[32]. Shklovskii has been mentioned before for his contributions to variable range hopping[27]. In the effective temperature framework, a charge carrier can increase its energy by an amount $\Delta E = qFa$ by hopping a distance a along an external electric field F. This energy term is interpreted as field-induced charge carrier ”heating”, because it promotes charge carriers to higher energy levels. Kemerink *et al.* managed to derive this common experimental observation of the field-induced energy amount alternatively using kinetic Monte Carlo simulations purely based on variable range hopping at high carrier densities[33]. The effective temperature correction is described by:

$$T_{\mathrm{eff}} = \sqrt{T^2 + T_0^2} \tag{4.6}$$

The crossover temperature T_0 describes the field-induced energy amount. To test if this formalism is relevant in the case of THz electric fields, here comes a mathematical example. In semicrystalline polymers, the hopping distance of charges depends on microstructure, interchain coupling, and disorder. Generally, the charge hopping distance lies within the range of $a \approx 10$ nm. THz spectroscopy probes the charge carriers on the nanoscale, so the displacement can be assumed to be on the same order as a. The electric field of the THz pulse in our lab is $F \approx 1$ kV/cm. The charge is the elementary charge $q = 1.602 \times 10^{-19}$ C. This would hypothetically result in a field-induced energy amount of: $\Delta E = qFa \approx 1$ meV. When this energy amount is expressed in Kelvin this yields: $T_0 = \Delta E / k_B = 12$ K. For doped polymers at high carriers densities, activation energies (around room temperature) are can be on the same order of magnitude with W_H is few meV. Therefore, the field-induced energy amount likely plays a significant role, but only at high carrier densities where the density of states around the Fermi energy is large, as predicted[33].

Most **delocalized transport models** are also referred to band-like (or metallic) transport models, since the charge transport happens in extended energy bands[23, 34, 24]. They are described by a power law of the form:

$$\sigma(T) = \sigma_{\text{band}} T^{-\beta} \tag{4.7}$$

The conductivity $\sigma_{\text{band}}\,(T)$ hereby is inversely dependent on thFere temperature. The exponent β is related to the scattering mechanisms such as electron–electron and electron–phonon scattering. In literature the exponent is often used phenomenologically. The exponent equals $\frac{1}{n+1}$ with n corresponding to the dimensionality[35]. This translates to β equals $\frac{1}{2}$ in the quasi-1-dimensional metal model for example[36]. In the disordered metal model, the exponent β is often determined as 2 phenomenologically but other references find the conductivity to be almost temperature-independent in disordered metals[37]. The exponents will influence how drastically the conductivity increases with decreasing temperature.

The **transient localisation model** is taking into account the soft nature of OSCs. As discussed largely in Chapter 2, OSCs are carbon-based materials assembled by weak van der Waals interactions. This leads to properties that can hinder a coherent band-like description. Firstly, flexibility results in pronounced thermal motions. This gives rise to high fluctuations in electronic coupling, which is often observed by spectroscopic techniques[3]. Secondly, the static dielectric constant of OSCs is typically very small (2–5)[38, 39]. To describe the charge transport in organic materials, Fratini and Ciuchi revisited the concept of transient localization (TL) and corrected the delocalized model by a TL term[25, 6, 40]. This explicit introduction of vibrational modes has gained significant agreement in the research field. The model is fairly successful in describing molecular OSCs and high-mobility polymers that have a dominant "band-like" charge transport. The temperature dependent conductivity is expressed by:

$$\sigma_{\text{band}}\left(T\right) = \sigma_{\text{band}}\left(T\right) + \delta\sigma_{TL}\left(T\right). \tag{4.8}$$

Here, the conductivity σ_{band} is depending on the diffusion coefficient and the temperature based on the Einstein relation:

$$\delta\sigma_{\text{band}}\left(T\right) = \sigma_{\text{band}}\left(\frac{eD}{k_{\text{B}}T}\right) \tag{4.9}$$

Analoguosly, the transient localization correction term for the conductivity $\delta\sigma_{\text{TL}}$ is also depending on the diffusion coefficient and the temperature. It contains the dynamical localization corrections δC_0

$$\delta\sigma_{\text{TL}}\left(T\right) = \sigma_{\text{TL}}\left(\frac{eD\delta C_0}{k_{\text{B}}T}\right) \tag{4.10}$$

Hereby, the e is the elementary charge, D is the diffusion length and δC_0 describes the dynamical localization corrections due to vibrational modes in organic materials like doped polymers. The expression has the desired form of a semi-classical band conductivity corrected by quantum effects. The conductivity σ_{band} is applicable for high-mobility polymers and crystalline OSCs. The transient localization correction δC_0 when assessed at low temperature (in the frozen disorder limit) contains relevant information on static localization when vibrations become negligible.

A long-lasting puzzle has been the interpretation of effectively **temperature-independent mobility (TIM)** in doped polymers[41, 42]. Yet, a temperature independent conductivity term σ_{TIM} has been derived from transient localization, whereby this effectively temperature-independent behavior occurs when the diffusion coefficient is proportional to T[42]. Using the Einstein relation from above with such a diffusion coefficient yields an overall independent σ_{TIM}.

$$\sigma_{\text{TIM}} \propto \left(\frac{eD}{k_{\text{B}}T}\right) \propto \left(\frac{eT}{k_{\text{B}}T}\right) \tag{4.11}$$

Recently, such a diffusion coefficient that is proportional to the temperature has been proposed for quasi-1-dimensional polymer chains.

$$D_{\text{chain}} \propto T \tag{4.12}$$

The charge transport model explaining effectively TIM with TL on polymer chains is called transient localized [42].

The idea of **heterogenous transport models** was established by Kaiser *et al.* and it describes tunneling between metallic islands, separated by a disordered metal[37, 43]. The heterogeneous transport model is based on a simple weighted sum of resistivities from previously established models. This "path of least resistance" model is often presented in the formalism of perturbation theory. In the original Kaiser description for doped polymers, it combines equation (4.7) with equation (4.5) and a temperature-independent term, which they denote as transport in a disordered metal ρ_{dm}. In terms of conductivity, one must invert the weighted sum of resistivities from the original equation:

$$\sigma(T)^{-1} = \rho(T) = f_{\mathrm{m}}\rho_{\mathrm{m}} \exp\left(-\frac{T_{\mathrm{m}}}{T}\right) + \left(\frac{1}{f_{\mathrm{s}}\rho_{\mathrm{s}} \exp\left(-\frac{T_1}{T_2+T}\right)} + \frac{1}{f_{\mathrm{dm}}\rho_{\mathrm{dm}}}\right)^{-1} \tag{4.13}$$

Or rewritten in terms of conductivity this equation reads as:

$$\sigma(T) = \frac{1}{\frac{f_{\mathrm{m}}}{\sigma_{\mathrm{m}}} \exp\left(-\frac{T_{\mathrm{m}}}{T}\right) + \frac{1}{f_{\mathrm{s}}\sigma_{\mathrm{s}} \exp\left(-\frac{T_1}{T_2+T}\right) + f_{\mathrm{dm}}\sigma_{\mathrm{dm}}}} \tag{4.14}$$

Here, the form factors f_i are representing weights from the contributing models. While I quite cynically name it the "path of least resistance" model, it does have its validity under certain circumstances. The name comes from the combinatory of three models which will fit most experimental datasets provided. The derivation of terms from perturbation theory is valid in a heterogeneous model though. With a similar logic, Brinkmann group recently described charge transport in aligned films[44] with a model denoted **heterogenous oriented structure (HOSt) model**. Thereby, they aim and succeed to disentangle the contributions of conductivity in the orientation of alignment $\sigma_{\parallel}$ and the conductivity perpendicular to it $\sigma_{\perp}$. A perturbation theory-based approach in my experience makes sense for polymer films where extraordinary heterogeneity is of direct interest, such as aligned films. Spin-coated polymer films with high doping levels where the reduced activation energy is tens of meV and the interconnectivity is high are not described well with the heterogeneous transport model, as seen in Figure

?? with experimental results in the next section. For THz conductivity that is sensitive to conductive regions over short-range distances even less so.

Recent models like the **semi-localized transport model (SLoT)** focus on a cohesive derivation from the Boltzmann formalism[45]. This relatively recent model describes the thermoelectric properties of doped polymer films more uniformly[46, 47, 48]. Only four years lie between the publication of the Kang–Snyder model[49], named after S. Dongmin Kang and G. J. Snyder, and the publication of the semi-localized Transport (SLoT) model[45]. The articles were published in 2017 and 2021 both in Nature Materials and notably, G. J. Snyder is a co-author on both articles. This work for charge transport in organic semiconductors is described **outside of the duality between localized and delocalized transport**. Instead it proposes a continuous description and therefore is applicable to describe different doping levels in OSCs. The SLoT model contributed an explicit dependence on the doping concentration. As such, the potential well depth $W_\mathrm{H}\,(c)$, was expressively defined as a function of the dopant concentration c. Moreover, the expression of the metallic contribution in terms of the Boltzmann formality $E{-}E_\mathrm{t}k_\mathrm{B}T$ leads to reasonable values for the Fermi energy. In the SLoT model the transport function is depending on the depth of the potential wells $W_\mathrm{H}\,(c)$, which itself is a function of the dopant concentration c:

$$\sigma_\mathrm{E}(E,T,c) = \begin{cases} 0, & E < E_\mathrm{t} \\ \sigma_0 \exp\left(-\frac{W_\mathrm{H}(c)}{k_\mathrm{B}T}\right)\left(\frac{E-E_\mathrm{t}}{k_\mathrm{B}T}\right), & E \geq E_\mathrm{t} \end{cases} \tag{4.15}$$

whereby $\sigma_\mathrm{E}(E,T,c)$ is the transport function, σ_0 is the reference conductivity, W_H is the hopping activation energy, material dependent constant, k_B is the Boltzmann constant, T is the temperature, E is the energy level, E_t is the threshold energy also called transport edge. The transport function $\sigma_\mathrm{E}(E,T)$ describes the electrical conduction at any electron energy (E) and temperature (T). Charge carriers with energies below the transport edge are not mobile. They hence have a transport function of zero value and do not contribute to conductivity. Charge carriers with energies above the transport edge have (i) a temperature and dopant concentration dependent term and (ii) an energy dependent term. The concentration dependence of the activation energy describes the charge screening effect, such that the activation barrier decreases with increasing doping concentration. The proof-of-concept system was P3HT doped with increasing concentrations of $\mathrm{FeCl_3}$, which resulted in activation energies between 110 meV and

9.6 meV[45]. Later, the group also presented the model for the thermoelectric properties of PBTTT[47]. The SLoT model assumes **homogeneous static disorder** which describes well the charge transport in organic crystals and ordered (high-mobility) polymer regions, while it does not take into account fluctuation-induced processes.

Fluctuation-induced tunneling and transient localization are phonon-assisted mechanisms affecting charge transport under specific conditions[30, 31, 29, 25, 6, 40, 50, 51]. Such fluctuations can contribute to charge transport around room temperature and disappear with low temperature when the phonon fluctuations vanish. Moreover, field-induced hopping[32, 33] can contribute to charge transport with an energy amount of about $\Delta E \approx 0.01$ eV for the THz experimental conditions as calculated in example **??**. Both fluctuation-induced and field-induced mechanisms together are denoted as transient mechanisms, because they dynamically vary with time.

Figure 4.2 provides an overview of the main charge transport models used in literature for doped polymers. These simulated curves show the characteristic temperature dependence for the input parameters (where applicable): a conductivity pre-factor of 100 S/cm, an activation energy of 10 meV or an energy difference to the transport edge of 100 meV. The charge transport model of doped polymers can fall into any of these categories depending on charge carrier density and degree of disorder.

Figure 4.2 (a) shows localized (hopping) models with varying exponent γ in black, blue and green. These models describe charge transport in systems with static disorder, where charges are localized in discrete states. Transport occurs *via* thermally activated hopping between these states, leading to conductivity that increases with temperature. It is commonly applied to disordered systems, such as polymers. The same panel (a) shows delocalized (band-like) models with varying exponent β in orange, red and purple. Band-like transport is assigned for systems where charges are delocalized and move coherently through extended bands. Then, the conductivity decreases with increasing temperature due to scattering effects. Figure 4.2 (b) depicts recently proposed models that aim to describe charge transport in doped polymers. First, the HOSt model in green is a novel approach to apply a heterogeneous transport for aligned polymer films. Besides it's advantages, the perturbation approach of calculating a sum of resistances, yields either a conductivity of 0 at 0 K (as seen for the simulated curve in green) or it will have a substantial delocalized contribution which is depending on the system not always reasonable. The semi-localized transport model in seen in Figure 4.2 (b) in yellow. Thereby, charges are semi-localized in static states, allowing for both thermally-activated hopping and intermediate band-like transport. In the last years it has gained a lot of attention and was applied to doped polymers. Lastly, in panel (b) a simulated curve in blue represents the semi-transient-localized transport (STLoT) model proposed in this thesis Chapter 7. Given the presented review, at high charge carrier densities and state-of-the-art materials reduce static disorder to approximately tens of meV. It yields parameters describing the energetic variation of localized electronic states similar to the SLoT model. The model shows a good description of the highly doped polymers presented in Chapter 7. As such, band-like transport occurs exclusively in Chapter 8 where an organic–inorganic hybrid material is investigated.

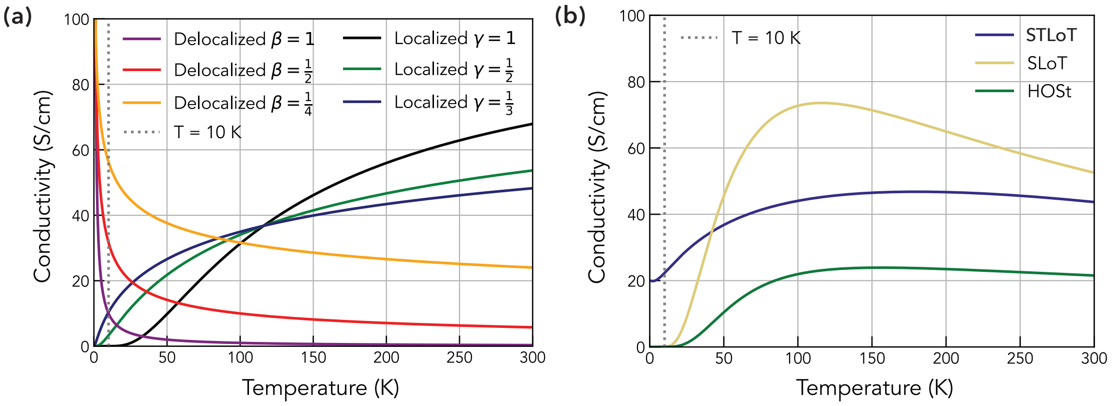

Figure 4.2: Overview of major charge transport models for doped OSC.

References for Chapter 4

[1] Margenau, H. & Roy, A. V. Science will never give us the answers to all our questions. Cosmos, Bios, Theos **6** (65) (1992).

[2] Shirakawa, H., Louis, E. J., MacDiarmid, A. G., Chiang, C. K. & Heeger, A. J. Synthesis of electrically conducting organic polymers: Halogen derivatives of polyacetylene, (ch). J. Chem. Soc., Chem. Commun. (16), 578–580 (1977).

[3] Noriega, R. et al. A general relationship between disorder, aggregation and charge transport in conjugated polymers. Nature Materials **12**, 1038–1044 (2013).

[4] Xiong, M. et al. Counterion docking: a general approach to reducing energetic disorder in doped polymeric semiconductors. Nature Communications **15** (1), 4972 (2024).

[5] Ossila. Four-probe method, macroscopic conductivity and electrode spacing. https://www.ossila.com/pages/sheet-resistance-theory **1** (1) (2024).

[6] Fratini, S. et al. Charge transport in high-mobility conjugated polymers and molecular semiconductors. Nature Materials **19**, 491–502 (2020).

[7] Li, J. et al. A stable solution-processed polymer semiconductor with record high-mobility for printed transistors. Scientific Reports **2**, 754 (2012).

[8] Liu, J. et al. High mobility emissive organic semiconductor. Nature Communications **6**, 10032 (2015).

[9] Salamin, Y. I. Electron acceleration in vacuum by a linearly-polarized ultra-short tightly-focused thz pulse. Physics Letters A **381** (35), 3010–3013 (2017).

[10] Preezant, Y. & Tessler, N. Carrier heating in disordered organic semiconductors. Physical Review B **74** (23), 235202 (2006).

[11] Northrup, J. E. Atomic and electronic structure of polymer organic semiconductors: P3HT, PQT, and PBTTT. Physical Review B **76** (24), 245202 (2007).

[12] Arkhipov, V. I., Emelianova, E. V. & Bässler, H. Analytic model of carrier mobility in doped disordered organic semiconductors. Physical Review B **72**, 235202 (2005).

[13] Hartenstein, B. & Bässler, H. Transport energy for hopping in a gaussian density of states distribution. Journal of Non-Crystalline Solids **191**, 34–39 (1995).

[14] Hoffmann, S. T., Bässler, H. & Köhler, A. What determines the inhomogeneous broadening of electronic transitions in conjugated polymers? The Journal of Physical Chemistry B **114** (51), 17037–17048 (2010).

[15] Abdalla, H., Zuo, G. & Kemerink, M. Range and energetics of charge hopping in organic semiconductors. Physical Review B **96** (24), 245203 (2017).

[16] Bässler, H., Hoffmann, S. T. & Köhler, A. Mapping the density of states distribution of organic semiconductors by employing energy resolved–electrochemical impedance spectroscopy. Advanced Functional Materials **31** (9), 2001020 (2020).

[17] Enengl, C. et al. Doping-induced absorption bands in P3HT: Polarons and bipolarons. ChemPhysChem **17** (23), 3836–3844 (2016).

[18] Moulé, A. J. et al. Quantifying polaron mole fractions and interpreting spectral changes in molecularly doped conjugated polymers. Advanced Electronic Materials **8** (4), 2100888 (2022).

[19] Tsokkou, D. et al. Excited state dynamics of a self-doped conjugated polyelectrolyte. Adv. Funct. Mater. **30** (9), 1906148 (2020).

[20] Wu, E. C. et al. Counterion control and the spectral signatures of polarons, coupled polarons, and bipolarons in doped P3HT films. Adv. Funct. Mater. **33** (19), 2213652 (2023).

[21] Rebetez, G., Bardagot, O., Affolter, J., Réhault, J. & Banerji, N. What drives the kinetics and doping level in the electrochemical reactions of PEDOT:PSS? Adv. Funct. Mater. **32** (5), 2105821 (2022).

[22] Cavassin, P. et al. Electrochemical doping in ordered and disordered domains of organic mixed ionic–electronic conductors. Adv. Mater. 2300308 (2023).

[23] Yamashita, Y., Matsumoto, T., Takahashi, K., Sakata, M. & Katagiri, H. Transition between band and hopping transport in polymer field-effect transistors. Advanced Materials **26** (48), 8169–8173 (2014).

[24] Kang, K., Lee, D., Kim, J. A., Kim, J. E. & Kim, H. 2d coherent charge transport in highly ordered conducting polymers doped by solid state diffusion. Nature Materials **15** (8), 896–902 (2016).

[25] Fratini, S., Mayou, D. & Ciuchi, S. The transient localization scenario for charge transport in crystalline organic materials. Advanced Functional Materials **26** (14), 2292–2315 (2016).

[26] Liu, K., Zhang, L., Huang, J. & Wang, Z. A quasi-2d polypyrrole film with band-like transport behavior and high charge-carrier mobility. Advanced Materials **35** (40), e2303288 (2023).

[27] Pollak, M. & Shklovskii, B. (eds) Hopping Transport in Solids Vol. 28 of Modern Problems in Condensed Matter Sciences (Elsevier, 1991).

[28] Brown, A. R., Pomp, A., Hart, C. M. & de Leeuw, D. M. A universal relation between conductivity and field-effect mobility in doped conducting polymers. Synthetic Metals **68**, 65–68 (1994).

[29] Sheng, P. Fluctuation-induced tunneling conduction in disordered materials. Physical Review B **21** (6), 2180–2195 (1980).

[30] Asadi, K., Li, M., Blom, P. W. M. & de Leeuw, D. M. Polaron hopping mediated by nuclear tunnelling in semiconducting polymers at high carrier density. Nature Communications **4**, 1710 (2013).

[31] Keene, S. T. & Salleo, A. Efficient electronic tunneling governs transport in conducting polymer-insulator blends. Journal of the American Chemical Society **144** (23), 10368–10376 (2022).

[32] Marianer, S. & Shklovskii, B. I. Effective temperature of hopping electrons in a strong electric field. Physical Review B: Condensed Matter **46** (20), 13100–13103 (1992).

[33] Abdalla, H., van de Ruit, K. & Kemerink, M. Effective temperature and universal conductivity scaling in organic semiconductors. Scientific Reports **5**, 16870 (2015).

[34] Senanayak, S. P., Hawker, R. B., Fallahpour, K., Nashat, S. & Friend, R. H. Room-temperature bandlike transport and hall effect in a high-mobility ambipolar polymer. Physical Review B **91** (11), 115302 (2015).

[35] Wang, Z. H., Scherr, E. M., MacDiarmid, A. G. & Epstein, A. J. Transport and epr studies of polyaniline: A quasi-one-dimensional conductor with three-dimensional "metallic" states. Physical Review B **45** (8), 4190–4202 (1992).

[36] Heinze, S., Tersoff, J. & Avouris, P. Quasi-one-dimensional transport in conducting polymer nanowires. Applied Physics A **49**, 2015–2033 (2007).

[37] Kaiser, A. B., Flanagan, G. U., Stewart, D. M. & Beaglehole, D. Heterogeneous model for conduction in conducting polymers and carbon nanotubes. Synthetic Metals **117** (1-3), 67–73 (2001).

[38] Armin, A. et al. Engineering dielectric constants in organic semiconductors. Journal of Materials Chemistry C **5** (15), 3736–3747 (2017).

[39] Sami, S. et al. How ethylene glycol chains enhance the dielectric constant of organic semiconductors: Molecular origin and frequency dependence. ACS Appl Mater Interfaces **12** (15), 17783–17789 (2020).

[40] Fratini, S. & Ciuchi, S. Dynamical localization corrections to band transport. Physical Review Research **2** (1), 013001 (2020).

[41] Nelson, S. F., Lin, Y.-Y., Gundlach, D. J. & Jackson, T. N. Temperature-independent transport in high-mobility pentacene transistors. Applied Physics Letters **72** (15), 1854–1856 (1998).

[42] Plyukhin, A. V. Hitchhiking transport in quasi–one-dimensional systems. Europhysics Letters (EPL) **71** (5), 716–722 (2005).

[43] Kaiser, A. B. Systematic conductivity behavior in conducting polymers: Effects of heterogeneous disorder. Advanced Materials **13** (12-13), 927–941 (2001).

[44] Limelette, P., Leclerc, N. & Brinkmann, M. Heterogeneous oriented structure model of thermoelectric transport in conducting polymers. Scientific Reports **13** (1), 21161 (2023).

[45] Gregory, S. A., Salleo, A. & Bao, Z. Quantifying charge carrier localization in chemically doped semiconducting polymers. Nature Materials **20** (10), 1414–1421 (2021).

[46] Hanus, R., Gregory, S. A., Adams, M. J., Graham, S. & Yee, S. K. Quantifying the effects of inhomogeneity and doping on the electronic contribution to thermal conductivity in semiconducting polymers. Advanced Electronic Materials **8** (11), 2200846 (2022).

[47] Gregory, S. A. et al. Quantifying charge carrier localization in pbttt using thermoelectric transport measurements. The Journal of Physical Chemistry C **127** (25), 12206–12217 (2023).

[48] Liu, Y. et al. Delocalized charge transport in thermoelectric composites of semiconducting carbon nanotubes wrapped with a p-type polymer. Advanced Electronic Materials (2024).

[49] Kang, S. D. & Snyder, G. J. Charge-transport model for conducting polymers. Nature Materials **16**, 252–257 (2017).

[50] Lemaur, V. et al. Resilience to conformational fluctuations controls energetic disorder in conjugated polymer materials: Insights from atomistic simulations. Chemistry of Materials **31** (17), 6889–6899 (2019).

[51] Rammal, H., Smith, F. & Doe, J. Transient localization from the interaction with quantum bosons. Physical Review Letters **132** (26), 266502 (2024).

5 Spectroscopy and Methods

> *"Spectroscopy, the ancient art, of piercing into light's own heart,*
> *With every hue, a story told, of atoms, bonds, and secrets old."*
>
> **Whispers of Light** by openAI.

5.1 Steady-state absorption

5.1.1 OSC pristine absorption

Organic semiconductors exhibit tunable absorption of light, making them highly effective materials for optoelectronic applications such as solar cells, photodetectors, and light-emitting diodes[11, 21, 49]. The absorbance arises from the excitation of electrons from the highest occupied molecular orbital (HOMO) to the lowest unoccupied molecular orbital (LUMO), corresponding to the material's bandgap. Unlike inorganic semiconductors, the bandgap of organic semiconductors can be precisely controlled by altering their molecular structure, side-chain engineering, or chemical composition. This tunability allows for the absorption of specific wavelengths of light, spanning from the ultraviolet to the near-infrared region. Their absorption spectra are typically hundreds of nanometer wide, and are influenced by molecular packing, aggregation, and microstructure. This sensitivity to microstructure enables optimization of light-harvesting efficiency but also introduces complexity, as aggregate states (e.g., H- or J-aggregates) can enhance or suppress absorption. Overall, the light absorption properties of organic semiconductors are both a fundamental and versatile feature, central to their performance in optoelectronic devices. As such, measuring the steady-state absorption of polymer films in both their pristine and molecularly doped states provides insights into electronic and structural properties.

5.1.2 OSC charged absorption

Upon doping of OSC, new electronic transition and hence absorption features emerge. They correspond to the formation of charged species usually identified as polarons and bipolarons. The absorption features serve as clear evidence of doping-induced charged species. These species exhibit distinct absorption peaks that are red-shifted compared to the pristine bandgap absorption. For the investigated OSC the new absorption features appear in the near-infrared to infrared region, depending on the materials backbone and energetics. The transitions are red-shifted because charged species occupy mid-gap states, effectively depleting the pristine bandgap transition and shifting the absorption to lower energies. Additionally, some ionized dopants themselves absorb in the visible region, contributing more information on effective molecular doping. Quantitative extraction of the charge carrier density is challenging; steady-state absorption spectroscopy and spectroelectrochemistry measurements should ideally be confirmed by complementary techniques such as X-ray Photoelectron Spectroscopy (XPS). To disentangle overlapping spectral features, techniques such as spectroelectrochemistry combined with multivariate curve resolution (MCR) are employed. This aims for the challenging deconvolution of individual species' absorption cross-sections. This detailed analysis provides critical insights into the doping-induced charged species in OSCs. Shifts or broadening of charged species' absorption features can indicate delocalization of charges and interactions between the polymer and dopant molecules. Changes in absorption are sensitive representations of structural and electronic modifications.

5.1.3 Experimental method

Steady-state absorbance spectra are measured on a PerkinElmer Lambda 950 spectrophotometer equipped with a 150 mm InGaAs integration sphere. To subtract the effect of the substrate, the transmittance of the clean substrate is measured too: $T_{\mathrm{substrate}}$ and $T_{\mathrm{substrate+film}}$. Subsequently, the absorbance A is calculated by:

$$A = \lg T_{\mathrm{substrate}} - \lg T_{\mathrm{substrate+film}} \quad . \tag{5.1}$$

5.2 Terahertz time-domain spectroscopy

5.2.1 THz gap in the electromagnetic spectrum

The electromagnetic spectrum spans a vast range of wavelengths and frequencies, from long-wavelength radio waves to short-wavelength γ rays, as illustrated in Figure 5.1. Each spectral range is uniquely useful in science and everyday life. For instance, radio waves are essential for communication technologies, microwaves for cooking, and visible light for illumination. Moving to higher frequencies, X-rays are invaluable in medical imaging, while γ rays are crucial in oncology and nuclear research. However, a significant region of the spectrum, known as the THz gap, exists between microwaves and infrared frequencies (around 0.1–10 THz). As seen in Figure 5.1, this region corresponds to wavelengths between approximately 3 mm and 300 μm and has long been challenging to access due to the lack of efficient sources and detectors.

The THz gap is particularly important because THz radiation bridges electronic and optical phenomena, with applications in material characterization, spectroscopy, and imaging. Historically, the development of ultrafast lasers and the discovery of non-linear optical effects have played a critical role in overcoming this gap. Techniques such as optical rectification and difference frequency generation utilize non-linear effects to generate THz frequencies, providing access to this underutilized part of the spectrum. Consequently, advancements in THz technology are driving innovations in fields ranging from telecommunications to biomedical diagnostics, underscoring its growing scientific and practical relevance.

5.2.2 Experimental method

Terahertz time-domain spectroscopy is a spectroscopic technique based on the response of a material to an ultrashort pulse of a THz electric field. The THz measurements were run on a setup powered by a pulsed laser (Coherent, Astrella) with a central wavelength of 800 nm, a pulse duration of 35 fs and a repetition rate of 1 kHz. It is based on an ultrafast pulsed laser with a central wavelength in the near-infrared (NIR) at 800 nm used to generate and detect the THz pulse. For both generation and detection of the THz pulse, one laser beam is used, requiring the use of a beam splitter. The generation of the THz pulse can be achieved by a non-linear optical process called optical rectification. Here, the 800 nm ultrashort pulsed beam used for generation passes

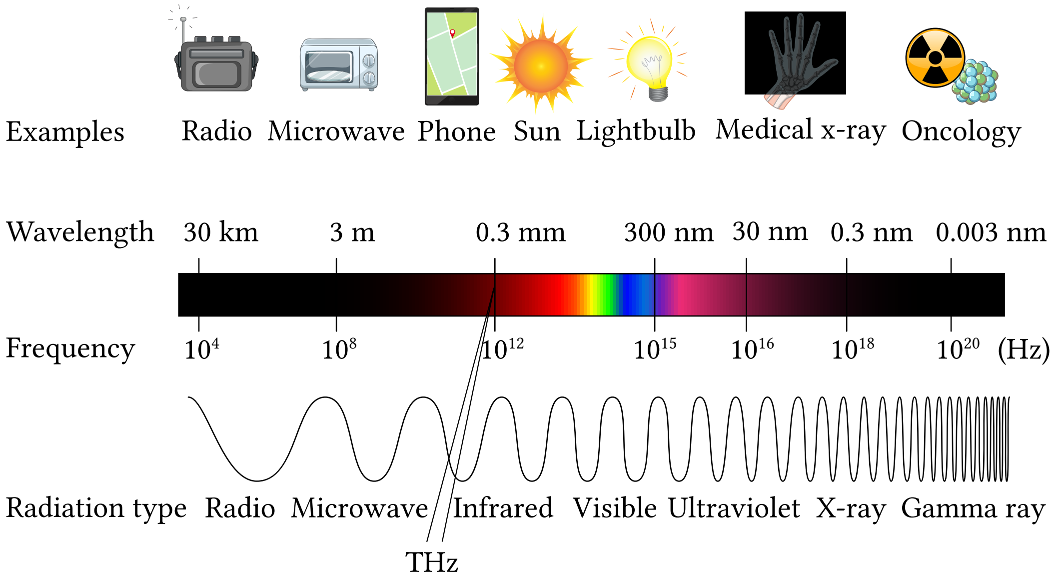

Figure 5.1: The electromagnetic spectrum and examples of application.

through a non-linear material, a 2 mm thick [110] zinc telluride (ZnTe) crystal. The resulting optical rectification of 800 nm ultrashort pulses leads to generation of a THz pulse that is around 1 ps of duration. Most materials show a significant transmission of electromagnetic radiation in the THz frequency range. One of the few exceptions is gold. Therefore parabolic gold mirrors are used to align and focus the THz pulses beam on the sample and later on the detection crystal. The detection of the THz beam can be achieved by a method called electro-optic sampling (EOS). EOS is based on the changes of the polarization of another 800 nm pulsed beam by the electric field of the THz pulse. Therefore, at the 1 mm thick ZnTe detection crystal, the THz pulse is spatially and temporally overlapped with the linearly polarized gating beam (using a colorPol VIS–IR polarizer, CODIXX). Here, the electric field of the THz beam is reconstructed by EOS, measuring the effect of the birefringence on the detection crystal, and scanning the gate arrival time over the THz waveform. In other words, the polarization change can be measured by photodiodes placed behind a Wollaston prism. By changing the time delay of the NIR detection pulse, the whole electric field of the THz pulse can be scanned, and the electric field of the THz pulse can be readily extracted. To modify the arrival time of the gate pulse, a translation stage is used.[1]

Figure 5.2 shows a scheme of the experimental method. The calculation of the THz conductivity from the THz measurements is described in the following section 5.2.3. The electric fields from sample and reference beam were first used to extract phase and magnitude, followed by fitting them to get the THz conductivity and subsequently fitting the conductivity results with the Drude–Smith model.

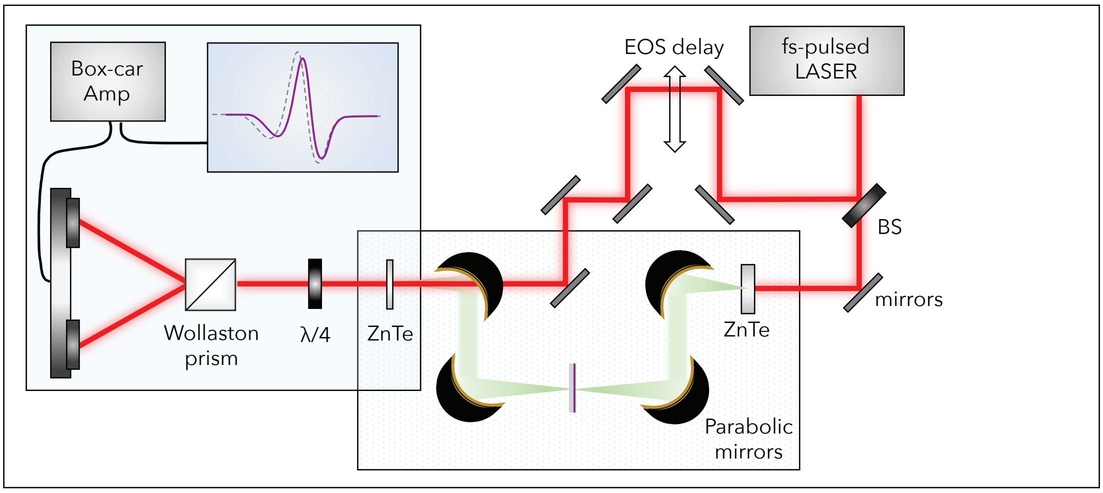

Figure 5.2: Schemtaic top-view of the THz-TDS setup.

5.2.3 THz conductivity

The technique of THz time-domain spectroscopy contains more information about the sample than a single value for the conductivity. The mathematical introduction of the THz conductivity is largely adopted from Maximilian Horn's Master thesis[2]. The methodology has been published manifold[3, 4, 5]. The complex conductivity is given by a real part $\sigma_{\mathrm{Re}}(\omega)$ and an imaginary part $\sigma_{\mathrm{Im}}(\omega)$ as a function of an oscillating electric field. As such, it is capturing both the real (conductive, energy dissipation) and imaginary (reactive, energy storage) components[6] of charge transport and is expressed as:

$$\tilde{\sigma}(\omega) = \sigma_{\mathrm{Re}}(\omega) + i\sigma_{\mathrm{Im}}(\omega) \tag{5.2}$$

The frequency dependence of $\sigma_{\mathrm{Re}}(\omega)$ and $\sigma_{\mathrm{Im}}(\omega)$ offers information on the conductivity and also the degree of localization of charge carriers. Delocalized charge carriers, move freely across the material, leading to a relatively weak frequency dependence at low to moderate frequencies, as their motion is more akin to ballistic transport. Localized charge carriers, on the other hand, reside on specific sites or states, leading to hopping transport as explained in chapter 4. Localized and delocalized charge transport have a different dependency on the frequency of the applied field. The typical frequency-dependent complex conductivity reoccurs in the results chapters of this thesis. Therefore, the THz conductivity is extracted from the complex refraction index $\tilde{n}_2(\omega) = n(\omega) + \mathrm{i}\kappa(\omega)$ with the real and imaginary part $n(\omega)$ and $\kappa(\omega)$ dependent on the angular frequency ω, respectively. This refraction index is not readily accessible and has to be retrieved numerically. The numeric calculation is based on the spectral component of the electric field of terahertz waves transmitted through substrate and sample (S_{sample}) as well as substrate alone ($S_{\text{reference}}$):

$$S_{\text{sample}}(\omega) = \eta(\omega) \times T_{12}(\omega) \times T_{23}(\omega) \times P_2(\omega, d) \times \sum_{k=0}^{+\infty} \{R_{21}(\omega) \times R_{23}(\omega) \times P_2^2(\omega, d)\}^k \times E(\omega) \tag{5.3}$$

$$S_{\text{reference}}(\omega) = \eta(\omega) \times T_{13}(\omega) \times P_1(\omega, d) \times E(\omega) \tag{5.4}$$

Here, the indices 1, 2, or 3 refer to the media the terahertz wave propagates through. For a film spin-coated on a flat glass surface, medium 1 is air (with $n_1 = 1$), medium 2 the polymer film and medium 3 quartz glass (with $n_3 = 2$). The substrates are clear fused quartz (TPG Technical Glass Products). To clarify the assignment of these media, Figure 5.2 shows a polymer thin film on a substrate in the measurement setup. $E(\omega)$ is the electric field of the terahertz wave, $\eta(\omega)$ summarizes the transmission, reflection, and propagation coefficients of media 1 and 3 by supposing negligible echoes of the terahertz wave. However, these factors are not negligible for medium 2 and the interface between two adjacent media. Therefore, the transmission coefficients $T_{\text{ab}}(\omega)$, the reflection coefficients $R_{\text{ab}}(\omega)$ and the propagation coefficient $P_{\text{n}}(\omega, d)$ have to be considered:

$$R_{\text{ab}}(\omega) = \frac{\tilde{n}_{\text{a}} - \tilde{n}_{\text{b}}}{\tilde{n}_{\text{a}} + \tilde{n}_{\text{b}}} \tag{5.5}$$

$$T_{\text{ab}}(\omega) = \frac{2\tilde{n}_{\text{a}}}{\tilde{n}_{\text{a}} + \tilde{n}_{\text{b}}} \tag{5.6}$$

$$P_{\text{n}}(\omega, d) = \exp\left[\mathrm{i}\,\tilde{n}_{\text{n}}\frac{\omega d}{c}\right] \tag{5.7}$$

In those formulas, $\tilde{n}_\mathrm{n}$ denotes the complex refraction index of the medium n. For media like air and glass, the refraction index can be rewritten to a real refraction index n_n. The coefficients $T_\mathrm{ab}(\omega)$ and $R_\mathrm{ab}(\omega)$ thus symbolize the transmission and reflection coefficient at the a–b interface. The propagation coefficient $P_\mathrm{n}(\omega, d)$ describes the propagation of the terahertz wave in medium n over a distance d with a velocity at the speed of light c. For the polymer film, this distance d is the film thickness. The part of Equation 5.4 summed by the sum symbol accounts for internal back-and-forth reflections—Fabry–Pérot contributions—of the terahertz wave between the different interfaces. It denotes

$$\mathrm{FP}(\omega) = \sum_{k=0}^{+\infty} \{R_{21}(\omega) \times R_{23}(\omega) \times P_2^2(\omega, d)\}^k = \frac{1}{1 - \left(\frac{\tilde{n}_2 - \tilde{n}_1}{\tilde{n}_2 + \tilde{n}_1}\right)\left(\frac{\tilde{n}_2 - \tilde{n}_3}{\tilde{n}_2 + \tilde{n}_3}\right) \times \exp\left[2\mathrm{i}\, \tilde{n}_2 \frac{\omega d}{c}\right]} \quad , \tag{5.8}$$

and the sum can be approximated by using the first order term $k = 1$ only. To simplify the analysis, the transmission coefficient $T(\omega)$ between the spectral components of the terahertz waveforms is calculated:

$$T(\omega) = \frac{S_\mathrm{sample}(\omega)}{S_\mathrm{reference}(\omega)} = \frac{2\tilde{n}_2(\tilde{n}_1 + \tilde{n}_3)}{(\tilde{n}_1 + \tilde{n}_2)(\tilde{n}_2 + \tilde{n}_3)} \times \exp\left[\mathrm{i}(\tilde{n}_2 - \tilde{n}_1)\frac{\omega d}{c}\right] \times \mathrm{FP}(\omega) \tag{5.9}$$

The only unknown value in this formula is $\tilde{n}_2$, parametrized by n and κ. Those can be retrieved by fitting Equation 5.9 with the measured $T_\mathrm{meas.}(\omega)$:

$$T_\mathrm{meas.}(\omega) = \frac{S^\mathrm{meas.}_\mathrm{sample}(\omega)}{S^\mathrm{meas.}_\mathrm{reference}(\omega)} \tag{5.10}$$

We split both $T(\omega)$ and $T_\mathrm{meas.}(\omega)$ in their corresponding magnitude $r = |T|$ and phase $\varphi = \arg(T)$. Both the natural logarithm of $|T|$ and the phase $\arg(T)$ have planar character when plotted versus n and κ. Therefore, we define the differences between $T(\omega)$ and $T_\mathrm{meas.}(\omega)$:

$$\delta\rho = \ln(|T(\omega)|) - \ln(|T_\mathrm{meas.}(\omega)|) \tag{5.11}$$

$$\delta\varphi = \arg(T(\omega)) - \arg(T_\mathrm{meas.}(\omega)) \tag{5.12}$$

Due to their linear character, we can use their squared values $\delta\rho^2$ and $\delta\varphi^2$ to find the minimum for a parabola where the parameters n and κ of $T(\omega)$ best describe $T_\mathrm{meas.}(\omega)$.

This is implemented by fitting

$$y = \left\{\delta\varphi^2 + 1\right\} \times x + \delta\rho^2 \tag{5.13}$$

$$= \left\{\left[\arg(T(\omega)) - \arg(T_{\text{meas.}}(\omega))\right]^2 + 1\right\} \times x + \left[\ln\left(|T(\omega)|\right) - \ln\left(|T_{\text{meas.}}(\omega)|\right)\right]^2 \tag{5.14}$$

with the linear function

$$y = 1 \times x + 0 \quad . \tag{5.15}$$

In this work, we use a non-negative least squares (NNLS) algorithm to implement the above-described fitting strategy. After having retrieved the parameters n and κ of $\tilde{n}_2(\omega)$, the THz conductivity $\tilde{\sigma}(\omega)$ can be calculated. The refractive index $\tilde{n}_2(\omega)$ is connected to the dielectric function or permittivity $\tilde{\varepsilon}(\omega)$ and the permeability μ of the material by

$$\tilde{n}_2(\omega) = n(\omega) + \mathrm{i}\kappa(\omega) = \sqrt{\tilde{\varepsilon}(\omega)\,\mu} \overset{\mu=1}{=} \sqrt{\tilde{\varepsilon}(\omega)} \quad . \tag{5.16}$$

For non-magnetic materials, the permittivity is $\mu = 1$, simplifying the formula. The dielectric function is a complex term featuring the real lattice component $\varepsilon_{\mathrm{L}}(\omega)$ and an imaginary part containing the vacuum permittivity $\varepsilon_0 = 8.854\,\mathrm{A\,s\,V^{-1}\,m^{-1}}$ and the THz conductivity $\tilde{\sigma}(\omega)$:

$$\tilde{\varepsilon}(\omega) = \varepsilon_{\mathrm{L}}(\omega) + \frac{\mathrm{i}\,\tilde{\sigma}(\omega)}{\omega\varepsilon_0} \tag{5.17}$$

Combining the Equations 5.16 and 5.17 and using the high-frequency dielectric constant ε_∞ for the lattice component $\varepsilon_{\mathrm{L}}(\omega)$ (in this work, we use $\varepsilon_\infty = 3$), we obtain the relation

$$\tilde{\varepsilon}(\omega) = n^2(\omega) + 2\mathrm{i}\,n(\omega)\kappa(\omega) - \kappa^2(\omega) = \varepsilon_{\mathrm{L}}(\omega) + \frac{\mathrm{i}\,\tilde{\sigma}(\omega)}{\omega\,\varepsilon_0} \overset{\varepsilon_{\mathrm{L}}(\omega)=\varepsilon_\infty}{=} \varepsilon_\infty + \frac{\mathrm{i}\,\tilde{\sigma}(\omega)}{\omega\,\varepsilon_0} \tag{5.18}$$

and finally an expression for the complex THz conductivity $\tilde{\sigma}(\omega)$ as well as its real ($\sigma_{\mathrm{Re}}(\omega)$) and imaginary ($\sigma_{\mathrm{Im}}(\omega)$) part:[4, 5]

$$\tilde{\sigma}(\omega) = \sigma_{\mathrm{Re}}(\omega) + \mathrm{i}\sigma_{\mathrm{Im}}(\omega) = \omega\,\varepsilon_0 \left\{2n(\omega)\kappa(\omega) + \mathrm{i}\left[\varepsilon_\infty - \left(n^2(\omega) - \kappa^2(\omega)\right)\right]\right\} \tag{5.19}$$

$$\sigma_{\mathrm{Re}}(\omega) = \omega\,\varepsilon_0\left[2n(\omega)\kappa(\omega)\right] \tag{5.20}$$

$$\sigma_{\mathrm{Im}}(\omega) = \omega\,\varepsilon_0\left[\varepsilon_\infty - \left(n^2(\omega) - \kappa^2(\omega)\right)\right] \tag{5.21}$$

Following this mathematical description of how the raw data yields the complex conductivity result, Figure 5.3 shows the (a) raw data in the time-domain, (b) magnitude, (c) phase, and (d) complex conductivity result for example data of P3HT anion exchange doped using Magic Blue and $\mathrm{TBAPF_6}$. In (a) the grey dashed curve shows the THz pulse transmitted through the reference substrate and the purple curve shows the THz pulse transmitted through the sample on the same reference substrate. The same colour code is kept. The (b) magnitude is higher in the reference measurement and attenuated in the sample measurement. The (c) phase is only slightly different between the reference and the sample, the signal is phase-shifted by only about 10 femtoseconds while our time resolution is limited to around 3 femtoseconds. This is the case because the example data is from a 60 nm spin-coated thin film. The (d) complex conductivity shows the real part $\sigma_{\mathrm{Re}}(\omega)$ and the imaginary part $\sigma_{\mathrm{Im}}(\omega)$ as a function of frequency. The real part has a value of around 230 S/cm and increases with a low slope with increasing frequency. The imaginary part is below zero and decreases with increasing frequencies. This is a typical complex conductivity shape of materials with a partly conductive and capacitive (localized) response to the THz electric field. This behavior is commonly described within the Drude–Smith model.

5.2.4 Drude–Smith model

To uncover the degree of localization, the Drude–Smith model (DSM) can be utilized.[6] The classical Drude model describes ballistic transport of charge carriers and incorporates the effect of backscattering. Smith's contribution was the extension by a term that phenomenologically captures additional localization events. The combined Drude–Smith model is expressed by:

$$\tilde{\sigma}_{\mathrm{DS}}(\omega) = \frac{Ne^2\tau}{(1-\mathrm{i}\,\omega\tau)\,m^*}\left(1+\frac{c_1}{1-\mathrm{i}\,\omega\tau}\right) \tag{5.22}$$

Here, ω is the angular frequency, N the carrier density, e the elementary charge, m^* the effective mass, τ the scattering time, and c_1 the localization parameter which can take values between 0 (which restores the Drude model because no charges are backscattered) and −1 (where all charges are backscattered and therefore localized). The scattering time τ describes the mean travelling time of charge carriers before being backscattered, e.g., due to chain endings or grain boundaries[7]. Fitting the THz conductivity $\tilde{\sigma}(\omega)$ received from Equation 5.19 with the Drude–Smith model, the values for N, c_1 and τ are retrieved, which can be used to improve the understanding of the charge transport

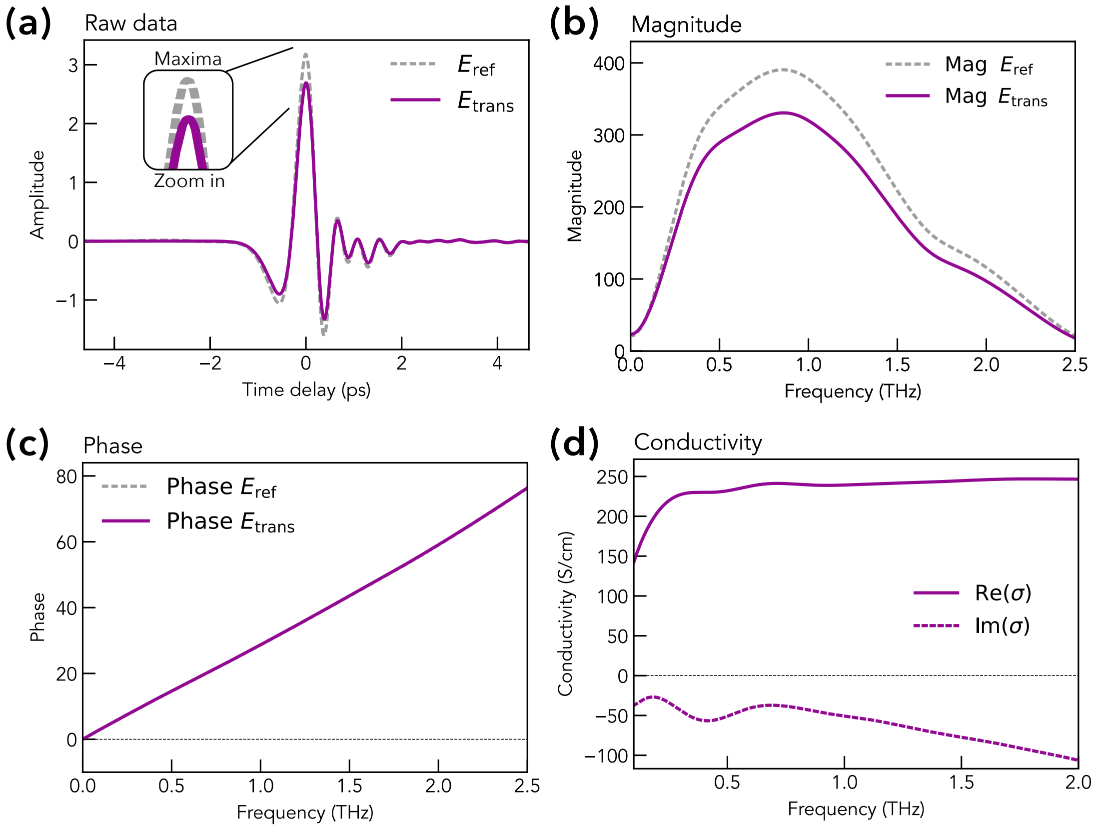

Figure 5.3: The electromagnetic spectrum and examples of application.

properties of the material and compare different doping methods. It has to be noted that we use the Drude–Smith model phenomenologically only. The localization parameter c_1 and the scattering time τ can stem from a combination of things including the microstructure of the polymer, the interaction between dopant anion and polymer chain, the interaction between the charges themselves. Thus, c_1 and τ only scratches the different scattering and localization processes and cannot be used to assign specific events.[8] In a representative doped polymer complex conductivity and DSM fit the real part σ_{Re} is positive and the imaginary part σ_{Im} is negative. I commonly compare the real part of the complex conductivity to my direct current conductivity. The light blue curve shows a DSM fit. Then, the real part $\sigma_{\text{Re}}(1\,\text{THz})$ at a frequency of 1 THz is the value that represents the short-range conductivity (nanoscale) and is denoted by Shortσ. The DSM is widely used to extract the effective mobility (μ_{eff}) in materials where charge carriers experience partial localization or scattering that deviates from the assumptions of purely free-electron motion. The mobility in the DSM is expressed as:

$$\mu_{\text{eff}} = \mu_{\text{Drude}}\,(1 + c_1) = \frac{e\tau}{m^*}(1 + c_1) \tag{5.23}$$

To sum up, THz-TDS in combination with the DSM provides a powerful framework to probe charge transport properties in materials, particularly in systems with disorder or partial localization. By analyzing the optical conductivity spectra, it is possible to extract critical parameters such as the carrier scattering time (τ), the effective mobility (μ_{eff}), and the backscattering parameter (c_1). These parameters give insights into the degree of carrier localization, with c_1 quantifying the extent of backscattering and deviations from Drude-like free-carrier transport. As such, the DSM allows to distinguish between charge carriers contributing to charge transport and those undergoing frequent scattering or localization. This makes it an indispensable tool for understanding the interplay between disorder, microstructure, and charge transport mechanisms in this thesis.

5.3 Implementation of cryogenic optical setup

5.3.1 Implementation and experimental method

One of the technical challenges of my doctoral work was the design, implementation, and testing of a cryogenic system integrated with terahertz time-domain spectroscopy (THz-TDS). This section details the critical considerations for the sample holder, radiation shield, and ultra-high vacuum (UHV) chamber, as well as the experimental procedures for assembly, calibration, and measurement.

The **sample holder design** provides both thermal and mechanical requirements while accommodating the optical requirements of THz-TDS. To ensure accurate temperature measurement, silicon diode temperature sensors were strategically positioned above and below the sample. This configuration optimized thermal conduction while leaving an unobstructed optical path for THz radiation. The holder also incorporated materials with low thermal expansion coefficients to reduce mechanical stress during temperature cycling.

A **radiation shield** was implemented to minimize thermal radiation from the surroundings and thereby optimizing the cooling efficiency. The shield design ensured compatibility with the optical windows needed for THz transmission while maintaining effective isolation. The cryogenic system is housed within a tailored **ultra-high vacuum chamber**. The windows of the chamber are THz-transparent and mounted on a movable crane to ensure low-vibration operation, which is essential for accurate optical measurements. The assembly and positioning emphasized precision alignment of optical windows in a 90° angle in respect to the THz beam path.

Next, transmission measurements of the substrate material during cooling and heating cycles between 300 and 6 K are done to rule out potential changes in optical properties of the substrate which could impact the **accuracy of the referencing method**. For each cryogenic THz-TDS measurement, a rigorous referencing method is employed during the measurement cycle. The referencing is done using a cleaned spot on the substrate, analogous to standard THz-TDS referencing techniques. Measurements were taken on the same spot of the sample throughout the cooling cycle, and the reference was measured again at low temperatures to control for any changes in the THz waveform during the cooling cycle. Several iterations of different sample and reference spots are measured at low temperature. The sample spot is constant during the heating cycle. The reference is taken again at room temperature to assess hysteresis between cooling and heating. The cooling and heating cycle are compared to control for any hysteresis in the temperature-dependent conductivity. Moreover, **potential dedoping** of the film is also evaluated by comparing steady-state absorbance spectra before and after the measurement cycle. As such, careful design, implementation, and testing of the cryogenic system enables precise THz-TDS measurements between 300 K and 10 K of the sample position. The cryostat is a closed-loop Helium cryostat (ARS 8200) with an operational temperature range between 300 and 6 K. The cold finger is equipped with a thermo heater sheet to be able to counter-heat and stabilize any temperature between 6 K and 150 K. Above 150 K, it is not recommended to use counter-heating to avoid hot pockets which can be damaging to the electrical wires in the close limited space. Two Si diodes are carefully placed above and below the sample position to get an accurate temperature measurement. The Si diodes come with a calibration curve, but a soft calibration with two points: room temperature and 77 K liquid nitrogen is repeated before operation. The temperature controller (Model 331 from Lakeshore Cryotronics) sets the heater efficiency and operation automatically and is used to gather three datapoints: set temperature, control temperature and sample temperature, every 10 seconds. The cryogenic information is implemented in the tailored LabView software

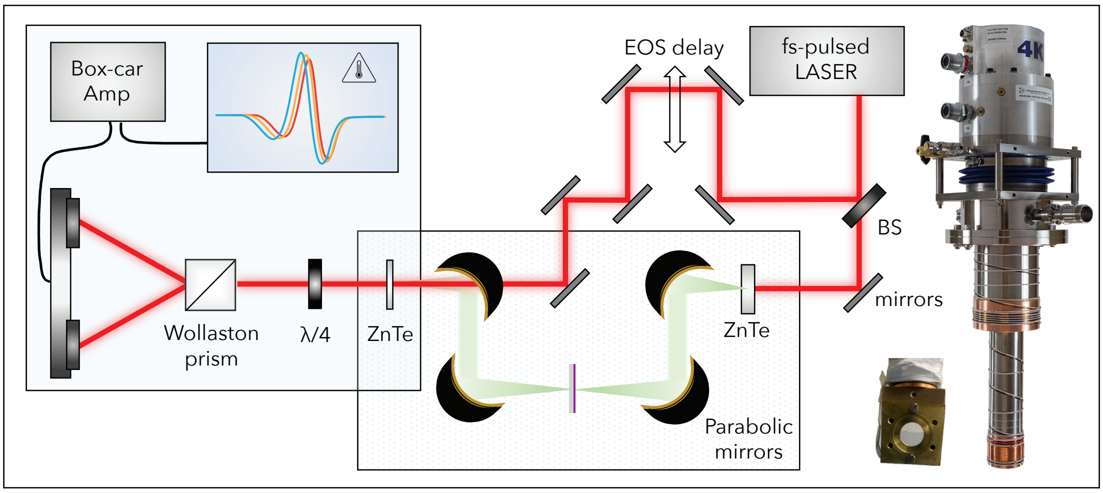

Figure 5.4: Scheme of the cryogenic THz TDS setup is based on the previous scheme.

for THz-time domain spectroscopy to connect a THz measurement to the accurate temperature. The temperature is measured every 10 seconds and averaged over the 300 seconds of each THz measurement.

5.3.2 Temperature-dependent THz conductivity

Figure 5.4 shows the type of results obtained by cryogenic THz-TDS, which I have established in the group. It demonstrates how versatile the experiment of THz-TDS with a cryogenic setup is. It is a powerful technique to study charge transport in doped polymers, because it measures the characteristic temperature-dependent conductivity and the THz complex conductivity as a direct observable. This yields information about the degree of localization of charges and the activation to charge transport. The Figure shows exemplary data to study of doped PDPP4T. THz-TDS is used to measure the material's response to a THz pulse, as illustrated schematically in panel (a). The THz pulse interacts with the material, causing attenuation of its amplitude and a time shift. By comparing the transmitted THz pulse with a reference (an empty substrate), the conductivity of the material can be extracted. A smaller transmitted THz pulse relative to the reference indicates higher material conductivity.

Panel (b) shows the transmitted THz pulse amplitude as a function of temperature. At room temperature (295 K), the transmitted pulse is attenuated and smaller in amplitude. As the temperature is lowered to 10 K, the transmitted amplitude increases, meaning the material's response with the THz pulse decreases with decreasing temperature. Panel (c) depicts the real part of the conductivity at a frequency of 1 THz $\sigma_{\mathrm{Re}}(1\ \mathrm{THz})$. The conductivity decreases as the temperature is lowered as calculated from the raw data in panel (b) by the calculation described in section 5.2.3. The lower conductivity at low temperatures indicates significant localization of charge carriers. Panel (d) shows the complex THz conductivity as a function of frequency. The real part σ_{Re} is positive over all frequencies and it decreases with temperature. The imaginary part σ_{Im} is negative over all frequencies. The negative imaginary component is characteristic of a Drude-Smith-like response, which indicates localized charge transport as described in section 5.2.4. In summary, the figure illustrates the use of cryogenic THz-TDS to

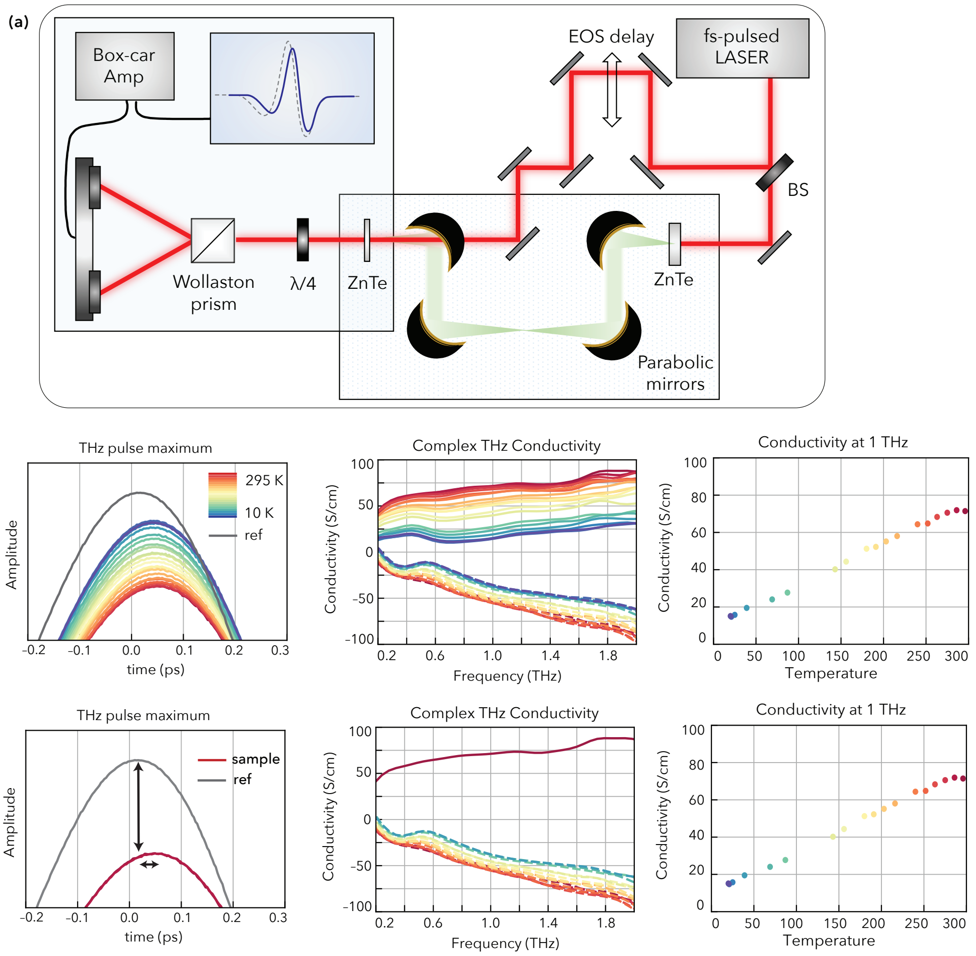

Figure 5.5: Scheme and type of results obtained from Cryogenic THz TDS. (Exemplary data of doped PDPP4T).

investigate the charge transport in doped polymers. The complex conductivity confirms localized or delocalized transport. Moreover, the degree of localization can change as a function of temperature. This methodology provides critical insights into the interplay between temperature and charge transport in materials.

5.4 Optical pump-terahertz probe spectroscopy

5.4.1 Experimental method

The optical pump–THz probe (OPTP) setup is based on the THz-TDS explained above. To implement an optical pump beam, a portion of the 800 nm ultrafast pulsed beam is used for optical parametric amplification (OPA). In Chapter 8 I use a 700 nm optical pump beam. The 700 nm output from a OPA (TOPAS-PRIME) is used to excite the sample. To generate a 700 nm beam from an 800 nm fundamental using the second harmonic (SH) of the signal in a OPA, the process involves two steps. First, the OPA generates a signal beam at 1400 nm through parametric down-conversion of the 800 nm pump in a nonlinear crystal. Next, the 1400 nm signal is passed through a second nonlinear crystal, optimized for second harmonic generation (SHG). In this step, two photons of 1400 nm combine to produce a single photon at 700 nm, achieving the desired wavelength. Figure 5.6 shows the OPTP setup with the fundamental laser beam in red

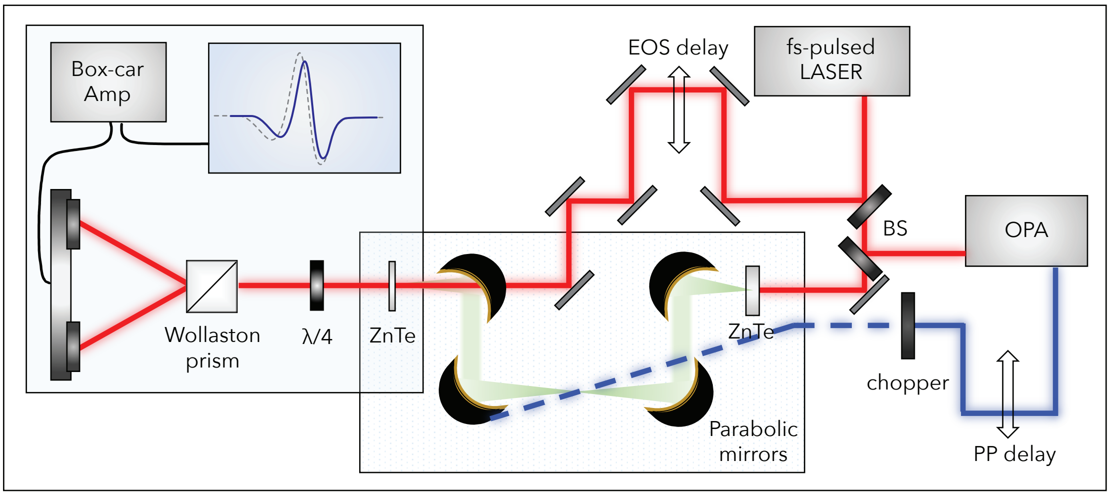

Figure 5.6: Schematic top-view of the OPTP setup showing the additional pump beam generated in the OPA.

(800 nm, around 40 fs pulsed with 1 kHz repetition rate) originating from the laser in the top right corner. There are three different colored beams in the scheme: red for the fundamental beam (800 nm), blue for the optical pump beam and green for the THz pulsed beam. The red beam hits the first beam splitter that splits the fundamental into two beams. One part goes into the optical parametric amplifier (OPA) which generates the optical pump beam, in this case the desired optical pump beam at 700 nm. The optical pump beam goes on the delay state (PP delay) and through a chopper before exciting the sample (pump diameter 3.0 mm) and ending after. The second part is split again to fulfill the purpose of THz generation and THz detection respectively. The THz generation occurs in a zinc telluride (ZnTe) nonlinear crystal by optical rectification. The THz beam is focused on the sample (probe diameter 1.5 mm). The transmitted THz beam is next focused on a second ZnTe crystal for detection by electro-optic sampling. Electro-optic sampling (EOS) is a technique used to measure the electric field of the transmitted THz pulse with high temporal and spatial resolution. It relies on the electro-optic (Pockels) effect, in which the polarization state of an optical beam (800 nm) is modulated by the electric field of the THz pulse as they interact in the second ZnTe nonlinear crystal. The pump beam is chopped at half frequency 500 Hz such that the immediate response of two sub-sequent THz pulses yields the differential THz pulse transmission.

5.4.2 THz photoconductivity

The OPTP setup is used to measure photoconductivity spectra or photoconductivity dynamics. When photo-induced charge carriers experience a THz electric field, they move. To measure the photoconductivity spectra over the entire THz waveform, I set the translation stage (PP delay) of the pump-THz delay at a fixed time after photoexcitation. For example, the translation stage (PP delay) is fixed at a delay of 10 ps after photoexcitation. Having the chopper set at half frequency in the optical pump beam allows me to measure $E_{\text{pump}}(\omega)$ and $E_{\text{pump}}(\omega)$ with two subsequent pump pulses. Then, I can scan the entire THz waveform by varying the translation stage (EOS delay) of electrooptic sampling. This is done for all EOS delays and hence angular frequencies ω to obtain the waveform. I use parenthesis, because I am measuring in the time-domain and need to do a Fourier transform to obtain the waveform as a function of angular frequency ω. To measure the photoconductivity dynamics, I set the translation stage

(EOS delay) to the maximum of the differential THz waveform. Having the chopper set at half frequency in the optical pump beam allows me to measure $E_{\text{pump}}(t)$ and $E_{\text{pump}}(t)$ with two subsequent pulses. Then, I can vary the time delay between optical pump and THz probe to get the dynamics of the maximum differential THz waveform. The photoconductivity is calculated from the differential signal using equation:

$$\sigma(\omega, t) = -\frac{n_0 + n_{\text{air}}}{Z_0 d} \frac{E_{\text{pumped}}(\omega, t) - E_0(\omega, t)}{E_0(\omega, t)} \tag{5.24}$$

Hereby, $n_0 \approx 1.76$ and $n_{\text{air}} \approx 1.00$ give the refractive index of the sapphire substrate and air respectively. $Z_0 = 376.7\Omega$ is the constant impedance of free space. d is the thickness of the sample, whereby it is important to use the thickness of the charge transport layer. $E_{\text{pump}}(\omega, t)$ and $E_0(\omega, t)$ is the transmitted THz electric field in the frequency domain of the photo-excited (pumped) and ground state (unpumped) material respectively. The difference signal $E_{\text{pump}}(\omega, t) - E_0(\omega, t)$ is very small though, around 10^{-4} times smaller than THz conductivity of doped OSC in reference to the substrate. The THz photoconductivity resulting from equation 5.24 can be analysed similarly to the described THz conductivity though. The photoconductivity spectra are analysed in analogy to the other chapters by applying the Drude-Smith model.

5.5 Non-spectroscopic Methods

In this methods section of my thesis I present a list of the techniques that I personally got training in and directly worked on. Thereby, I demonstrate a diverse skillset combining my core expertise in spectroscopy with complementary techniques from the FemtoMat group and my international research stays. Moreover, the thesis contains additional methods *via* collaborations which are: GIWAXS, spectroelectrochemistry and kinetic Monte Carlo simulations. The detailed description on collaboratory methods are given in the results chapters where relevant. This is also a reminder to find the diverse contributions of me and other researcher to this thesis in Appendix One.

5.5.1 Electrical (macroscopic) conductivity

The macroscopic conductivity is measured using a commercial setup from Ossila specifically designed to measure conductivities of polymer films. The compact linear four-point probe system (TypeG product code is T2001A4) provides precise and reliable measurements of sheet resistance and resistivity in thin films by minimizing contact resistance effects through its spaced collinear probe configuration, ensuring accurate characterization of conductive materials. The experimental setup consists of four spring-loaded electrodes with rounded tips to avoid piercing the soft polymer thin films. The electrodes have a fixed distance of 1.27 mm and linear arrangement. The force of the electrodes on the film is also predetermined by the setup and the spring-loaded electrodes. The electrodes are placed on the sample by moving a micrometer screw on the sample stage. The outer electrodes apply a current and the voltage drop between the inner electrodes is measured for different currents. The slope of the I / V curve is then used to calculate the sheet resistance R_S.[9] For small samples, correction parameters might apply based on the film surface dimensions. The typical dimensions of my polymer samples are 16 x 25 mm (optimized for my optical sample holders). Using this sheet resistance in combination with the film thickness d leads to the macroscopic (or 4PP conductivity) σ_{4PP}:

$$\sigma_{4PP} = \frac{1}{R_S \times d} \tag{5.25}$$

At least six positions on the sample are measured in addition to the automatic averaging of 100 I / V measurements by the equipment software to minimize measurement errors.

5.5.2 Film thickness

The film thickness is an essential parameter for the calculation of the conductivity. The calculation of the conductivity is based on the sheet resistance R_S (see Eq. 5.25), which is inversely proportional to the thickness. Thickness and roughness of prepared samples were determined using white light interferometry (WLI) with a Bruker CountourGT optical profiler with 5x magnification. Moreover, the thicknesses were confirmed using a Bruker Dektak Pro profiler. In both cases, at least 12 positions (on at least 2 scratches) on the sample were measured and averaged. For WLI, a white light beam is split into two beams. One of the beams is focused on the film surface with the film lying on top of a platform tiltable and movable in the direction of the beam propagation. The other beam is focused on a fixed surface. Using this setup, interference patterns are created by overlapping both beams. When moving the platform where the film is mounted, the interference pattern changes, enabling the device to calculate the surface topology. This method can either be used to reveal grains in the surface topology that might limit charge transport or to measure the film thickness. For the latter use case, the film had to be scratched to unveil the underlying substrate. Subsequently, the distance between the surface of the substrate and the surface of the film was measured.

5.5.3 Seebeck coefficient and Power Factor

The Seebeck coefficient is a measure of an induced thermoelectric voltage in response to a temperature difference across a material, as induced by the Seebeck effect. The Seebeck coefficient is measured using a home-built system with a linear temperature gradient across one sample orientation. This enables the precise determination of thermoelectric properties by measuring the voltage response to a controlled temperature gradient across a material, providing critical insights into its thermoelectric charge carrier properties and energy conversion efficiency. The Seebeck measurements were done on 15 x 15 mm samples with linear gold electrodes evaporated on the sample. The steady-state absorbance before and after the experiments did not show any dedoping or degradation between sample preparation, electrode evaporation under ultra high vacuum or Seebeck measurements.

$$S = -\frac{\Delta V}{\Delta T} \tag{5.26}$$

The Power factor is calculated from the room temperature Seebeck coefficient and electrical conductivity Long σ. The Power Factor in thermoelectric materials is calculated by the equation below. Hereby, power factor PF is typically expressed in μW/mK^2 , the Seebeck coefficient S in μV/K and the Long σ in S/m.

$$PF = S^2 \cdot \sigma \tag{5.27}$$

5.5.4 Hall effect

The topic of Chapter 7 is charge transport in doped polymer films. Therefore, I measure the Hall effect in doped polymer samples. The Hall effect leads to a voltage difference (the Hall voltage) across an electrical conductor that is transverse to an electric current in the conductor and to an applied magnetic field perpendicular to the current. I used a LakeShore cryotronics HMS-TT FastHall Station. The equipment comes with a 1.8 T stron magnet and the Hall voltage is measured with spring-loaded gold electrodes *versus* a platinum electrode also in the magnetic field. The sample dimensions are 10 x 10 mm films on quartz coated glass and evaporated gold electrodes in the van der Pauw geometry. The Hall coefficient, R_H, in organic semiconductors reflects contributions from both band-like and hopping transport mechanisms, which are influenced by the mobility and density of charge carriers. Thereby, only band-like charge carriers contribute and disordered materials often give a suppressed Hall coefficient. The Hall coefficient can be expressed as:

$$R_H = \frac{n_b \mu_b^2}{q(n_b \mu_b + n_h \mu_h)^2},$$

where n_b and μ_b are the carrier density and mobility for band-like transport, and n_h and μ_h are the carrier density and mobility for hopping transport. Here, q is the elementary charge. This distinction is crucial for interpreting Hall effect measurements in disordered organic semiconductors, where mixed transport behaviors are common. The ratio of of positive and negative charge carriers, p/n, reflects the balance between p-type (holes) and n-type (electrons). For p-doped OSC, a close-to-unity p/n ratio is usually a good indicator for a correct experiment. Work by Podzorov largely promote the relevant experimental steps for organics specifically.

5.5.5 Thermal activation energy

The thermal activation energy is determined by four distinct methods. First, the electrical (macroscopic) thermal activation around room temperature. Second, the THz (short-range) thermal activation around room temperature. Third, the thermal activation energy, in the frozen disorder limit, i.e. below 50 K when all vibrational modes and transient degrees of freedom should be frozen. And last, the thermal activation energy over the entire temperature range range of 300-10 K using the presented STLoT model. To determine the electrical (macroscopic) thermal activation the conductivity Longσ of doped polymer films is measured at varying temperatures between 290 K and 310 K using 10 x 10 mm samples with evaporated gold electrodes in van der Pauw geometry. The conductivity of the films is calculated from the thermoelectric voltage drop measured by a Keithley 2400 Digital Sourcemeter. The change in conductivity was plotted on a logarithmic scale against the inverse temperature to obtain an Arrhenius type plot. The thermal activation was extracted from the slope of the Arrhenius plot.

The thermal activation is also obtained from the nanoscale conductivity Shortσ of doped polymer films. Therefore, a closed-loop Helium cryostat is used, the thermal activation from a simple Arrhenius plot in analogy to the macroscopic thermal activation is extracted from the 240 to 300 K range. The sample geometry for optical measurements was around 15 x 25 mm on clear fused quartz substrates (TPG Technical Glass Products). Moreover, the reduced activation energy is extracted from the STLoT model and Zabrodskii analysis, as described in great detail where relevant in Chapter 7.

References for Chapter 5

[1] Krauspe, P., Banerji, N. & Réhault, J. Effective detection of weak terahertz pulses in electro-optic sampling at kilohertz repetition rate. J. Opt. Soc. Am. B **37** (1), 127–132 (2020).

[2] Horn, M. *Doping Optimization of Glycolated Polythiophene* Master Thesis, University of Hamburg, Faculty of Mathemtaics and Natural Sciences (2023).

[3] Duvillaret, L., Garet, F. & Coutaz, J.-L. A reliable method for extraction of material parameters in terahertz time-domain spectroscopy. IEEE J. Sel. Top. Quantum Electron. **2** (3), 739–746 (1996).

[4] Ulatowski, A. M., Herz, L. M. & Johnston, M. B. Terahertz conductivity analysis for highly doped thin-film semiconductors. J. Infrared Milli. Terahz Waves **41** (12), 1431–1449 (2020).

[5] Lloyd-Hughes, J. & Jeon, T.-I. A review of the terahertz conductivity of bulk and nano-materials. J. Infrared Milli. Terahz Waves **33** (9), 871–925 (2012).

[6] Smith, N. V. Classical generalization of the drude formula for the optical conductivity. Phys. Rev. B **64**, 155106 (2001).

[7] Tsokkou, D., Cavassin, P., Rebetez, G. & Banerji, N. Bipolarons rule the short-range terahertz conductivity in electrochemically doped P3HT. Mater. Horiz. **9**, 482–491 (2022).

[8] Cocker, T. L. et al. Microscopic origin of the Drude–Smith model. Phys. Rev. B **96**, 205439 (2017).

[9] Ossila. Four-probe method, macroscopic conductivity and electrode spacing. https://www.ossila.com/pages/sheet-resistance-theory **1** (1) (2024).

6 Glycolated side-chains of polymers

> *"Imagine you are at a party and everyone dances with their arms stretched out straight from their bodies.*
> *No wonder why nobody wants to work with alkyl side-chains."*
>
> Dr. Kaila Yallum.

This chapter is based on an article in preparation for the Journal of Materials Chemistry C. The project was realized in collaboration with these researchers. Please find everyone's valuable contributions that enabled the project in Appendix One.

Eva Röck, Demetra Tsokkou, Emmy Järsfall, Sepideh Zokaei, Jaime Martín, Christian Müller, Martijn Kemerink, Natalie Banerji.

6.1. Origin of the enhanced conductivity in doped polythiophenes with glycolated side-chains

Abstract

Doped polythiophenes are popular materials for organic electronic devices such as photovoltaics, transistors, photodetectors or biosensors. Many of their advantageous properties like flexibility, semi-transparency and solution-processability are based on their semi-crystalline microstructure. The study of glycolated polythiophenes is booming and amongst other advantages these materials show higher conductivity. This chapter aims to enlighten which parameters improve the conductivity by how much by systematically looking at the short- and long-range conductivity of a model system with alkyl- and oligoether glycol side-chains. My experiments show a 10-fold improved conductivity on the short-range and a 100-fold improved conductivity on the long-range for the glycolated polythiophene. Combining experiment and numerical simulation, the increase is explained with contributions of the parameters (i) dielectric constant, (ii) energetic disorder, (iii) spatial confinement and (iv) long-range order.

6.1.1. Introduction

Polythiophenes are a prominent class of conjugated polymers used in organic semiconductors. Polythiophenes with glycolated side-chains are investigated extensively, due to improved ion transport and conductivity [1-5]. Yet the origin of the enhancement is not fully understood. Moreover, how the findings in the context of organic electrochemical transistors might translate to the context of molecular doping is not so clear. Glycolated side-chains simultaneously influence the dielectric constant, energetic disorder and microstructure[1-9]. This work investigates the origin of the enhanced conductivity in doped conjugated polymers with glycolated side-chains by employing THz time-domain spectroscopy (TDS) and kinetic Monte Carlo simulations (kMC).

Doping level and nature of charge carriers

Molecular doping of conjugated polymers refers to the introduction of small molecules that undergo a redox reaction with the polymer. In p-type doping, a hole is created and different energy levels within the band gap are arising. The radical dopant anion stays in the film with different binding energies depending on polymer:dopant combination[10]. This process shifts the Fermi level, enabling the generation of mobile charge carriers[10-13]. In conjugated polymers, doping induces charged species called polarons [+], which are quasi-particles formed by the combination of a charge and its surrounding lattice distortion[14]. With higher doping levels, [+] can pair up to form doubly charged species [++], which have different electronic properties and contribute differently to conductivity[13-17]. Multiple-charged species with more than two times the unit charge are also possible, but probability of formation is low. The doping efficiency is typically defined by the ratio of number of charge carriers generated to total dopant anion concentration. The doping level is defined by the number of charge carriers per repeating unit (or thiophene unit). Depending on the driving force of doping, which is proportional to the energy difference between HOMO level of the polymer and LUMO level of the dopant, one can assume integer charge transfer[12, 18, 19]. The doping level can be estimated by steady-state absorbance[15]. The steady-state absorbance depicts bands from neutral and charged species [+] and [++] and in the case of F_4TCNQ also the bands from the ionized dopant. While it is not fully quantitative to compare the absorbance of ionized dopant peaks in a convoluted absorbance spectrum, the density of ionized dopant can give an upper limit[8, 12].

Microstructure

The electronic properties of doped polythiophenes are closely tied to their microstructure[20-24]. Polythiophenes form semi-crystalline microstructure, with ordered regions and disordered regions, where the molecular packing and alignment of polymer chains affect charge transport[23, 24]. Ordered microstructures have higher conductivity and better charge mobility due to higher chain planarity and efficient $\pi-\pi$ stacking between polymer chains. In contrast, disordered regions often show reduced conductivity and hindered charge transport. Nevertheless, charge transport across distances of disordered materials can be retained as well[25, 26].

Doping affects microstructure

Doping not only modifies the electronic properties of polythiophene films but also significantly influences their microstructure[22, 27]. Doping of polythiophene semiconductors can have positive or negative effects on the microstructure of the films. The incorporation of dopant anions alters the packing of polymer chains, which can increase disorder or disrupt crystalline regions, affecting overall charge transport. Adding dopant anions into the polymeric matrix often deteriorates the self-assembled structure and has negative effects on the resulting conductivity such as seen for the combination of P3HT and F_4TCNQ[22, 27]. The F_4TCNQ dopant molecules are known to selectively dope the crystalline regions, which have a higher (less negative) ionization energy level than the disordered regions and therefore a bigger doping driving force. Especially, when polymer and dopant are co-processed in the same solution before spin-casting the non-covalent interactions before self-assembly can lead to interruption scaling with the dopant concentration[27]. The sequential doping method after self-assembly of the neat P3HT film reduces doping-induced disorder[21, 28-30].

An ordered intercalation of dopant anions driven by non-covalent interactions can have positive effects on the microstructure as well. Beneficial intercalation of F_4TCNQ has also been reported for $P(g_42T\text{-}T)$[23]. While neat $P(g_42T\text{-}T)$ is considered a highly disordered system, that does not show π–π-stacking, the doped polymer shows an improved orientation of the edge-on crystallites with increasing glycol composition [31]. It has been shown that the F_4TCNQ vapor-doped $P(g_42T\text{-}T)$ has a relatively low Gaussian disorder of 0.055 eV[32]. Generally, polar polythiophenes with higher solubilities in the processing solvent prefer to orient in a face-on rather than edge-on orientation[4].

The energetic disorder

Structural, conformational and energetic disorder are linked. As such, the energetic disorder is studied in the context of conductivity as well[21, 23, 28, 33]. The density of states for polymers is often described by localized states separated in distance and energy in the framework of variable range hopping. The energy distance between these states is high when the energetic disorder is high. As such, energetic disorder makes it harder for charge carriers to hop to neighboring states. Simulations of variable range hopping models describe the energetic disorder as the width of the density of states. Jacobs *et al.* have suggested that a low energetic disorder, not electrostatic interactions, is the main parameter for improved conductivity in doped polymers[34]. Thereby, they studied the binding energies, microstructure and conductivity of conjugated polymers with varying counterions. In general, the electrostatic interactions are often controlled with counterion variation [35]. On the other hand, Kroon et al. investigate the conductivity of P($g_4$2T-T):F_4TCNQ and rationalize clearly for favorable binding energies in comparison to P3HT based on increased thermal stability [5]. The overlap of Coulomb traps with increasing doping levels has been investigated extensively. It is not clear if this finding comparing different ion sizes can be translated to electrostatic interactions of polymers with different dielectric constants.

The dielectric constant

Typically, polymers have a low dielectric constant ($\varepsilon_r = 2$–5) over a wide range of frequencies from the THz to optical range [1, 3, 36]. At low dielectric constants electrostatic interactions between generated charge carriers (hole–hole repulsion) and between charge carriers and dopant counterions need to be considered. This results in inherently large binding energies of several hundred millielectronvolts for generated charges in doped conjugated materials [1]. It has been shown that only a small fraction of charges actively participates in transport due to electrostatic interactions[37, 38]. Only at very high doping levels, the dopant counterions are sufficiently close to each other so that their electrostatic potential wells overlap and allow bound charges to become mobile [39]. The dielectric constant of conjugated polymers has a positive effect on their conductivity. A higher dielectric constant in these materials can enhance charge carrier mobility by reducing Coulombic interactions between charges and dopant ions, thereby facilitating improved conductivity. This effect is particularly significant in doped conjugated polymers, where increased dielectric screening mitigates the binding energy of charge carriers, promoting their movement through the polymer matrix[40, 41]. This interplay between dielectric properties and charge transport mechanisms underscores the importance of dielectric constant in determining the electrical performance of conjugated polymers[36]. Furthermore, structural modifications, such as the incorporation of glycolated side chains, can increase the dielectric constant of conjugated polymers. Tailoring the dielectric properties through chemical design could be a strategy to optimize the conductivity of conjugated polymers[42, 43]. Doping also affects the dielectric constant of a polymer:dopant combination, but the effect diverges at doping levels above 8%. Comin *et al.* recently proposed a treatment based on local polarizabilities for doped organic semiconductors (such as pentacene:F_4TCNQ), which describes an increase of the bulk dielectric constant with increasing doping loads until the mentioned doping level of 8%. It is worth noting that I am controlling for similar doping levels and therefore consider the dielectric constant of the pristine polymer with alkyl ($\varepsilon_r = 2.5$) or oligoether glycol ($\varepsilon_r = 5$) side-chains[36, 43, 44].

The spatial confinement

Spatial confinement in conjugated polymers can arise from a variety of structural and external factors. Strong π−π interactions lead to regions where charge carriers are effectively confined along the stack, which can limit lateral transport in directions perpendicular to the stacking[23, 24, 34]. More key factors that can lead to spatial confinement are chain entanglement or aggregation of polymer chains. Aggregation of dopant clusters can also introduce spatial confinement. Particularly, high concentrations of dopants can cluster, creating regions of high charge density that limit the mobility of carriers within these zones. Also, the presence and structure of side-chains influence how closely polymer backbones can pack together. Bulky or rigid side chains create steric hindrance, preventing tight packing and leading to isolated or confined regions within the polymer[4, 24, 45]. Regions with different degree of disorder and energetics might also display mismatched electronic properties, leading to confined charge states[24, 46-48]. By understanding these sources of confinement and their effect on conductivity, researchers can manage processing and doping conditions to reduce charge confinement, ultimately leading to enhanced conductivity.

Aim of this study

Due to the strong relationship between the microstructure and the conductivity of doped polythiophenes, I investigate the conductivity over short- and long-range distances separately. The quotient between long-range conductivity and short-range conductivity in doped polythiophenes represents the microstructural effects to conductivity, which I call **restoration**. The steady-state absorbance gives an estimate of the density of ionized dopant and moreover gives an idea about the nature of the induced charge carriers (singly charged [+] and doubly charged [++] percentages). The absorbance provides information about all present bands and their relative ratios. THz-TDS probes selectively the conductive portions of a film, hence the method is blind to immobile charge carriers. Moreover, the short-range conductivity spectra yield information about the number of **mobile charge carriers** and their mobility separate from long-range (macroscopic) structural effects. The combination of experimental and simulated short-range conductivity spectra gives a numerical understanding of the input parameters and their effect on the resulting complex conductivity. I utilize electrical four-point probe, steady-state absorbance, THz-TDS and kMC simulations to investigate the effect of (i) dielectric constant, (ii) energetic disorder and (iii) spatial confinement on the short-range conductivity spectra. Is the enhanced short- and long-range conductivity of doped polythiophenes with glycolated side-chains explained based on the parameters of dielectric constant, energetic disorder and spatial confinement?

To reach this aim, I present a study on doped polymer films of (i) the recently reported oligoethylene functionalized polythiophene P($g_4$2T-T) [14, 15] and (ii) the well-studied model system P3HT [12], both doped with F_4TCNQ. The short-range conductivity spectra obtained by THz-TDS are complemented by kMC simulations using a near-neighbor hopping model. The kMC simulations are described in detail previously[46, 49] and the relevant parameters are explained in the supplementary section S.0. Methods. This provides detailed and numerical understanding about the impact of energetic disorder, dielectric constant, and spatial confinement on the complex conductivity.

6.1.2 Results and Discussion

Film preparation and structural characterization

Our model systems P($g_4$2T-T):F_4TCNQ and P3HT:F_4TCNQ can have vastly different microstructure based on batch variation, the film preparation and doping method. Figure 1 (a) shows the molecular structure of the polythiophenes P3HT and P($g_4$2T-T) with its polar side chains and three covalently linked thiophene units, as well the dopant F_4TCNQ. Moreover, it shows a vertical energy axis with the ionization energies of the polythiophenes being −4.5 eV for P($g_4$2T-T) and −5.2 eV for P3HT, and the electron affinity of the dopant being −5.2 eV as reported. Using similar mole ratios of F_4TCNQ per thiophene unit I therefore expect P($g_4$2T-T) to be oxidized more readily. Two doping methods are depicted step by step in Figure 1 (b), co-processing on top and sequential doping below. The scheme includes the preparation of nanometer thin films and micrometer thick films from the same solution. The quality of THz spectroscopy signal scales with the thickness, which is the reason for preparing thick films, while thin films are used to determine the nature of charge carriers by steady-state absorbance. The long-range conductivity is measured on thick and thin films and is comparable. For co-processing, a solution of polymer:dopant is mixed and spin-coated to obtain nanometer thin films or dropcast to obtain micrometer thick films. In sequential processing, a polymer solution is spin-coated to obtain neat nanometer thin films, which sequentially are doped by spin-coating a dopant solution on top. By alternating neat polymer solution and doping, one can increase the thickness to micrometer films based on dopant induced solubility control (DISC)[50].

Since the microstructure is closely related to doping conditions and batch specification, I include GIWAXS experiments. Here, P($g_4$2T-T) is co-processed with 15 mol% F_4TCNQ per thiophene unit in a 1:1 mixture of chloroform and acetonitrile. The abovementioned aggregation difficulties are successfully reduced when P3HT is co-processed with 13 mol% F_4TCNQ in chlorobenzene at an elevated temperature of 80°C. From the co-processed solutions, I make spin-coated thin films (~56 nm) and drop-casted thick films (~12 μm). Moreover, more ordered P3HT films are prepared from 10 g/l solution in xylene and sequentially doped by spin-coating an orthogonal doping solution of F_4TCNQ (1 g/l in dichloromethane) on top. The batch specifications and spin coating conditions can be found in the methods and materials subchapter.

Our model systems P($g_4$2T-T):F_4TCNQ and P3HT:F_4TCNQ all indicate a semi-crystalline microstructure with a slight shift in position and intensity of the 020 $\pi-\pi$ stacking peak, as seen in the GIWAXS 2D linecuts in Figure 1 (c).

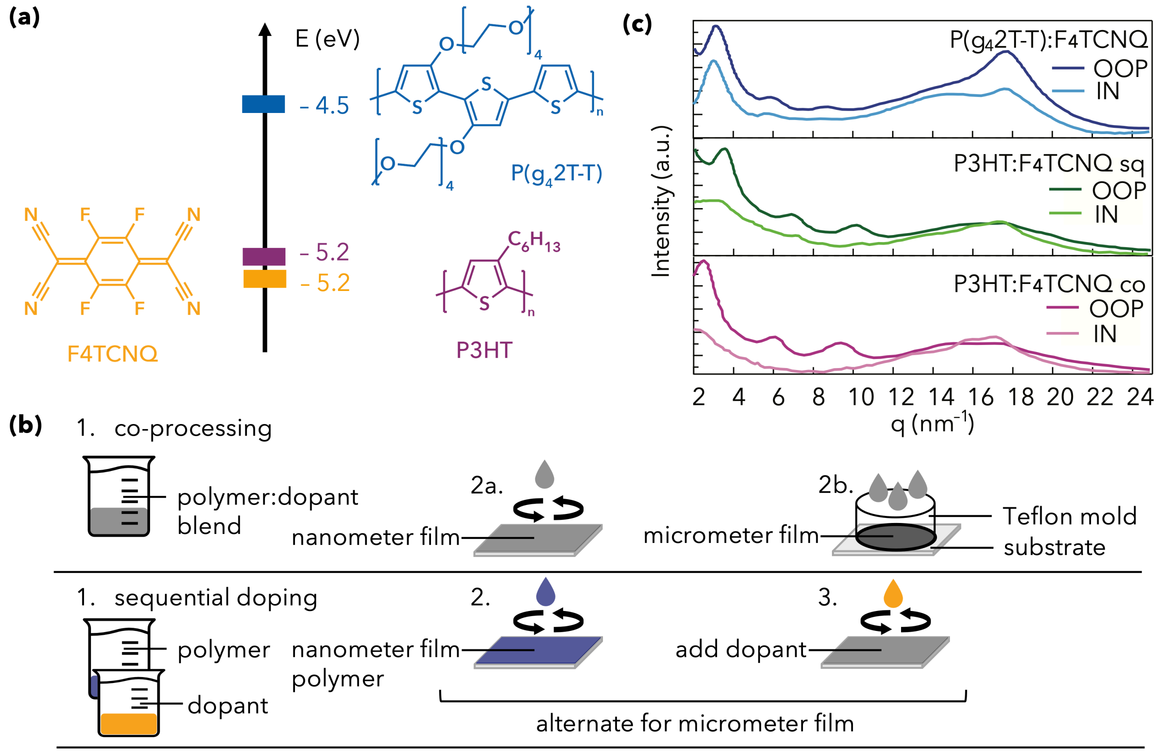

Figure 1: (a) Chemical structures of dopant and polythiophenes including energy levels for doping. (b) step-by-step schematic for the preparation of doped polythiophene films with co-processing or sequential doping. Nanometer films are prepared for UV-Vis, GIWAXS and temperature dependent long-range conductivity. Micrometer thick films are prepared for short-and long-range conductivity. (c) Linecuts of GIWAXS indicating the semi-crystalline microstructure of the doped polythiophene films.

Doped P(g$_4$2T-T) depicts a strong π–π stacking peak at 17.7 nm^{-1} in the out-of-plane direction (OOP), much larger than the amorphous halo at 15 nm^{-1}. From the peak position and broadness, the cumulative disorder g and the coherence length of crystallites CCL is extracted; the detailed calculation is shown in the supplementary together with table S1.1. of the resulting values. The coherence length of the π–π stacking peak is 1.7 nm; in comparison to P3HT that has a smaller coherence length of 1.0 nm (sq) or 0.9 nm (co). In addition, doped P(g$_4$2T-T) features a stronger π–π stacking peak, implying that the polymer is more ordered compared to doped P3HT. In agreement with this trend, doped P(g$_4$2T-T) has the lower cumulative disorder with 19% in comparison to doped

P3HT 24% (sq) or 25% (co). Moreover, the coherence length in the in-plane direction is calculated as well, which are summarized in Table 1 together with the mentioned out-of-plane values. The investigated polythiophenes preferentially orient edge-on the substrate and in-plane the characteristics between them are more similar (IP *CCL*=1.8±0.2 nm).

Table 1: Peak position q, peak full width at half maximum Δq, paracrystallinity g and coherence length CCL from the GIWAXS OOP and IP line cuts.

Sample	q **(nm^{-1})**	Δq **(nm^{-1})**	g **(%)**	CCL **(010) (nm)**
OOP				
P($g_4$2T-T)	17.7	3.8	19	1.7
P3HT sq	17.5	6.1	24	1.0
P3HT co	17.2	7.0	25	0.9
IP				
P($g_4$2T-T)	17.6	3.9	19	1.6
P3HT sq	17.4	3.2	17	2.0
P3HT co	17.2	3.8	19	1.7

From short- to long-range conductivity

I study the conductivity of doped polythiophene films over short- and long-range distances by using THz spectroscopy and four-point probe respectively. Figure 2 (a) shows a visualization of the two techniques and the measured distances. The distance for the long-range is defined by the electrode spacing of 1.2 nm in the aligned four-point probe. The distance for the short-range is defined by the duration of a THz pulse of around 1 picosecond, during this short duration the charge carriers move on the order of 10 nanometers. The short-range conductivity can be interpreted as the intrinsic limit of conductivity in the doped polythiophene film, while the long-range can be interpreted as a restoration over distances that are relevant for macroscopic device geometries. Hence, the long-range conductivity will always be smaller or equal to the short-range one. The quotient between Long σ/ Short σ I define as **restoration over longer distances**. I measure the conductivity over the short-and long-range and the results can be seen in the histogram in Figure 2 (b), where the colored bars represent the short-range conductivity of the doped polythiophene films, and the grey bars represent the long-range. To give more detailed insight into the transport physics, I also measure the long-range conductivity as a function of temperature. Then, the activation energy for thermally activated transport can be extracted from an Arrhenius type plot as shown in Figure 2 (c). The room temperature conductivity Long σ and the activation energy E_a are shown as an inset.

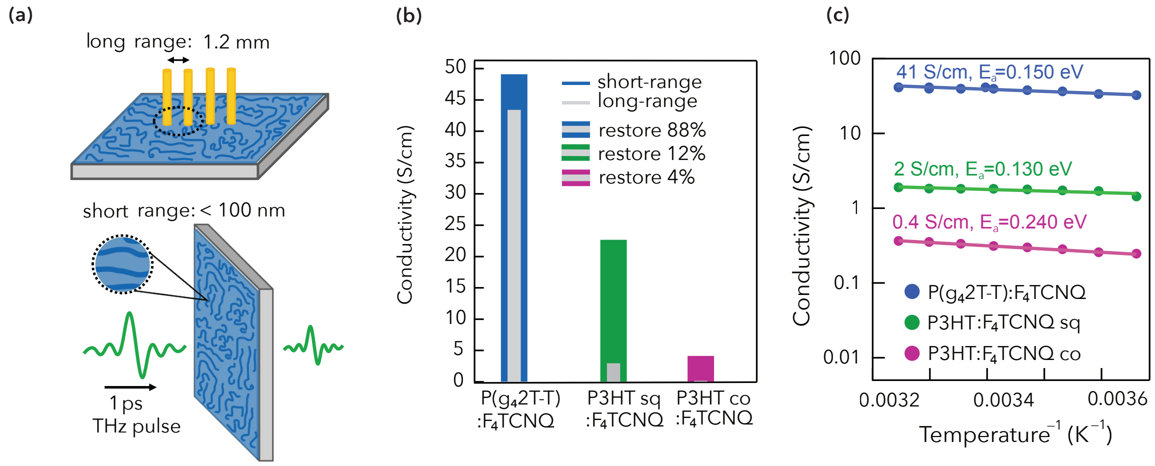

Figure 2: (a) Visualization of short- and long-range conductivity experiment. (b) Histogram of short-range conductivity in color and long-range conductivity in grey of the doped polythiophene films (μm). The ratio between the two, which I interpret as the restoration of the intrinsic conductivity, is shown as an inset. (c) Temperature dependent conductivity of the doped polythiophene films (60 nm).

This innovative comparison of Long σ and Short σ uncovers major impairments in conductivity over longer distances in the P3HT:F$_4$TCNQ system which are improved with sequential processing and almost entirely overcome in the P(g$_4$2T-T):F$_4$TCNQ system. The glycolated polythiophene doped P(g$_4$2T-T) restores 88% over the longer distances. On the contrary, the doped P3HT has only few percent of the conductivity restored over longer distances, with a small improvement with the sequential doping method from 4% (co-processed) to 12% (sequential). The temperature dependence of the conductivity as shown in Figure 2 (c) shows that the doped films have a similar activation energy to charge transport between 130 meV and 240 meV. The thermal activation is a good indication to later employ kMC simulations of a variable range hopping model. The charge transport and activation energy are doping level dependent, but the investigated films are in a similar regime. There is not a different doping regime that could explain the high restoration of P($g_4$2T-T):F_4TCNQ over longer distances. Note that the measurement of Long σ and Short σ are done on the same thick films. For absorbance measurements in the next section, also thin films were produced from the same solution and the Long σ of thin films (20–56 nm) and the Long σ of thick films (2–25 µm) is the same. Please see Table 2 for a comprehensive overview of the conductivity over different distances on thick films and the Long σ conductivity on thin films.

Table 2: Thickness and conductivities for the prepared doped polythiophene films.

Sample	**Thick (µm)**	**Short σ (S/cm)**	**Long σ (S/cm)**	**Thin (nm)**	**Long σ (S/cm)**
P($g_4$2T-T):F_4TCNQ	12	49	43	56	41
P3HT:F_4TCNQ sq	2	23	3	33	2
P3HT:F_4TCNQ co	25	4	0.2	20	0.4

Nature of charge carriers

This section describes the number and nature of doping-induced charge carriers in the model systems P($g_4$2T-T) and P3HT based on steady-state absorbance, seen in Figure 3. The polythiophene P($g_4$2T-T) gets doped more readily given the higher doping driving force, based on the energy levels seen in Figure 1 (a). At a first glance at Figure 3, all three prepared systems show the typical features of charged species in polythiophenes. The neutral band absorbing between 400–650 nm is reduced. The ionized F_4TCNQ^- peaks are clearly present at 760 nm and 860 nm[8]. The charged species absorb around 800 nm and in the IR. Indeed, the bandgap of P($g_4$2T-T):F_4TCNQ seems fully depleted at the used 15 mol%. To clarify if the enhanced conductivity in P($g_4$2T-T):F_4TCNQ is a result of (i) a higher number of doping-induced charge carriers or (ii) of the nature of charge carriers (singly charged [+] and doubly charged [++]), I use combined spectroscopic techniques. To estimate the contributions of neat and charged species I utilize spectroelectrochemistry, as previously published[17, 51] and described in the SI. The procedure gives us the decomposed spectra for each of the species: **neutral ordered, neutral disordered, singly charged [+] and doubly charged [++]**, as well as their relative cross-sections. The SI contains a comparative analysis on why both neutral ordered and disordered need to be considered. The decomposed species and the spectrum of ionized F_4TCNQ^- are used to fit the absorbance of the chemically doped films, as shown in Figure 3. The black curve is the absorbance and the grey dashed is the fit. Then, the percentages (relative contributions) are estimated by comparing the absorbance of a specific species to the absorbance of all species corrected with the relative cross section intensity, using Beer–Lambert law. Please refer to the supplementary section S.5. for the mathematical details and cross-sections in tabular form. First, looking at the F_4TCNQ^- anion peaks in the visible, one can conclude that all doped polythiophenes show a similar concentration of charges per cubic centimeter ($2.0\times10^{20} \pm 0.5\times10^{20}$ cm^{-3}). This means that the count

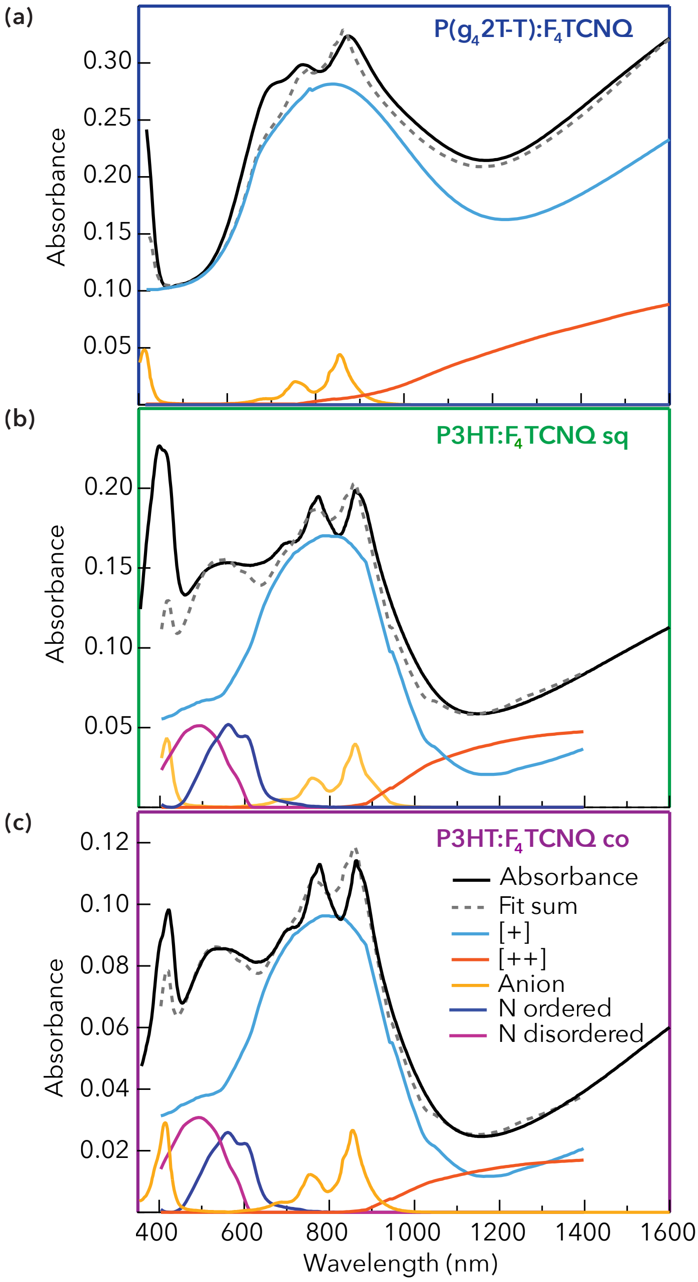

Figure 3: UV/VIS/NIR absorbance with least square fits by a linear combination of species relative cross sections determined by spectroelectrochemistry.

of charge carriers cannot explain the 10–100 fold increase (short–long range) in conductivity for P($g_4$2T-T):F_4TCNQ in comparison to P3HT:F_4TCNQ. This analysis of the steady-state absorbance of anions gives us no information about how mobile these charge carriers are. Therefore, I dive deeper into the nature of the charge carriers. For polythiophenes it has been previously reported that with increasing doping levels at one point the conductivity starts to decrease again; this is rationalized with sub-band filling in the density of states[52]. The **rise of doubly charged species [++] at high doping levels is an indicator** thereoff[17], which clarifies the motivation to compare the species in greater detail. The remaining band in the absorbance of P3HT:F_4TCNQ films shows that these films have at least 20% of neutral sites left. Interestingly, of those 20% of neutral sites it seems that both ordered and disordered contribute, even though the energetics indicate that neutral ordered sites would be doped first. The SI shows that just one neutral species (disordered alone) does not describe the absorbance well. On the other hand, in P($g_4$2T-T):F_4TCNQ the neutral species are fully depleted. The percentages of singly charged [+] and doubly charged [++] species can also be estimated in a similar fashion. Also the comparison of relative cross-sections is found in supplementary section S.5. The spectrum of P($g_4$2T-T):F_4TCNQ has a relatively high absorbance above 1000 nm with a significant portion of [++] carriers. In this doping regime it is known that doubly charged [++] carriers help the conductivity[17]. Besides the contribution of [++] carriers in P($g_4$2T-T):F_4TCNQ, also a significant red-shift and peak broadening

Table 3: Neutral and oxidized species in the doped polythiophene films. The species contribution to the overall absorbance is given in % of the sum of all species. Since on the UV-Vis films we also measured the long-range conductivity, these values are included as well.

Sample	P($g_4$2T-T): F_4TCNQ	P3HT: F_4TCNQ co	P3HT: F_4TCNQ sq
Thin (nm)	56	20	33
Long σ (S/cm)	41	0.2	3
N dis (%)	0	9	8
N ordered (%)	0	11	12
[+] carriers (%)	77	69	64
[++] carriers (%)	23	11	16
F_4TCNQ^- (cm^{-3})	2.4×10^{20}	1.7×10^{20}	1.6×10^{20}
Ratio [++] to [+]	30:100	16:100	25:100

of the [+] carrier band plays a role. Between, P($g_4$2T-T) and P3HT both co-processed with F_4TCNQ, a similar density of total charges from the F_4TCNQ^- anion peak, but the [++] to [+] ratio is higher for P($g_4$2T-T) (30% versus 16%). In P3HT:F_4TCNQ sequential the [++] to [+] ratio is 25%, which is in between the one of P($g_4$2T-T) and P3HT co-processed. Based on the conductivity and absorbance results and previous findings, I suspect that in this doping regime a higher [++] to [+] ratio is a first indicator for improved mobility and conductivity. To conclude this section, the number of total charge carriers ($2.0\times10^{20} \pm 0.5\times10^{20}$ cm^{-3}) and the nature of charge carriers is not the reason for the enhanced conductivity in the polymer with oligoether glycol side-chains.

Short-range complex conductivity spectra in experiment and simulation

While the number and nature of doping-induced charge carriers are similar in the model systems, that does not imply that the number of mobile charge carriers and their mobility are similar as well. To adequately quantify the number of mobile charges and their mobility, THz-TDS and DSM fitting is conducted in the next section. THz spectroscopy is sensitive to conductive parts of the films only. Hence, in contrary to steady-state absorbance, THz probes exclusively mobile charge carriers. The investigation of short-range conductivity spectra provides valuable information on this matter, which helps clarify the enhancement in conductivity of conjugated polythiophenes with glycolated side-chains independent from long-range microstructure.

To obtain detailed physical insight about the differences on the short-range, Figure 4 shows experimental and simulated short-range conductivity spectra. On the left are experimental complex conductivity spectra for the model system presented in (a) absolute values in S/cm and (c) normalized in the center of our experimental THz range at 1 THz. For example the blue curves, representing the real and imaginary part for P($g_4$2T-T):F_4TCNQ, both are normalized by the real value 49 S/cm. The legend clarifies that the real part is above zero (solid curves), while the imaginary part for localized systems is below zero (dashed). The curve in a lighter shade is a fit of linked real and imaginary part using the Drude-Smith model. On the right are simulated complex conductivity spectra with input parameters of energetic disorder of 0.05–0.1 eV and dielectric constant of 2.5–5. KMC simulations were published previously[46, 53] and performed for the doping concentration of 10^{-1} on a rectangular grid of 10x10x10 with a lattice parameter of 1.8 nm. Similarily, (b) shows absolute values in S/cm and (d) shows normalized values to the center of our experimental THz range at 1 THz. The comparison of experiment and simulation in panel (a) and (b) shows **good overall agreement**.

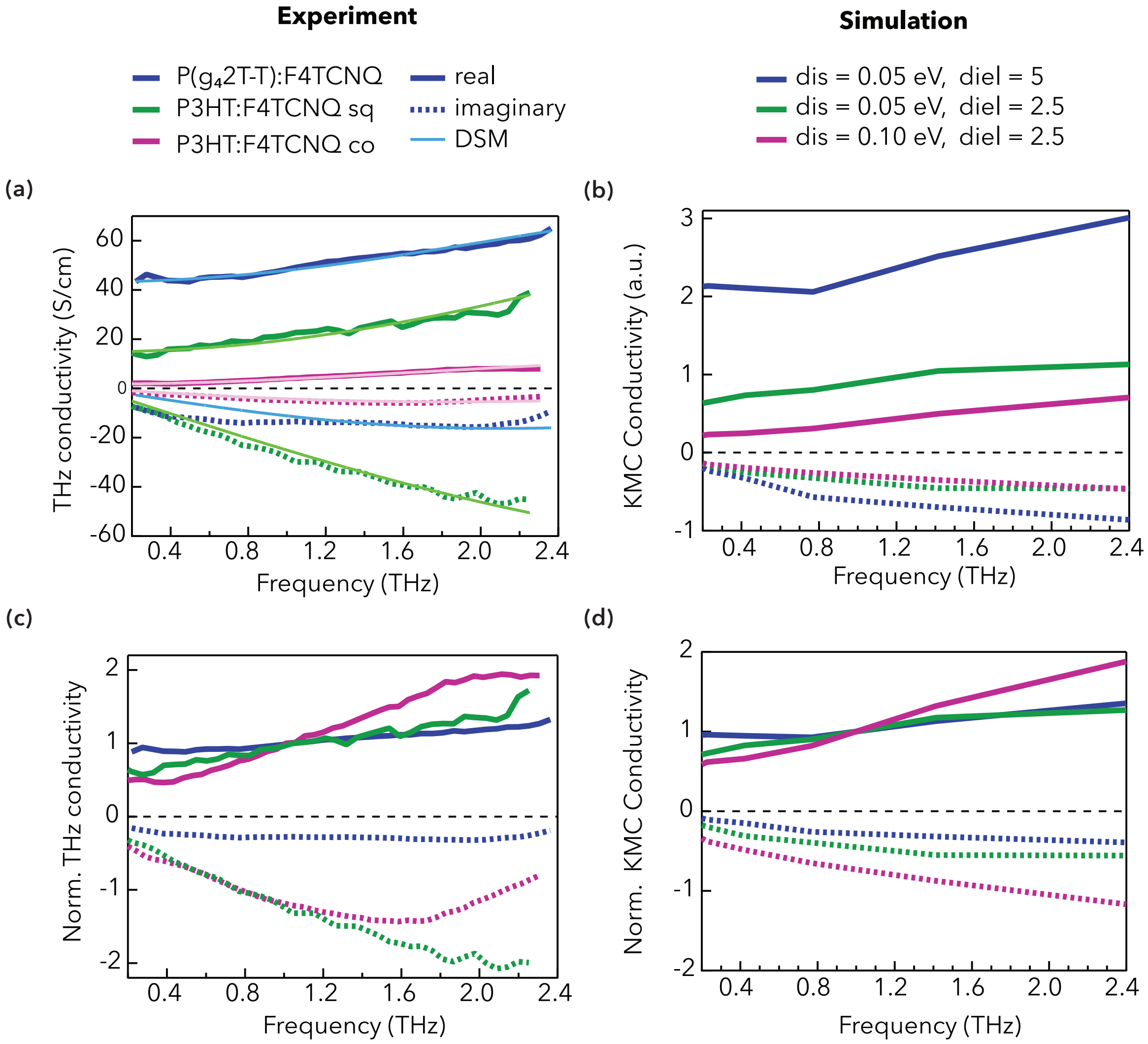

Figure 4: Short-range complex conductivity spectra from experiment and simulation. Complex conductivity of doped polythiophene films (a) in S/cm (c) normalized to real part being 1 at 1 THz. (b) Complex conductivity simulations with input variables energetic disorder and dielectric constant (b) in S/cm (d) normalized to real part being 1 at 1 THz.

The presented simulations have the same trend in the real part of the complex conductivity in terms of absolute value and frequency-dependent slope. When looking at panel (c) and (d) that plots the normalized frequency dependence, it is evident that also the frequency dependence of P(g$_4$2T-T):F$_4$TCNQ is caught nicely in the simulation. However, the experiment shows a steeper frequency dependence in P3HT:F$_4$TCNQ. That indicates that there is a **phenomenon that suppresses the imaginary part** of P3HT: F$_4$TCNQ, which is not caught by the simulations varying energetic disorder and dielectric.

This phenomenon suppressing the imaginary part might be key for the enhanced conductivity and restoration. The DSM includes the parameters: the density of mobile charge carriers denoted by N, the scattering time τ, the effective mass m^*, the angular frequency ω of a time-dependent electric field in our case a THz pulse, and lastly c_1 is the revised localization parameter. Please see the fits in Figure 4 (a) to see the agreement between the experimental observation and the fit. The fitting parameters are shown in table 4. First, the density of mobile charges N is not the origin of the enhanced conductivity of the glycolated material. To be clear about the number of total charge carriers, the nature of total charge carriers and the number of mobile charge carriers is not responsible for the enhanced conductivity in P(g$_4$2T-T):F$_4$TCNQ in this work. The fit suggests that the number of mobile carriers between P(g$_4$2T-T):F$_4$TCNQ and P3HT:F$_4$TCNQ sequentially doped are in an intermediate field (20% and 40%). The enhanced conductivity with oligoether glycol side-chains is rather related to the mobility of charge carriers (7 cm^2/Vs). On the other hand, the low conductivity of P3HT:F$_4$TCNQ when employing the co-processed doping is likely due to the limited number of mobile charge carriers of only few percent. In other words, the sequential processing improved the density of charge carriers that are participating in transport but not their mobility (1–2 cm^2/Vs). **THz spectroscopy probes exclusively mobile charge carriers**. The fitting parameters give valuable differences in the density of mobile charges N, the percentage of mobile charges in comparison to the total density of ionized dopant and the mobility of charges μ_{eff}. With the DSM fitting parameters and equations from the methods in Chapter 4, I calculate the effective mobility of charge carriers μ_{eff} including scattering and a static localization parameter. The following table shows the resulting values for the short-range conductivity. The localization parameter c_1 and the scattering time τ in the DSM are phenomenological. The parameters contain various localization events that are not discussed in this chapter. Generally, a longer time between "scattering" events τ, or a localization parameter $-1 \leq c_1 \leq 0$ close to 0, contribute to the mobility. These two parameters hence should always be considered together. Interesting is also the mobility μ_{Drude} that describes the necessary mobility under the assumption of the Drude model without additional localization events in polymers.

Table 4: Fit parameters, calculated percent of mobile carriers and their mobility. Density of charges contributing to the conductivity N, the localization parameter c_1, the scattering time τ, THz- and effective- mobility values μ_{Drude} and μ_{eff}.

	N (10^{19} cm^{-3})	c_1	τ (fs)	Percent of F_4TCNQ^-	μ_{eff} (cm^2/Vs)	μ_{Drude} (cm^2/Vs)
P($g_4$2T-T): F_4TCNQ	4	−0.74	25	20 ± 10 %	7	26
P3HT: F_4TCNQ co	0.4	−0.93	35	3 ± 2 %	2	36
P3HT: F_4TCNQ sq	10	−0.95	15	40 ± 10 %	1	16

The lower localization (−0.74), intermediate scattering time (25 femtoseconds) and the high effective mobility (7 cm^2/Vs) of P($g_4$2T-T):F_4TCNQ together indicate that the charge carriers this materials **experience a smaller confinement**. The obtained mobilities of P3HT and P($g_4$2T-T) are high in comparison to literature values[54]. Especially, the 2 cm^2/Vs mobility in co-processed P3HT:F_4TCNQ co are repeated to ensure reproducability. The supplementary Figure S.8.1. shows that an increased doping level from 15mol% to 23mol% in co-processed P3HT leads to a lower mobility of 0.3 cm^2/Vs. This lower mobility is in line with literature indicating aggregation with F_4TCNQ in the ordered domains of P3HT. While I was not able to secure the resources to validate the mobilities with complementary techniques like Hall effect measurements, the THz mobilities presented here are reproducible. The comparison of doped polymer mobilities from the THz technique including the Drude–Smith model versus Hall effect mobilities and transistor conductivities is a separate research project in the group. The comparison between the materials is telling of a substantial difference in the mobility of charge carriers. This is in line with literature while the mechanism behind the difference in mobility is not conclusive[5].

To verify this main finding from the previous section, spatial confinement is incorporated in the kinetic Monte Carlos simulations. In the simulation spatial confinement is incorporated by **removing the periodic boundary conditions**, such that a charge is confined to 10 sites in the z-direction. The kMC simulations with additional spatial confinement show a suppressed imaginary part and an increased slope, as seen in Figure (a)–(b). Panel (a) shows the complex conductivity spectra with real part (solid) and imaginary part (dashed) on the same frequency axis as the experimental THz frequency range. Panel (b) shows a smaller frequency range and a linear fit to extract the slopes around 1 THz. **A steeper slope**, i.e., a bigger frequency-dependence of the conductivity, **translates to a smaller Long σ conductivity**. In other words, a steep slope describes a small low-frequency conductivity and that describes a small Long σ conductivity. The figure contains all permutations of input parameters: dielectric constant 0.05 eV or 0.1 eV, dielectric constant of 2.5 or 5. Moreover, the figure contains the simulations with spatial confinement in yellow and rose. Panel (b) shows that with spatial confinement the slope increases to close to 1. By removing the periodic boundary conditions, the charges are restricted to 10 sites in the z-direction. It shows the ability to move over ten sites in a variable range hopping model with static localization. The next section presents key figures of merit in a histogram to finally compare all relevant parameters at once.

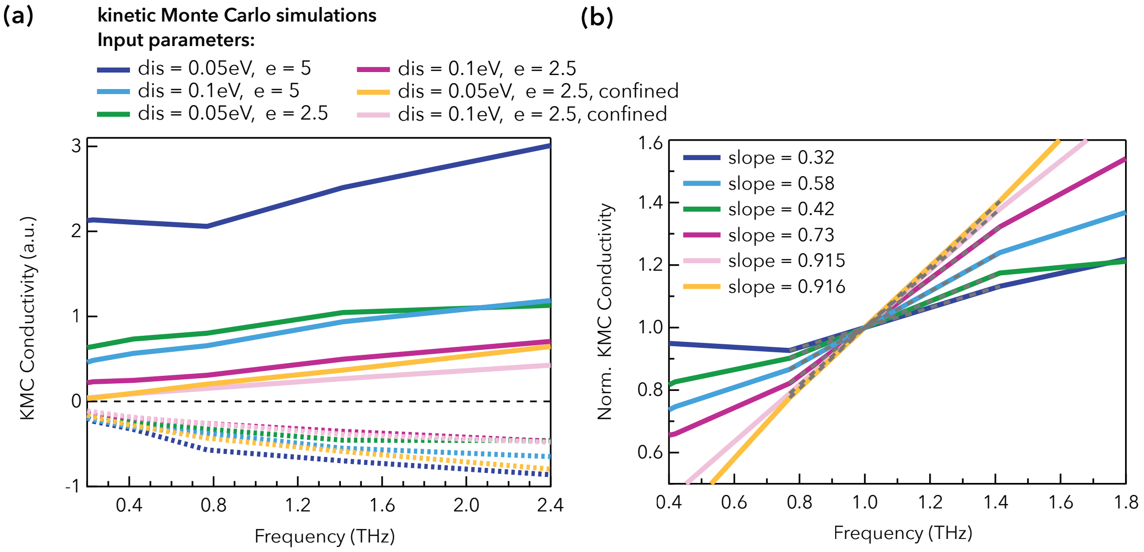

Figure 5: kinetic Monte Carlo simulations on different axis scaling (a) similar frequency range of THz experiment, (b) full simulated range, (c) normalized real parts between 0.4 and 1.8 THz including linear fits to determine the slope. (d) Input parameters with color code.

Origin of enhancement in conductivity

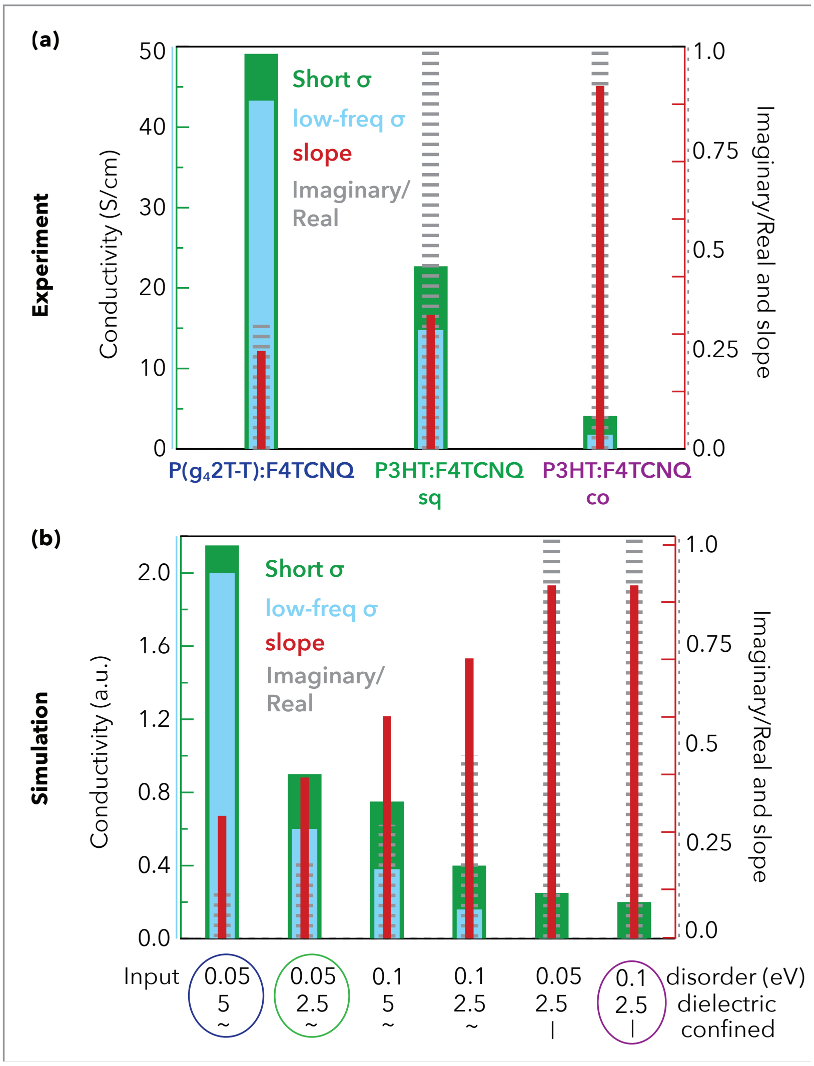

Figure 6: Selected output parameters in different colored histograms from (a) the THz experiment and (b) kinetic Monte Carlo simulations. The real part at 1 THz (green), the real part at 0 THz (turquoise), the ratio between imaginary and real part (grey) and the slope of the real part between 0.8 and 1.4 THz (red).

Since the many complex conductivity spectra in Figure 5 are complex to dissect, this section shows how relevant figures of merit of the complex conductivity differ in experiment and simulation. This verifies the contributions of energetic disorder, dielectric constant and spatial confinement to the enhanced conductivity in the polymer with oligoether glycol side-chains. Using the complex conductivity spectrum of the experimental data from the P(g$_4$2T-T):F$_4$TCNQ doped film in supplementary section S.7., it is explained in visual detail how the experimental figures of merit **Short σ, low-frequencyσ, Im/ Real part, and slope** are extracted. Here the figures of merit are described in words. The value Short σ is given by the real part of the complex conductivity spectrum at 1 THz (green). The low-frequency conductivity σ is given by extrapolating the real part of the complex conductivity spectrum to 0 THz (turquoise). The quotient of

Imaginary/Real is calculated by dividing the absolute values of imaginary and real complex conductivity at 1 THz (grey) and the slope is given by the increase of a linear fit of the real part between 0.8 and 1.4 THz (red). Figure 6 (a) shows the figures of merit **Short σ, low-frequency σ, Imaginary/ Real and slope** as histogram bars with different colors. Here, the bars on the top are extracted from the experimental data seen in Figure 5 (a). On the left for P($g_4$2T-T):F_4TCNQ, in the middle for P3HT:F_4TCNQ sq and on the right for P3HT:F_4TCNQ co. The bars in the bottom panel represent the simulations. **Comparing the top and the bottom panel**, the figures of merit on the most left in (a) and (b) are describing very similar conductivity spectra. The simulation using an energetic disorder of 0.05 eV and dielectric constant of 5 show the same general trend in comparison to the experimental conductivity spectra of P($g_4$2T-T):F_4TCNQ. The complex conductivity of P3HT:F_4TCNQ sq is described well by kMC with energetic disorder of 0.05 eV and dielectric constant of 2.5 but needs additional spatial confinement. The simulated spatial confinement to 10 sites, represented by the second bar counting from the right-hand side, is stronger than seen for the P3HT:F_4TCNQ sq. Therefore, I suggest spatial confinement of 15-20 sites in one orientation would describe the observations better. The complex conductivity of P3HT:F_4TCNQ co is described by kMC with dielectric constant of 2.5 and spatial confinement. It is interesting to see the strong influence on the simulated conductivity, when a spatial confinement of 10 sites in z direction is introduced. The model input for spatial confinement thereby assumes full backscattering when one of the borders in z-direction is met by a charge carrier. For experimental conditions in polythiophenes, the conjugation length is estimated to extend over few sites. The modelled confinement of 10 sites in z-direction therefore is not trivially strongly confined. In the structural characterization of P3HT:F_4TCNQ there is no trivial indication for aggregated clusters of F_4TCNQ. The improvement of spatial confinement and the excellent short- to long-range restoration upon introduction of glycolated side-chains indicate that the enhanced conductivity stems from smaller structural and energetic disorder. This does not imply long-range order, but rather better flexibility (resilience) for energetic variations occurring in the film or **smaller energetic variations across the film**.

6.1.3 Conclusions

The introduction of oligo-ethylene glycol side chains simultaneously impacts the dielectric constant, the energetic disorder, packing and microstructure. I utilize THz time-domain spectroscopy, electrical four-point probe, steady-state absorbance and kinetic Monte Carlo simulations to numerically disentangle these impacts on the improved conductivity. The **conductivity is very well restored from short-range to long-range distances in the system P($g_4$2T-T):F_4TCNQ** (88 %, 49 S/cm). The conductivity increases 10-fold on short-range distances and 100-fold on millimeter distances when comparing alkyl and oligoether glycol side chains, which shows that the used comparative method is highly relevant. The complex conductivity spectra from THz TDS show an **intermediate density of mobile charges** (10–30% of total ionized dopant density), but **improved mobility** (7 cm^2/Vs, assuming a Drude-Smith model). With combined experimental and simulated complex conductivity spectra, this work could numerically identify different contributions. In the kMC model with a doping level of 0.1 holes per repeating unit, varying the energetic disorder from 0.1 eV to 0.05 eV doubles the real conductivity. Varying the dielectric constant from 2.5 to 5, also doubles the real conductivity. Interestingly, the **positive effect from low energetic disorder is even stronger** in high dielectric systems such as glycolated polymers. To fully explain the enhanced conductivity though, one needs to consider a **lower spatial confinement**. Therefore, the enhanced conductivity is assigned to the energetic disorder, the dielectric constant and lower spatial confinement, while the number of total charge carriers, the nature of charge carriers ([+] or [++]), and the number of mobile charge carriers is controlled for and constant. The findings align with literature suggesting that polar side-chains in conjugated polymers facilitate better charge injection and transport by stabilizing charge carriers. The research interest in molecular structure–conductivity relationships is immense and particularly numerical simulations and THz TDS is a powerful combination to study the effects **selectively in conductive portions** of doped polymer films.

Supplementary Information

Origin of the enhanced conductivity in doped polythiophenes with glycolated side-chains

S.0. Methods and Materials

Batch specifications

The synthesis route of P($g_4$2T-T) is described in detail previously[5]. The number-average molecular weight Mn = 24 kg/mol and polydispersity index PDI = 3.3 respectively. P3HT is purchased from Solaris Chem (CAS:104934-50-1) with a regioregularity of 88 %, number-average molecular weight Mn = 30-50 kg/mol and a polydispersity index of PDI = 2.4 and F_4TCNQ is purchased from Ossila (CAS:29261-33-4).

Film preparation including detailed steps and conditions

As mentioned in the main text, P($g_4$2T-T) is co-processed with 15 mol% F_4TCNQ per thiophene unit in a 1:1 mixture of chloroform and acetonitrile. The polymer and dopant are first dissolved separately for 2 hours at room temperature, then mixed for 1 hour before spin-coating thin films and dropcasting several micrometer thick films in a Teflon mold. P3HT is co-processed with 13 mol% F_4TCNQ in chlorobenzene in the analogue manner, while stirring and drying of the thick films happens at elevated temperature to avoid beforementioned aggregation (80°C). Thin films of the co-processed films are prepared from the same solution by spin-coating 80 µl at 1000 rpm for 60 seconds. From the co-processed solutions, spin-coated thin films (~56 nm) and drop-casted thick films (~12 µm) are prepared. Moreover, more ordered P3HT films are prepared from 10 g/l solution in xylene and sequentially doped by spin-coating an orthogonal doping solution of F_4TCNQ (1g/l in dichloromethane) on top. This sequential doping techniques allows to produce thin films as described (~30 nm) and thick films by alternating spin-coating of pristine P3HT and F_4TCNQ (~2 µm). The alternating sequential doping is based on the additive solution deposition developed in the Moulé group[50]. The Long-range conductivity was controlled and did not vary substantially up to 12 layers. I do acknowledge that the layering method would be interesting to study in THz-TDS and it is considered in the research group.

UV-NIR Absorbance and Spectroelectrochemistry

The steady-state electronic transitions for each thin film are gathered with an absorbance spectrometer including an integration sphere (Perkin Elmer Lambda 950). Electrochemical measurements were performed with freshly prepared solutions of [EMIM][BF_4] in dry and degassed acetonitrile (0.1 M) using a custom made three-electrode setup in a standard 1cm x 1cm quartz cuvette. Polymer films were spin-coated from pyridine (10 g/L) onto ITO coated glass (R ~ 150 Ohm/sq), which served as the working electrode. A Pt and Ag wire served as the counter and pseudo-reference electrode. The potentials were calibrated versus the Ferrocene/Ferrocenium (Fc/Fc+) redox couple. A series of UV-NIR absorption spectra were recorded at different constant oxidation potentials between -0.33 V and +0.37 V vs. Fc/Fc^+ and plotted the change in absorbance relative to the spectrum of the undoped polymer.

White Light Interferometry (WLI)

Thickness and Roughness of prepared samples were determined using an optical profiler with 5x magnification (Bruker CountourGT). The thickness is calculated as the average from at least 12 positions close to the center of the polymer film. The thicknesses from white light interferometry have been compared to and are consistent with measurements from a surface profiler (Bruker Dektak-150).

THz time domain spectroscopy (THz-TDS)

The THz time domain spectroscopy (THz-TDS) setup is based on the output of the same regeneratively-amplified Ti:sapphire laser system (Coherent Astrella) as used for the TA. The 800nm output with an average power of 6.5 W and ~35 fs pulse duration at 1 kHz repetition rate is reduced to 35 µW to generate the probe beam. The THz probe pulses are generated via optical rectification in a 2mm [110] ZnTe crystal. The THz probe pulse is detected by electro-optic sampling in another 1 mm [110] ZnTe crystal. The system from the ZnTe generation crystal, sample holder, to the detector camera is encapsulated and in nitrogen atmosphere to exclude THz absorption by air humidity. The immediate response of the THz electric field to the charges in the photoexcited material yields the ground state conductivity. It is obtained from the Fourier transform of the THz probe response to the doped film and the Fourier transform of the transmitted THz pulses through the substrate. It is broadly employed for contact-free conductivity measurements in the field of biochemistry[55-57] and materials science[58-60].

Kinetic Monte Carlo simulations

Kinetic Monte Carlo (KMC) simulations describe the motion of charge carriers in a doped disordered system. KMC simulations similar to the ones presented in previous studies [46, 53] were performed for the doping concentration of 10^{-1}, which is comparable to the one used experimentally, on a rectangular grid of 10x10x10 with a lattice parameter of 1.8 nm. In each simulation the results were averaged over at least 10 random configurations. Typically, simulations run for long times to assure steady state conditions and that charge carriers reach room temperature. In these simulations the dielectric constant and the energetic disorder are varied, see S. Figure 0. Both charge carriers and dopant ions are randomly added on the lattice sites at a similar concentration and all Coulomb interactions of charge carriers with all surrounding dopants and other charge carriers are recalculated after every hopping event. The dopant sites are included as static charges on the lattice. Only nearest-neighbour hopping events are considered. The initial energy level of charge carriers is chosen from a Gaussian density of states and hopping rates are calculated using Miller Abrahams expression. The energy barrier for charges to occupy a dopant is taken as the energy difference between the HOMO of the host material in this case the P3HT polymer and the LUMO of the dopant in this case F_4TCNQ ($\Delta E = 0.24$ eV). The film microstructure is taken into consideration in the energetic disorder parameter that is included in the energy distribution of the sites, while the nanoscale ordering of the doped films is not explicitly accounted for. By increasing the material dielectric constant, the Coulomb interactions between the charges and charge-dopant interactions are expected to be screened.

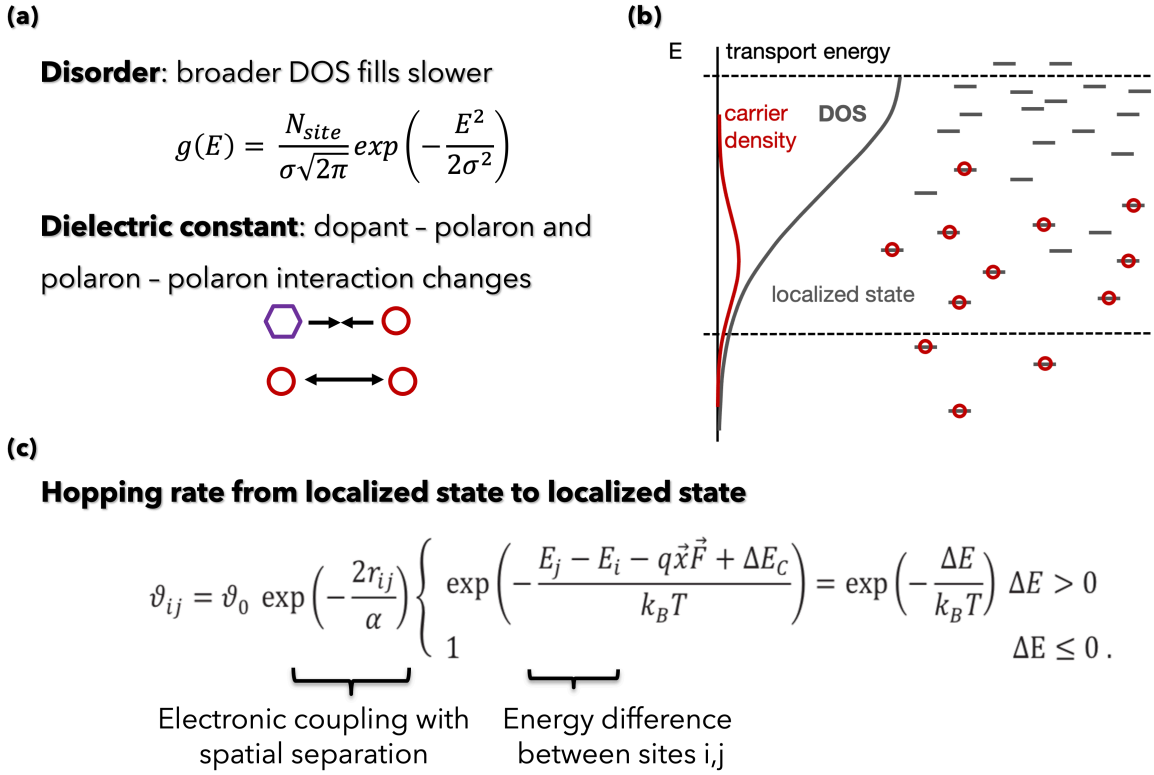

S. Figure 0. Visualization of the variable range hopping model with (a) the varied parameters (b) the distribution in the density of states and (c) the effect on the hopping rate simulated with kinetic Monte Carlo simulations.

Direct current (DC) conductivity

The long-range conductivity of doped polymer films is measured using a compact four-point probe system (Ossila Four Point Probe TypeG) at room temperature. The room temperature values are dimension and thickness corrected results repeated on three spots on the same thick films as used for THz time domain spectroscopy. Additionally, the conductivity is measured at 25 different temperatures between 40°C and -190°C. This method gives insight into the transport mechanism and is used to probe the thermal activation barrier to remove charges from the dopant counterion, which depends inter alia on the dielectric constant ε_r.

Grazing-Incidence Wide-Angle Scattering

The structural disorder of doped polymer thin films is observed by Grazing Incidence Wide-Angle X-ray Scattering (GIWAXS). The measurements were performed at the BL11 NCD-SWEET beamline at ALBA Synchrotron Radiation Facility (Spain). The scattering patterns were recorded using a Rayonix® LX255-HS area detector, which consists of a pixel array of 1920 × 5760 pixels (H × V) with a pixel size of 44 × 44 μm^2. The incident X-ray beam energy was set to 12.4 eV (0.9998 Å) using a channel cut Si (1 1 1) monochromator. The incident angles were set 0.05, 0.1, 0.12, 0.15 degrees.

Data are expressed as a function of the scattering vector (q), which was calibrated using Cr2O3 as standard sample, obtaining a sample to detector distance 201.7 mm and 200.5 mm. To perform the analysis of the diffraction patterns, the 2D patterns were integrated, corrected with respect to the reference and the 1D profiles were extracted using Fit2D software. The crystallinity of the ordered domains in the films is estimated by the width of the scattering peak. From the width one can calculate the coherence length by applying the Scherrer equation:

$$CCL = \frac{2\pi K}{\Delta q}$$

where K is the shape factor (~0.9-1)145 and Δq is full width half maximum of the peak.

Meanwhile the cumulative disorder can be calculated by the paracrystallinity parameter g, which describes the disorder in π−π-stacking.

$$g = \sqrt{\frac{\Delta q}{2\pi q_0}}$$

Where q_0 is the peak center position and Δq is full width half maximum of the peak.

S.1. Preparation differences and P3HT microstructure (GIWAXS)

The microstructure of polythiophene films is strongly dependent on batch-to-batch variations and doping conditions. The GIWAXS measurements for structural characterization of P3HT films in our case had to be repeated.

In the case (a) a semicrystalline structure for co-processed P3HT using 13% F_4TCNQ per thiophene unit is observed. These films were prepared under the exact same conditions as the films in the main text for all characterization techniques. The semi-crystalline microstructure and a small improvement from co-processing to sequential doping (refer to main text), corresponds to reports in literature as well.

In the case (b) mainly an amorphous halo at 15 1/nm is present. The GIWAXS results in both cases look very similar independent of the doping method, i.e. sequential or co-processing. Hence, below only co-processed P3HT is shown. This degree of disorder is unexpected at the given doping level and I suspect that the films were not processed at elevated temperature like in the main text. I decided that the GIWAXS run (a) is representable for the investigated films since they were processed by the main author who is also responsible for all optically and electrically characterized films.

Due to this repetition the data shown in the main text for P($g_4$2T-T) and P3HT is not from the same synchrotron run, but from GIWAXS experiments two months apart. The P($g_4$2T-T) film was not repeated in the second run because of the limited material amount.

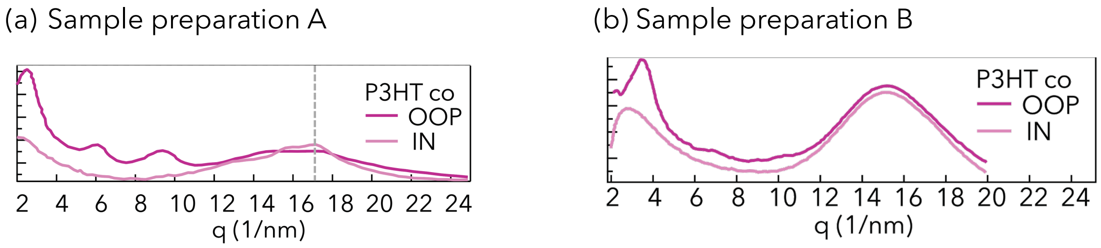
(a) Sample preparation A

(b) Sample preparation B

S. Figure 1: GIWAXS out of plane (OP) and in plane (IP) linecuts of P3HT:F_4TCNQ co-processed from different experiment series; (a) film prepared in in exact same conditions as films in main text for all optical and electrical techniques. (b) film prepared in Sweden by unknown but GIWAXS measured on the same synchrotron run as doped P($g_4$2T-T) film run.

S.2. Absorbance of doped P($g_4$2T-T) and P3HT films normalized

The absorbance od doped polythiophene films gives information about the doping level and the nature of the charge carriers. The absorbance of the investigated model systems normalized to the P2 band are shown. In accordance to the section in the main text, it is evident that the band gap of P($g_4$2T-T):F_4TCNQ is fully bleached. The F_4TCNQ anion peaks, absorbing at 760 nm and 860 nm as well as the NIR band indicate a similar doping level between the three films.

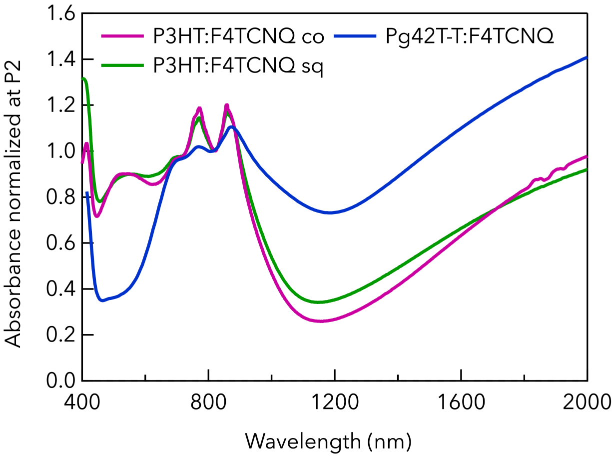

S. Figure 2: Absorbance spectra of the doped polythiophene films normalized at the P2 band.

S.3. Neutral disordered and ordered to fit the absorbance

The nature of charge carriers in the doped polythiophene films is studied. The absorbance cross sections for neutral and charged species in P3HT as reported in our group previously. Our model system P3HT:F_4TCNQ is widely studied in the field, and it is commonly accepted that F_4TCNQ dopes the more ordered regions first due to the beneficial energy offset. It is necessary to clarify, if for our doping levels one can use only the Neutral disordered cross section to fit the absorbance of the doped P3HT films. However, both Neutral disordered and ordered domains are still contributing to the overall absorbance of the doped film. This appears to be independent of the doping method, which is why the supplementary figure shows only co-processed.

i. Absorbance of neat P3HT corresponding to sequential and co-processed

The supplementary figure shows the absorbance of the neat P3HT films corresponding to (a) the sequential doping method which uses Xylene and (b) the co-processed doping method which uses Chlorobenzene. The dashed line represents the fit, i.e. the sum of neutral disordered and ordered. In the neat films the contribution from ordered and disordered neutral sites is balanced independent of the solvent. There possibly is a slight increase in the neutral ordered contribution for the xylene film, since this fit is minimally worse at the red-shifted shoulder centered at 600 nm.

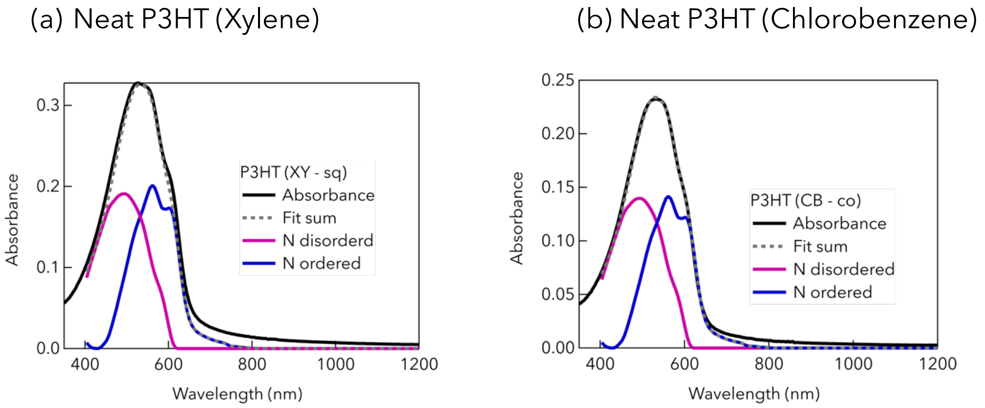
(a) Neat P3HT (Xylene)

(b) Neat P3HT (Chlorobenzene)

S. Figure 3: Absorbance spectra fitted with cross sections for neutral disordered and ordered.

ii. Absorbance fit of doped P3HT without neutral ordered

After clarifying the contributions of neutral disordered and ordered relative cross sections to the neat film absorbance, the same contributions in the doped film absorbance are investigated. As discussed in the main text, the P3HT films still have around 20% of neutral sites left with the investigated doping conditions. Since neutral ordered sites typically have a bit lower energy–red shifted, it is necessary to clarify if those neutral ordered sites are doped and depleted more than the neutral disordered sites. However, the fit for the doped P3HT absorbance is best when again a balanced contribution between neutral ordered and disordered is used. Supplementary figure 4 shows (a) the least squares fit with only neutral disordered sites in contrast to (b) the least squares fit with a balanced contribution of neutral ordered and neutral disordered similar to the neat film fits above.

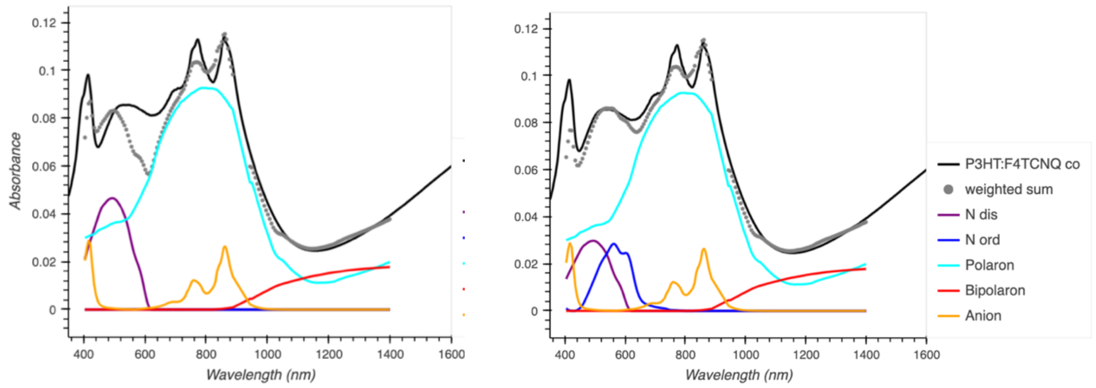

(a) Fit without neutral ordered

(b) Fit with neutral ordered

S. Figure 4: Absorbance spectra of doped P3HT fitted with and without the cross section of the neutral ordered species.

S.4. Reproducability with different P3HT films

Since the nature of the charge carriers is highly depending on film preparation, the results are validated with several repetitions. The colored columns in the following table represent the results of the films from the exact same solution as the THz thick films as seen in the main text. In comparison, columns P3HT: F_4TCNQ co (2) and (3) represent repetitions of co-processed P3HT with slightly thinner (12 nm) and thicker (30 nm) films. The fluctuations in conductivity, anion concentration, and relative percentages are reasonable within error. Given the flaws of the analysis method, the method yields valuable information on the presence/absence of distinct species nontheless. More on this topic is provided in the next supplementary section called Spectroelectrochemistry.

Moreover, on the topic of reproducibility with P3HT films, it is interesting to see how higher regioregularity can compensate effects the nature of the charge carriers and also the conductivity results. Therefore, a film of P3HT:F_4TCNQ sequential doped and layered is prepared. The film preparation of the P3HT:F_4TCNQ sequential film from the main text is reproduced, but with using 98% RR (M1011 from Ossila, Mw=60). The comparison in table S1. shows that the doping level seems to be reproducible and the [++] to [+] ratio is also in the same range, showing a small decrease from 25:100 (88% RR) to 16:100 (98% RR). This results in a conductivity which is not improved by the higher regioregularity.

Table S1: Neutral and oxidized species in the doped polythiophene films. The species contribution to the overall absorbance is given in % of the sum of all species. Since on the UV-Vis films I also measured the long-range conductivity, these values are included as well.

Sample	P(g$_4$2T-T): F$_4$TCNQ (THz)	P3HT: F$_4$TCNQ co (2)	P3HT: F$_4$TCNQ co (3)	P3HT: F$_4$TCNQ co (THz)	P3HT: F$_4$TCNQ sq (THz)	P3HT: F$_4$TCNQ sq (98% RR)
Thin (nm)	56	12	30	20	33	99
Long σ (S/cm)	41	0.3	0.4	0.2	2.8	1.8
N dis (%)	0	14	10	9	8	9
N ordered (%)	0	11	11	11	12	14
[+] carriers (%)	77	67	61	69	64	66
[++] carriers (%)	23	8	18	11	16	11
F$_4$TCNQ$^-$ (cm^{-3})	2.4e20	2.0e20	1.3e20	1.7e20	1.6e20	2.1e20
Ratio BP:P	30:100	12:100	29:100	16:100	25:100	16:100

In contrary, I see a small decrease in conductivity, which is supported by literature of doubly charged [++] carriers helping the conductivity in this regime. To investigate the effect of regioregularity on the complex conductivity, the following figure shows (a) THz complex conductivity in S/cm and (b) normalized to 1 at 1 THz with a scaled imaginary part.

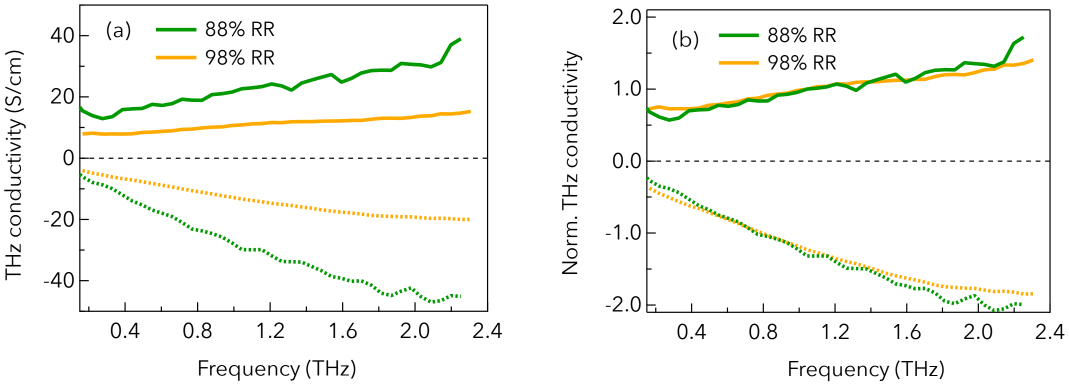

S. Figure 5: THz complex conductivity (a) in S/cm and (b) normalized to 1 at 1 THz.

S.5. Spectroelectrochemistry

This section describes the spectroelectrochemistry and how I determine the values presented in the section “nature of charge carriers”. The supplementary figure 5 shows (a) the absorbance of doped polythiophene P(g$_4$2T-T) in black, together with least squares fit using only relative cross sections of singly charged [+], doubly charged [++] carriers and F$_4$TCNQ$^-$ anion. I see that the dashed curve in grey, representing the fit, matches the experimental data well. To yield the relative cross sections used here and in the main text, I start with spectroelectrochemistry. In spectroelectrochemistry, one uses a thin film of the polymer on an ITO coated substrate in an encapsulating cell filled with a an electrolyte solution. One measures the UV/VIS/NIR absorbance while applying a voltage, in reference to a pseudo-reference electrode. This applied voltage injects ions from a surrounding electrolyte into the polymer film whereby the film gets electrochemically doped to counterbalance those injected charges. Electrochemical measurements were performed with freshly prepared solutions of [EMIM][BF4] in dry and degassed AcN (0.1 M) using a custom made three-electrode setup in a standard 1cm quartz cuvette. Polymer films were spin-coated from pyridine (10 mg/ml) onto ITO coated glass, yielding around 70 nm thin film of P(g$_4$2T-T). The ITO coated glass (R ~ 150 Ohm sq-1) served as the working electrode. A Pt and Ag wire served as the counter and pseudo-reference electrode. The potentials were calibrated versus the Ferrocene/Ferrocenium (Fc/Fc+) redox couple. I then recorded a series of absorbance spectra at different constant oxidation potentials between -0.2 V and +0.8 V versus Fc/Fc$^+$ and plotted the change in absorbance for all potentials in S. figure 5 (b).

Chronoamperometry of the same system quantifies the number of injected charges for the applied potentials. In other words, S. figure 5 (b) represents the absorbance spectra for each doping level. Then, I use a mathematical tool called Multivariate curve resolution (MCR) to deconvolute overlapping spectra of independent species. This procedure has been published and cited for P3HT previously, while here I extract the spectra of independent species present in doped P($g_4$2T-T). The subfigure (b) shows the quality of the MCR fit in grey dashed curves. S. figure 5 (d) shows the spectra of independent species: neutral ordered, neutral disordered, singly charged [+] carriers, and doubly charged [++] carriers for doped P($g_4$2T-T) and doped P3HT on top of each other. Hereby, I use normalized intensities relative to the highest cross section of neutral ordered, because I could not quantify the injected charges accurately due to surface effects on the 70 nm thin films. This challenge also has been published previously for the investigation of P3HT, but in our case I want to know the relative contributions and the nature of charge carriers in chemically doped P($g_4$2T-T), so I was not hindered by that. S. figure 5 (d) shows that the relative ratios and shapes of the four species are generally similar in P3HT and P($g_4$2T-T), while there are some differences relevant to discuss. First, all peaks are red-shifted for P($g_4$2T-T) which is consistent to our expectations for polythiophenes with oligoethylene glycol side-chains. I find a shift in the [+] carriers band from 800 nm to 860 nm and for the [++] carriers the peak is red-shifted out of our detection range (above 2000 nm). The [+] band also appears broader. Once the spectra of independent species are deconvoluted with MCR, I can use them to fit the absorbance of doped P($g_4$2T-T). Therefore, I am comparing electrochemical and chemical doping. The best quality fit is achieved when the [+] band is blue-shifted and broadened for the dry film of chemical doping, as depicted in S. figure 5 (c). All other extracted spectra are kept as obtained from the electrochemistry. Lastly, I use the best fit of the absorbance of doped P($g_4$2T-T) to calculate the relative percentage of independent species in the film. The Beer-Lambert law provides for each individual species the relative species concentration:

$$c_{species,rel} = \frac{A_{rel} \cdot \ln(10)}{\sigma_{rel} \cdot d}.$$

Whereby A_{rel} is the relative absorbance in the fit S. figure 5 (a), σ_{rel} is the relative cross section from (d), $\ln(10)$ is a constant taking into account that the absorbance is calculated from a logarithm with base 10 of the transmission, while the absorbance cross section is defined over the natural logarithm with base e, and d is the thickness of the film.

To get the final relative percentage I divide the relative species concentration by the sum of all species such that:

$$\sum\nolimits_{species} C_{species,rel} = 100\%.$$

To give an example, I calculate the relative percentages of [+] carriers and [++] carriers in the doped P(g$_4$2T-T) film. For both species I use the relative intensity at 2000 nm, which is the maximum of the bands. The first steps are the relative species concentrations, which are quantitatively meaningless unless compared to each other because of the quantification challenge mentioned above.

$$C_{polaron,rel} = \frac{0.313 \cdot \ln(10)}{0.65 \cdot d} = 2e7,$$

$$C_{bipolaron,rel} = \frac{0.11 \cdot \ln(10)}{0.69 \cdot d} = 0.6e7.$$

Finally, I can devide calculate the sum of those present species.

$$\sum\nolimits_{species} C_{species,rel} = 2.6e7.$$

To get the relative percentages of [+] and [++] carriers as presented in the main text.

$$P_{[+],rel} = \frac{2e7}{2.6e7} = 77\%.$$

$$P_{[++],rel} = \frac{0.6e7}{2.6e7} = 23\%.$$

Since this is a relative calculation, it would mathematically be identical without the constant thickness and factor of the logarithm, yet the equations are described as are to clarify that one could be quantitative if the cross sections are known. This relative analysis helps to explain the nature of the charge carriers, since the interplay of [+], [++] and induced charge carriers have influence on the conductivity in doped polythiophenes.

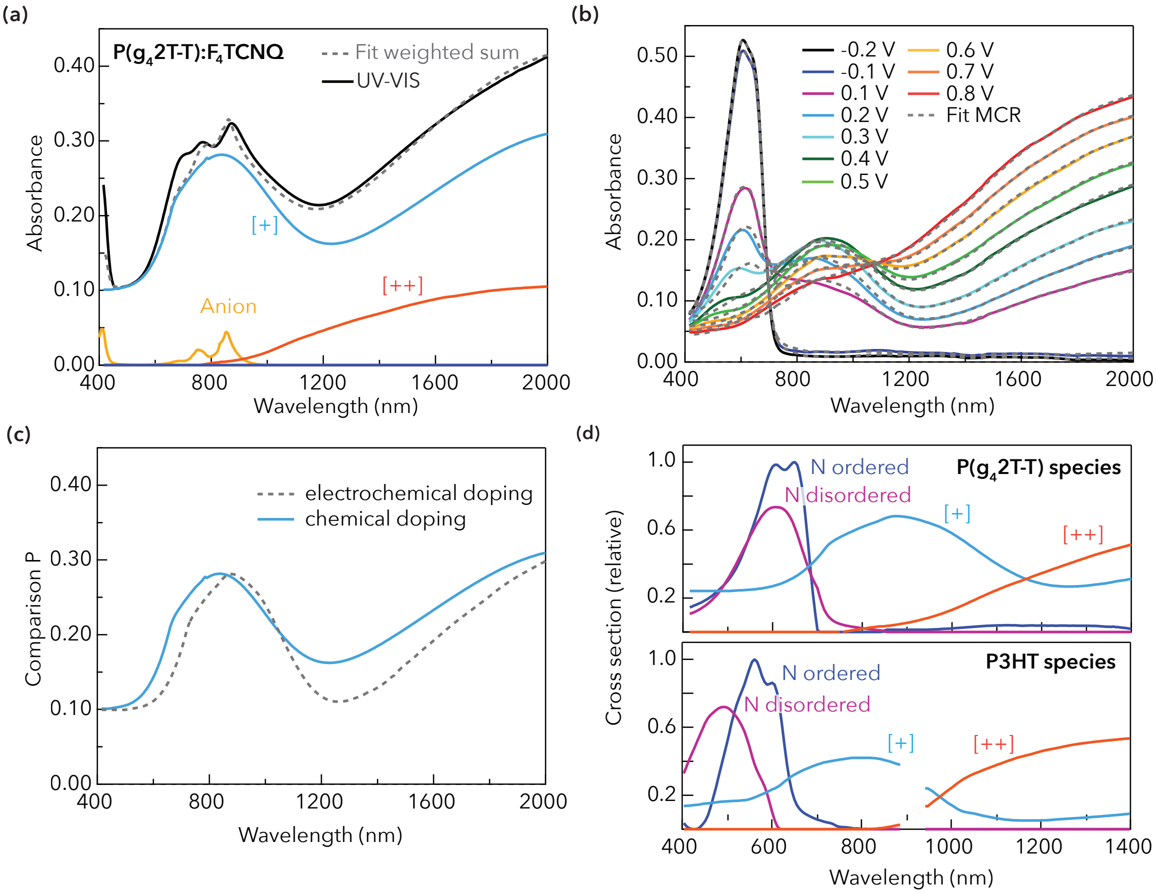

S. Figure 6: (a) Absorbance of the doped P(g$_4$2T-T) film (black curve) together with a fit (grey dashed curve) of a linear combination using the spectra of the independent species singly charged [+] carriers, doubly charged [++] carriers and F_4TCNQ^- anions. (b) Electrochemical doping of a P(g$_4$2T-T) film including the MCR fit (grey dashed curve) used to determine: (c) the difference of the [+] band in electrochemical and chemical doping. (d) the relative species cross sections.

S.6. Presented Drude-Smith Model fits

First, in S. Figure 7 are the best fits for the experimental data used to determine the DSM parameters. From left to right the complex conductivity of P(g42T-T):F_4TCNQ (blue), P3HT:F_4TCNQ co (magenta) and P3HT:F_4TCNQ sq (green). The corresponding parameters are shown as an inset. Note that that the density of mobile charges varies from $4 \cdot 10^{18}$ cm^{-3} and $1 \cdot 10^{20}$ cm^{-3}. This should be considered when comparing the scattering time and localization parameter. Moreover, the scattering time and the localization parameter have a similar effect on the shape of the curves. A longer scattering time and a more negative localization parameter independently flattens the curves and increases the real part in relation to the imaginary part; i.e. when applying this fairly phenomenological model. Yet I take away major findings: The P3HT:F_4TCNQ sequentially doped has significantly more charges that are contributing to the higher conductivity in comparison to the same material co-processed. On the other hand, the higher conductivity in P(g$_4$2T-T):F_4TCNQ is not coming from a higher total charge density or a higher contributing charge density. It is coming from a combination of parameters that are increasing the mobility of the present charges.

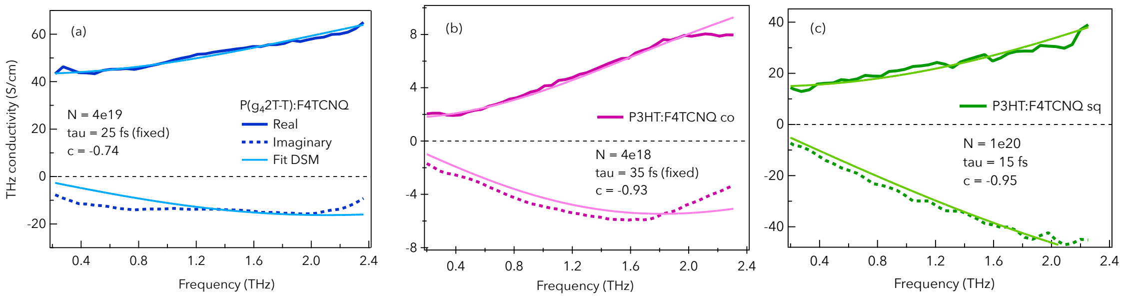

S. Figure 7: Drude smith model fits with fitting parameters as an inset for films of (a) P(g$_4$2T-T):F_4TCNQ, (b) P3HT:F_4TCNQ co, and (c) P3HT:F_4TCNQ sq.

Considerations and resilience in the Drude Smith Model fits

While the scattering time of films with a similar molecular structure and doping level could be expected to have similar scattering times. The differences in side-chains or processing can lead to different microstructure which will have an effect on the scattering time. S. Figure 8 shows the fits when trying to fix the scattering time for all samples to 22 fs.

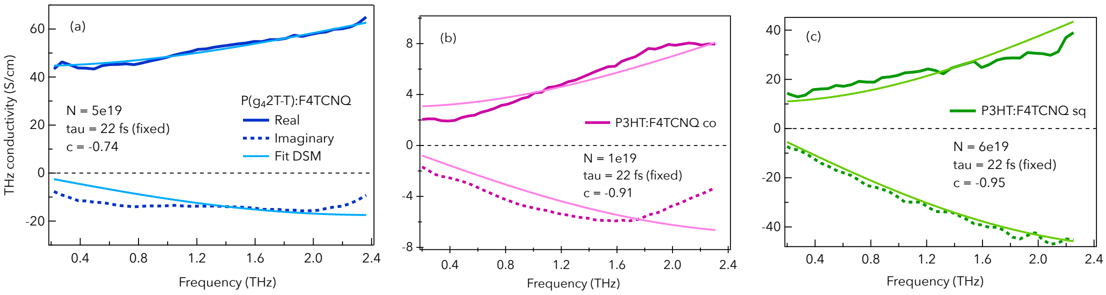

S. Figure 8: Drude smith model fits with fixing scattering time.

What happens when density N in the Drude Smith model is fixed to the number of anions determined? In the following S. Figure 9 are three subsequent subfigures for each dataset. The three panels from left to right represent 100 %, 10 % and 5% of doping induced charges carriers are mobile. The total doping induced charge carriers are estimated based on dopant anion density as shown in the absorbance section. From top to bottom are the three different data sets. As seen in the following graphics from left to right, by decreasing the N, in the fit tau increases. In very simple paraphrasing: imagine by decreasing N, one is forcing a lower amplitude, then to maintain some degree of fitingt, the slope increases. From this consideration, and from this fitting series the likely density of mobile charge carriers N (in percent of number of anions estimated as $2.0 \cdot 10^{20} \pm 0.5 \cdot 10^{20}$ cm^{-3}) for each dataset are: Intermediate for P(g$_4$2T-T):F$_4$TCNQ with 10—30 % of the number of anions. Low for P3HT:F$_4$TCNQ co with 1–5 % of the number of anions. Intermediate–High for P3HT:F$_4$TCNQ with 30–50 % of the number of anions.

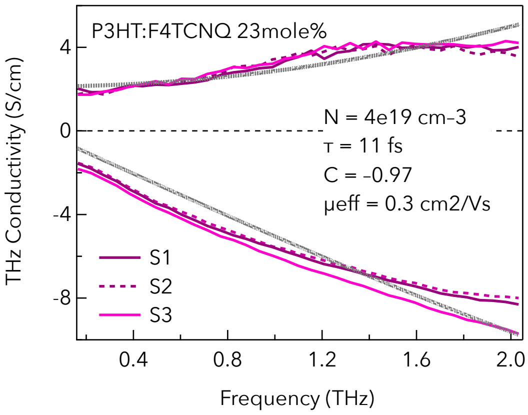

S. Figure 8.1: Drude smith model fits of P3HT:F4TCNQ co with higher doping level 23mol%.

S. Figure 9 to clarify the range of possible charge carrier densities N, as well as corresponding scattering times τ and localization parameters c_1. The resulting charge carrier densities in relation to the density of dopant anions ($2 \cdot 10^{20}$) is (a) $4 \cdot 10^{19} \approx 20\%$ (b) $4 \cdot 10^{18} \approx 2\%$ and (c) $1 \cdot 10^{20} \approx 50\%$.

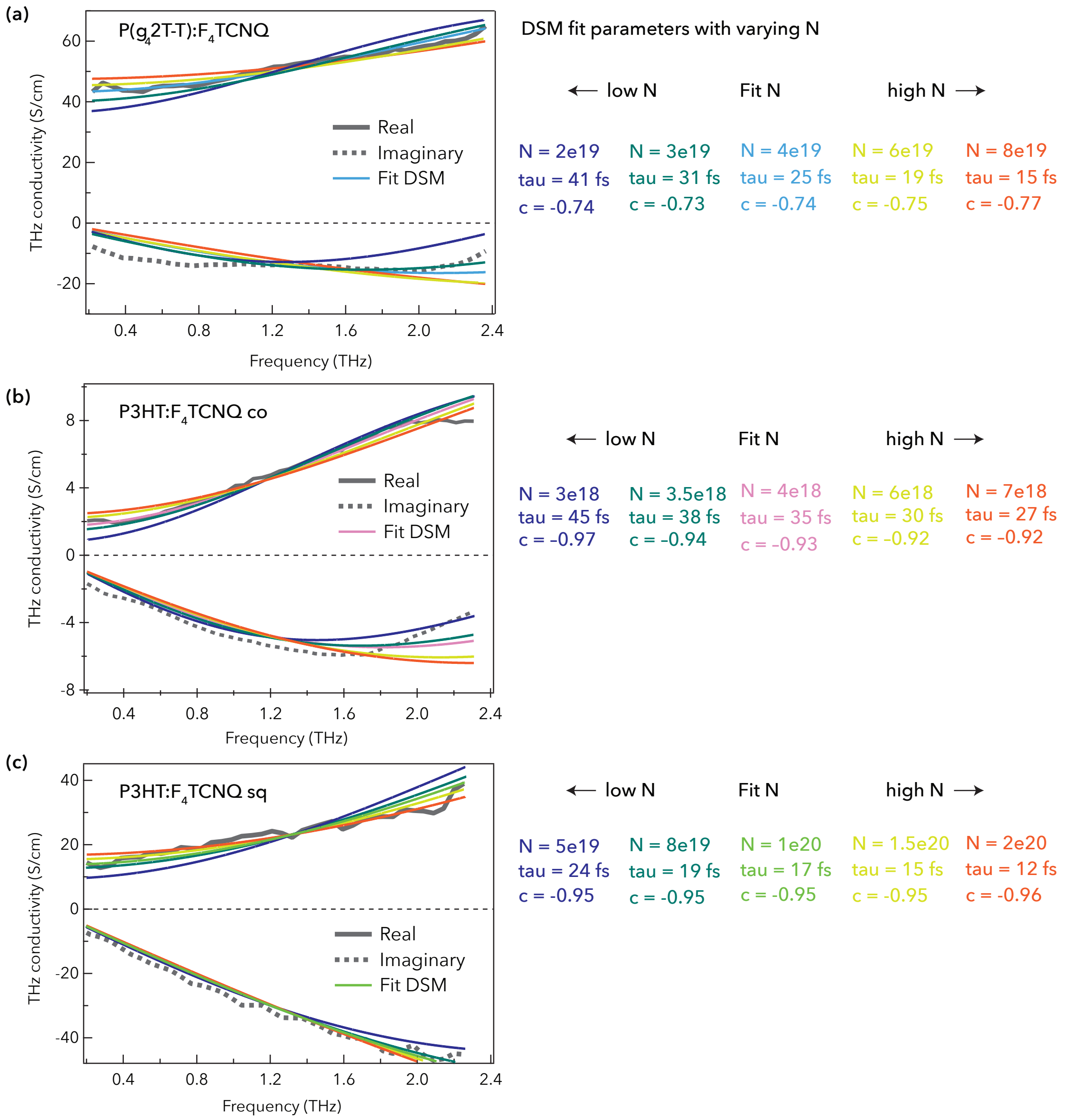

Figure 9: Drude smith model fits with varying charge carrier density N color coded and given in cm^{-3}. (a) Pg_42T-T:F_4TCNQ, (b) P3HT:F_4TCNQ co-processed and (c) P3HT:F_4TCNQ sequential.

Taking the turquoise and yellow fits as the lower and upper limit respectively that gives the ranges (a) 15%–30% for Pg$_4$2T-T:F$_4$TCNQ, (b) 1.7%–3% for P3HT:F$_4$TCNQ co-processed and (c) 40%–75% for P3HT:F$_4$TCNQ sequentially processed. Given the high inacurracy of the density of dopant anions these percentages must be interpreted conservatively.

The effect of the varying charge carrier density N on the other DSM fit parameters are deduced. An increasing charge carrier density N leads to a decreasing scattering time τ in the model. The localization parameter c_1 remains rather stagnant but is slightly increasing with increasing N for the systems Pg$_4$2T-T:F$_4$TCNQ and P3HT:F$_4$TCNQ sequentially processed, but not for P3HT:F$_4$TCNQ co-processed.

S.7. Figures of merit for enhanced conductivity

Using a complex conductivity spectrum seen in S. Figure 7 (a) this section shows how the figures of merit **Short σ, Imaginary/Real, low-frequency σ and Slope** are extracted. Here the same color code is used as in the main text. The Short σ is given by the real part of the complex conductivity at 1 THz (green). The low-frequency σ is given by extrapolating the Drude Smith model fit (grey dashed) of the real part to 0 THz (turquoise). The quotient of Imaginary/Real is calculated by dividing the absolute values of imaginary and real complex conductivity at 1 THz (peach) and the slope is given by the increase of a linear fit of the real part between 0.8 and 1.4 THz (red).

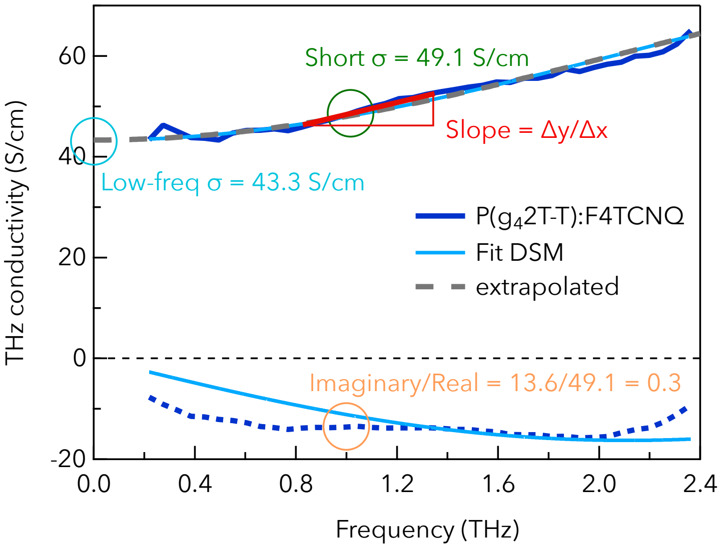

S. Figure 10: Visual explanation how the figures of merit **Short σ, Imaginary/Real, low-frequency σ and Slope** are extracted from a complex conductivity spectrum.

Intuitively, the low-frequency conductivity is directly related to the slope of the real part of the conductivity. The higher the slope of the real part, the lower the low-frequency conductivity. Both introduced parameters provide insight into the conductivity over different distances, since the low-frequency conductivity translates to longer distances. To determine the low-frequency conductivity, here the Drude Smith model fit is extrapolated to 0 THz. Notably, the often-used equation to calculate the low-frequency conductivity by Short σ (1+c) is not sufficient. This equation simplified assumes that the observed complex conductivity is directly proportional to the frequency, which does not describe the complex conductivity well.

The following three graphics show the extrapolated Drude Smith model that is used to determine the real part of the conductivity at low frequencies. This is related to the long-range conductivity. By comparison to the experimental data, I find that this method is more accurate to catch the mechanism for the short- long range restoration than the sometimes-reported simplified equation long-range = short-range(1+c); i.e. the short- to long-range restoration cannot be described by a simplified linear model.

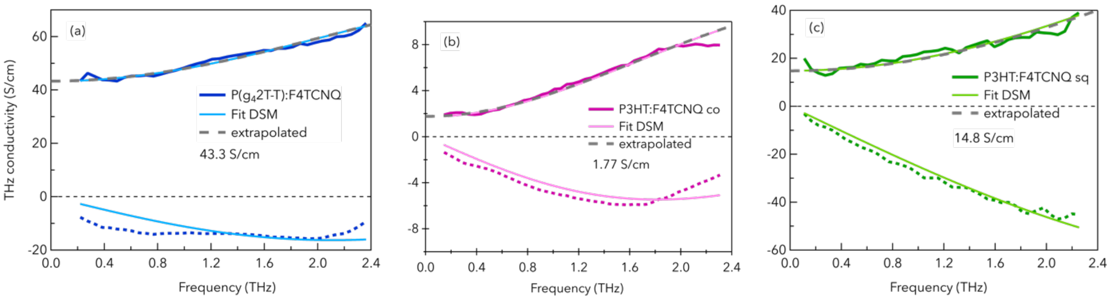

S. Figure 11: Extrapolation of DSM fits of the complex conductivity spectra yielding the low-frequency conductivity.

S.8. Figures of merit for enhanced conductivity

Intuitively, the low-frequency conductivity is directly related to the slope of the real part of the conductivity. The higher the slope of the real part, the lower the low-frequency conductivity. Both introduced parameters provide insight into the conductivity over different distances, since the low-frequency conductivity translates to longer distances. To determine the low-frequency conductivity, here the Drude Smith model fit is extrapolated to 0 THz. Notably, the often-used equation to calculate the low-frequency conductivity by Short σ (1+c) is not sufficient. This equation simplified assumes that the observed complex conductivity is directly proportional to the frequency, which does not describe the complex conductivity well. The low-frequency conductivity as determined by the DSM matches the long-range conductivity exactly.

Table S.8.1. Experimental figures of merit for the complex conductivity.

Experiment	Short σ (S/cm)	Im/Real σ	slope	Long σ (S/cm)	Low-freq σ (S/cm) Short σ (1+c)	Low-freq σ (S/cm) extra DSM	Restoration (%)
P(g$_4$2T-T): F$_4$TCNQ	49	0.3	0.25	43	13	43	88
P3HT: F$_4$TCNQ co	4	1.2	0.95	0.2	0.3	2	4
P3HT: F$_4$TCNQ sq	23	1.3	0.39	3	1	15	12

To determine the low frequency conductivity, I used to different methods. From the comparison to the experimental results, it is clear, that the simplified linear relation Long = Short(1+c) is not sufficient. Please see the previous chapter in the SI for the extrapolated DSM fits at 0 THz.

Table S.8.2. Simulation and the resulting figures of merit of the complex conductivity.

Simulation	Short σ (a.u.)	Imσ/Reσ (%)	slope	Low-freq σ (S/cm)
dis.=0.05 e. = 5	2.15	0.2	0.32	2.0
dis.=0.05 e.=2.5	0.90	0.44	0.42	0.6
dis.=0.1 e.=5	0.75	0.54	0.58	0.38
dis.=0.1 e.=2.5	0.40	0.75	0.73	0.16
dis.=0.05 e.=2.5, confine	0.25	1.90	0.92	0.0
dis.=0.1 e.=2.5, confine	0.20	2.50	0.92	0.0

References for Chapter 6

1. Armin, A., et al., *Engineering dielectric constants in organic semiconductors.* Journal of Materials Chemistry C, 2017. **5**(15): p. 3736-3747.
2. Sami, S., et al., *How Ethylene Glycol Chains Enhance the Dielectric Constant of Organic Semiconductors: Molecular Origin and Frequency Dependence.* ACS Appl Mater Interfaces, 2020. **12**(15): p. 17783-17789.
3. Meng, B., J. Liu, and L. Wang, *Oligo(ethylene glycol) as side chains of conjugated polymers for optoelectronic applications.* Polymer Chemistry, 2020. **11**(7): p. 1261-1270.
4. Moser, M., et al., *Ethylene Glycol-Based Side Chain Length Engineering in Polythiophenes and its Impact on Organic Electrochemical Transistor Performance.* Chemistry of Materials, 2020. **32**(15): p. 6618-6628.
5. Kroon, R., et al., *Polar Side Chains Enhance Processability, Electrical Conductivity, and Thermal Stability of a Molecularly p-Doped Polythiophene.* Adv Mater, 2017. **29**(24).
6. Giovannitti, A., et al., *Controlling the mode of operation of organic transistors through side-chain engineering.* Proc Natl Acad Sci U S A, 2016. **113**(43): p. 12017-12022.
7. Nielsen, C.B., et al., *Molecular Design of Semiconducting Polymers for High-Performance Organic Electrochemical Transistors.* J Am Chem Soc, 2016. **138**(32): p. 10252-9.
8. Kiefer, D., et al., *Double doping of conjugated polymers with monomer molecular dopants.* Nat Mater, 2019. **18**(2): p. 149-155.
9. Hofmann, A.I., et al., *Highly stable doping of a polar polythiophene through co-processing with sulfonic acids and bistriflimide.* J Mater Chem C Mater, 2018. **6**(26): p. 6905-6910.
10. Tietze, M.L., et al., *Fermi level shift and doping efficiency inp-doped small molecule organic semiconductors: A photoelectron spectroscopy and theoretical study.* Physical Review B, 2012. **86**(3).
11. Tietze, M.L., et al., *Elementary steps in electrical doping of organic semiconductors.* Nat Commun, 2018. **9**(1): p. 1182.
12. Pingel, P. and D. Neher, *Comprehensive picture ofp-type doping of P3HT with the molecular acceptor F4TCNQ.* Physical Review B, 2013. **87**(11).
13. Enengl, C., et al., *Doping-Induced Absorption Bands in P3HT: Polarons and Bipolarons.* Chemphyschem, 2016. **17**(23): p. 3836-3844.

14. Moulé, A.J., et al., *Quantifying Polaron Mole Fractions and Interpreting Spectral Changes in Molecularly Doped Conjugated Polymers.* Advanced Electronic Materials, 2021.
15. Sahalianov, I., et al., *UV-to-IR Absorption of Molecularly p-Doped Polythiophenes with Alkyl and Oligoether Side Chains: Experiment and Interpretation Based on Density Functional Theory.* J Phys Chem B, 2020. **124**(49): p. 11280-11293.
16. Stallhofer, K., et al., *Dynamics of Short-Lived Polaron Pairs and Polarons in Polythiophene Derivatives Observed via Infrared-Activated Vibrations.* The Journal of Physical Chemistry C, 2019. **123**(46): p. 28100-28105.
17. Tsokkou, D., et al., *Bipolarons rule the short-range terahertz conductivity in electrochemically doped P3HT.* Mater Horiz, 2022. **9**(1): p. 482-491.
18. Jacobs, I.E. and A.J. Moule, *Controlling Molecular Doping in Organic Semiconductors.* Adv Mater, 2017. **29**(42).
19. Lüssem, B., M. Riede, and K. Leo, *Doping of organic semiconductors.* PSS physica status solidi (a), 2013. **210**(1): p. 9-43.
20. Bockmann, M., et al., *Structure of P3HT crystals, thin films, and solutions by UV/Vis spectral analysis.* Phys Chem Chem Phys, 2015. **17**(43): p. 28616-25.
21. Chew, A.R., et al., *Sequential Doping Reveals the Importance of Amorphous Chain Rigidity in Charge Transport of Semi-Crystalline Polymers.* J Phys Chem Lett, 2017. **8**(20): p. 4974-4980.
22. Duong, D.T., et al., *The chemical and structural origin of efficient p-type doping in P3HT.* Organic Electronics, 2013. **14**(5): p. 1330-1336.
23. Hynynen, J., et al., *Enhanced Electrical Conductivity of Molecularly p-Doped Poly(3-hexylthiophene) through Understanding the Correlation with Solid-State Order.* Macromolecules, 2017. **50**(20): p. 8140-8148.
24. Noriega, R., et al., *A general relationship between disorder, aggregation and charge transport in conjugated polymers.* Nat Mater, 2013. **12**(11): p. 1038-44.
25. Neusser, D., et al., *High Conductivities of Disordered P3HT Films by an Electrochemical Doping Strategy.* Chemistry of Materials, 2020. **32**(14): p. 6003-6013.
26. Keene, S.T., et al., *Efficient Electronic Tunneling Governs Transport in Conducting Polymer-Insulator Blends.* J Am Chem Soc, 2022. **144**(23): p. 10368-10376.
27. Gao, J., et al., *The effect of 2,3,5,6-tetrafluoro-7,7,8,8-tetracyanoquinodimethane charge transfer dopants on the conformation and aggregation of poly(3-hexylthiophene).* Journal of Materials Chemistry C, 2013. **1**(36).

28. Jacobs, I.E., et al., *Comparison of solution-mixed and sequentially processed P3HT:F4TCNQ films: effect of doping-induced aggregation on film morphology.* J. Mater. Chem. C, 2016. **4**(16): p. 3454-3466.
29. Liu, Y., et al., *Sequential deposition: optimization of solvent swelling for high-performance polymer solar cells.* ACS Appl Mater Interfaces, 2015. **7**(1): p. 653-61.
30. Wang, S., et al., *Sequential Doping of Ladder-Type Conjugated Polymers for Thermally Stable n-Type Organic Conductors.* ACS Appl Mater Interfaces, 2020. **12**(47): p. 53003-53011.
31. Finn, P.A., et al., *Effect of polar side chains on neutral and p-doped polythiophene.* Journal of Materials Chemistry C, 2020. **8**(45): p. 16216-16223.
32. Xu, K., et al., *Ground-state electron transfer in all-polymer donor-acceptor heterojunctions.* Nat Mater, 2020. **19**(7): p. 738-744.
33. Thomas, E.M., et al., *Role of Disorder Induced by Doping on the Thermoelectric Properties of Semiconducting Polymers.* Chemistry of Materials, 2018. **30**(9): p. 2965-2972.
34. Jacobs, I.E., et al., *Structural and Dynamic Disorder, Not Ionic Trapping, Controls Charge Transport in Highly Doped Conducting Polymers.* J Am Chem Soc, 2022. **144**(7): p. 3005-3019.
35. Xiong, M., et al., *Counterion docking: a general approach to reducing energetic disorder in doped polymeric semiconductors.* Nat Commun, 2024. **15**(1): p. 4972.
36. Scheunemann, D., et al., *Charge transport in doped conjugated polymers for organic thermoelectrics.* Chemical Physics Reviews, 2022. **3**(2).
37. Gregg, B.A., S.-G. Chen, and R.A. Cormier, *Coulomb forces and doping in organic semicondcutors.* Chem. Mater., 2004. **16**.
38. Liu, J., et al., *Overcoming Coulomb Interaction Improves Free-Charge Generation and Thermoelectric Properties for n-Doped Conjugated Polymers.* ACS Energy Letters, 2019. **4**(7): p. 1556-1564.
39. Arkhipov, V.I., et al., *Analytic model of carrier mobility in doped disordered organic semiconductors.* Physical Review B, 2005. **72**(23).
40. Duhandzic, M., et al., *Carrier Screening Controls Transport in Conjugated Polymers at High Doping Concentrations.* Phys Rev Lett, 2023. **131**(24): p. 248101.
41. Drakopoulos, S.X., et al., *Universal Scaling of DC Conductivity with Dielectric Interfacial Polarization in Conjugated Polymers.* Macromolecules, 2024. **57**(6): p. 2661-2668.
42. Pooja, et al., *Factors affecting the electrical conductivity of conducting polymers.* Carbon Letters, 2022. **33**(2): p. 307-324.

43. Elbayoumy, E., et al., *Dielectric Permittivity, AC Electrical Conductivity and Conduction Mechanism of High Crosslinked-Vinyl Polymers and Their Pd(OAc)(2) Composites.* Polymers (Basel), 2021. **13**(17).
44. Warren, R., P.W.M. Blom, and N. Koch, *Molecular p-doping induced dielectric constant increase of polythiophene films determined by impedance spectroscopy.* Applied Physics Letters, 2023. **122**(15).
45. Kettner, O., et al., *Mixed Side-Chain Geometries for Aggregation Control of Poly(fluorene-alt-bithiophene) and their Effects on Photophysics and Charge Transport.*
46. Abdalla, H., G. Zuo, and M. Kemerink, *Range and energetics of charge hopping in organic semiconductors.* Physical Review B, 2017. **96**(24).
47. Hofmann, A.I., et al., *Chemical Doping of Conjugated Polymers with the Strong Oxidant Magic Blue.* Advanced Electronic Materials, 2020. **6**(8).
48. Untilova, V., et al., *Control of Chain Alignment and Crystallization Helps Enhance Charge Conductivities and Thermoelectric Power Factors in Sequentially Doped P3HT:F4TCNQ Films.* Macromolecules, 2020. **53**(7): p. 2441-2453.
49. Cornelissen, T.D., et al., *Kinetic Monte Carlo simulations of organic ferroelectrics.* Phys Chem Chem Phys, 2019. **21**(3): p. 1375-1383.
50. Murrey, T.L., et al., *Additive solution deposition of multi-layered semiconducting polymer films for design of sophisticated device architectures.* Journal of Materials Chemistry C, 2019. **7**(4): p. 953-960.
51. Cavassin, P., et al., *Electrochemical Doping in Ordered and Disordered Domains of Organic Mixed Ionic-Electronic Conductors.* Adv Mater, 2023. **35**(35): p. e2300308.
52. Cho, K.G., et al., *Sub-Band Filling and Hole Transport in Polythiophene-Based Electrolyte-Gated Transistors: Effect of Side-Chain Length and Density.* Advanced Functional Materials, 2023. **33**(37).
53. Zuo, G., H. Abdalla, and M. Kemerink, *Impact of doping on the density of states and the mobility in organic semiconductors.* Physical Review B, 2016. **93**(23).
54. Holliday, S., J.E. Donaghey, and I. McCulloch, *Advances in Charge Carrier Mobilities of Semiconducting Polymers Used in Organic Transistors.* Chemistry of Materials, 2013. **26**(1): p. 647-663.
55. Smolyanskaya, O.A., et al., *Terahertz biophotonics as a tool for studies of dielectric and spectral properties of biological tissues and liquids.* Progress in Quantum Electronics, 2018. **62**: p. 1-77.

56. Neu, J. and C.A. Schmuttenmaer, *Terahertz Spectroscopy and Density Functional Theory Investigation of the Dipeptide L-Carnosine.* Journal of Infrared, Millimeter, and Terahertz Waves, 2020. **41**(11): p. 1366-1377.
57. Sizov, F.F., *Infrared and terahertz in biomedicine.* Semiconductor Physics Quantum Electronics and Optoelectronics, 2017. **20**(3): p. 273-283.
58. Fischer, B., et al., *Chemical recognition in terahertz time-domain spectroscopy and imaging.* Semiconductor Science and Technology, 2005. **20**(7): p. S246-S253.
59. McIntosh, A.I., et al., *Terahertz spectroscopy: a powerful new tool for the chemical sciences?* Chem Soc Rev, 2012. **41**(6): p. 2072-82.
60. Johnston, M.B., et al., *Low-energy vibrational modes in phenylene oligomers studied by THz time-domain spectroscopy.* Chemical Physics Letters, 2003. **377**(1-2): p. 256-262.

7 Charge transport in polymers

> *"Life is a great tapestry. The individual is only an insignificant thread in an immense and miraculous pattern."*
>
> Albert Einstein.

This chapter is divided into three parts. In the first part, I derive the semi-transient-localized transport model for doped polymers. The second and third part are based on two independent articles in preparation for Advanced Materials. Their completion would not have been possible without the efforts of these researchers. Please find everyone's detailed contributions to the two projects in Appendix One.

Eva Röck, Maximilian Horn, Nesibe Akmanşen-Kalayci, Lize Bynens, Wouter Maes, Sarah Tolbert, Natalie Banerji

Eva Röck, Diego Garcia Vidales, Nesibe Akmanşen-Kalayci, Maximilian Horn, Lize Bynens, Badr Jismy, Olivier Bardagot, Nicolas Leclerc, Wouter Maes, Benjamin Schwartz, Sarah Tolbert, Natalie Banerji

7.1 Semi-transient-localized transport model for doped polymers

Abstract

This section logically derives the charge transport model presented in this thesis: the semi-transient-localized transport (STLoT) model. The STLoT model combines the semi-localized transport model and field- and fluctuation-induced processes *via* a crossover temperature. Below the crossover temperature, static disorder dominates which leads to a weak localization. Above the crossover temperature, static disorder is effectively screened by field- and fluctuation- induced transient processes such that charge carriers can move freely.

7.1.1 Introduction

The HOMO density of states at high carrier density

With doping, the conductivity of conjugated polymers increases manifold[1-5] and is described by the product of charge carrier density (n) and mobility (μ):

$$\sigma \propto n \times \mu. \qquad (1)$$

In other words, *how many* charge carriers (n) are moving *how fast* (μ) through a material in response to an applied electrical field. Both parameters n and μ

yield limitations that need to be discussed **in the context of molecular doping of polymers**.

The discussed structural changes are key to determine the resulting localization. Yet, the perspective needs to be extended to the density of states to get a more complete picture of localization. At increasing doping levels, the density of states around the Fermi energy is high and the energetic difference between states is small. A small energetic difference between states represents a small disorder in the framework of variable range hopping. This aligns with a smaller localization of charge carriers at high doping levels. Yet, a further increase in doping level leads to sub-band filling and hence additional localization based on electrostatic interactions. In other words, a high density of holes in the HOMO can result in hole-hole repulsion, which leads to a dip in available states around the Fermi energy. Sub-band filling and the corresponding formation of a Coulomb gap has been reported with electrochemical[6, 7] and molecular doping of polythiophenes[8, 9]. Moreover, kinetic Monte Carlo simulations numerically including electrostatic interactions in the conductivity of polymers showcase the drop at high carrier densities as well[10]. The type of charge carriers in this picture are often left implicit. Figure M.1. shows an energy levels scheme including the charge carrier density in a (Gaussian) DOS. (a) Shows a broader DOS than (b). The characteristic parameters are (i) the activation energy W_H given by the energy difference between the peak of the carrier density and the transport edge and (ii) the energy difference between the transport edge energy and the Fermi energy. All carriers (holes) in the shaded area contribute to transport. Figure M.1. (c) shows also an energy level scheme highlighting the role of the charge carrier density.

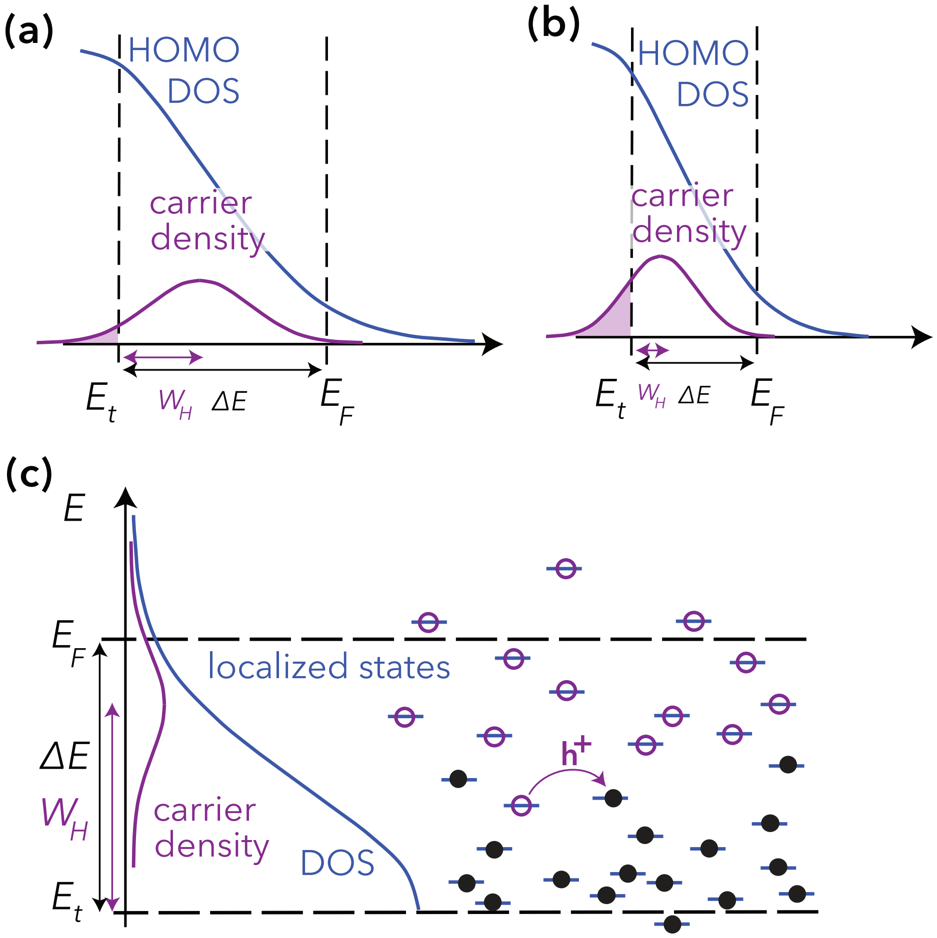

Figure M.1. Scheme of (a) broad and (b) narrow density of states.

Beyond the duality of localization

Given the literature review in Chapter 4, charge transport in doped polymers can lie on the axis between fully delocalized (band-like) to fully localized (hopping) transport. Hopping transport is characterized by localized electronic states and an activation energy to transport. The variation in energies of electronic states is interpreted as energetic disorder. When the energetic disorder and the variation in energies of electronic states becomes very small, the electronic states form a band with indistinguishable energies. Such band-like transport is characterized by highly delocalized charges and the absence of an activation energy. Several hopping transport models and several band-like transport models have been proposed for conjugated polymers. Often, conjugated polymers are described as a sum of hopping and band-like terms in the heterogeneous transport model. The heterogeneous transport model is based on different transport properties in different domains as the name suggests, which typically fits the results of semi-crystalline polymer films[11]. The heterogeneous transport model is recently applied for temperature rub-aligned films with aligned ordered domains and disordered domains by Brinkmann's group for example[12]. The duality of band-like and hopping transport has been revised though. Particularly, the pioneering work of Kang and Snyder in 2017 and its extension by Gregory *et al.* in 2021 has provided a big leap towards a universal transport model for doped polymers. They introduced the semi-localized transport (SLoT) model that treats the transition between hopping- and band-like transport as a continuum[9, 13]. In the SLoT model the charge transport is universally in line with the Boltzmann formalism. It accounts for the doping concentration dependence of the activation energy $W_{\mathrm{H}}(c)$ and yields physically reasonable Fermi energies ($E_{\mathrm{Fermi}} - E_{\mathrm{t}} < 1$ eV). The transport function in the SLoT model is given by equation (2).

$$\sigma_{\mathrm{E}}(E,T) = \begin{Bmatrix} 0, (E < E_{\mathrm{t}}) \\ \sigma_0 \exp\left(-\frac{W_{\mathrm{H}}(c)}{k_{\mathrm{B}}T}\right) \times \left(\frac{E - E_{\mathrm{t}}}{k_{\mathrm{B}}T}\right), (E \geq E_{\mathrm{t}}) \end{Bmatrix} \tag{2}$$

The transport function $\sigma_{\mathrm{E}}(E,T)$ describes the charge transport at any electron energy (E) and temperature (T). Charge carriers with energies below a transport edge E_{t} are not mobile. They hence have a transport function of zero and do not contribute to conductivity. Charge carriers with energies above the transport edge have (i) a temperature and dopant concentration dependent term and (ii) an energy dependent term. The temperature- and dopant concentration- dependent term $\sigma_0 \exp\left(-\frac{W_{\mathrm{H}}(c)}{k_{\mathrm{B}}T}\right)$ describes localized (hopping) transport. This term contains the temperature independent pre-factor σ_0 and the reduced activation energy W_{H}. It is described by an exponential decay with W_{H}, the Boltzmann constant $k_{\mathrm{B}} = 8.617\mathrm{e}{-5}$ eV and temperature T. The energy wells W_{H} are decreasing for increasing dopant concentration until hole-hole repulsion takes over as mentioned in the previous section. The energy dependent term $\left(\frac{E-E_t}{k_{\mathrm{B}}T}\right)$ describes delocalized (band-like) contributions to the total transport. The degree of localization can be described roughly by the reduced activation energy W.

$$W = \frac{\mathrm{d}\ln(\sigma)}{\mathrm{d}\ln(T)} \qquad (3)$$

Here, the derivation of $\ln(\sigma)$ in regard to $\ln(T)$ describes the curvature of the generalized temperature-dependent conductivity. The localized term contributes a concave temperature dependence, and the delocalized term contributes a convex temperature dependence to the universal charge transport function in equation (2). One very important remark is that the reduced activation energy W is dimensionless. The activation energy W_{H} in terms of energy is obtained by multiplying W with ($-k_{\mathrm{B}}T$). When plotting W versus the temperature on a log-log scale, a negative slope represents the degree of charge localization. A positive slope represents indicates that delocalized transport is dominating. The activation energy, has been studied for the system P3HT:FeCl as a function of doping level. Thereby, W_{H} decreases from 110 meV to 9.6 meV[13]. In 2023, it was applied to PBTTT:FeCl with W_{H} decreasing from 160 meV to band-like transport (0 meV) with doping concentration[9]. In many doped polymers (including P3HT, PBTTT, 2DPP-TEG) a crossover temperature T_0 occurs, where $W = \frac{\mathrm{d}\ln(\sigma)}{\mathrm{d}\ln(T)} < 0$ above T_0 and $W = \frac{\mathrm{d}\,ln(\sigma)}{\mathrm{d}\,ln(T)} > 0$ below T_0[14-18]. The observation of $W = \frac{\mathrm{d}\ln(\sigma)}{\mathrm{d}\ln(T)} < 0$ points in the direction of band-like transport above the crossover temperature T_0. This can be confirmed by an ideal Hall effect[17] and Drude-like optical absorption, i.e. complex conductivity[19]. The SLoT model assumes homogeneous static disorder and its formalism stems from organic crystalline semiconductors or highly ordered polymers.

Extension to transient mechanisms

The concept of transient mechanisms such as transient localization originating from vibrational modes has been developed by Sheng *et al.* and is revisited by Fratini and Ciuchi[19-22]. Fluctuation-induced tunnelling has been identified to play a role in the charge transport of disordered domains. For example, in ultra dilute polymer:insulator blends like PEDOT:PSS or P($g_4$2T-TT):PEG by Salleo's group[23]. The contributions of tunnelling to transport in highly doped polymers are not fully understood. Field-induced carrier heating[1] is also a transient mechanism, that could contribute to

---

[1] The estimate upper limit for field-induced carrier heating for the THz experiment in this work is calculated to be approximately 12 K (1 meV) in Chapter 4.2.2.

transport at high carrier density[24-26] while the upper limit in THz time-domain spectroscopy is expected to be 12 K (1 eV). Hence, other mechanisms, especially fluctuation-induced tunneling, are expected to be more important. Moreover, **the resilience to conformational fluctuations has been identified to play a key role** in determining the energetic disorder[27, 28]. These transient mechanisms are non-neglectable in soft materials such as polymers, particularly when static disorder is small. Such transient mechanisms may quench the activation energy above the crossover temperature, which sometimes is interpreted as activation-less delocalized transport. A decreasing mobility at cryogenic temperature can aid to assign transient mechanisms instead of delocalized transport, in this case one speaks of the frozen disorder limit[29, 30]. Therefore, delocalized transport cannot be assigned purely based on temperature-dependent conductivity around room temperature. Only in combination with coherent charge transport in Hall effect experiments or a positive imaginary part in the complex conductivity one can clearly assign localized/delocalized transport.

7.1.2 Results and discussion

Transport physics of the semi-transient-localized transport model

Simply put, when static disorder is small (on the order of tens of meV), transient mechanisms are sufficient to bring charge carriers to energetic states that have such small energy difference that they are effectively indistinguishable from band-like transport.

Extending the SLoT model to these transient mechanisms is interesting and relevant to describe doped polymers. I denote this charge transport model **semi-transient localized transport model (STLoT)**. The physically reasonable parameters of the SLoT model remain, and the temperature-independent static disorder can still be assessed at cryogenic temperature, i.e., in the frozen disorder limit. To include the transient mechanisms, I borrow the crossover temperature T_0 as seen in the fluctuation-induced tunneling model[74] or field-induced hopping[26, 84]. The reduced activation energy of state-of-the-art polymers at high charge carrier density is typically tens of meV. Before moving on to internal causes for the crossover temperature, I want to mention a possible external field-induced energy amount given by $\Delta E = k_{\mathrm{B}} T_0$. For example, a field-induced energy amount of $\Delta E = 0.01$ eV translates to a crossover temperature of $T_0 = 116$ K. When the activation energy of a material is lower than the field-induced energy amount $W_{\mathrm{H}} = \Delta E$, it is possible that charge carriers experience field-induced "heating" of T_0. This results in a correction of the characteristic temperature-dependence which allows for a non-zero conductivity at low temperatures. Therefore, I utilize the semi-transient-localized transport model and aim to describe the entire experimental range of 10–300 K with one function. This is achieved by simply substituting the temperature T with an effective temperature $T_{eff} = \sqrt{T^2 + T_0{}^2}$. Then, for temperatures below crossover, **static disorder dominates and for temperatures above a crossover, transient mechanisms assist quasi band-like transport**. The STLoT model is given by:

$$\sigma_{\mathrm{E}}(E,T) = \begin{Bmatrix} 0, (E < E_{\mathrm{t}}) \\ \sigma_0 exp\left(-\frac{W_{\mathrm{H}}(c)}{k_{\mathrm{B}}\sqrt{T^2 + T_0{}^2}}\right) \times \left(\frac{E - E_{\mathrm{t}}}{k_{\mathrm{B}}\sqrt{T^2 + T_0{}^2}}\right), (E \geq E_{\mathrm{t}}) \end{Bmatrix} \quad (4)$$

The transport function $\sigma_{\mathrm{E}}(E,T)$ is described by $\sigma_0 \exp\left(-\frac{W_{\mathrm{H}}(c)}{k_{\mathrm{B}}T}\right) \times \left(\frac{E-E_{\mathrm{t}}}{k_{\mathrm{B}}T}\right)$ and the transient mechanisms are introduced via a crossover temperature T_0 that typically takes values below 180 K (15 meV). One advantage of the STLoT (and SLoT) formalism is that the conductivity is a direct function of the energetic disorder. The transport function in equation (4) is integrated over all available energies to obtain the conductivity in equation (6). Therefore, the transport function multiplied by the Fermi-Dirac distribution $\left(-\frac{d\mathcal{F}}{dE}\right)$ is integrated over all available energies as in equation (5)[13]. This allows me to express the temperature-dependent conductivity $\sigma_{\mathrm{STLoT}}(T)$ as a function of $W_{\mathrm{H}}, \Delta E$ and T_0.

$$\sigma_{\mathrm{STLoT}}(T) = \int_0^\infty \sigma_{\mathrm{E}}(E,T) \times \left(-\frac{d\,\mathcal{F}}{d\,E}\right) \mathrm{d}E \quad (5)$$

Integration over energies from 0 to ∞ then gives the conductivity in equation (6).

$$\sigma_{\mathrm{STLoT}}(T) = \sigma_0 \exp\left(-\frac{W_{\mathrm{H}}(c)}{k_{\mathrm{B}}\sqrt{T^2 + {T_0}^2}}\right) \times \left(\frac{\Delta E}{k_{\mathrm{B}}\sqrt{T^2 + {T_0}^2}}\right) \quad (6)$$

The activation energy W_{H} and the difference in energy levels ΔE together are necessary to describe the density of states, as shown in the energy level scheme in Figure M.1. The crossover temperature denoted by T_0 is the temperature below which static disorder dominates (and above which transport is band-like with transient disorder). Lastly, σ_0 is a temperature-independent pre-factor for the conductivity.

Proof-of-concept based on model systems P3HT:MB and PBTTT:MB

Given the above mathematical expressions, the connection to experimental observation is done by studying the characteristic temperature dependence of conductivity for two well-known model systems. The temperature-dependent conductivity curves for doped P3HT and PBTTT are shown together with curves of selected charge transport models. Therefore, around 50 nm thin films of P3HT and PBTTT are spin-coated from 10 g/l polymer solutions in 1,2-o-Dichlorobenzene (oDCB). Doping is done by immersion in an 0.6 mM Magic Blue solution in acetonitrile. The THz-TDS conductivity is measured for temperatures between 300 and 10 K and shown in Figure M.2. The THz conductivity for P3HT:MB (in red) and PBTTT:MB (in blue) is shown with fits by the (a) activated hopping model[2] (b) the heterogeneous transport[3] model

---

[2] Given by equation 4.6 in the review of Chapter 4.2.2: $\sigma_0 \exp\left(-\frac{W_{\mathrm{H}}(c)}{k_{\mathrm{B}}T}\right)$.

[3] Given by equation 4.16 in the review of Chapter 4.2.2.

(c) the SLoT model and (d) the STLoT model. The corresponding fit parameters are shown as an inset, to discuss their respective meaningfulness.

Figure (a) shows the activated hopping model described in the classical Arrhenius form with an exponent of $\gamma = 1$. Activated transport is typically used to extract the activation energy from the slope of $\ln(\sigma)$ versus T^{-1}. For the model systems, the activated transport model does not describe the entire temperature range well. For P3HT:MB activated hopping between 300 K and around 140 K transitions to a stagnant conductivity below 140 K, while the activated hopping model continues to exponentially decrease giving 0 conductivity at 0 K. For PBTTT:MB activated hopping can not describe an initial rise of the conductivity with cooling from 300 K to around 200 K. Consequently, the residual of the fit curves is high over a portion of the temperature range. **Getting the activation energy from an activated hopping model around room temperature, often underestimates the activation energy by neglecting phonon-assisted transport**. Nevertheless, using the activated transport model at specific temperature ranges is a good starting point to assess the general degree of localization.

Figure (b) shows the heterogeneous transport model in the Kaiser description as presented in Chapter 4.2.2. The limitations of this model become evident when looking at the resulting parameters. It predicts a metallic contribution of the order of 50’000 S/cm, negative crossover temperatures, and parameters that remain elusive in physical interpretation.

Figure (c) shows the SLoT model to describe the temperature-dependent conductivity of the model systems. The model under the homogeneous static disorder assumption does not describe the MB-doped polymer films well. The

SLoT model does not pick up the effective temperature-independent behavior of the model systems. Notably, even in this extreme case with a poor fit, the resulting parameters are physically plausible yielding activation energies W_{H} and energy differences to the transport edge ΔE below 0.1 eV. Comparing the two the model systems, PBTTT:MB has a higher temperature-independent conductivity σ_0, a lower activation energy W_{H}, a lower energy difference to the transport edge ΔE, and a lower crossover temperature T_0. The resulting crossover temperatures T_0 between $100-200$ K align with published values for a crossover regime in doped polymers[14-18] and the theoretically derived crossover from a variable range hopping model at high carrier density[24]. In the STLoT model, the crossover temperature is explained by transient mechanisms that play a role at high carrier density where the density of states around the Fermi energy is high. When the DOS around the Fermi energy is high, even small transient energies of 10-15 meV can screen the static disorder.

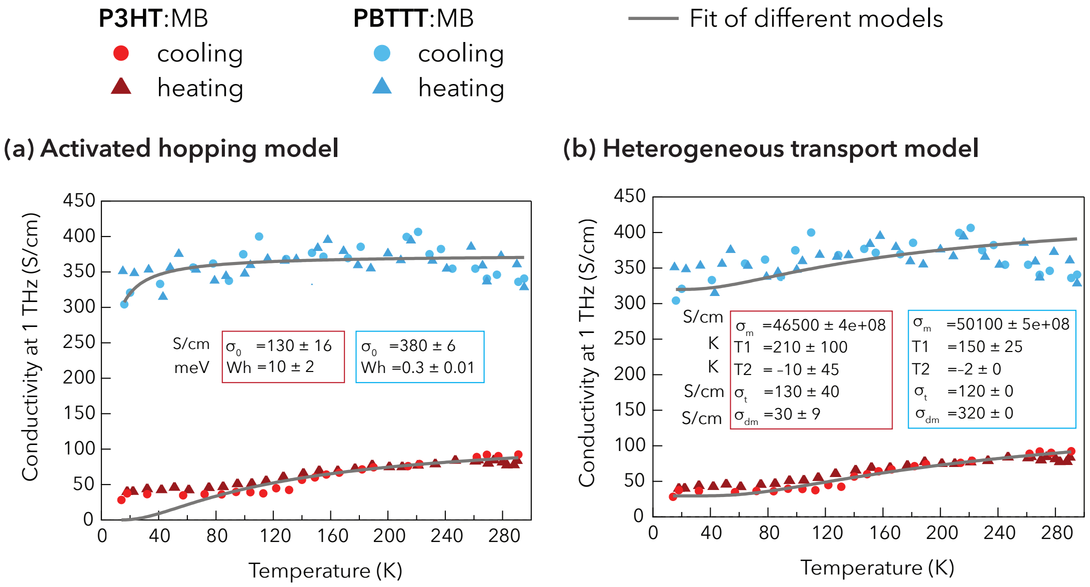

(a) Activated hopping model

(b) Heterogeneous transport model

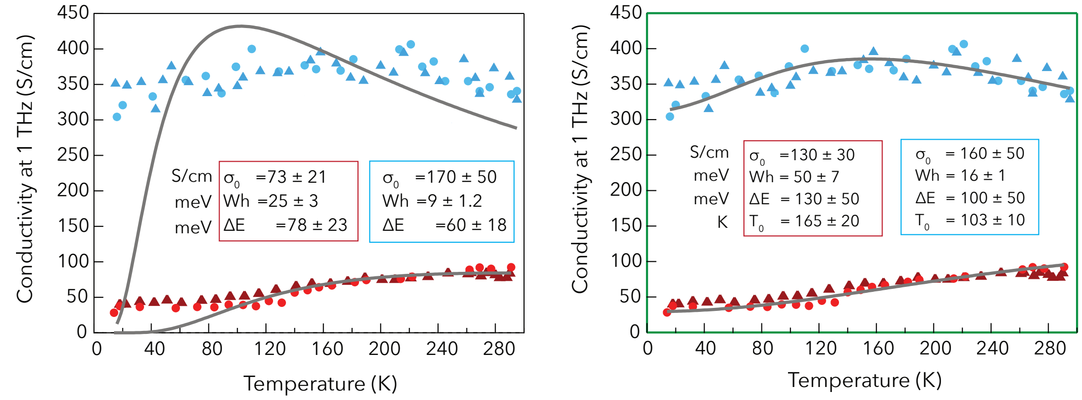

(c) Semi-localized transport model

(f) Semi-transient-localized transport model

Figure M.2. Comparison of charge transport models on experimental data of MB-doped P3HT and PBTTT. Fit parameters are shown as an inset.

7.1.3 Conclusions

This section derives the charge transport model presented in this thesis: the semi-transient-localized transport (STLoT) model. Basing on the semi-localized transport model, it is cohesively derived within the Boltzmann formalism and extended by a crossover temperature T_0 which describes transient mechanisms to charge transport including field- and fluctuation-induced hopping or tunneling. The STLoT model is successfully tested on state-of-the-art model systems of doped polymers: P3HT:MB and PBTTT:MB. The charge transport in these model systems is showing weak localization by static disorder and for temperatures above a crossover, transient mechanisms assist transport. PBTTT:MB indicates quasi band-like transport above the crossover temperature, which would need to be validated with either a coherent Hall effect or a Drude-like complex conductivity spectrum. While all models come with their limitations, the STLoT model allows for an appropriate estimatimation of the reduced activation energy W_H, the energy difference to the transport edge ΔE, temperature-independent conductivity pre-factor σ_0, and crossover temperature T_0 and is utilized in Chapter 7 of this thesis.

7.2 Anion exchange mitigates doping-induced disorder in polythiophene Pg_32T-T

Abstract

The structural and energetic disorder in conjugated polymers is a subject to doping. Doping-induced microstructural and energetic changes represent a potential limit in the conductivity of doped polymers and lack systematic understanding. The polythiophene with tri-ethylene glycol side-chains Pg_32T-T yields >600 S/cm upon doping with Magic Blue or F_4TCNQ and anion exchange doping (AED) with a delicate relationship with the employed doping method. While both dopants Magic Blue (MB) or F_4TCNQ show an individual ceiling in the conductivity of doped Pg_32T-T, AED represents a promising doping method that overcomes these ceilings and enhances the conductivity. Cryogenic THz time-domain spectroscopy and GIWAXS are used to identify the underlying differences between the doping methods. The enhancement between MB-doping and AED stems from mitigated doping-induced structural disorder. AED of Pg_32T-T yields microstructural improvements that come with a smaller activation energy to charge transport W_H, a smaller energy difference to the transport edge ΔE, and a lower crossover temperature T_0 for transient mechanisms assisting charge transport.

7.2.1 Introduction

Conductivity in doped polymers

Doped polymers are processable, flexible, lightweight and conductive materials for organic electronic applications[31, 32]. Their charge transport properties are typically governed by the doping level and by static disorder originating from their complex microstructure[33]. However, at present few well-understood strategies exist to determine and manage how doping effects the disorder, i.e. known as doping-induced disorder. Polymer films have a complex microstructure of ordered and disordered regions that determines the potential and limitation of charge transport of doping-induced charge carriers[33]. Particularly the packing in ordered regions affects the possible overlap of charge carrier wavefunctions and with it the charge transport[8, 33]. The paracrystallinity of ordered regions is typically named as the major parameter to enhance conductivity[8, 9, 33]. It is well known that molecular doping affects the paracrystallinity and with it comes the risk of doping-induced charge localization[34-39]. Besides paracrystallinity, also the size[9] and interconnectivity[33] of conductive ordered regions play a major role. Nevertheless, charge transport in disordered regions can contribute as well, whereby the distance between ordered regions, i.e. the size of the disordered regions, is overcome via tunneling or thermal activated hopping[23, 33, 40-42]. Tunneling and hopping in soft materials such as polymers can be phonon-assisted when vibrational modes of the material contribute to effective charge transport[20-23, 40, 43].

Overcoming limitations associated with p-doping

Molecular doping of polymers generates charge carriers via a redox reaction[1-5]. The ionized dopant remains in the film to stabilize the doping-induced charge carriers. Achieving high doping levels and high conductivities is not a straightforward aim. For example, let's discuss the combination of poly(3-hexylthiophene) (P3HT) and dopant 2,3,5,6-tetrafluoro-7,7,8,8-tetracyanoquinodimethane (F_4TCNQ) since it has been widely studied[2, 37, 39, 44-47]. The driving force of molecular p-doping is given by the energetic offset (ΔE) between the HOMO of the polymer and the LUMO of the dopant. The conductivity in F_4TCNQ doped polythiophenes seem to reach a ceiling when dopant intercalation disrupts the polymer packing in ordered regions[2, 39, 44-47]. The effect can be delegated using vapour deposition[2] or incremental doping concentrations[37]. Moreover, the driving force for doping with F_4TCNQ is limited by its LUMO energy level of −5.2 eV. Hence, many common polymers are not efficiently p-doped by F_4TCNQ and require stronger oxidants to reach high doping levels. To name examples, the donor-acceptor polymers based on diketopyrrolopyrrole like PDPP3T (HOMO −5.2 eV) or the conjugated polymer F8T2 (HOMO −5.5 eV) are widely used in organic electronic research but cannot be molecularly doped well using F_4TCNQ[48-52]. Stronger oxidants for p-doping, are investigated and overall improve the understanding of dopant–polymer interactions[45, 48, 53]. For the glycolated polythiophene Pg_42T-T double doping; i.e. the reduced dopant F_6TCNNQ^{-} undergoing another redox reaction to F_6TCNNQ^{2-} yielding two doping-induced carriers has been reported[54]. The development of strong oxidant tris(4- bromophenyl)ammoniumyl hexachloroantimonate (Magic Blue or MB) proved to effectively dope polymers with HOMO energy beyond −5.2 eV[48]. Magic Blue also shows spontaneous modulation doping in aligned polymer films, which improves the charge carrier mobility by selective integration of the dopant into more disordered regions[45, 55]. In spontaneous modulation doping, selective integration of the dopant hence reduces packing disruptions in the ordered regions which are essential for charge transport. Moreover, ion exchange doping is a powerful tool to exchange the radical dopant counterions after they served the redox reaction with a polymer chain[49, 56, 57]. Already the first article by Yamashita *et al.* showed an improved conductivity and coherent transport of PBTTT upon anion exchange between F_4TCNQ^- and $TFSI^-$ from the electrolyte LiTFSI[56]. The role of the counterion size and location have been investigated since with the observation that counterion size plays a minor role, while conductivity increases together with a reduction in structural and dynamic disorder[8, 58]. Structural disorder in doped polymers represents chain misalignment, chain torsion, disruption and variation in stacking distances. Dynamic disorder represents transient fluctuation of the electronic coupling between molecular units because of vibrational modes. Simply put, **small disorder leads to weak localization of charge carriers**. Recently in 2024, Lu *et al.* pointed out structural changes and an increase in face-on orientation in Pg_32T-T films at high doping levels[59]. These structural changes lead to a decrease in mobility and hence conductivity, which is referred to as “over doping”. Molecular doping, especially in polythiophenes sensitive to “over doping”, are accompanied with structural changes that induce localization. Anion exchange doping is considered a two-step process of doping (driven by ΔE) and subsequent exchange of ions (driven entropically by grand excess of stable ions)[49, 56, 57]. Yet, the electrolyte might affect the polarity of the doping solution, doping rate, and hence the resulting degree of disorder. To conclude this section, the use of strong oxidant Magic Blue and **anion-exchange doping might improve doping-induced limitations regarding charge localization** while maintaining a high number of charge carriers.

Charge carrier formation in structural regions

In polymers[4], singly charged [+] and doubly charged [++] quasiparticles are the entities through which charge transport is accomplished. The quasiparticles are referred to as polaron and bipolarons respectively. Atoms in the polymers matrix move as these particles drift along the chain which results in an increment in the effective mass of the charge carrying particles. As such, the polymer matrix influences the localization of polarons and bipolarons.

Molecular doping happens on the seconds time-scale. The assignment of absorbance bands to polaron and bipolaron species remains a topic of discussion[60-63]. Electron paramagnetic resonance supports the assignment and correlates the bands with the para- and diamagnetic nature of polarons and bipolarons[42]. I did not do a spin-confirming (EPR) or Coulomb counting experiment in this study. However, as far as common polythiophenes are concerned, the assignment to polarons and bipolarons as reported is reasonable[62, 64, 65]. Therefore, the dynamic changes in the absorbance of particular bands carry valuable information on the formation of [+] and [++]. The formation of [+] and [++] absorbance bands can be estimated by time-resolved steady-state absorbance. During doping the neutral absorbance band depletes. The formation of [+] and [++] absorbance bands happens at different rates and in different regions as seen by in-situ Raman spectroscopy in electrochemical[66] and molecular doping[67]. These findings show on the model system P3HT, that the doping process is significantly different in the ordered and disordered polymer regions. As a result, [++] are formed faster and are thermodynamically more favored in disordered polymer regions. The

---

[4] With the exception of polyacetylene.

[+] formation results in an increased effective conjugation length and in planarization of the charged chain segments, in contrast to [++] formation which results in a decrease of the effective conjugation length and in an increased amount of disorder.

Material choice and doping method

The ceiling in conductivity for molecular doping of a state-of-the-art polythiophene Pg$_3$2T-T is investigated. The interconnectivity of doped Pg$_3$2T-T films is estimated by comparing macroscopic- Long$\boldsymbol{\sigma}$ (>1 mm) and nanoscale- Short$\boldsymbol{\sigma}$ (<100 nm) conductivity. The ordered regions are characterized by grazing incident wide-angle X-ray scattering (GIWAXS). The delicate relationship between molecular doping and structural changes in ordered regions is highlighted. The dopant and electrolyte concentrations are optimized to yield high conductivity using electrical four-point probe, cryogenic THz time-domain spectroscopy (THz-TDS), GIWAXS and steady-state absorbance, also measured "in-situ" during molecular doping to capture the doping rates with millisecond resolution. Besides the interconnectivity and conductivity also the degree of localization of doping-induced charge carriers is estimated by the complex conductivity (by THz-TDS), the reduced activation energy (W_H) and the energetic term $(E - E_t)$. Figure P.1. shows the energy levels and chemical structures for the investigated polythiophene Pg$_3$2T-T and the dopants F$_4$TCNQ as well as Magic Blue. It shows the molecular structure of the electrolyte TBAPF$_6$ used for anion exchange doping. It also shows two schematic insets: First, the doping mechanism in anion exchange. For anion-exchange doping, a polymer film is immersed in a doping solution that contains the dopant and an electrolyte. The doping solution is with an orthogonal solvent, that swells the polymer. Charge transfer between the dopant and the polymer occurs resulting in a positively charged polymer site and a negatively charged radical dopant ion. The radical dopant anion is exchanged with a more stable electrolyte anion. The orthogonal solvent of choice here is acetonitrile, because it is redox stable over a large window and swells the polythiophenes sufficiently. The second scheme in Figure P.1. shows the trend of conductivity with increasing concentration of MB-doping concentration. In polythiophenes the conductivity increases with increasing MB-doping concentration until an optimum conductivity. When the doping concentration increases further upon the optimum the conductivity starts to decrease. This decrease could be due to sub-band filling (localization) or due to doping-induced structural changes. The effect can be mitigated by anion-exchange doping supporting the latter: doping-induced structural changes with MB. Anion exchange doping using the strong oxidant Magic Blue and the electrolyte $TBAPF_6$ leads to high doping levels and high conductivities in polymers. This work showcases the optimum conductivity and its origin in Pg_32T-T doped with Magic Blue and anion exchange with PF_6^- reaching high charge carrier density ($N>10^{21}$) and high conductivity (600 S/cm). This means almost every polymer site is charged. The effect of anion exchange doping and high doping levels in general on the conductivity, charge transport and the localization of charges in polymers can be observed directly with temperature-dependent conductivity measurements. The cryogenic THz-TDS experiment is suggested as a powerful tool to observe the characteristic temperature-dependent conductivity and degree of localization simultaneously.

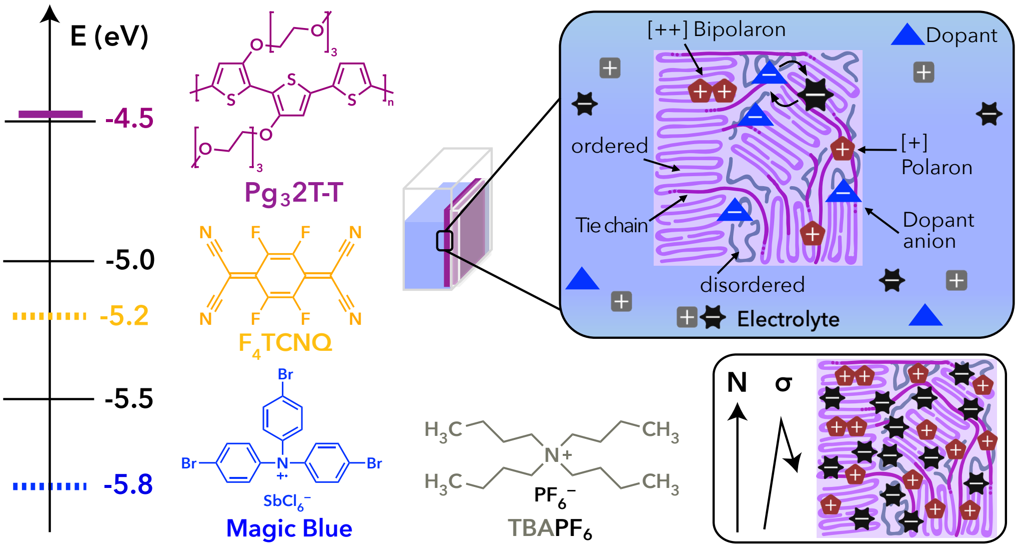

Figure P.1. Energy levels and chemical structures of polymer Pg$_3$2T-T (HOMO −4.46 eV) and dopants F4TCNQ (LUMO −5.2 eV) as well as Magic Blue (LUMO −5.8 eV). Chemical structure of TBAPF$_6$ used for anion exchange. Scheme of doping as well as increasing number of doping-induced charges N leads to increasing conductivity until a point of optimum. Further increase in N leads to drop in conductivity.

7.2.2. Results and Discussion

The ceiling in conductivity based on dopants

The steady-state absorbance of neat and doped Pg$_3$2T-T is depicted in Figure P.2. Doping with Magic Blue (a) in comparison to doping with F$_4$TCNQ (b) shows different ceilings in the resulting doping level and conductivity. The absorbance and corresponding conductivity are shown for three representative doping levels. All films shown here were immersed in the doping solutions for 200 seconds. In both panels the purple curve shows the neat polymer Pg32T-T absorbance with a band around 525 nm. In (a), upon doping with 110 µM MB in acetonitrile, the 525 nm band is almost fully depleted. The bands corresponding to the charged species red-shifted from the bandgap become evident. The transitions corresponding to the singly charged species, polaron [+] occur at 850 nm and at 2500 nm. In (a), with a higher doping concentration of 285 µM MB, the bandgap is fully depleted and the ratio between the [+] band at 850 nm and the absorbance in the NIR changes. The change in the ratio is attributed to the formation of doubly charged species. The transition corresponding to the doubly charged species, bipolaron [++] occurs in the NIR and the ratio between mentioned features [825 nm]:[2500 nm] changes from 0.45:0.6 (or 1:1.33) to 0.45:0.65 (or 1:1.44). The [++] band is broad and difficult to deconvolute from the [+] transitions. However, the highest doping concentration of 570 µM MB shows a depletion of the [+] band at 850 nm indicating that the absorbance comes dominantly from doubly charged species. This doping level comes with an increase in [++] absorbance and a decrease in conductivity to 130 S/cm; which is referred to as “over doping”. The **ceiling for conductivity for MB-doping is 390 S/cm**, where the bandgap is fully depleted while the formation of [++] is intermediate.

In Figure P.2. (b) the doping concentration of 570 µM F_4TCNQ shows a remaining band from neutral polymer sites at 525 nm. The [+] bands are present. The absorbance of the bands at 800 nm and 2500 nm is 0.45 with a ratio between the bands of about 1:1. Moreover, the peaks at 420 nm, 760 nm and 860 nm are stemming from ionized F_4TCNQ^- in the doped films[54, 68]. At this doping level, the absorbance from [++] is neglectable and the conductivity is 80 S/cm. Increasing doping concentration to 465 µM and 600 µM fully depletes the neutral band at 525 nm. These two doping concentrations lead to stagnant doping level shown by identical absorbance. Notably, the study of Lu *at al.* finds a comparable ceiling for the conductivity in Pg$_3$2T-T with FeCl$^-$ doping than I do with MB-doping[59]. This ceiling is likely related to similar structural changes, which we will see in microstructural characterization later.

At these doping levels the ratio of [825 nm]:[2500 nm] is 0.5:0.65 (or 1:1.33), so lower than for both blue curves in (a) of 110 µM and 285 µM MB. While the ratio between the absorbances at [825 nm]:[2500 nm] could be an indicator for an optimal balance between charged species [+]:[++], in this thesis, I am only referring to it for practical reasons to describe the shape of the absorbance. The **conductivity for F$_4$TCNQ-doping reaches a ceiling at 290 S/cm**. In this study, the conductivity with increasing doping concentration of F$_4$TCNQ plateaus in conductivity. There is no drop in conductivity for even higher dopant concentrations in this case.

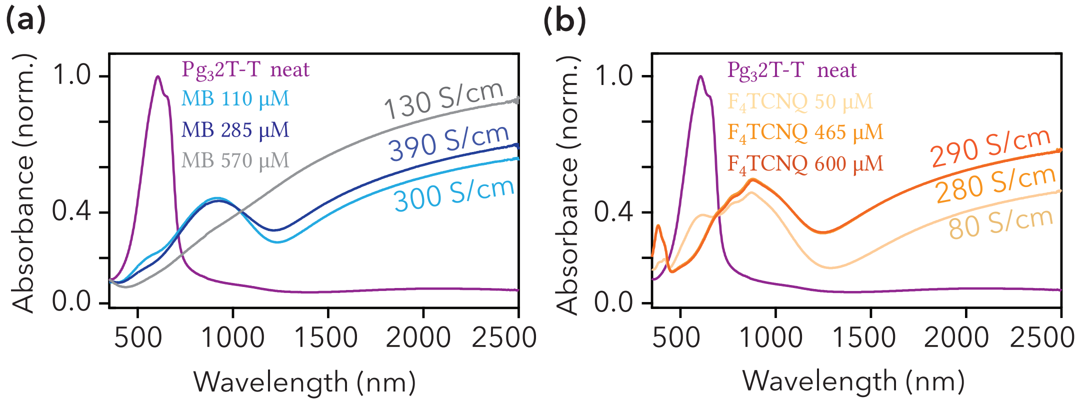

Figure P.2. Steady-state absorbance spectra of Pg$_3$2T-T upon doping with (a) MB or (b) F$_4$TCNQ.

Anion exchange overcomes the ceiling in conductivity

For AED-doped films, the driving force of the process is still determined by the HOMO–LUMO energy difference between polymer and dopant. Thus, the doping level does not alter much as seen by similar absorbance spectra in Figure P.3. The Figure shows absorbance spectra for anion exchange doping using the optimum dopant concentrations determined in the previous section. In (a) a dopant concentration of 285 µM MB with varying electrolyte concentration between 40 mM and 385 mM $TBAPF_6$. In (b) a dopant concentration of 600 µM F_4TCNQ with varying electrolyte concentration between 75 mM and 775 mM $TBAPF_6$. Note how all electrolyte concentrations are of great excess in comparison to the dopant concentration. The excess is at least 100 times of the dopant concentration to ensure an efficient exchange equilibrium[57]. The anion exchange doped films show very similar absorbances. The anion exchange only alters the ratio between the bands associated with [+] and [++] slightly. What is interesting is that in (a) for MB-doping the absorbance of the immersed doping (ID) film without anion exchange is below all others. In (b) for F_4TCNQ-doping the absorbance of the ID film without anion exchange doping is above all others in the wavelength range below 1200 nm. I associate this residual absorbance to the ionized F_4TCNQ^- as mentioned in the previous section. Based on the $F4TCNQ^-$ peaks in the visible and the 100 times excess of electrolyte over dopant, I assume a full exchange efficiency. The absorbance in the IR region, above 1200 nm, for the ID film again is below all others. The fact that this residual absorbance of the ionized F_4TCNQ^- disappears with anion exchange doping is reassuring a complete anion exchange to $PF6^-$, which does not absorb in the measured UV-NIR range. All anion-exchange doped films here have an absorbance with a ratio of approximately 0.45:0.7 (or 1:1.55). There is a slight difference in the absorbance around 1400 nm. Perhaps the bipolaron [++] contribution is easier to read, where the two polaron [+] bands have a valley. Figure P.3. panels (c) and (d) show conductivities corresponding to the absorbances in (a) and (b). The conductivity is plotted against the electrolyte concentration in the anion exchange doping solution. The conductivity at 0 mM electrolyte concentration again is showing the ceiling in MB-doping of 390 S/cm and the ceiling in F_4TCNQ-doping of 290 S/cm. **All anion exchange doped films lie above those ceilings**. There is an optimum electrolyte concentration for anion-exchange doping that yields conductivity of >600 S/cm. The optimum electrolyte concentration is different for MB-doping and F_4TCNQ-doping. It is highlighted in pink color in Figure P.3. (a)-(d). The optimum electrolyte concentration is 115 mM for MB-doping and 575 mM for F_4TCNQ-doping. The quotient between the optimum electrolyte concentration (Figure P.3) and the optimum dopant concentration (Figure P.2.) is calculated. For MB this quotient is (115 mM)/(285 µM)≈400 and for F4TCNQ this quotient is (575 mM)/(600 µM) ≈960. The quotient that is typically recommended in literature is >100, while the optimization based on conductivity here gives higher electrolyte concentrations. The method of anion exchange doping might not change the general driving force, but the electrolyte affects the polarity of the solvent in which the polymer film sits for 200 seconds. This could be an explanation for the high electrolyte concentration optimum. The polarity of the solvent changes the swelling of the polymer film, and potentially the doping kinetics. Time-resolved absorbance during the doping process shows the rate at which the neutral band depletes and the [+] and [++] bands increase. Indeed, the doping kinetics become slower with increasing electrolyte concentration in AED. Time-resolved absorbance and the doping rates are shown in the supplementary section S.1. Differences in swelling and the doping rates might affect ion intercalation and the resulting microstructure. To summarize the findings of Figure P.3., when starting from optimized dopant concentrations that reach a ceiling in conductivity, AED improves the conductivity even more.[5]

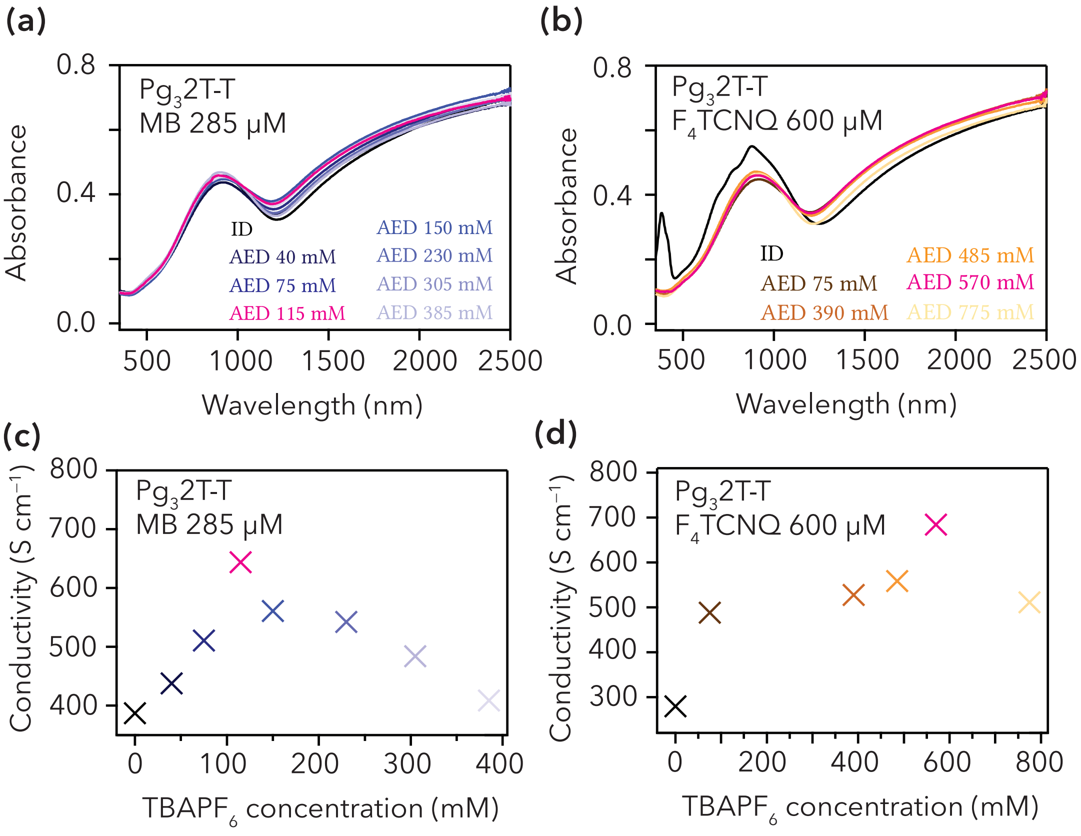

Figure P.3. Steady-state absorbance spectra of Pg$_3$2T-T upon doping with (a) MB or (b) F$_4$TCNQ. Here, with anion exchange doping varying the electrolyte concentration. (c) and (d) show the conductivity for the films that correspond

---

[5] Thanks to this insightful doping optimization during Maximilian Horn's Master project, I went on to investigate doping-induced disorder in Pg$_3$2T-T to understand the mitigation effects upon anion exchange.

to the absorbance spectra. The film with optimum conductivity >600 S/cm is highlighted in pink.

Next, Figure P.4. shows that starting from an "over doping" MB-concentration, AED also improves the conductivity. This means AED can mitigate doping-induced limitations that otherwise lead to over doping. Figure P.4. shows the steady-state absorbance spectra of slightly over doped polymer films with MB and anion-exchange of MB. It also shows F_4TCNQ and anion-exchange of MB, where no over doping is observed. The dopant concentrations were not more than 5% higher than the previous optimum, so approximately 300 µM MB and 630 µM F_4TCNQ. The AED concentrations are 115 mM and 575 mM $TBAPF_6$. Figure P.4. visualizes that also for "over doping" the anion-exchange improves the conductivity to 570 S/cm. Optimized anion-exchange doping, as presented here, leads to an intermediate ratio between the NIR and the visible absorb-ance. Doped Pg$_3$2T-T films which show the optimum conductivity, occur to have an absorbance spectrum in between the solid orange and magenta curves in Figure P.5. Here, the absorbance spectra are scaled to have an intuitive comparison between the NIR and Vis

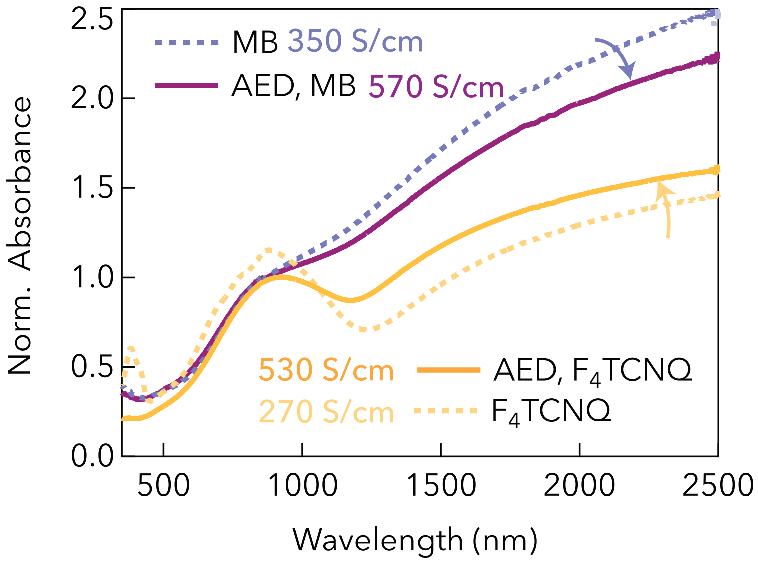

Figure P.4. Absorbance spectra for Pg$_3$2T-T comparing doping methods.

absorbance. For spectroscopists these absorbance spectra can be a first guide to optimize doping in Pg$_3$2T-T in the future. To investigate anion-exchange doping and its optimum with electrolyte concentration more, GIWAXS[6] is utilized in the next section. This technique provides the microstructural key parameters of the ordered conductive regions. The microstructural changes upon MB-doping and anion exchange will be clarified as well as the role of the electrolyte concentration. After, the doping-induced disorder can be investigated by cryogenic THz-TDS, reconnecting the microstructure to charge localization and activation energy for charge transport.

Comparison between MB-doping and anion exchange doping

Conductivity optimum corresponds to paracrystallinity

The pristine Pg$_3$2T-T films, MB-doped films and AED doped films with varying TBAPF$_6$ electrolyte concentrations are characterized by GIWAXS[7]. Figure P.5. shows GIWAXS 2D images representing these films. At least three replicates of neat and doped Pg$_3$2T-T films are averaged to obtain the averaged paracrystallinity disorder and peak area, because there are significant salt peaks from the electrolyte in the anion-exchange doped images. The (100) peak corresponds to the lamellar stacking direction. This peak helps identify the orientation of the chains relative to the substrate. When focusing on the (100) orientation in the patterns, the results show

---

[6] The following sections shows MB doping exclusively. The cryogenic THz results from both dopants can be found in the supplementary section S.5.

[7] The F$_4$TCNQ films are also characterized by GIWAXS, but I did not receive the results in time, and F$_4$TCNQ was done on a Pg$_3$2T-T batch with minor differences. The Pg$_3$2T-T batch shown here is identical with all Pg$_3$2T-T results presented in Chapter 7.2 and 7.3.

mostly edge-on orientation. As a reminder, a scheme of edge on and face-on assembly on the substrate is shown in Figure P.6. (a). the orientations of polymer chains (edge-on and face-on) in a thin film are distinguished by the direction of their π-stacking and alkyl stacking relative to the substrate. These orientations are critical for understanding charge transport and molecular packing in conjugated polymers like polythiophenes. The edge-on population corresponds to polymer chains oriented with their π-stacking direction (conjugated backbone) perpendicular to the substrate, while the side chains lie parallel to the substrate. The π-π stacking peak appears along the out-of-plane direction (q_z), close to the meridional axis. The face-on population corresponds to polymer chains oriented with their π-stacking direction parallel to the substrate, and the side chains extending perpendicular to the substrate. Then, the π-π stacking peak appears in the in-plane direction (q_{xy}). However, upon doping a weaker face-on population and structural changes occur. In the MB-doped film (b) this leads to a halo around the q_{xy} centre. For the AED films this feature decreases again. As a result, AED with 40 mM $TBAPF_6$ concentration is more similar to the pristine film (c) and (a) than the MB-doped film (b). These findings are in accordance to the face-on population seen with MB-doping of the same polymer for "over doping" in this recent article[59]. This structural changes explain the ceiling in conductivity upon doping with MB. Moreover, upon anion exchange, this feature is improved, which explains that AED overcomes this ceiling. A comparison between the different electrolyte concentrations also indicates the origin of the optimum in conductivity. Therefore, the paracrystallinity disorder is calculated and shown in Figure P.6. (b). When calculating the paracrystallinity disorder from the presented GIWAXS 2D images, there is a clear minimum in structural disorder for one electrolyte concentration. The electrolyte concentration which shows an optimum in conductivity corresponds to a significant drop in paracrystallinity disorder to <5%. The paracrystallinity disorder for other electrolyte concentrations is around 10%.

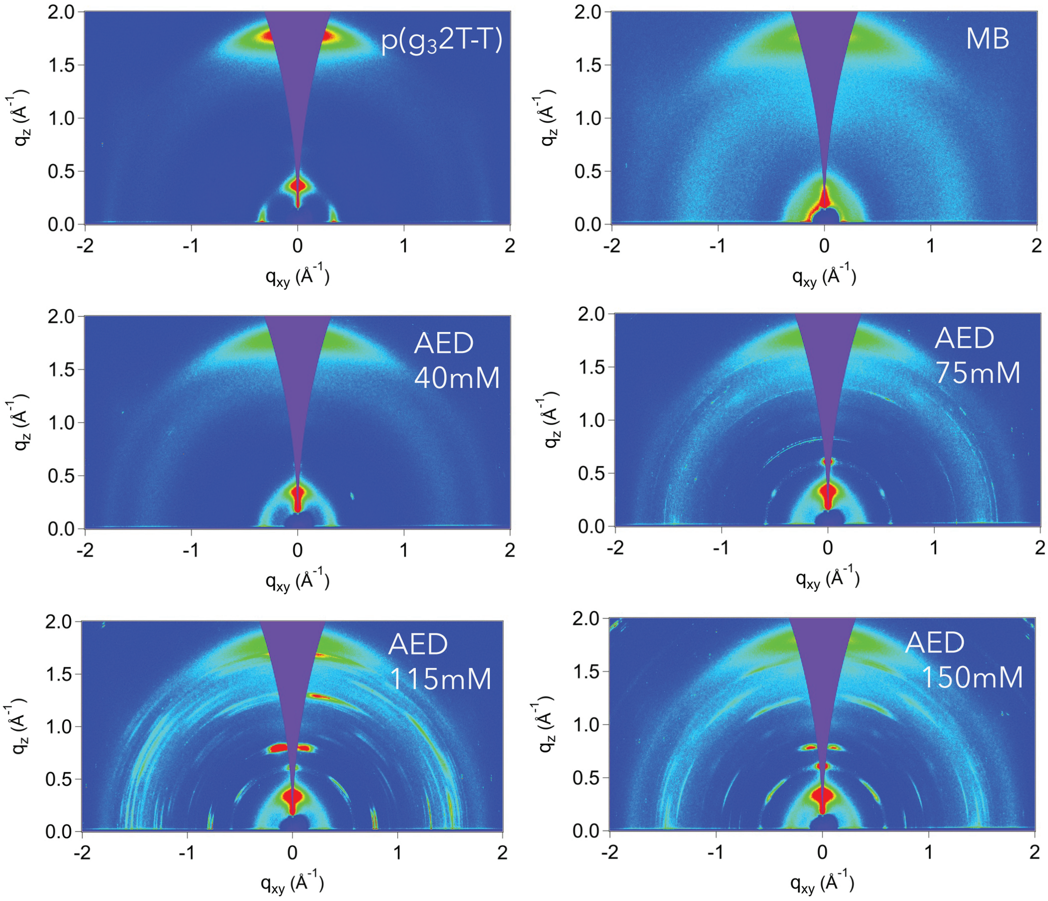

Figure P.5. GIWAXS 2D images for (a) pristine Pg32T-T, (b) MB-doped and (c-f) MB-doped with anion exchange varying the electrolyte concentration.

This means that **all electrolyte concentrations mitigate the negative effect from MB over doping**. The other electrolyte concentrations have a similar paracrystallinity to the pristine films. The improved disorder of < 5% is reproducible between three replicates doped with this electrolyte concentration. The Figure P.6. (b) also shows integrated (100) peak areas. The (100) peak area, representing lamellar stacking, decreases by more than 80%

upon MB-doping compared to the pristine Pg32T-T. The (100) peak area continuously increases from this low value with increasing electrolyte concentration. The (100) peak area keeps increasing with electrolyte concentration above the identified conductivity optimum.

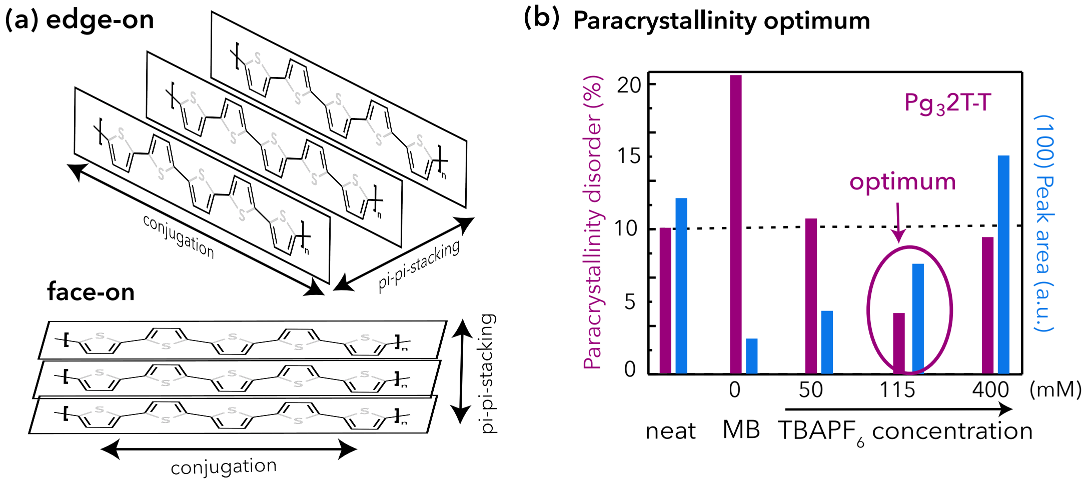

Figure P.6. (a) edge-on versus face-on orientation, (b) optimum in paracrystallinity disorder at 115 mM. (c) complex conductivity of MB versus AED, (d) DSM fit parameters show optimum in effective mobility.

All so far presented findings point into the direction of an optimum in the doping-induced localization with carefully optimized anion exchange doping. The excellent interconnectivity of conductive regions, the optimum in conductivity and paracrystallinity indicate benefit the degree of localization upon anion-exchange doping method of Pg32T-T. Next, I aim to estimate the doping-induced disorder and its improvement upon anion exchange doping in terms of activation energies to transport.

Doping-induced disorder observed by cryogenic complex conductivity

A closer look at THz conductivities and temperature-dependent conductivity by cryogenic THz-TDS determines the degree of interconnectivity and degree of localization of charges for different doping methods of Pg$_3$2T-T. For this measurement series, I use the previously determined optimized doping methods (or ceilings): (i) Pg$_3$2T-T doped with 285 µM MB, (ii) doped with 285 µM MB and anion exchange with 115 mM TBAPF$_6$, (iii) doped with 575 µM F$_4$TCNQ and (iv) doped with 575 µM F$_4$TCNQ and anion exchange with 575 mM TBAPF$_6$. The following Table P.1. shows the film thickness d, the macroscopic (>1 mm) conductivity Longσ , the nanoscale (<100 nm) conductivity Shortσ from THz-TDS (before the cryogenic measurements) at room temperature. As such, the quotient Longσ/Shortσ is an estimate for the interconnectivity over macroscopic distances and it is close-to-unity in both doping methods. Pg$_3$2T-T at high doping levels shows an excellent interconnectivity.

Table P.1. Comparison of interconnectivity by doping method showing the quotient between Longσ/Shortσ.

Quantity Units	d nm	Longσ S/cm	Shortσ S/cm	Longσ/ Shortσ	Color code
MB	42	350	375	95%	🟦
MB, AED	39	570	570	99%	🟪

Again, the values confirm the ceiling in conductivity with MB-doping, while the interconnectivity is excellent for all films. The interconnectivity is also not reduced in the MB, AED film that previously shows the worsened paracrystallinity disorder and a smaller (100) peak area. This indicates that the doping-induced structural changes do not inhibit interconnectivity for effective macroscopic charge transport at room temperature. However, temperature-dependent conductivity is a very sensitive technique to study disorder in terms of the reduced activation energy. The smaller the activation energy, the weaker the localization of charge carriers. **A small activation energy leads to a weak temperature-dependent conductivity, while a big activation energy leads to a quickly decreasing conductivity with cooling**. Figure P.7. (a) shows the temperature-dependent THz conductivity for Pg$_3$2T-T wit MB-doping and with AED. It is immediately evident that the doping method has a strong influence on the shape of the curves. Figure (b) shows the same curves normalized at room temperature, which emphasizes the differences in their temperature-dependence even more. Therefore, the relative real conductivity $\boldsymbol{\sigma_{Re}}(10\ \mathrm{K})/\boldsymbol{\sigma_{Re}}(295\ \mathrm{K})$ is introduced as an intuitive key parameter. For MB-doping the real conductivity yields 50% at 10 K in comparison to room temperature. For AED-doping the real conductivity yields 65% at 10 K. Both values are supporting a weak activation energy and a deviation from pure hopping type transport.

The effect of MB-doping leads to a relatively stronger temperature-dependence. MB-doping which we have assigned to have negative structural effects has a more pronounced conductivity decrease with lower temperatures. I relate the structural changes to an increase in the activation energy (energetic disorder) which in turn leads to a strong temperature-dependence. Here, anion exchange mitigates or even improves the structural changes which is seen in a weaker temperature-dependence. Figure (c) shows the corresponding steady-state absorbance spectra normalized at 860 nm. As a reminder of the absorbance presented earlier, which was related to “over doping” with MB.

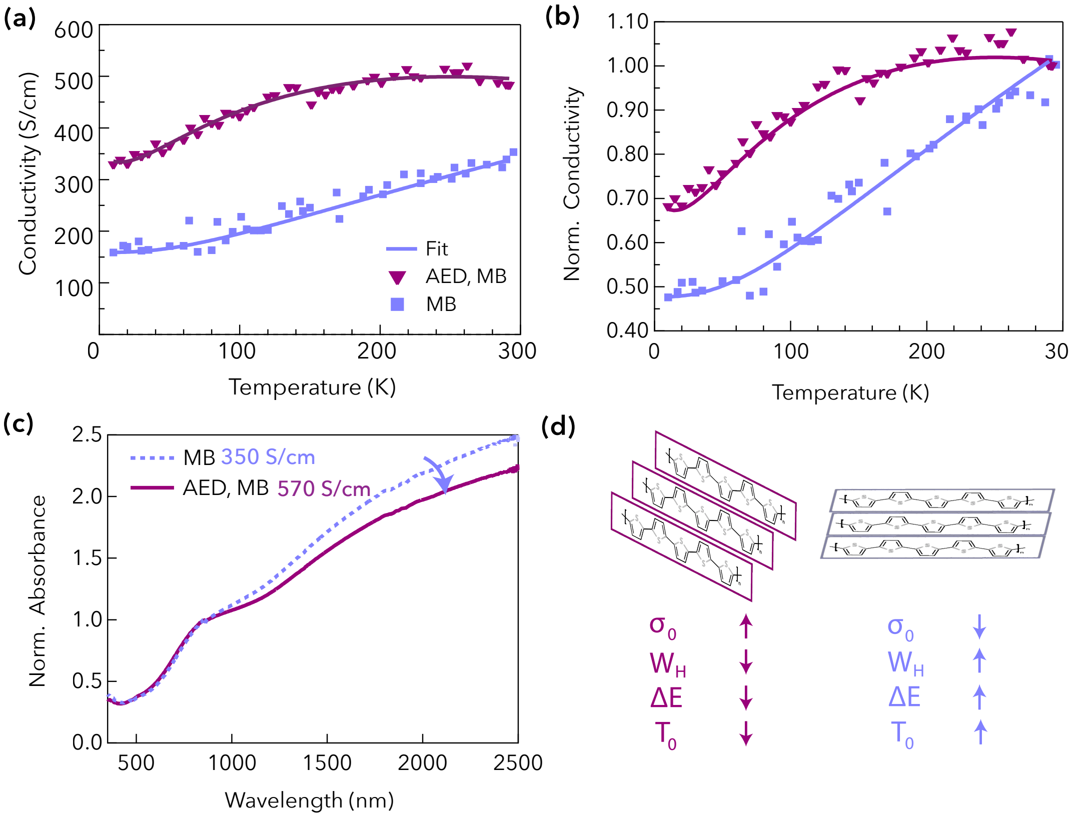

Figure P.7. (a) Conductivity versus temperature of MB- and AED- doped films. (b) Conductivity normalized at room temperature. For (a) and (b) the solid lines are a fit to equation. (c) Absorbance of polythiophene with different doping methods.

The solid lines in (a) and (b) are fits with the proposed STLoT model given by equation (6). The charge transport model matches the experimental findings well and allows me to extract the parameters of interest. To estimate the doping-induced disorder, the STLoT model yields three parameters. The reduced activation energy (W_H) for hopping states, the energy difference to the transport edge (ΔE) and the crossover temperature (T_0) for transient mechanisms (such as tunneling, transient localization by vibrational modes and/or field-induced charge carrier heating collectively) above which the transport is indistinguishable from band-like transport. Moreover, the conductivity scales with a temperature-independent pre-factor $\boldsymbol{\sigma_0}$. The fit parameters are given in Table P.2 together with an estimated error from the model residuals but at least 20%. **First, MB driven "over doping" and the corresponding structural changes lead to an increased activation energy** as expected. The resulting activation energy W_H for MB-doping (40 meV) is reduced by AED (30 meV). The conductivity scales with a negative exponential of the activation energy so W_H has a big influence. Not only on the absolute conductivity value but also on the decline of the temperature-dependent conductivity.

Table P.2. Fit parameters for semi-transient localized transport model. Estimated error of >20%.

Quantity Units	σ_0 S/cm	T_0 K	W_H meV	ΔE meV	Color code
MB	300± 60	180± 40	40± 10	130± 20	🟦
MB + PF_6^-	420± 90	150± 30	30± 4	100± 20	🟪

It leads to an increased crossover temperature T_0. That can be interpreted in combination with the activation energy and separately. Naturally, when the activation energy is big and dominated by static disorder, transient mechanisms do not contribute to transport at low thermal energy. Separately from the activation energy, one can imagine that the face-on orientation and its difference in environment might influence transient mechanisms directly. Vibrational modes are governed by the sub-nanometer arrangement and not the microstructure. A systematic understanding of fluctuation-induced transport mechanisms is yet to be built. It would be highly interesting to study the crossover temperature on a well-known model system systematically. In general crossover transitions are usually identified by different exponents in hopping type models. Then one exponent is used for one temperature range and another exponent is used for another temperature range. In this case it marks a transition from hopping-like to band-like based on transient mechanisms. MB-doping also yields a higher energy difference to the transport edge ΔE than the AED doped material. When the energy difference is high, the DOS is broadened. In a broadened density of states charges get localized in tail states and have a big energy difference to contribute to transport (transport edge). The temperature-independent pre-factor σ_0 is not lower within the error. Notably, all extracted fit parameters yield reasonable values. For the investigated state-of-the-art polymer at high doping levels, reasonable parameters are on the order of: 0−100 meV for the reduced activation energy and below 1 eV for the energy difference. Figure P.7. (d) shows a visual summary of the findings achieved with the presented model related to MB “over doping”.

To connect the identified doping-induced disorder with the corresponding mobility of charge carriers, I utilize THz-TDS in combination with DSM analysis. The THz conductivity for MB-doping and AED-doping is compared at room temperature and at cryogenic temperature. Figure P.8. shows the THz conductivity at 295 K and 10 K for (a) MB-doping and (b) AED. The real part of the complex conductivity is shown as a solid line above zero. The panels are plotted on the same axis scale for easy comparison. The real part at room temperature increases from (a) MB to (b) AED by the same factor as discussed earlier. The imaginary part of the conductivity is shown as a dashed line and lies below zero. The imaginary part does not scale with the same factor as the real conductivity does. The imaginary part is flatter and closer to zero for AED-doping. **This imaginary part in relation to the real part indicates less charge localization and a higher mobility**. The light blue curves show the THz conductivity at cryogenic temperature. Still comparing the doping-methods, but at low temperature the same trend occurs: an increased real part and a smaller close-to-zero imaginary part with AED doping. The trend of the THz conductivity with cooling is very interesting. In both samples the real and imaginary part decreases. For MB-doping the imaginary part decreases more and becomes steeper at 10 K. To obtain the charge mobility from the THz conductivity, the DSM is used. The tightly dashed lines in (a) and (b) represent the DSM fits of the data.[8] Figure P.8. (d) shows the mobility obtained from the THz conductivity at room temperature on the right-hand-side and at 10 K on the left hand-side. The percentages show the intuitive parameter of the relative real conductivity $\sigma_{Re}(10\ \mathrm{K})/\sigma_{Re}(295\ \mathrm{K})$. The number of charge carriers thereby remains constant at a high density of around 5×10^{21} cm^{-3}. The mobility at room temperature of Pg$_3$2T-T doped with (bottom right) MB is 0.4 cm^2/Vs and it improves to (top right) 0.6 cm^2/Vs with AED. At low temperature, one speaks of the frozen disorder limit. In the frozen disorder limit, the doping-induced disorder is even more visible. The mobility, in the frozen disorder limit, drops to 0.2 cm^2/Vs with MB-doping. AED due to its lower activation energy and lower energy difference to the transport edge is less temperature-dependent and has a mobility of 0.4 cm^2/Vs. All DSM fit parameters are summarized in the supplementary tables S.3.1 and S.3.2. To complement the STLoT model, I also conducted the well-established Zabrodskii analysis described by equation (3). To extract the Zabrodskii plot

---

[8] The Drude-Smith model analysis and its limitations is not shown repeatedly. I refer to Chapter 5 “Spectroscopy and Methods” or the supplementary S.0.

slope (degree of localization) and the corresponding energy in meV, the temperature range needs to be separated in different regimes. This separation in literature is very common and it supports the implication of a crossover temperature earlier. In literature, the crossover temperature represents a transition from Mott to Efros-Shklovskii (ES) hopping type transport. This interpretation of the crossover temperature is not feasible for the presented doped polymer films, because of the high conductivity retained at low temperature $\sigma_{Re}(10\text{ K})/\sigma_{Re}(295\text{ K})$. The temperature-dependent conductivity does not support a crossover from one hopping transport to another hopping transport with the given systems. Therefore, a crossover from Mot to ES transport can be ruled out. For all temperature regimes, the Zabrodskii analysis for MB-doped Pg$_3$2T-T shows small negative slopes. Small negative slopes represent very weakly localized charge carriers. In the low temperature regime (frozen disorder limit) the localization is bigger than at room temperature. At all temperatures, the localization here is below 1 meV. Since the Zabrodskii analysis is not separating static disorder in hopping states and transient disorder in band-like states, and explicitly includes the positive contribution of the latter, the resulting overall efactivation energy is much lower. This energy represents the effective activation of static and transient mechanisms together. The Zabrodskii analysis confirms weakly localized charge carriers, and it confirms the slightly increasing localization in the frozen disorder limit. This confirms the necessity of a crossover temperature. Quasi delocalized transport without the crossover T_0 to static disorder hopping would manifest in the opposite trend, i.e. more delocalized at low temperature, because scattering events limiting delocalized transport decrease with cooling. A fully delocalized transport also does not correspond to the negative imaginary parts and the resulting mobilities. The weakened localization around room temperature likely comes from transient transport mechanisms that are suppressed in the frozen disorder limit. The transient mechanisms that contribute to band-like transport above T_0 can include tunneling, electron-phonon coupling and/or field-induced hopping. However, **the flat s-shaped temperature-dependence indicates a crossover temperature where static disorder dominates** rather than delocalized transport. This aligns better with the observation of a weak localization that slightly increases with cooling.

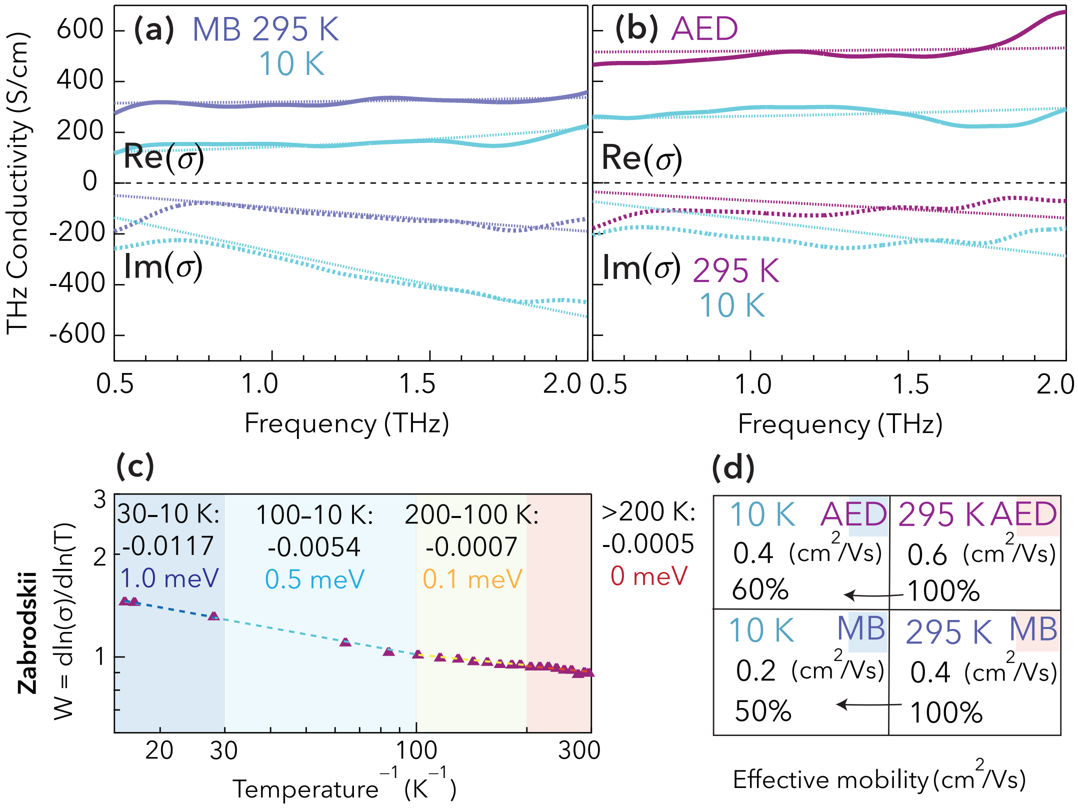

Figure P.8. Complex THz conductivity of Pg32T-T doped with (a) MB and (b) AED. (c) Zabrodskii analysis of the temperature-dependent conductivity for the MB doped material. (d) Effective mobility and percentage of σ_{Re}(10 K)/σ_{Re}(295 K).

This is further backed up by a negative imaginary THz conductivity that is decreasing with cooling and the resulting mobility. For the energetics these observations imply a **high density of states near the Fermi level** such that temperature changes do not significantly influence the availability of states for conduction.

7.2.3. Conclusion

The impact of doping methods on the complex conductivity and charge transport properties in a state-of-the-art polythiophene Pg_32T-T is studied. For this polythiophene, “over doping” with the strong oxidant Magic Blue occurs which decreases conductivity, increases structural disorder, and a face-on population in the microstructure. This introduces a ceiling in conductivity for MB-doping in this polythiophene Pg_32T-T of around 390 S/cm. Anion exchange doping optimizes the microstructure and shows lower doping-induced disorder and improved lamellar stacking. This leads to a conductivity reaching 600 S/cm. Anion-exchange with PF_6^- overcomes the ceiling in conductivity for two selected dopants. Hence, anion exchange doping is a promising route to obtain high doping levels with minimized doping-induced disorder. A lower activation energy, a narrower density of states and a higher density of states around the Fermi energy for AED have been directly confirmed by cryogenic THz time-domain spectroscopy. The semi-transient localized transport model is presented to interpret the energetics. The activation energy vanishes around room temperature indicating band-like transport, yet a Drude–Smith response of the complex conductivity indicate a very weak transient localization. The weak localization increases with cooling until static disorder dominates at low temperature. Upon AED, Pg_32T-

T yields high conductivities on the nanoscale (Shortσ) and on the macroscale (Longσ). As such, it shows close-to-unity interconnectivity of conductive domains. Cryogenic THz-TDS is a powerful technique to investigate the charge transport and degree of localization in doped polymers, because it yields both the characteristic temperature-dependence of the conductivity and the frequency-dependent complex conductivity as a direct observable.

7.3. Vanishing weak charge localization in highly doped conjugated polymers

Abstract

Doped conjugated polymers are promising materials for organic electronic and thermoelectric applications, with their performance closely tied to doping-induced microstructural and energetic disorder. This study investigates the conductivity, interconnectivity, and charge localization in highly doped polymers. Short-range (THz time-domain spectroscopy, THz-TDS) and long-range (linear four-point probe) conductivity measurements reveal close-to-unity interconnectivity. Cryogenic THz-TDS provides insights into charge localization from room temperature to 10 K. A series of conjugated polymers with varying backbones and glycolated side-chains were doped using Magic Blue (MB) and anion exchange doping (AED) with $TBAPF_6$. The best performance, with a conductivity of 4810 S cm^{-1} and a thermoelectric power factor of 230 μW m^{-1} K^{-2}, was achieved for a polythienothiophene with triethylene glycol side-chains (Pg_3BTTT) *via* AED. All polymers showed vanishing charge localization at room temperature, increasing slightly at cryogenic temperatures. AED effectively reduces doping-induced disorder, lowering the activation energy for charge transport. These findings highlight the importance of mitigating energetic disorder through advanced doping strategies, robust backbones, and glycolated side-chains to enhance the conductivity of doped conjugated polymers.

7.3.1. Introduction

Molecular doping of conjugated polymers plays an essential role in modulating the charge carrier density n and with it the conductivity σ. The simple expression "σ proportionally increases with n" however does not hold true when doping also induces changes in structural and energetic disorder[41]. Doping-induced charges in polymers generally occupy localized electronic states in a (Gaussian[69]) distribution of the density of states (DOS). The DOS in a polymer stems from a complex interplay of its chemical structure, microstructure, and external factors like temperature and doping[25]. These factors determine the distribution of states. The energetic disorder describes variations in the energy levels of states in the DOS. Figure 1 (a) shows a scheme of the DOS in a polymer HOMO level upon p-doping, visualizing the effect of charge carrier density and energetic disorder. When doping induces structural and energetic disorder, the DOS broadens and the variations in the energy levels of states increases. This is called doping-induced localization of charges. Finding doping methods that reduce structural and energetic disorder therefore is a promising route to obtain high conductivity in doped polymers[8, 35, 58, 70]. The energy difference between the transport edge energy and the Fermi energy is denoted ΔE and the average activation energy to transport is denoted W_{H}. These two parameters are the key figures to describe localized charge transport in doped polymers and to compare doping-induced localization from state-of-the-art doping methods. The semi-localized transport (SLoT) model developed by Gregory *et al.* in 2021[13] led to a big leap in the direction

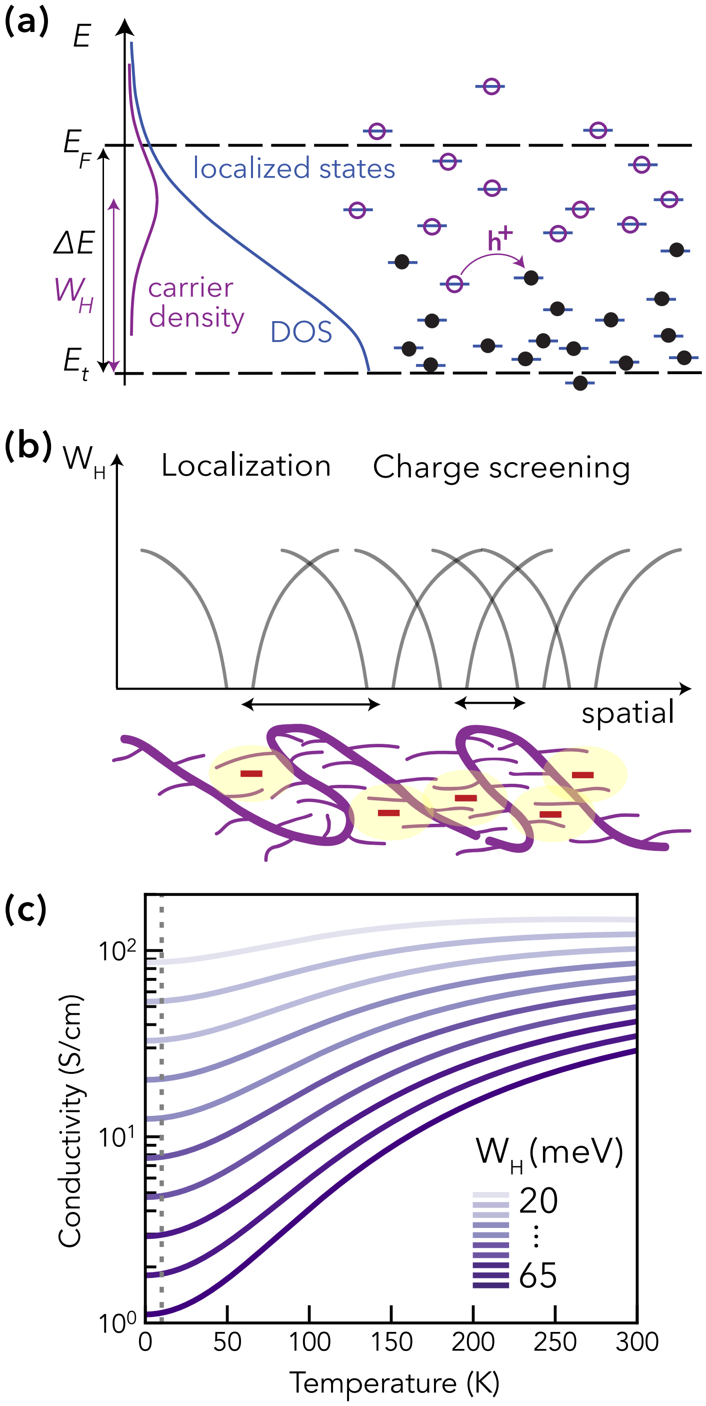

Figure 1. Representation of (a) localized electronic states for p-doping, (b) Charge screening effect, and (c) the effect on conductivity versus temperature.

of a universal mathematical description of charge transport in doped polymers. The model has been developed with the aim of quantifying charge localization in doped polymers such as P3HT[13] or PBTTT[9]. In this description the activation energy denoted W_{H} is explicitly a function of the doping conc-entration. At high doping levels W_{H} decreases with increasing doping concentration due to an effect called charge screening (or Coulomb screeening). Charge screening occurs when many ionized dopant molecules are in spatial proximity to each other. Then, Coulomb potential wells originating from ionized dopant molecules start to overlap and their combined trap potential weakens. This is shown schematically in Figure 1 (b). Since the activation energy W_{H} decreases with high doping levels, the chracteristic temperature-dependent conductivity becomes more flat. Figure 1 (c) visualizes the effect that W_{H} has on the temperature-dependent conductivity. Here the conductivity is plotted for ten different W_{H} between 20 and 65 meV as a function of temperature given by equation (1). The SLoT model is successful when a constant W_{H} is assumed over the temperature range of interest. Indeed, one assumes a constant static disorder stemming from the microstructure of polymers. This static disorder is usually expected to dominate the overall energetics[8]. However, experimental observations show a varying W_{H} with temperature[14, 71]. The Zabrodskii analysis shows the temperature coefficient $W = \frac{\mathrm{d}\ln(\sigma)}{\mathrm{d}\ln(T)}$ and is used to classify the degree of charge localization at a defined temperature range[9, 13, 72, 73]. When W_{H} increases with cooling one speaks of dominantly localized charge transport. In many doped polymers (including P3HT, PBTTT, 2DPP-TEG) a crossover temperature occurs where $W < 0$ above and $W > 0$ below the crossover temperature T_0[14-18]. The observation of $W < 0$ points in the direction of band-like transport above the crossover temperature. This can be confirmed by an ideal Hall effect[17] and Drude-like optical absorption, i.e. complex conductivity[19]. To avoid the separation of the temperature-dependent conductivity into different regimes of temperatures, equation (1) the semi-transient localized transport model STLoT is used. Thereby, the effect of temperature on W_{H} is included via a crossover temperature T_0 below which fluctuation-induced energetic variations are neglectable in comparison to static disorder[74]. Above this temperature fluctuation-induced changes in the energetic landscape are significant. The STLoT model allows the extraction of meaningful values for W_{H} and ΔE and moreover quantify the crossover temperature T_0 at which temperatures transient fluctuations play a relevant role for charge transport in doped polymers. Fluctuations, such as thermal phonon modes, can contribute to the overall charge transport when the activation energy W_{H} is only in the order of tens of meV. The transient (dynamical) corrections to band-like transport in high-mobility organic semiconductors has been largely shaped by Simone Fratini and Sergio Ciuchi[19-22] and has received acknowledgement in the field[22]. Equation (1) shows how the conductivity is a direct function of the energy level distribution as shown in Figure 1 (a). This allows to express the temperature-dependent conductivity $\sigma_{\mathrm{STLoT}}(T)$ as a function of $W_{\mathrm{H}}, \Delta E$ and T_0:

$$\sigma_{\mathrm{STLoT}}(T) = \sigma_0 \exp\left(-\frac{W_{\mathrm{H}}(c)}{k_{\mathrm{B}}\sqrt{T^2 + {T_0}^2}}\right) \times \left(\frac{\Delta E}{k_{\mathrm{B}}\sqrt{T^2 + {T_0}^2}}\right) \quad (1)$$

Hereby, the temperature is denoted by T. The Boltzmann constant is denoted by k_{B}. The activation energy is denoted by W_{H} and the difference in energy levels ΔE. The crossover temperature denoted by T_0 is the temperature below which static disorder dominates (and dynamic disorder is neglectable). Lastly,

σ_0 is a temperature-independent pre-factor for the conductivity. Cryogenic THz spectroscopy is a powerful tool to obtain the characteristic temperature-dependent conductivity together with the degree of localization at room temperature and in the low-temperature limit. The low-temperature limit $T \rightarrow 0$ thereby gives the frozen disorder, so the static disorder in absence of fluctuation-induced phenomena[29]. The THz conductivity spectrum contains information about the conductive (Re) and localized (Im) response of charge carriers in a material to an electric field[75, 76]. To support the THz conductivity and estimate the degree of charge localization and the effective mobility, the Drude–Smith model (DSM) analysis is used[77]. The complex conductivity in the DSM is expressed as a function of the angular frequency and given in the SI. The DSM provides an estimate for the effective mobility at room temperature and in the frozen disorder limit.

7.3.2. Results and Discussion

Film preparation and doping with the strong oxidant Magic Blue

The conjugated polymers are dissolved in common solvents[9], spin-coated[10] and the resulting thin films subsequently immersed in a doping solution. The doping solution contains either Magic Blue alone or Magic Blue and the electrolyte $TBAPF_6$ in acetonitrile for anion-exchange doping[11]. Acetonitrile is an orthogonal solvent for all studied polymers, and it is redox-stable, which is relevant for the employed doping method[36]. Figure 2 shows (a) the chemical structures of the investigated conjugated polymers, (b) dopant and ionic salt and (c) an energy diagram indicating the HOMO energy levels of the conjugated polymers (color coded) and the LUMO level of the dopant (dashed). Based on the offset between the LUMO level of the dopant (−5.8 eV) and the HOMO level of the different materials, all materials are expected to oxidize efficiently. Thereby, the Pg_32T-T and Pg_3BTTT polymers, bearing

---

[9] Sample preparation is done in inert atmosphere using anhydrous solvents: Chloroform ($CHCl_3$) for triethylene glycolated polymers: Pg_32T-T and Pg_3TTT. 1,2-o-Dichlorobenzene (oDCB) for P3HT, PBTTT-C_{14} (referred to as PBTTT) and PBTTT-^8O (referred to as PBTTT^{8}O). Chlorobenzene (CB) for PDPP3T, PDPP4T and F8T2.

[10] The films were spin-coated hot: 35°C for polymers in $CHCl_3$, 80–110°C for polymers in CB or oDCB. Spin-coating for 60 seconds at 1000 rpm with polymer contentrations between 8 mg/ml and 10 mg/ml. PBTTT, PBTTT^{8}O and Pg_3BTTT were annealed at 210°C.

[11] The used dopant and electrolyte concentration was c(MB)=0.275 mM and c($TBAPF_6$)=115 mM for Pg_32T-T or c(MB)=0.6 mM and c($TBAPF_6$)=25 mM for all others. The immersion time was 200 seconds. The lower concentrations for Pg_32T-T is used to avoid over-doping as previously published[28].

glycol side-chains, oxidize the most readily with HOMO (−4.8 eV). The HOMO levels for PBTTT^{8}O lies at −4.95 eV, in between Pg$_3$BTTT and the alkyl PBTTT (−5.11 eV). P3HT has a similar HOMO level (−5.2 eV) as the DPP-based copolymers. Nonetheless, DPP-based copolymers show higher mobilities due to their D-A structure favoring interchain transport. That does not necessarily translate to MB doped films and the intrinsic conductivity though. Lastly, F8T2 has a low-lying HOMO level (−5.5 eV) and the lowest doping driving force. Figure 2 (d) shows the conductivity of polymer films upon doping with MB. The conductivity measured on the macroscopic scale is denoted Longσ and the THz conductivity is denoted Shortσ. The colored bars represent the Longσ and Shortσ conductivity to estimate the interconnectivity of conductive regions in the spin-coated films over long (millimeter) distances and over short (<100 nanometer) distances. The conductivity is shown on a logarithmic scale, because Pg$_3$BTTT outperforms other polymers by more than an order of magnitude yielding 3140 S cm^{-1} **upon MB-doping**.

The highest conductivities are seen for polythienothiophenes (PTTs): highest for triethylene glycol side-chains Pg$_3$BTTT, followed by 650 S cm^{-1} PBTTT^{8}O[78][12] and 420 S cm^{-1} for PBTTT with alkyl side-chains[13]. The polythiophene (PT) with triethylene glycol side-chains Pg$_3$2T-T has a conductivity of 350 S cm^{-1}. P3HT yields 100 S cm^{-1} upon MB-doping.

---

[12] C$_{12}$ side-chains with glycolation on position 8 as previously described and published.

[13] PBTTT-C$_{14}$; I recommend to see supplementary Chapter S.0. for all batch specifications.

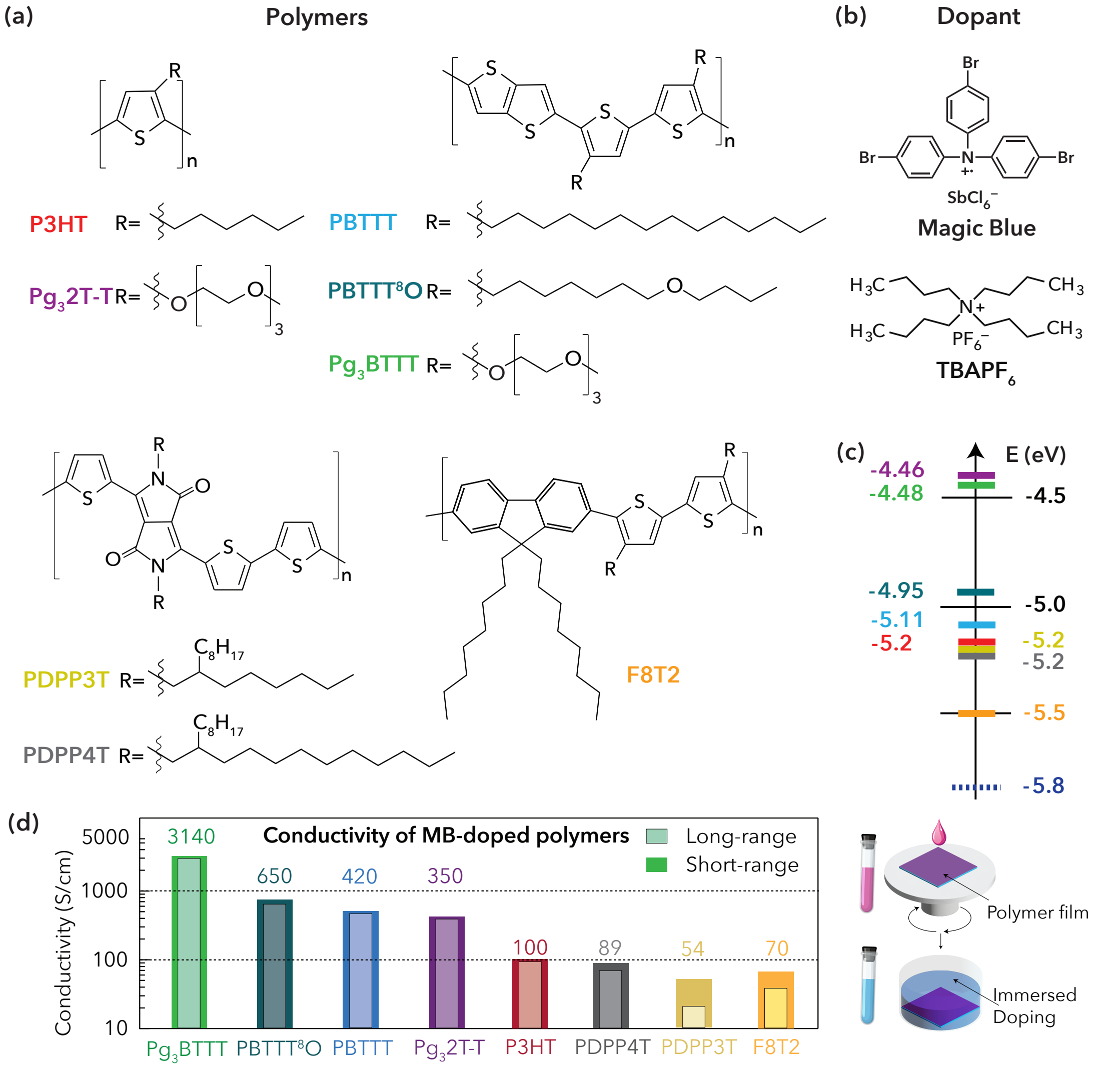

Figure 2. Chemical structure and name of (a) polymers and (b) dopant and electrolyte for ion-exchange. (c) HOMO energy levels of the polymers color-coded. (d) Long- and short-range conductivity upon MB-doping.

The DPP-based copolymers fall below the 100 S cm^{-1} mark with 89 S cm^{-1} for PDPP4T and half of that 45 S cm^{-1} for PDPP3T. F8T2, which has the HOMO level of −5.5 eV could also be effectively doped with MB and yields 70 S cm^{-1}. The Longσ and Shortσ conductivity is generally similar to each other, indicating excellent interconnectivity of conductive regions. The **quotient of**

Longσ/Shortσ is an estimate for the interconnectivity and is above 80% for most materials upon MB-doping. The Shortσ signal by THz-TDS scales with the thickness of the sample. Obtaining doped polymer films with conductivities above 100 S cm^{-1} allows the use of spin-coated thin films between 30–50 nm in THz-TDS. For polymers that yield a conductivity below 100 S cm^{-1}, the signal in THz-TDS is small, which necessitates the preparation of thicker films. This is the main reason why Pg$_3$BTTT, PBTTT^{8}O, PBTTT, Pg$_3$2T-T and P3HT are shown in the main text and PDPP4T, PDPP3T and F8T2 are shown in the SI. The preparation of thicker films is done by the dopant-induced solubility control (DISC) proposed by the Moulé group[79]. As such, sequential films of 4 layers[14] are prepared to obtain around 450 nm thick films. For comparison MB-doped P3HT is shown for both; i.e. thin and thick film sample preparation. The Longσ conductivity is measured for each of the 4 layers and appears comparable. The thickness of spin-coated and MB-doped polymer films, their conductivity results and the comparison between Longσ and Shortσ is given in Table 1. To conclude, MB effectively dopes all investigated systems. Polythienothiophenes and polythiophenes show high conductivity with a large improvement with glycolated side-chains. Pg$_3$BTTT with triethylene glycol side-chains shows the highest conductivity of 3140 S cm^{-1} with >90% interconnectivity.

DPP-based copolymers show a twice as high conductivity of 89 S cm^{-1} for 4T side-chains *versus* 45 S cm^{-1} with 3T side-chains. The longer side-chains give a higher conductivity in this copolymers, maybe providing a separator

---

[14] Prepared as described for the thin films but with 15 mg/ml such that 1 layer is 100 nm, but still measurable in UV-Vis steady-state absorbance to check the doping level.

function for the electron-accepting diketopyrrolopyrrole units[51, 80]. Yet, the MB-doped PDPP4T and PDPP3T have decent conductivities in comparison to reported values that range from 0.1–400 S cm^{-1}[48, 51, 80, 81].

Table 1: Conductivity values for the Magic Blue doped films (ID).

Quantity	d	Longσ	Shortσ	Longσ/ Shortσ	Color code
Units	nm	S cm^{-1}	S cm^{-1}		
Pg$_3$BTTT	47	2870	3140	91%	🟩
PBTTT^{8}O	43	555	650	85%	🟦
PBTTT	40	390	420	94%	🟦
Pg$_3$2T-T	30	324	354	92%	🟪
P3HT	88	92	100	93%	🟥
P3HT	455	72	87	83%	🟥
PDPP4T	464	76	89	86%	⬛
PDPP3T	626	19	54	35%	🟨
F8T2	444	59	70	84%	🟧

These materials show excellent interconnectivity of conductive domains.

Improvement upon anion exchange doping

Figure 3 (a) shows the conductivity results comparing MB-doping and anion exchange doping with electrolyte TBAPF$_6$. Again, the Longσ is obtained by electrical four-point probe and Shortσ is obtained by THz conductivity, where σ_{Re}(1 THz). For the investigated materials the Longσ and Shortσ conductivity improves when employing anion exchange doping. The only exception is PBTTT, which yields a conductivity of 420 S cm^{-1} for both MB-doping and AED-doping. Note that the conductivity axis is logarithmic again. The improvement is highest for P3HT, where upon AED the conductivity reaches 230 S cm^{-1}, which is 2.3 times more than for MB-doping. The conductivity of Pg$_3$2T-T is 510 S cm^{-1} upon AED, which is 1.4 times more than upon MB-doping. The conductivity of PBTTT^{8}O yields 845 S cm^{-1}, which is 1.3 times more. Lastly, the conductivity of Pg$_3$BTTT shows a record value of 4810 S cm^{-1} upon AED, which is a 1.5 times improvement in comparison to 3140 S cm^{-1} by MB-doping. Moreover, for anion exchange doping the **interconnectivity is close-to-unity in all investigated systems**. This is a fascinating improvement and appears to be a general trend. Moreover, the complex conductivity $\sigma_{\mathrm{Re}} + i\sigma_{\mathrm{Im}}$ yields the conductive (Re) and localized (Im) response of charges to an electric field. A negative imaginary part thereby is a response from localized charges. The more negative, the more localized are the carriers[77]. The complex THz conductivity is seen in Figure 3 (b,c,d) for the three most conductive polymers, the PTTs. The PTs depict similar trends and are given in the SI. 23 reveals that the most conductive polymers have a flat imaginary part close to the zero line. The imaginary part becomes flatter with AED while the real part increases in magnitude. This means that the charges in these samples experience very weak localization. The increase in the real part corresponds to the increase in (a), where the darker bar represents the σ_{Re}(1 THz). Figure 3 includes a DSM fit (dashed line) describing the experimental complex conductivity well. The extracted effective mobility improves upon AED while the corresponding density of charge carriers is stagnant between MB-doping and AED. **AED improves the mobility while the density of charge carriers is comparable.**

To verify the effective mobility and the distinction between localized/delocalized charge transport, Hall effect experiments are conducted. It is reported that localized (decoherent) charge transport manifests itself in a suppressed Hall mobility[17]. The standard polymers P3HT and PBTTT give typical Hall mobilities with 0.3 cm^2/Vs for doped P3HT and 1.2 cm^2/Vs for doped PBTTT. The Hall effect hole/electron ratios are close to 100/0 indicating hole transport as expected for p-doping. The Hall mobilities for the polymers with triethylene glycol side-chains however do not show an ideal Hall effect. Unexpectedly, the mobility is low (0.1–0.3 cm^2/Vs), the charge density is high (3–7×10^{22} cm^{-3}) and the hole/electron ratios are unreasonable 35/65. Such an underdeveloped Hall effect speaks against delocalized charge transport and motivates further investigations of the degree of charge localization in doped

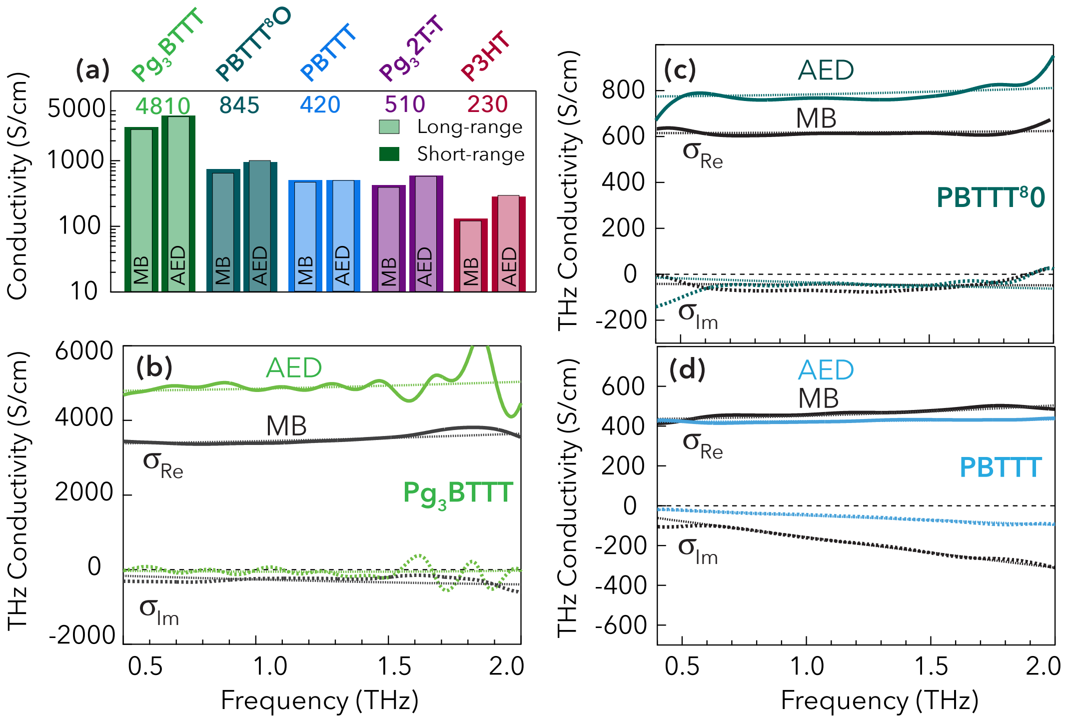

Figure 3. (a) Long- and short-range conductivity. (b,c,d) THz conductivity spectra of doped PTT structures. MB-doping versus AED doping.

polymers. A comparison between the conductivity, mobility and carrier density from Hall and THz is found in the SI section S.4. To further investigate the enhanced AED mobility, steady-state absorbance and GIWAXS are employed. This aims to understand the nature of the underlying doping-induced charged species and doping-induced structural changes.

Optical and microstructural characterization

The elaborated dependency between the doping-induced structural changes and the resulting charge transport, reminding Figure 1, necessitates an optical and microstructural characterization of the doped films. This section elaborates the optical and microstructural changes upon anion exchange doping in comparison to MB-doping and how they manifest in the resulting conductivity. The absorbance spectra of neat and doped conjugated polymer films yield information about the optoelectronic properties and the doping level. Most of the conjugated polymers investigated in p-doping studies exhibit a bandgap in the visible range. Figure 4 (a) shows the neat absorbance spectra of the investigated polymers. Hereby, the polymers bearing triethylene glycol side-chains Pg_32T-T and Pg_3BTTT have both a neutral absorbance band centered around 610 nm (2.0 eV), while the polymers with less polar side-chains ($PBTTT^8O$, PBTTT, P3HT) show a blue-shift in the neutral band, more centered around 530 nm (2.3 eV). As seen in Figure 2 (chemical structures), there is a **rise in the HOMO energy level due to the inductive donating effect of the oxygen in α-position of the backbone**. A higher HOMO energy level thereby tends to decrease the bandgap and red-shifts the absorbance corresponding to the neutral band. Upon doping, the bandgap associated with the neutral system decays, while bands associated with the charged system rise in the near infrared. Figure 4 (b) shows a comparison of the polymers when anion-exchanged with PF_6^-. Here, doping with MB fully depletes the neutral band. The spectra are normalized at the polaron (P2) band maximum between 780–860 nm (1.6–1.4 eV). The normalization makes the **relative intensity of the red-shifted bands** more evident. Above 1000 nm there is a rise in absorbance originating from both the singly charged [+] and doubly charged [++] species. In (b) the doped Pg_32T-T and Pg_3BTTT spectra are overlapping, which suggests that a similar doping level is achieved and also a similar relative intensity of [+] and [++] such that the absorbance curves overlap. This similitude is reassuring as these two polymers have similar HOMO energy levels and similar (pristine) microstructure. The other materials $PBTTT^8O$, PBTTT and P3HT also have a high doping level and a fully depleted neutral band. P3HT has a pronounced infrared absorption with a rounded shape indicating a doubly charged (bipolaron) band centered at 1400 nm. The comparison of different polymers upon AED shows high doping levels with fully depleted neutral bends. Next, the comparison between the relative intensities of charged species between MB-doping and AED is elaborated. Figure 4 (c) shows a comparison of the materials when doped with MB (dashed) *versus* AED with PF_6^- (solid). In this study the absorbance of the solid curve always lies above the dashed curve, indicating that here anion exchange doping leads to a minimally higher absorbance originating from charged species. Hereby the spectra are not normalized, just corrected with the thickness of the film. The same trend without the thickness correction can be seen in the SI Figure S.0.2. To interpret the doping-induced spectral changes in greater detail Figure 4 (d) depicts again the comparison of the materials when doped with MB (dashed) *versus* AED (solid), here normalized at the P2 band maximum. Thereby, I see a clear trend that for Pg_3BTTT, $PBTTT^8O$ and PBTTT the AED (solid) leads to a higher NIR absorbance than the MB (dashed) doping. In contrary, for Pg_32T-T and P3HT, the AED (solid) leads to a lower NIR absorbance. These trends are highlighted with the arrows. This is indicating that anion exchange doping here shifts the relative intensities between charged species, even though the effect is small. In other words, AED might yield more doubly charged species in PTTs in comparison to singly charged species (and less doubly charged species in PTs). Literature on Raman spectroscopy during doping[65-67] shows how the formation of [++] bipolaronic species, increasing the NIR absorbance, is related to negative structural changes for polythiophenes. A reduced NIR absorbance for PTs hence might be an indicator for mitigation of negative doping-induced structural changes. For PTTs, in contrary, no such literature on negative structural effects with [++] formation exists to my best knowledge. This feeds speculations about the link between charged species and structural changes in different types of polymers. Given the continuous increase in conductivity for PTTs, "over doping"[59] is not observed for the presented doping methods. So far, **PTTs appear to be more resilient to doping-induced structural changes than PTs**. Next, the doping-induced structural changes are investigated in more detail. The microstructural characterization by GIWAXS yields the paracrystallinity disorder in the ordered conductive regions and the (100) peak area representing the lamellar $\pi-\pi$ stacking. Additional structural characterization of the interconnectivity of ordered conductive regions is challenging. Scanning tunneling electron microscopy (STEM) and conductive atomic force microscopy (c-AFM) are good complementary techniques to GIWAXS[82] but have not been available to confirm the high interconnectivity seen in the close-to-unity quotient of Longσ/Shortσ. Figure 4 shows (e) the GIWAXS paracrystalline disorder and (f) the integrated (100) peak area for pristine and doped polymer films. The polymers with triethylene glycol side-chains Pg$_3$2T-T and Pg$_3$BTTT have a higher conductivity than their alkyl-side-chain versions. The paracrystallinity disorder for pristine films of Pg32T-T and Pg3BTTT films is about 10%. Upon MB-doping the paracrystallinity doubles more or less to 20%. Hereby, indeed Pg3BTTT shows a smaller doping-induced structural disorder. Upon anion exchange doping paracrystallinity reduces to <5% for doped Pg32T-T indicating a mitigation of doping-induced disorder. For doped Pg3BTTT this mitigating effect occurs as well even though the effect is smaller. The supplementary section S.1. shows paracrystallinity and (100) peak area for a series of different anion-exchange electrolyte concentrations to confirm this observation. The paracrystallinity disorder of pristine P3HT is also about 10% and increases upon MB-doping to around 17%. Anion exchange doping, repeatedly, decreases the paracrystallinity significantly. PBTTT was the single polymer were the conductivity between MB-doping and AED remained similar. Unfortunately, for PBTTT the edge-on polymorphism made it difficult to obtain a paracrystallinity disorder within a reasonable error. Therefore, for this polymer only the (100) peak area is shown, see panel (b). The peak area is of the same order of magnitude in comparison to the other polymers, while the MB-doped ID film has the highest peak area. For this combination of PBTTT and MB literature is still sparce. On aligned films of PBTTT, spontaneous modulation doping by MB has been suggested[45]. However, it is known that PBTTT has more substantial π–π stack alignment and a more oversized pocket in the lamellar region for anion intercalation than P3HT. Therefore, PBTTT doping with MB does not disrupt the crystallinity but rather undergoes doping-induced crystallization. For Pg32T-T, Pg3BTTT and P3HT the (100) peak area follows the same trend. This is seen when comparing the neat, ID and AED histogram bars in Figure 4 (f). Thereby, MB-doped polymers yield the lowest (100) peak area and it improves upon AED. To sum up, the conductivity is improved for most polymers (Pg32T-T, Pg3BTTT and P3HT) upon anion exchange in comparison to MB-doping. These polymers show a decrease in paracrystallinity and an increase in (100) peak area with AED. The extend for the structural changes is strongest for Pg$_3$2T-T.

The expectional polymer in this series is PBTTT, where the paracrystallinity disorder could not be determined within reasonable error and the (100) peak area is high for MB-doping. This system shows similar conductivity when MB-doping or AED was employed. To quantify the doping-induced energetic disorder, variations in activation energies to transport are investigated.

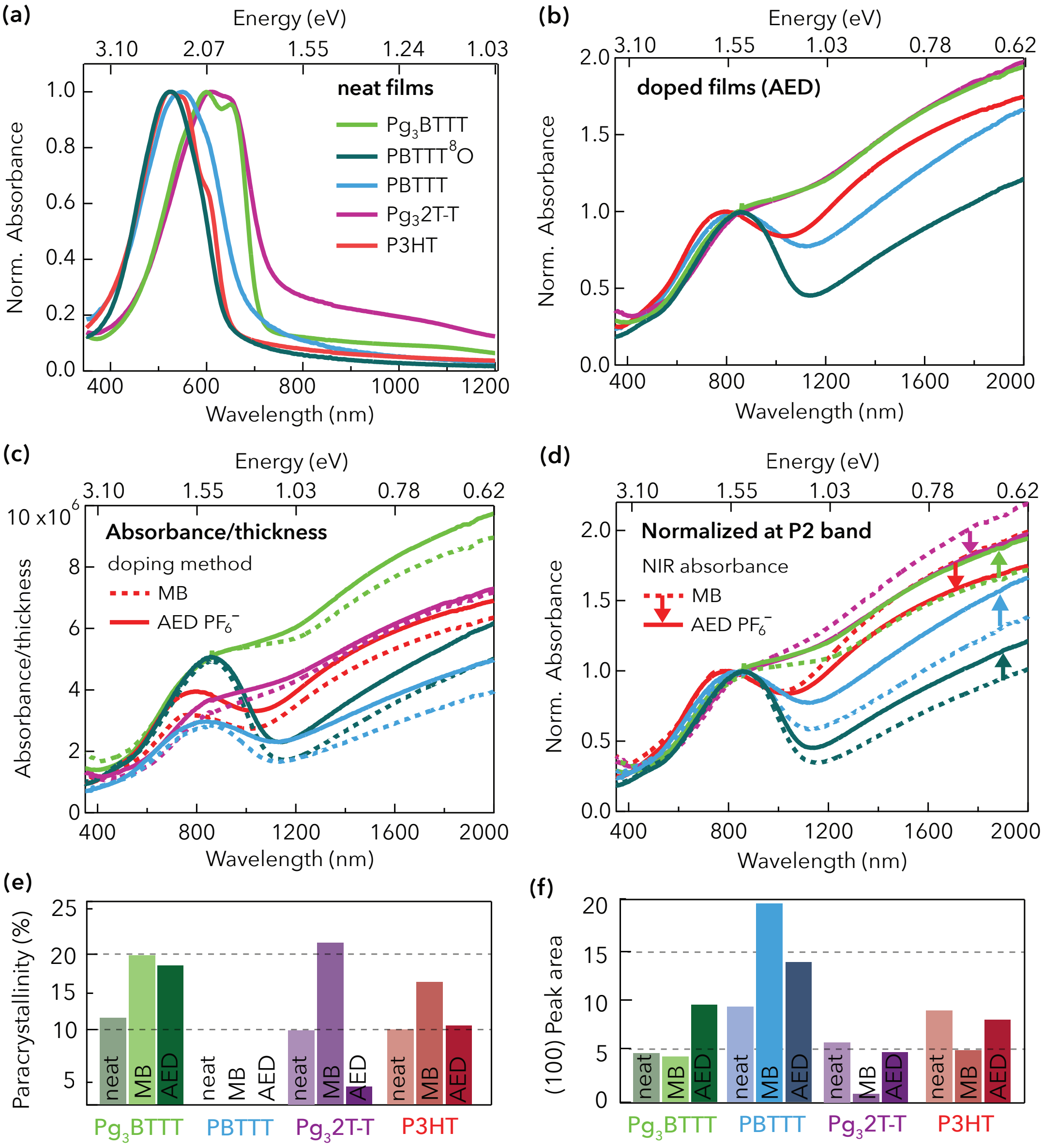

Figure 4: Absorbance spectra of the investigated conjugated polymers. (a) Neat films. (b) Spectra normalized at the P2 band maximum of films doped with AED. (c) Films doped with both doping methods. Spectra are devided by the thickness of the films. (d) Films doped with both doping methods. The spectra are normalized at the P2 band. The arrows show if anion exchanged films have a higher or lower NIR absorbance than the MB films. (e) Paracrystallinity disorder and (f) (100) Peak area.

Temperature-dependent conductivity

This section looks at the temperature-dependent short-range conductivity σ_{Re}(1 THz) from cryogenic THz-TDS, comparing MB doping and AED for all polymers. Figure 5 (a) shows the conductivity of MB-doped polymers as a function of temperature. The conductivity axis is plotted on a logarithmic scale to depict all materials clearly. Overall, the conductivity does not change much with temperature. The conductivity is more or less stagnant above 200 K. The conductivities of Pg_3BTTT , PBTTT^{8}O and PBTTT even have a small increase in conductivity with cooling above 200 K. Below 200 K the conductivity decreases monotonously but very weakly. In (b) the temperature dependent conductivity curves are normalized to the room temperature value, to compare the increase/decrease with respect to the value at 295 K. Therefore, the **thermal activation at room temperature is vanishingly small**. The vanished thermal activation around room temperature is confirmed by macroscopic conductivity using temperature-dependent four-point probe measurements as well. The absence of thermal activation above approximately 200 K is confirmed by an Arrhenius and Zabrodskii analysis in the SI section S.5. The vanishing thermal activation leads to **high conductivity $\boldsymbol{\sigma_{\mathrm{Re}}}$ of the doped polymers at cryogenic temperatures**. The value σ_{Re}(10 K)/σ_{Re}(295 K) is an intuitive key parameter. PBTTT and PBTTT^{8}O have a relative conductivity of 90% at 10 K in comparison to 295 K. Pg_3BTTT has a relative conductivity of 70% at 10 K in comparison to 295 K. P3HT and $Pg_3$2T-T retain a conductivity of about 40% at 10 K. Such weak temperature-dependence and the sigmoid shape can be described well with the STLoT model given by equation (1) and shown as a solid fit curve in Figure 5 (a, c). Figure 5 (c) shows the temperature-dependent conductivity for AED polymers. The dashed lines here represent the MB curves as well to compare the improvement by AED. For all polymers the AED conductivity is higher at all temperatures. In Figure (d) the AED conductivities are normalized at room temperature. There, the conductivity of PTTs is constant or slightly increasing above 200 K and constant below until the 10 Kelvin experimental limit. As such they have relative value $\sigma_{\mathrm{Re}}(10\ \mathrm{K})/\sigma_{\mathrm{Re}}(295\ \mathrm{K})$ of 80%. The conductivity of polythiophenes decreases monotonously and retains around 50–60% conductivity at cryogenic temperature $\sigma_{\mathrm{Re}}(10\ \mathrm{K})/\sigma_{\mathrm{Re}}(295\ \mathrm{K})$. The shape of the temperature-dependent conductivity reveals more information. To put the weak temperature-dependence of the conductivity into context and generalize the findings, the SI section S.6. shows the temperature-dependent conductivity for DPP-based copolymers and F8T2. To take the analysis a step further towards a universal description of charge transport in doped polymers the STLoT model is applied. The solid curve through the data points in Figure 5 (a) and (c) represent the STLoT fit. In this framework, the conductivity is a direct function of the distribution of energies in the DOS. Therefore, it represents a numerical model to investigate doping-induced disorder and its effect on the DOS. The SI Figure S.6.1. shows the conductivity *versus* temperature and fit for each polymer separately on a bigger scale than here. The data cannot be described by the semi-transient localization (SLoT) model alone assuming static disorder over all temperatures. It needs the explicit consideration of a crossover temperature. The occurance of a crossover temperature is typical for several doped polymers[14-18]. The interpretation thereof is usually a crossover from Mott to ES hopping, but remains a topic of discussion. An anomalous Hall effect and the weal localization increasing with cooling provide some evidence for transient mechanisms to transport, which may include tunneling, electron–phonon coupling, or field-induced hopping[19-22, 29, 30]. Transient mechanisms therefore could contribute to the weak localization at room temperature, because they increase with temperature. The crossover to band-like transport with weak localization corrections is the most likely interpretation. This continuous crossover has been previously observed and described as localized states that are so close together that they are indistinguishable to band-like transport[83].

Table 2 gives the extracted STLoT fit parameters. The results shows that the temperature independent pre-factor σ_0 is enhanced for AED of the investigated polymers. The crossover temperature T_0 is the same between AED and MB-doping of Pg_3BTTT, $PBTTT^8O$ and PBTTT. In the STLoT framework this indicates similar transient transport, for example a similar effect of vibrational modes and field-induced carrier heating. The THz field-induced carrier heating is estimated to be around 12 K (1 meV) based on the effective temperature introduced by Marianer *et al.*[26, 84].

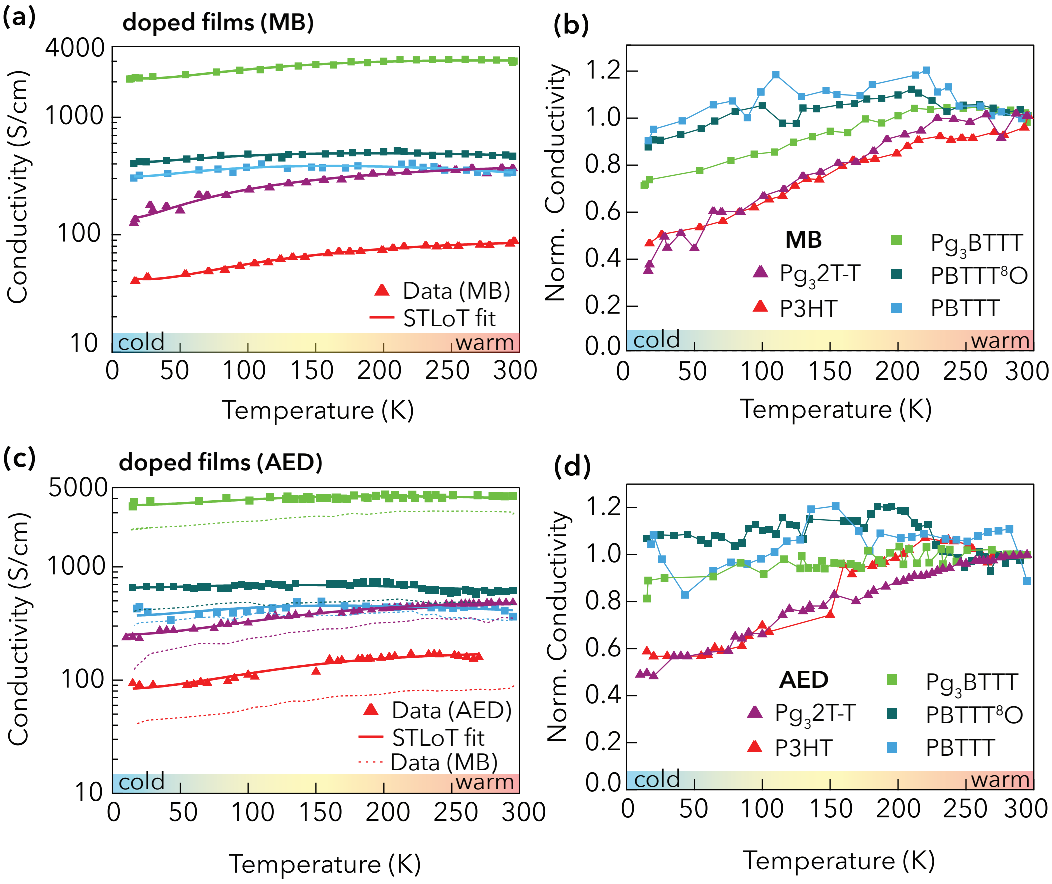

Figure 5: Temperature dependent THz conductivity of doped polymers. Conductivity over temperature for (a) MB-doping and (c) AED where the solid line represents the semi-transient localization fit. Conductivity normalized at room temperature for (b) MB-doping and (d) AED.

Therefore, it can play a small role at high carrier densities when the static disorder is of similar magnitude. T_0 is lower for P3HT, Pg$_3$2T-T upon AED. The microstructure in these polythiophenes with AED showed improved paracrystallinity and lamellar stacking. Comparing the activation energy W_H between the doping methods shows that AED can reduce the activation to transport.

Table 2. STLoT fit for polymers upon AED (left) or MB (right) doping. The error on these fit parameters is estimated to be at least 20%.

σ_0 S cm^{-1}	T_0 K	W_H meV	ΔE meV	Quantity Unit	σ_0 S cm^{-1}	T_0 K	W_H meV	ΔE meV	
2680	140	20	90	Pg$_3$BTTT	2250	140	30	100	🟩
560	140	20	60	PBTTT^{8}O	400	140	20	70	⬛
320	100	20	60	PBTTT	300	100	20	60	🟦
420	150	30	100	Pg$_3$2T-T	300	180	40	130	🟪
140	140	30	100	P3HT	90	170	40	110	🟥
AED					MB				

Particularly the polymers which had a lower value (50%) for σ_Re(10 K)/σ_Re(295 K) with MB-doping show an localization energy of 40 meV. The polymers that have higher value (80%) for σ_Re(10 K)/σ_Re(295 K) for either of the doping methods show the same localization energy of 20 meV. This is not necessarily trivial given that the real conductivity σ_{Re}(295 K) is always significantly higher with AED. PBTTT is an interesting exception. This material did not show microstructural improvement and shows the same parameters unless a small (<10%) improvement in the temperature independent pre-factor σ_0. The parameters that describe the shape of the conductivity *versus* temperature are unchanged. The energy difference to the transport edge $\Delta E = E_\mathrm{F} - E_\mathrm{t}$ is lower for all polymers except for PBTTT. This energy difference describes a high density of states near the Fermi level. At a high density of states near the Fermi level, temperature changes do not significantly influence the availability of states for conduction.

The frozen disorder limit

In systems where charge carriers interact strongly with the "lattice", like polarons in conjugated polymers do, the activation energy can depend on the temperature due to the changing influence of phonon scattering or lattice vibrations. Such fluctuation-induced transient processes increase with temperature and thereby change the energetic variations and contribute to charge transport. The low temperature analysis describes the frozen disorder limit. The complex THz conductivity at room temperature and at cryogenic temperature is presented in Figure 6. This gives information about the effect of temperature on the conductive (σ_{Re}) and localized (σ_{Im}) response of charges to an electric field. The more positive the real part (σ_{Re}), the more conductive is the material. The more negative the imaginary part (σ_{Im}), the more localized the charge carriers.

Lastly, also the frequency-dependent slope gives information about the localization of charge carriers. A positive slope with increasing frequency is easiest to describe in a hopping model: as the frequency increases, carriers can more readily respond to the oscillating electric field, resulting in enhanced conductivity. At the same time, a suppression of conductivity at low frequency occurs when charge carriers are localized. A flat slope indicates the lack of localization or scattering events. Figure 6 (a) shows the complex conductivity for MB-doped Pg$_3$BTTT. The green line represents room temperature conductivity (295 K), and the turquoise line represents low temperature conductivity (10 K). All doped polymers show very weak localization with a negative imaginary part. The PTTs have an imaginary part very close to the zero line. The room temperature conductivity is higher and flatter than the low temperature conductivity. This shows an increased localization with cooling, which means that when vibrational modes freeze, the mobility decreases.

This leads to the conclusion that transient mechanisms supported by vibrational modes contribute positively to charge transport and partly screen the small (tens of meV) static disorder. The same trend is observed for PBTTT^{8}O and PBTTT in Figure 6 (c) and (e) and for Pg$_3$2T-T and P3HT shown

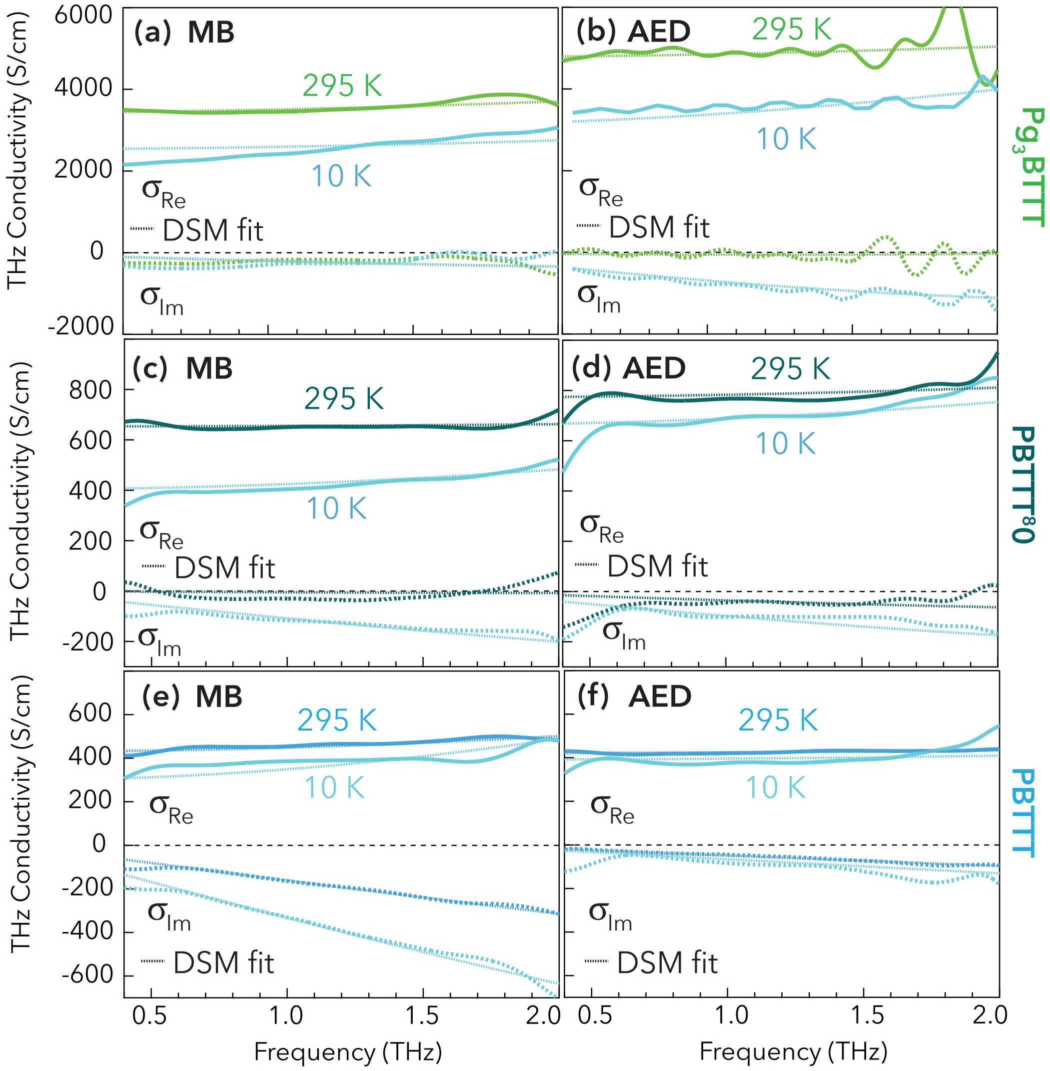

Figure 6. THz conductivity and DSM fits for polythienothiophens doped by (left) MB or (right) AED.

in the SI Figure S.3. Upon AED of the investigated polymers, the real conductivity improves and the imaginary part tendentially flattens. As for the microstructure and the room temperature characterization, PBTTT is not improving its real conductivity upon AED. This has been related to the resilient lamellar stacking and a recrystallisation with MB-doping in the previous section. It is fully cohesive that the same trend is observed in Figure 6 (e) and (f). To have an overarching estimate of how these trends in the complex conductivity manifest in the effective mobility of doped polymers, the complex conductivity is fitted with the Drude–Smith model. The dashed lines in Figure 6 and SI Figure S.3. represent the fits. The full list of fit parameters is also found in the SI section S.3.

Table 3: Conductivtiy values for the films doped with MB and AED with PF$_6^-$. All values presented from the DSM have an estimated error of 25%.

Quantity	μ_{eff} 295 K	μ_{eff} 10 K	μ_{eff} 295 K	μ_{eff} 10 K	
Units	cm^2/Vs	cm^2/Vs	cm^2/Vs	cm^2/Vs	
Doping	AED		MB		
Pg$_3$BTTT	8	5	6	5	🟩
PBTTT^{8}O	5	4	4	3	🟦
PBTTT	0.8	0.7	0.9	0.7	🟦
Pg$_3$2T-T	0.6	0.3	0.4	0.2	🟪
P3HT	0.5	0.2	0.4	0.2	🟥

The effective mobilities at 295 K and 10 K are calculated and shown in Table 3. The highest mobility of around 8 cm^2/Vs is seen for AED of Pg$_3$BTTT at room temperature. The changes in conductivity with cooling and doping method can be explained by changes in the mobility without varying the density of carriers. Table 3 therefore summarizes the main trends: AED improves the mobility of investigated polymers apart from PBTTT. The mobility of PTTs drops less with cooling in comparison to PTs. Glycolated side-chains, in particular triethylene glycol side-chains, enhance the mobility leading to mobilities up to 8 cm^2/Vs for Pg_3BTTT and 5 cm^2/Vs for Pg_3BTTT upon AED.

Lastly, Table 4 shows the Seebeck coefficient (*S*) and Power factor (*PF*) at room temperature to be able to compare the materials and doping methods also in terms of their thermoelectric performance. Therefore, samples with bigger dimensions were prepared[15]. The conductivity is remeasured using a comparable distance between thermal gradient and electrode spacing in the Seebeck and conductivity measurement respectively.

The Seebeck coefficient rapidly decreases with increasing doping level, showing an inverted relationship in comparison to the conductivity with increasing doping level[85-87]. The polymer that stands out uniquely is Pg_3BTTT that shows a high thermoelectric PF of >200 $\mu W\ m^{-1}\ K^{-2}$. This makes Pg_3BTTT promising for thermoelectric applications, given that previously reported high *PF* for doped polymers are on the order of magnitude of 100–200 $\mu W\ m^{-1}\ K^{-2}$ like the other materials presented here. High *PF* reported in literature are 120 $\mu W\ m^{-1}\ K^{-2}$ for PBTTT doped by F_4TCNQ[85] or 160 $\mu W\ m^{-1}\ K^{-2}$ for aligned P3HT doped by a Molybdenum Dithiolene Complex[86].

---

[15] 15 x 15 mm with a thermal gradient over the distance of about 12–14 mm. The conductivity was remeasured with an electrode spacing of around 10 mm, instead of the conductivity Long σ previously shown with 1.3 mm.

Table 4: Conductivity values for the doped polymers with AED (left) and MB (right). All measured values presented in this table have an estimated error of 20%. Majorily the thickness measurement is inducing this significant error on other measured quantities.

σ	*S*	*PF*	Quantity	σ	*S*	*PF*
S/cm	μV/K	μW m^{-1} K^{-2}	Units	S/cm	μV/K	μW m^{-1} K^{-2}
4300	23	230	Pg$_3$BTTT	2300	29	200
750			PBTTT-^{8}O	470		
400	18	13	PBTTT	380	22	18
520	19	19	Pg$_3$2T-T	340	22	16
120	42	21	P3HT	90	33	10
AED				MB		

The Seebeck coefficients are also tendentially higher in AED, which is a finding that is in accordance with a higher mobility rather than variation in doping level. The improvement is higher for the polythiophenes than the polythienothiophenes. This clearly shows the cohesive relationship between charge transport, conductivity and power factor. PBTTT with its recrystallisation using MB-doping is behaving differently than other polymers that showed improved microstructure with AED. **Understanding and managing doping-induced disorder in polymers is a highly promising route to higher conductivity and higher power factor**.

7.3.3. Conclusions

Anion exchange doping has a positive effect on the conductivity and charge transport in state-of-the-art polymers. A comparison between conductivity across different length scales shows excellent interconnectivity of polymers doped with Magic Blue and anion exchange doping. Based on GIWAXS and steady-state absorbance, anion exchange doping comes with a different relative intensity of charged species ([+]/[++]), improved paracrystallinity of ordered regions and better lamellar stacking. Cryogenic THz time-domain spectroscopy allows the comparison of doping-induced disorder between MB-doping and AED. AED mitigates doping-induced disorder and leads to smaller localization and in turn higher conductivities. At cryogenic temperatures, in the frozen disorder limit, the effect from static disorder dominates and gives a maximum activation energy of 10–40 meV. At elevated temperatures the activation energy becomes weaker until it vanishes. AED leads to lower activation energies in all polymers except for PBTTT, which undergoes a recrystallisation upon MB-doping, there both methods yield equal performance. Polythienothiophenes are particularly resilient to doping-induced disorder yielding band-like transport and the high conductivity and power factor up to 4800 S cm^{-1} and 230 μW m^{-1} K^{-2} respectively. Even though DPP polymers have D–A structures with reportedly high mobilities, they have smaller conductivity and higher localization, showing that reported high mobilities cannot compensate for charge carrier density and the doping-induced energetic landscape. In general, mitigating energetic disorder *via* modern doping methods, resilient backbones and glycolated side-chains is an important strategy to enhance the conductivity of doped conjugated polymers.

Supplementary Information

Charge transport in doped polymers

S.0. Methods

Batch specifications

The polymer Pg$_3$2T-T is a tailor-made polythiophene with triethylene glycol side-chains. The polymer Pg$_3$BTTT is a tailor-made derivative of PBTTT with triethylene glycol side-chains. PBTTT-C14 was also synthesized by the same collaborator to ensure that synthesis and high-quality processing is comparable to the glycolated derivatives. These materials were synthesized according to published synthesis routes[44, 45]. PBTTT8O is also a tailor-made material provided by collaboration with Nicolas Leclerc group as published[46]. Cyclic voltammetry and GPC/MALDI time of flight measurements were done preliminary to estimate relevant energy levels (HOMO/LUMO) and molecular weight (M_w). The M_w for the glycolated polymers could not be determined exactly using the above, because the signal extended above 50 kDA, which is above experimental limitations.

Pg$_3$2TT: HOMO = −4.46 eV, LUMO = −2.82 eV, batch-number: LB-195

Pg$_3$BTTT: HOMO = −4.48 eV, LUMO = −2.86 eV, batch-number: LB-188

PBTTT^{8}O: HOMO = −4.8 eV, LUMO = −2.9 eV, M_w = 30 kDA, batch-number: NL-1122.

PBTTT: HOMO = −5.11 eV, LUMO = −2.73 eV, M_w = 28 kDa, M_n = 39 kDa, D = 1.39, batch-number: IU-343

Moreover, the polymers P3HT, PDPP3T, PDPP4T and F8T2 were purchased from Ossila. The manufacturers published energy levels, molecular weights M_w, regioregularity (RR) and CAS-numbers are given here.

P3HT: HOMO = −5.2 eV, LUMO = −3.2 eV, M_w = 60 kDa, RR = 97.6%, CAS: 104934-50-1

PDPP3T: HOMO = −5.17 eV, LUMO = -3.61 eV, M_w = 67 kDa, CAS: 1198291-01-8

PDPP4T: HOMO = −5.2 eV, LUMO = −4.0 eV, M_w = 84 kDa, CAS: 1267540-03-3

F8T2: HOMO = −5.5 eV, LUMO = −3.1 eV, M_w = 64 kDa , CAS: 210347-56-1

Film preparation

Polymers were spin-coated with a polymer concentration between 8–10 mg/ml. The polymer solutions were stirred in solvents at elevated temperature for at least 3 hours. Solvents used were anhydrous chloroform CF (Pg_32T-T and Pg_3BTTT), anhydrous chlorobenzene CB (P3HT, PDPP3T, PDPP4T, F8T2), and anhydrous 1,2-dichlorobenzene DCB (PBTTT, $PBTTT^8O$); all purchased from Sigma Aldrich. The films were spin-coated at (1000-2000 rpm, 60 seconds) elevated temperatures, the temperature depends on the used solvent 35°C (CF), 80°C (CB, DCB). PBTTT, $PBTTT^8O$ and Pg_3BTTT are annealed at 110°C for 20 minutes. Based on steady-state absorbance the annealing recrystallizes PBTTT, $PBTTT^8O$, while for Pg_3BTTT no absorbance shift was seen.

Doping

The optimized doping concentrations are clearly stated in the main text. To ensure the same doping level when comparing immersed doping (ID) and anion-exchange doping (AED), I weighed the dopant in a vial and dissolved it in acetonitrile at double of the desired concentration. Then I added the same volume to either acetonitrile or acetonitrile containing the electrolyte in a 1:1 ratio. Moreover, the doping volume was controlled and we doped in tailored doping molds made from Teflon. At least 1.1 ml of doping solution was added to ensure a constant doping concentration in the solution with immersion time. Doping in a droplet (meniscus) or sequential spin-coating can lead to lower doping levels.

Steady-state absorbance

The steady-state absorbance is measured using a Perkin Elmer Lambda 950 including an integration sphere in transmission mode. The absorbance is calculated from the transmission T% and the absorbance of the substrate is subtracted as seen in the Methods Chapter 5. In the main Figure the absorbance are either normalized or corrected by minor differences in thickness between the spin-coated films. Therefore, Figure S.0.2. shows the non-normalized absorbance of the doped films.

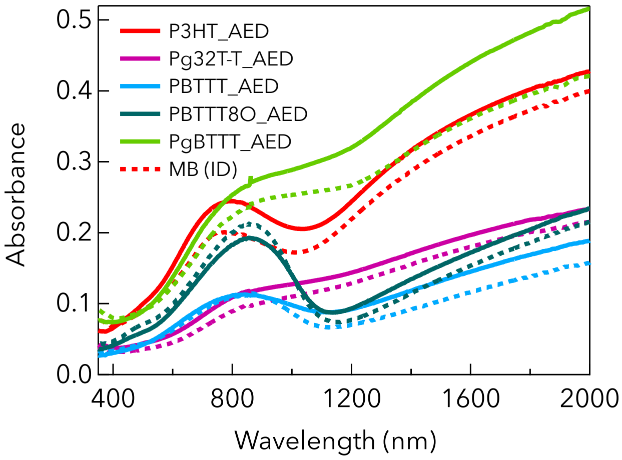

Figure S.0.2. Absorbance (non-normalized) for the doped polymers.

On the topic of batch-to-batch variations of the polymer Pg$_3$2T-T. The batch used for all presented measurements in the manuscript was synthesized by Lize Bynens from Wouter Maes' group. Since the conjugated polymers with triethylene glycol side-chains have a very low ionization energy (HOMO around −4.5 eV), the materials are very prone to oxygen doping. The following figure S.0.1. shows the neat absorbance of the material, whereby the violet curve labeled Pg$_3$2T-T (M) stems from a different batch. (M) depicts a more pronounced shoulder at 650 nm and less absorbance in the NIR indicating less oxygen doping. Overall, the absorbance spectrum of neat Pg$_3$2T-T (M) resembles the record material Pg$_3$BTTT. The absorbance of doped films looks almost identical, resulting in the same features and doping levels. The comparison between doped films from these Pg$_3$2T-T batches, shows minor improvements for the batch (M) and very reproducible trends for both the long/short and 10 K/295 K results.

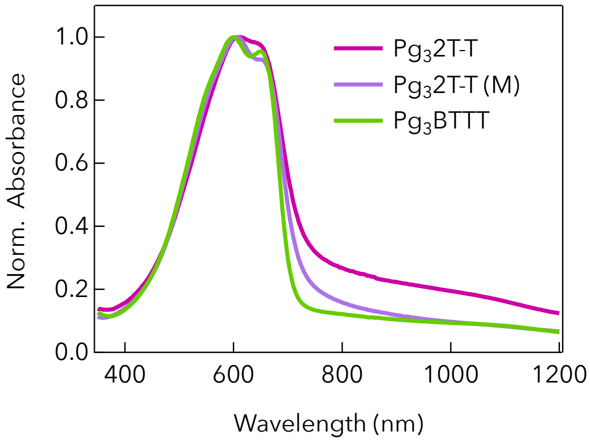

Figure S.0.1. Absorbance of neat films with triethylene glycol side-chains.

Structural characterization GIWAXS

Grazing-Incidence Wide-Angle X-ray Scattering (GIWAXS) is used for characterizing structural properties of the polymer samples. The experiment involves directing a beam of X-rays at a wide incidence angle onto the polymer film surface. The scattered X-rays are then detected on a 2D detector, which records the diffraction patterns. These patterns provide detailed information about the polymer's molecular packing, crystallinity, orientation, and degree of order. The paracrystallinity parameter is extracted by fitting the diffraction peaks using models such as the Scherrer equation. The 100 peak width (Δq) in reciprocal space is inversely proportional to the domain size and is influenced by paracrystalline distortions. The relationship between peak broadening and disorder is used to calculate the paracrystalline disorder g, which quantifies the extent of disorder in the ordered regions of the polymer films. The paracrystallinity disorder values are calculated from the FWHM of the lameller overtone peaks (100), (200) and (300). In some cases we had to use just (100) and (300), because (200) was almost fully suppressed. The broadening of the peaks are partly due to the crystallite size and partly due to the microstrain effect (paracrystallinity disorder). While finite crystallite size is independent of diffraction order, microstrain causes progressive broadening of diffraction peaks at higher order. Therefore, the slope obtained from the width progression with increased diffraction order (FWHM vs n^2) is giving the paracrystallinity disorder and leaving the crystallite size effect. Using just one peak would not give us the actual g value. Moreover, the 100 peak area is extracted. The peak area in GIWAXS is directly related to the volume fraction of the crystalline domains in the polymer sample. To extract the peak area, the scattering profile is deconvoluted into individual peaks using fitting techniques like Gaussian or Lorentzian functions.

Grazing-Incidence X-Ray Scattering (GIWAXS) samples are prepared on 1.5 x 1.5 cm Si <100> substrates. The data is collected at Stanford Synchrotron Radiation Lightsource (SSRL) Beamline 11-3 with 12 keV energy of X-Ray beam at 0.12° incidence angle. Obtained 2D patterns are processed by using Nika and WAXSTools packages built for IgorPro. The integrated patterns in out-of-plane and in-plane orientations are baselined and peak fit to Voigt. Out-of-plane integration from 0-10 radial angle is used to acquire (100) peak area and the full-width at half-maxima (FWHM) of the lamellar peaks. Paracrystallinity disorder is calculated by using the FWHM of lamellar overtones, (100), (200) and (300), by using the Williamson-Hall method.

S.1. Mitigating effect of AED upon MB-doping

S.1.1. Electrolyte concentration dependence in GIWAXS

Figure S.1.1. shows the paracrystalline disorder and the integrated (100) peak area for pristine and doped polymer films of polymers with triethylene glycol side-chains (a) Pg$_3$2T-T and (b) Pg$_3$BTTT. The paracrystallinity disorder for pristine films of Pg$_3$2T-T and Pg$_3$BTTT films is about 10%. Upon MB-doping the paracrystallinity doubles more or less to 20%.

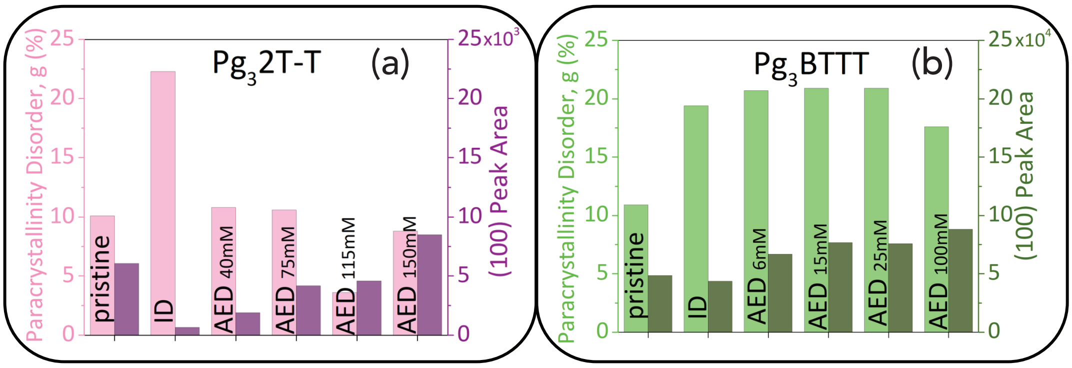

Figure S.1.1. GIWAXS paracrystallinity disorder and (100) peak area of pristine and doped films of (a) Pg$_3$2T-T and (b) Pg$_3$BTTT with increasing AED electrolyte concentration.

However, anion exchange doping does not mitigate the doping-induced structural changes in Pg$_3$BTTT to the same extent that it does in Pg$_3$2T-T. The paracrystallinity remains around 20% for anion-exchange doped Pg$_3$BTTT without a clear optimum. For the highest TBAPF$_6$ concentration there is a small decrease. The structural changes upon AED are different though. In doped Pg$_3$2T-T the anion exchange concentration optimum of 115 mM TBAPF$_6$ leads to a peak in the conductivity of around 600 S/cm. In contrary, the conductivity of Pg$_3$BTTT increases continuously with dopant and/or anion concentration for all investigated concentrations. Importantly, the polymer Pg$_3$BTTT is investigated for anion concentration up until 100 mM. At this highest concentration there is a small decrease in paracrystalline disorder. Therefore, investigating higher concentrations is planned.

S.1.2. GIWAXS 2D images

This section shows the GIWAXS 2D patterns that the calculated microstructural parameters are based on. Experimental details are given in the SI section S.0.

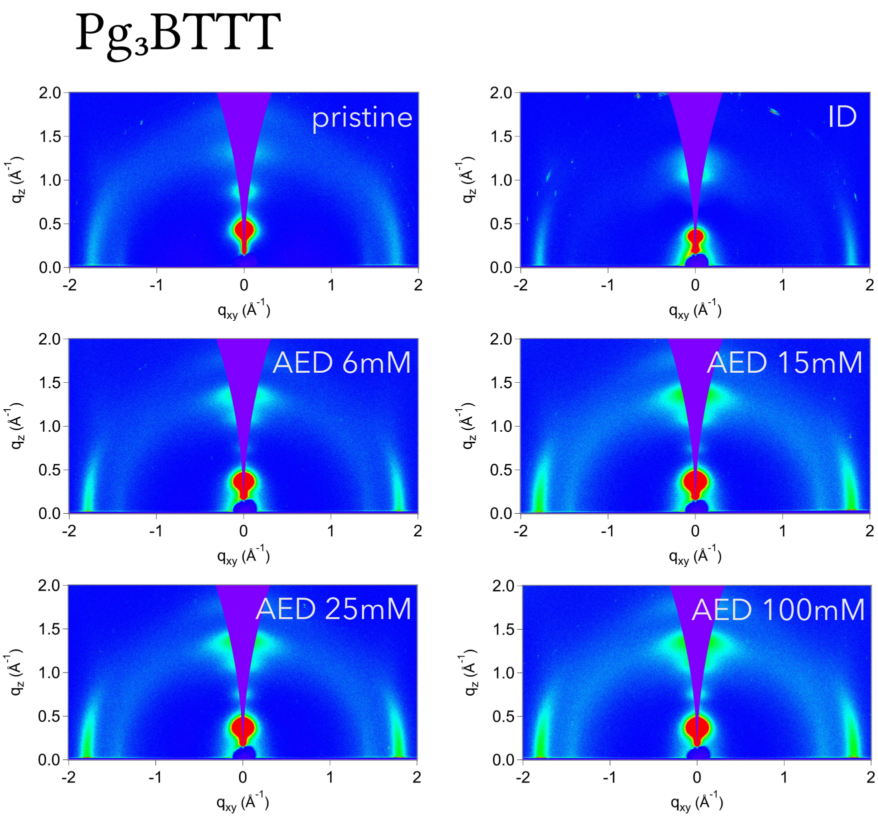

Figure S.1.2. The GIWXAS 2D patterns for pristine, immersed doping (ID) with MB and anion exchange doping (AED) with $TBAPF_6$ for Pg_3BTTT. MB-doping concentration of 285 uM and anion exchange using varying $TBAPF_6$ concentrations shown as an inset.

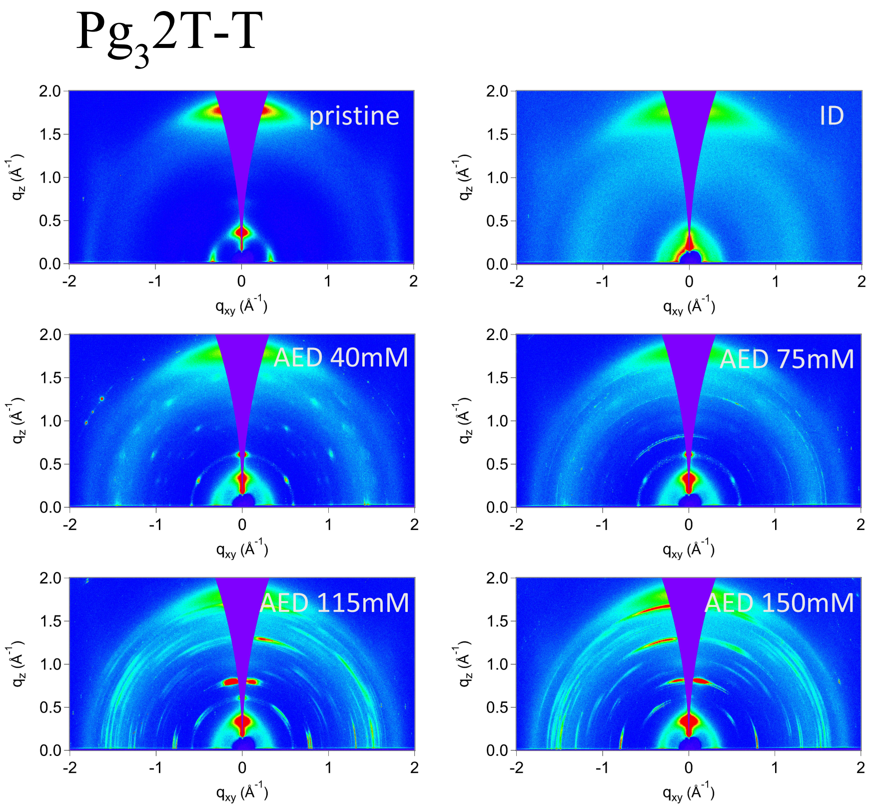

Figure S.1.3. The GIWXAS 2D patterns for pristine, immersed doping (ID) with MB and anion exchange doping (AED) with $TBAPF_6$ for Pg_32T-T. MB-doping concentration of 285 uM and anion exchange using varying $TBAPF_6$ concentrations shown as an inset.

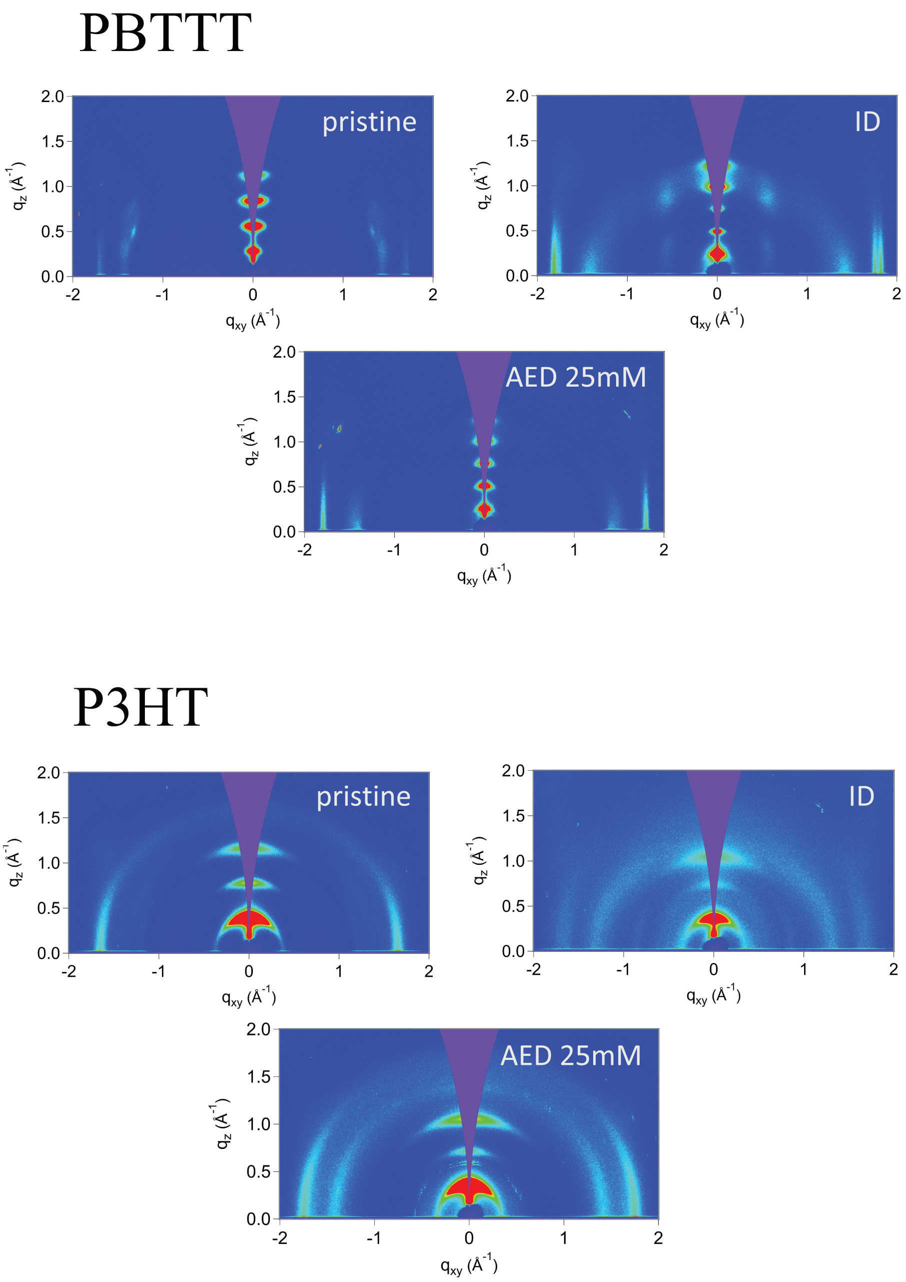

Figure S.1.4. The GIWXAS 2D patterns for pristine, immersed doping (ID) with MB and anion exchange doping (AED) with TBAPF$_6$ for (top) PBTTT and (bottom) P3HT.

S.1.3. Doping-induced disorder including F_4TCNQ doping of Pg_32T-T

Because no GIWAXS results for F_4TCNQ-doped Pg_32T-T on the polymer batch was available at the point in time of my hand-in, I focused on Magic Blue and the interesting observation of over-doping. Nevertheless, comparing the doping-induced disorder between the two dopants MB and F_4TCNQ, as well as anion exchange, is so intriguing that I am going to describe it here as well. For this measurement series, I use the previously determined optimized doping methods (or ceilings): (i) Pg_32T-T doped with 285 μM MB, (ii) doped with 285 μM MB and anion exchange with 115 mM $TBAPF_6$, (iii) doped with 575 μM F_4TCNQ and (iv) doped with 575 μM F_4TCNQ and anion exchange with 575 mM $TBAPF_6$. The following Table P.1. shows the film thickness *d*, the macroscopic (>1 mm) conductivity Longσ , the nanoscale (<100 nm) conductivity Shortσ at room temperature (before the cryogenic measurements). As such, the quotient Longσ/Shortσ is an estimate for the interconnectivity over macroscopic distances and it is >90% in all doped films. Pg_32T-T at high doping levels shows an excellent interconnectivity.

Table P.1. Comparison of interconnectivity by doping method showing the quotient between Longσ/Shortσ.

Quantity	d	Longσ	Shortσ	Longσ/ Shortσ	Color code
Units	nm	S/cm	S/cm		
F_4TCNQ	70	270	270	99%	🟨
F_4TCNQ+AED	40	530	570	93%	🟧
MB	42	350	375	95%	🟦
MB+AED	39	570	570	99%	🟪

Again, these values confirm the ceiling in conductivity with MB-doping and F4TCNQ-doping respectively, while the interconnectivity is excellent for all films. Temperature-dependent conductivity is a sensitive technique to study localization in terms of the reduced activation energy. A small activation energy leads to a weak temperature-dependent conductivity, while a big activation energy leads to a quickly decreasing conductivity with cooling according to the presented STLoT charge transport model shown in equation (4). Figure P.7. (a) shows the temperature-dependent THz conductivity for Pg_32T-T doped with four different methods. It is immediately evident that the doping method has a strong influence on the shape of the curves. Figure (b) shows the same curves normalized at room temperature, which emphasizes the differences in their temperature-dependence even more. To extract the degree of localization using the STLoT model is employed.

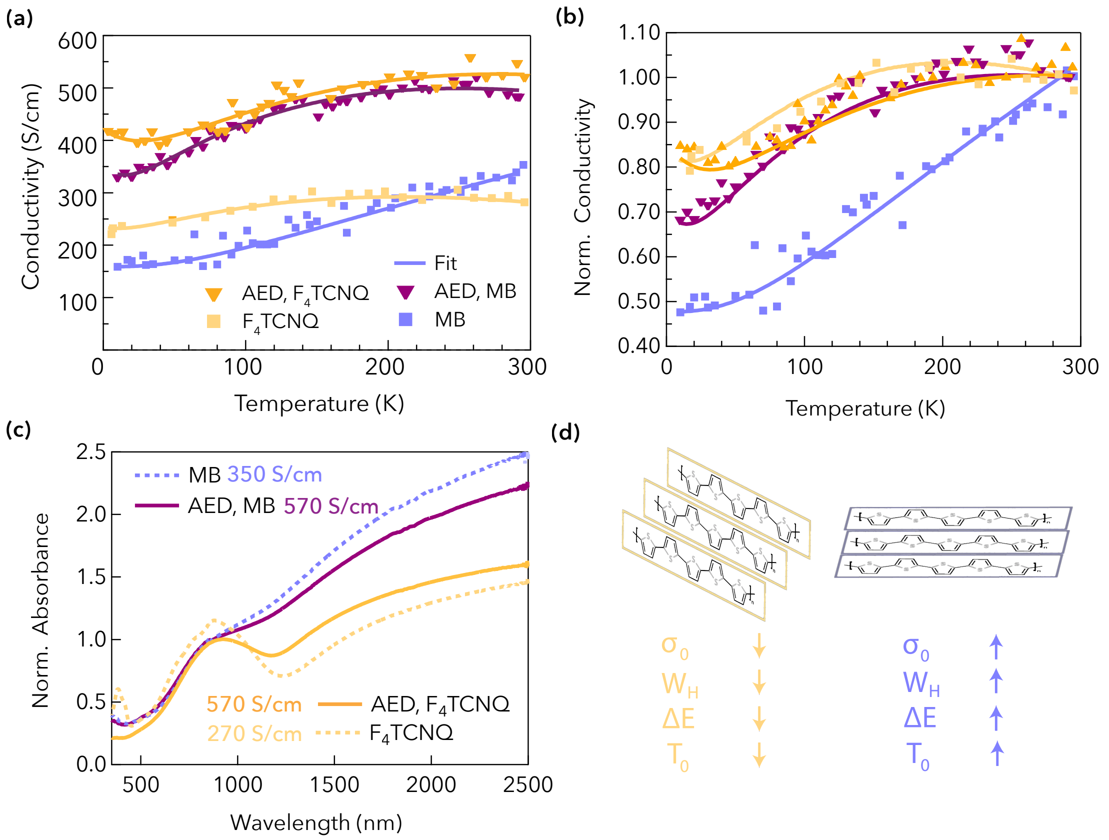

Figure S.1.5. (a) Conductivity versus temperature of the MB films and F_4TCNQ + PF_6^- films as the worst and best transport films. (b) Conductivity normalized at room temperature. For (a) and (b) the solid lines are a fit to equation. (c) Absorbance of polythiophene with different doping methods.

The solid lines in (a) and (b) represent fits with the proposed STLoT model given by equation (4). The charge transport model matches the experimental findings well and allows me to extract the parameters of interest. The extracted fit parameters are given in Table P.2 together with an estimated error from the model residuals but at least 20%. Figure P.7. (d) shows a visual summary of the findings achieved with the presented model related to MB “over doping”.

Table S.1.5. Fit parameters for semi-transient localized transport model. Estimated error of >20%.

Quantity	σ_0	T_0	W_H	ΔE	Color code
Units	S/cm	K	meV	meV	
F_4TCNQ	190± 40	130± 30	20± 4	90± 20	🟨
F_4TCNQ + PF_6^-	400± 80	170± 40	30± 6	100± 20	🟧
MB	300± 80	180± 40	40± 10	130± 20	🟦
MB + PF_6^-	350± 70	120± 30	20± 4	90± 20	🟪

MB-doping driven "over doping" and the corresponding structural changes lead to an increased activation energy as expected. It also leads to an increased crossover temperature T_0 and an increased energy difference to the transport edge ΔE. The resulting activation energy of 40 meV is the highest of all compared doping methods. The other doping methods also give interesting information about the underlying charge transport. F_4TCNQ-doping for example shows that the lowest conductivity 270 S/cm in the effective measured conductivity (Table P.1.). It also shows the lowest 190 S/cm (temperature-independent) model pre-factor. The activation energy on the contrary is among the lowest with 20 meV. On the contrary, from the data in Figure S.1.5. (a) and the fit parameters in Table S.1.5. F_4TCNQ-doping has a very weak temperature dependence that corresponds to an activation energy of 20 meV. Notably, all extracted fit parameters yield reasonable values with tens of meV for the reduced activation energy and around 100 meV with small differences based on the doping method, which matches the experimental observations.

S.2. Localized transport with n- or p-type doping

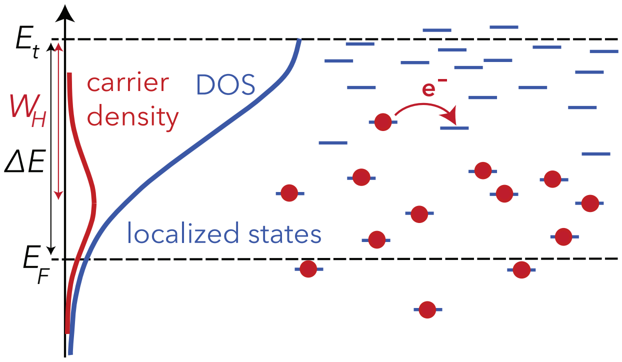

Figure 1. Scheme of localized electronic states.

The top panel depicts the representation of “bottom-up” filling of the density of states for n-type doping. Here, the DOS represents a LUMO energy level, where the Fermi level is lower in energy. Doping induces electrons in the LUMO level.

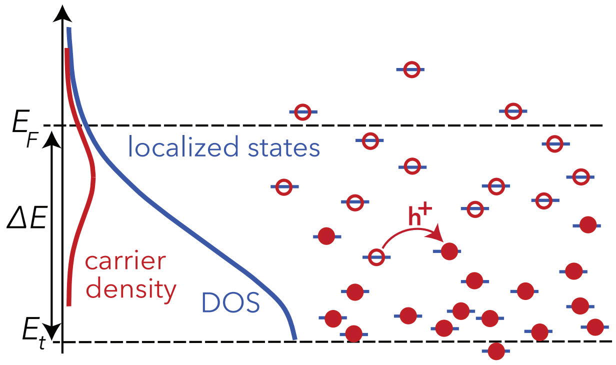

Figure S.2. Scheme of localized electronic states for p-doping. The DOS represents the HOMO.

Below is the visualization in the case of p-type doping. The figure shows electrons as filled circles and holes as open circles and a gradual filling of the density of states. The density of states hereby represents the upper edge of the HOMO energy level. The carrier density represents the holes and the Fermi energy is depicted as the upper dashed line.

S.3. THz conductivity with DSM

The Figure S.3.1. shows THz conductivity spectra with Drude–Smith fits corresponding to the mobility shown in the main text. Hereby, the MB doped films are always in the panel on the left and anion exchange doped films are always in the panel on the right. It shows polythiophenes P3HT and Pg$_3$2T-T. The light blue color always represents the THz conductivity at 10 K. The doped polymers show the same trends as the materials shown in the main text. Hereby, the real part of the complex conductivity decreases and the imaginary part of the conductivity becomes steeper and more negative at cryogenic temperatures. The decrease in conductivity is assigned to the mobility rather than the carrier density as well. The PTs seen in Figure S.3.1. show a higher tempertature dependence than PTTs, while nevertheless >40% of the conductivity at room temperature is restored at 10 K. The complex conductivity spectra are fit with the DSM. The entire list of DSM fit parameters are presented in Table S.3.1. for AED and MB-doping.

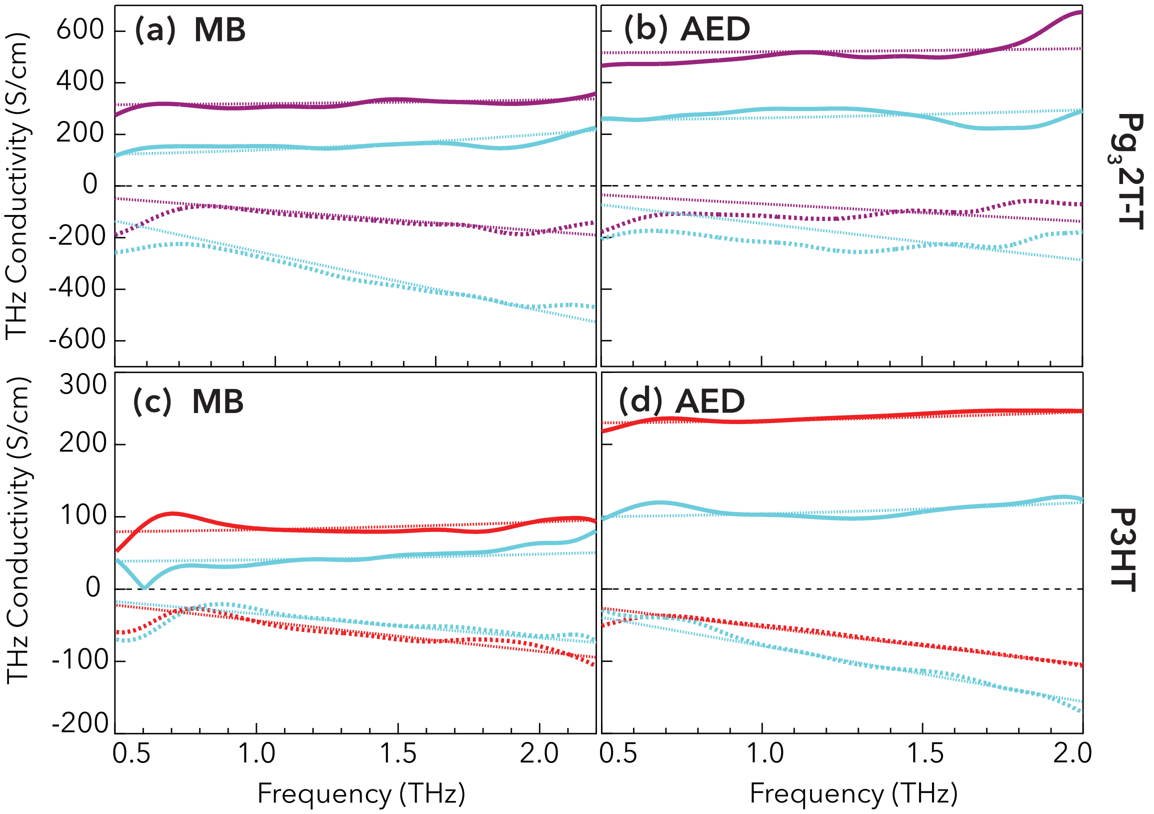

Figure S.3.1. THz conductivity and DSM fits for PTs doped by (a) MB or (b) AED.

MB-doping and AED of conjugated polymers results in different DSM fit parameters: charge carrier density *N*, scattering time τ and localization parameter c_1. The improved conductivity can be predominantly assigned to an improved effective mobility which is presented in the main text and here as well for completion together with the carrier density *N*. The carrier density remained mostly stagnant when comparing MB-doping and AED according to the DSM fits. Even the fit parameters for P3HT suggest a higher carrier density with AED, the improved mobility is a consistent result for all polymers that were included in the study. In the DSM, the scattering time τ and the localization parameter c_1 together influence the calculated effective mobility. See Chapter 5 for a detailed description. While these two parameters are co-dependent in the DSM fit and should be considered together, the localization parameter c_1 does explain the mobility trends pretty well. The localization parameter c_1 is consistently closer to 0 when AED is employed. This shows that AED mitigates doping-induced disorder which results in less localized charges. The localization parameter becomes slightly closer to -1 with cooling. Hence, in the frozen disorder limit, the localization increases slightly showing that a weak localization and fluctuation-assisted corrections are observed.

Table S.3.1: Conductivity values for the films doped with AED and MB-doping. All values presented from the DSM have an estimated error of 25%.

Quantity	Shortμ 295 K	Shortμ 10 K	N 295 K	N 10 K	τ 295 K	τ 10 K	c_1 295 K	c_1 10 K
Units	cm^2/Vs	cm^2/Vs	cm^{-3}	cm^{-3}	fs	fs	fs	fs
AED								
Pg$_3$BTTT	8	5	3×10^{21}	3×10^{21}	17	18	-0.53	-0.74
PBTTT^{8}O	5	4	1×10^{21}	1×10^{21}	15	13	-0.7	-0.7
PBTTT	0.8	0.7	3×10^{21}	3×10^{21}	5	5	-0.84	-0.86
Pg$_3$2T-T	0.6	0.3	5×10^{21}	5×10^{21}	5	5	-0.89	-0.95
P3HT	0.5	0.2	3×10^{21}	3×10^{21}	5	5	-0.90	-0.96
ID								
Pg$_3$BTTT	6	5	3×10^{21}	3×10^{21}	16	15	-0.62	-0.65
PBTTT^{8}O	4	3	1×10^{21}	1×10^{21}	9	13	-0.53	-0.81
PBTTT	0.9	0.7	3×10^{21}	3×10^{21}	8	11	-0.89	-0.94
Pg$_3$2T-T	0.4	0.2	5×10^{21}	5×10^{21}	5	5	-0.92	-0.98
P3HT	0.4	0.2	1×10^{21}	1×10^{21}	6	6	-0.94	-0.96

S.4. Hall effect measurement

I measure the conductivity and the Hall mobility in the same geometry. The corresponding charge carrier density is calculated indirectly. The results are shown in a comparative manner in Table S.4. while the general results are also described in the main text. The comparison between literature values, Hall mobility and THz mobility indicates that the Hall mobility is underdeveloped for the doped polymers bearing glycolated side-chains. Together with the THz complex conductivity this speaks against a fully developed band-like charge transport. This observation is non-trivial given the high conductivity of the polymers.

Table S.4.1. Hall effect measurement results in comparison to THz-TDS.

Polymer↓	Method	Long σ (S/cm)	d (nm)	μ (cm^2/Vs)	N (cm^{-3})
P3HT	THz	262	62	1.0	3×10^{21}
P3HT	Hall	230	52	0.3	3×10^{21}
Pg$_3$2T-T	THz	620	39	2.1	2×10^{21}
Pg$_3$2T-T	Hall	382	95	0.1	3×10^{22}
PBTTT	THz	517	13	1.9	2×10^{21}
PBTTT	Hall	350	67	1.2	2×10^{21}
Pg$_3$BTTT	THz	3022	55	5.4	2×10^{21}
Pg$_3$BTTT	Hall	2870	65	0.3	7×10^{22}

S.5. Arrhenius and Zabrodskii analysis

This supplementary Figure S.5. shows the Zabrodskii and Arrhenius plot for MB-doped polymer films. Both analysis methods confirm a crossover temperature somewhere between 50 and 200 K. The so-called Zabrodskii analysis is shown in panel (c) and (d). In the Zabrodskii analysis, the derivative: $W = \frac{\mathrm{d}\,ln(\sigma)}{\mathrm{d}\,ln(T)}$ is plotted on a log-log-scale. So, how does the reduced activation energy W change with temperature T. In (c) at low temperatures, the reduced activation energy W has a negative slope *versus* T. In (d) the reduced activation energy W is constant *versus* T. The slope k is shown as an inset, it can be an indicator for the dominant charge transport. The activation energy is shown as an inset calculated by $W_H =- W\ k_B\ T$. The linear fits in regime I correspond to an activation energy of several hundreds of meV, while the linear fits in regime II correspond to a vanished activation energy. The corresponding Arrhenius-type plots with all activation energies, can be found in the supplementary section S.5. So from this type of analysis I learn that the activation energy is somewhere between hundreds of meV and zero. The effective activation energy itself, as I defined it in Figure 1 (a), is a function of temperature. Based on this analysis the activation energy in the frozen disorder limit is smallest with 165 meV for doped Pg₃BTTT. Based on this analysis Pg₃2T-T has the highest activation energy in the frozen disorder limit.

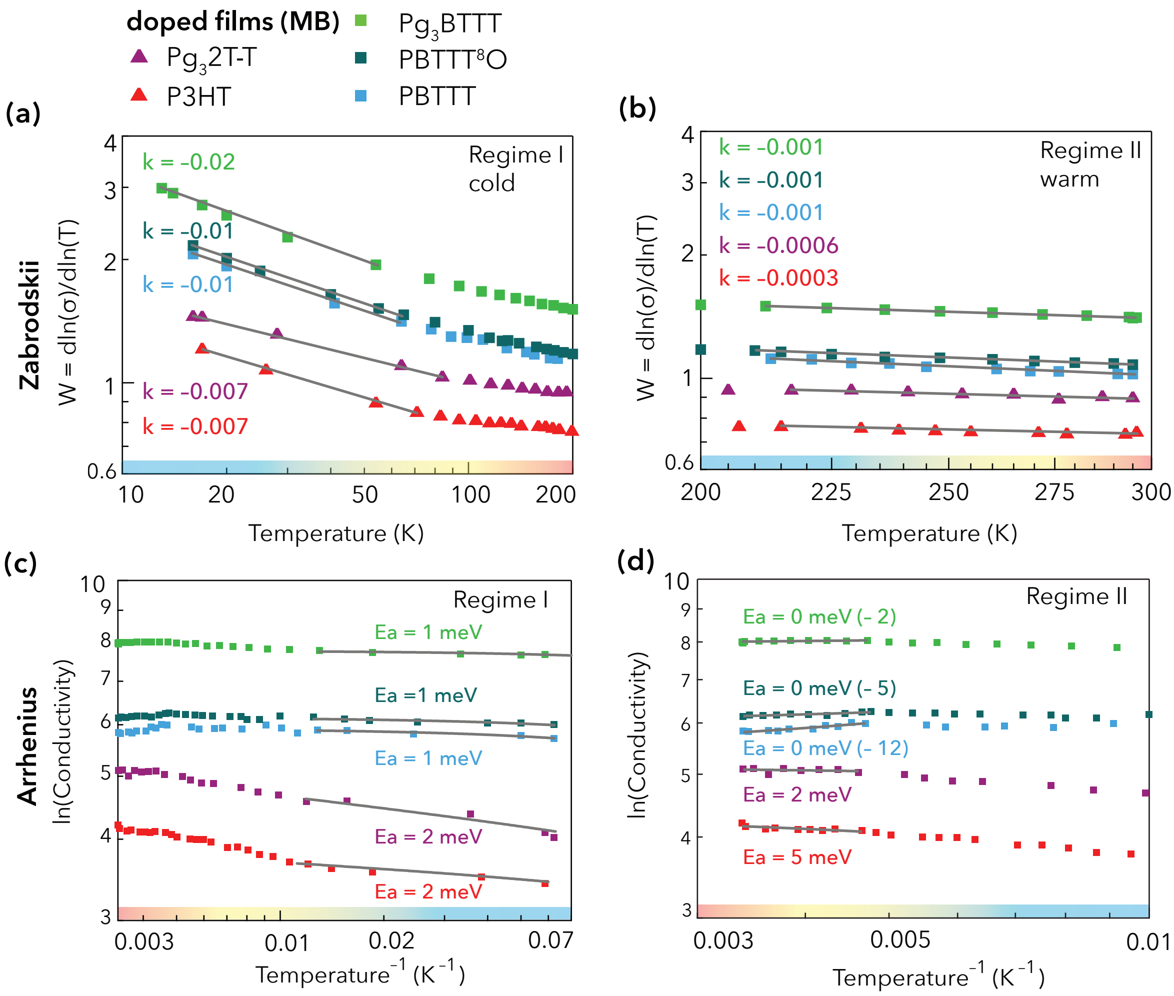

Figure S.5. Zabrodskii analysis in two different temperature regimes (a) < 50 K, (b) > 200 K. The slope k shown as an inset shows weak charge localization. Arrhenius plot, where the linear fit times Boltzmann constant gives the Arrhenius activation energies. (c) < 50 K and no activation (d) > 200 K.

The Arrhenius plot assumes a simple activated hopping model. Figure S.5. shows linear fits of the Arrhenius plot at two different temperature regimes (c) around room temperature 295–225 K and (d) at low temperatures 10–100 K. The activation energies are calculated by slope $k = -\frac{Ea}{k_B}$. While the charge transport of doped polymers is very commonly described by this model, this analysis treats charge transport as a duality. This model is not the most accurate tool to extract activation energies, because it fits only few data points. It is not taking into account direct observable phenomena of charge transport in doped polymers such as: crossover temperatures, band-like transport, tunneling or transient localization. The vanished activation energy above approximately 200 K has been confirmed by macroscopic and nanoscale conductivity measurements.

S.6. Semi-transient localized model full temperature range

The semi-transient localization model is a framework to estimate the doping-induced disorder. In this framework, the conductivity is a direct function of the distribution of energies in the DOS. This supplemenatary Figure S.6.1. shows the conductivity of MB-doped polymers *versus* temperature. The weak temperature dependence and sigmoid shape can not be described by pure hopping models. The data can also not be described by the semi-transient localization (SLoT) model, it needs the explicit consideration of fluctuation-induced processes or an unknown heterogeneous contribution. Since the THz conductivity measures the conductivity on the short-range scale, the former seems more applicable. Moreover, fluctuation-induced mechanisms are widely accepted in the research field of polymers and researchers attempt to correct the understanding of charge transport including them.

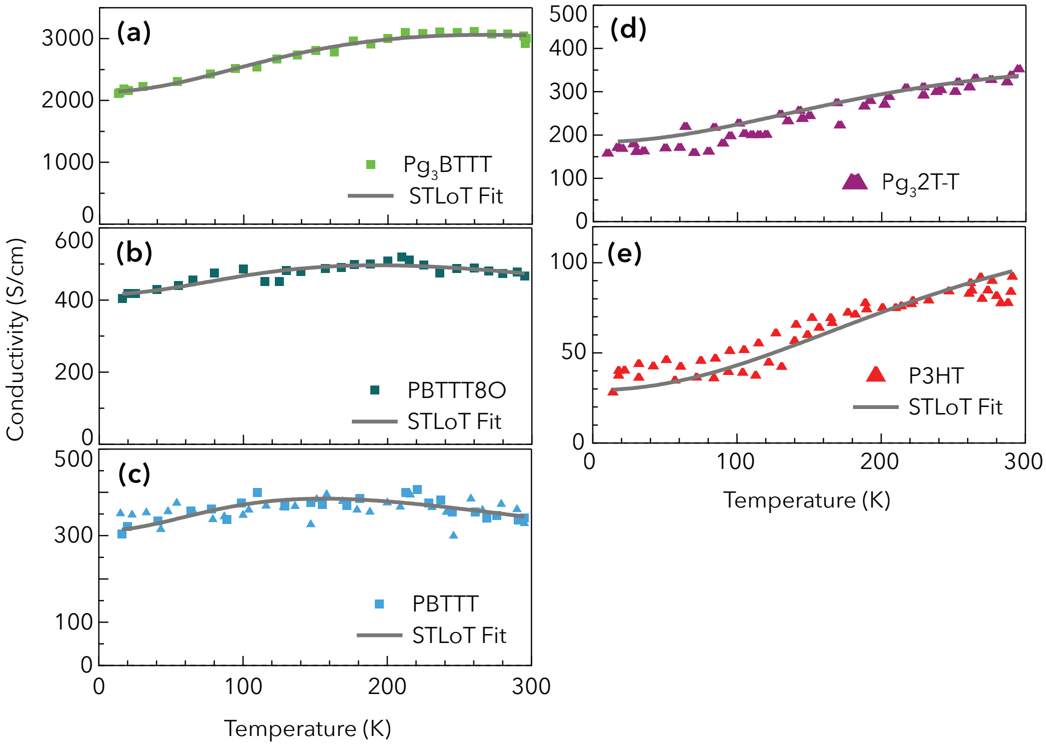

Figure S.6.1. STLoT fits of MB-doped polymers.

S.7. Generalized findings with DPP and F8T2 structures

High interchain mobility cannot compensate for charge screening effect

I aim to generalize the findings on charge transport by including DPP and F8T2 structures and investigate their temperature dependent conductivity. The DPP structures have a D–A type structure, which was designed for improved interchain transport and indeed high mobilities of up to 8 cm^2/Vs were reported. Since the DPP structures have a similar HOMO level as P3HT, I expect sufficient doping using the strong oxidant Magic Blue. Moreover, I include the structure F8T2 which has a lower-lying HOMO level. The steady-state absorbance spectra for pristine and MB-doped PDPP4T, PDPP3T and F8T2 are shown in Figure S.1.1. (c) and (d) respectively. Because the conductivities for F8T2 and the DPP polymers are lower, it is necessary to prepare thicker films for the THz time domain spectroscopy. To prepare the thicker films, I used the layering method, doping induced solubility control, proposed by Moulé *et al.*[30]. I studied the electrical conductivity of the films with 1,2,3 and 4 layers to confirm that the doping level and conductivity is consistent with an increasing amount of layering. Based on the thickness dependent THz signal, I prepared 2 layers of MB-doped P3HT, PDPP4T, F8T2 or 3 layers of MB-doped PDPP3T. The following Table S.1.1. shows the conductivity results of the thick films. First I see that the multilayer P3HT film has comparable characteristics to the thin films presented in the main text. It shows conductivities around 70 S/cm that drops to 46% of that value with cooling to 10 K. A general trend that I observe, is that the higher the overall conductivity, the higher also the quotient of Longσ/Shortσ. This parameter is used to describe the interconnectivity and the observed trend could originate from reduced localization with higher doping levels. The lowest Longσ/Shortσ conductivity restoration here is 35% for PDPP3T, which is still a relatively high value if we keep in mind Chapter 6 of this thesis. The quotient of Shortσ(10K)/Shortσ(295K) shows that the DPP structures have more localized transport (24%–33%). This indicates that the donor-acceptor type molecules with reported high mobilities can not compensate for the lacking charge screening effect. Surprisingly, F8T2 which has the lowest doping driving force performs decently in the middle range with around 60 S/cm, a Longσ/Shortσ restoration of 84% and a Shortσ(10K)/Shortσ(295K) restoration of 36%.

Table S.2.1. Parameters that describe the charge transport for thick films of doped polymers.

Quantity	d	Longσ	Shortσ	Shortσ 295 K	Shortσ 10 K	Longσ/ Shortσ	Shortσ 10K/ Shortσ 295K
Units	nm	S/cm	S/cm	S/cm	S/cm		
P3HT	455	73	89	67	31	83%	46%
PDPP4T	464	76	89	75	18	86%	24%
PDPP3T	626	19	54	52	17	35%	33%
F8T2	444	59	70	46	17	84%	36%

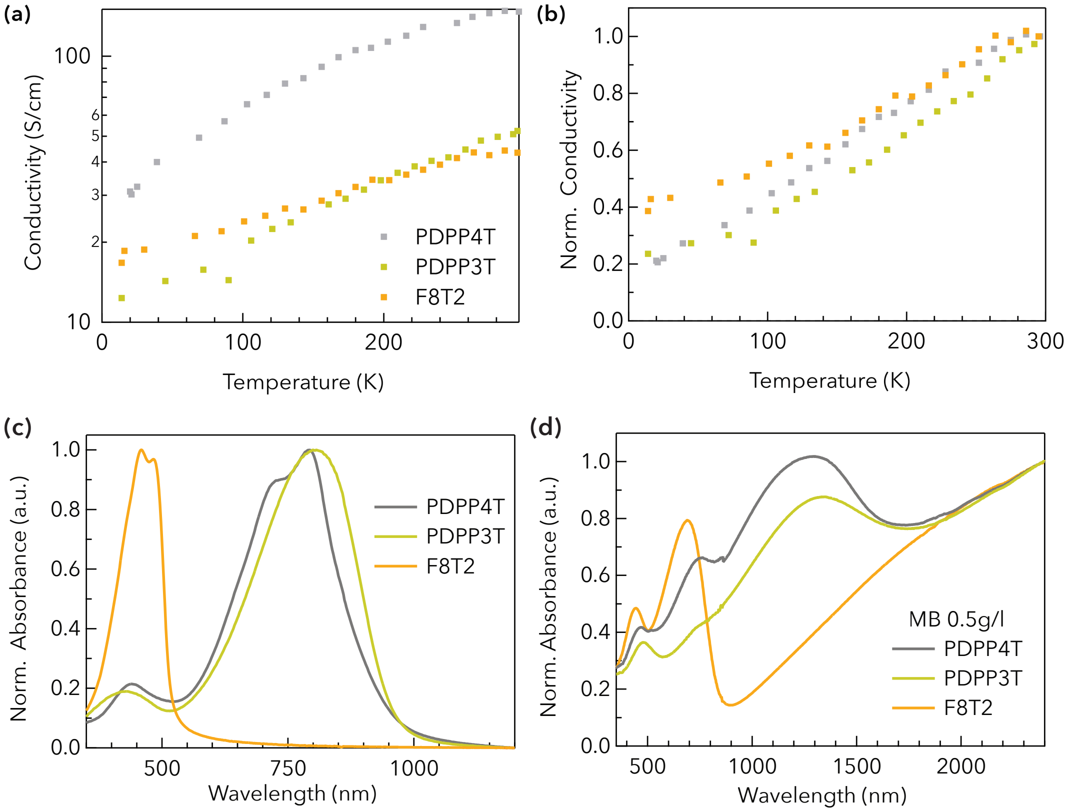

Figure S.2.1. (a) Temperature dependent THz conductivity for DPP structures and F8T2, (b) normalized at room temperature, (c) steady-state absorbance spectra and (d) doped absorbance spectra.

References for Chapter 7

1. Tietze, M.L., et al., *Elementary steps in electrical doping of organic semiconductors.* Nat Commun, 2018. **9**(1): p. 1182.
2. Pingel, P. and D. Neher, *Comprehensive picture ofp-type doping of P3HT with the molecular acceptor F4TCNQ.* Physical Review B, 2013. **87**(11).
3. Hynynen, J., et al., *Enhanced Electrical Conductivity of Molecularly p-Doped Poly(3-hexylthiophene) through Understanding the Correlation with Solid-State Order.* Macromolecules, 2017. **50**(20): p. 8140-8148.
4. Lüssem, B., M. Riede, and K. Leo, *Doping of organic semiconductors.* PSS physica status solidi (a), 2013. **210**(1): p. 9-43.
5. Chiang, C.K., et al., *Electrical Conductivity in Doped Polyacetylene.* Physical Review Letters, 1977. **39**(17): p. 1098-1101.
6. Cho, K.G., et al., *Sub-Band Filling and Hole Transport in Polythiophene-Based Electrolyte-Gated Transistors: Effect of Side-Chain Length and Density.* Advanced Functional Materials, 2023. **33**(37).
7. Tjhe, D.H.L., et al., *Non-equilibrium transport in polymer mixed ionic-electronic conductors at ultrahigh charge densities.* Nat Mater, 2024.
8. Jacobs, I.E., et al., *Structural and Dynamic Disorder, Not Ionic Trapping, Controls Charge Transport in Highly Doped Conducting Polymers.* J Am Chem Soc, 2022. **144**(7): p. 3005-3019.
9. Gregory, S.A., et al., *Quantifying Charge Carrier Localization in PBTTT Using Thermoelectric and Spectroscopic Techniques.* J Phys Chem C Nanomater Interfaces, 2023. **127**(25): p. 12206-12217.
10. Koopmans, M., et al., *Electrical Conductivity of Doped Organic Semiconductors Limited by Carrier-Carrier Interactions.* ACS Appl Mater Interfaces, 2020. **12**(50): p. 56222-56230.

11. Kaiser, A.B., et al., *Charge transport in conducting polymers.* Molecular Crystals and Liquid Crystals, 2004. **415**(1): p. 115-124.
12. Limelette, P., N. Leclerc, and M. Brinkmann, *Heterogeneous Oriented Structure model of thermoelectric transport in conducting polymers.* Sci Rep, 2023. **13**(1): p. 21161.
13. Gregory, S.A., et al., *Quantifying charge carrier localization in chemically doped semiconducting polymers.* Nat Mater, 2021. **20**(10): p. 1414-1421.
14. Yamashita, Y., et al., *Transition between band and hopping transport in polymer field-effect transistors.* Adv Mater, 2014. **26**(48): p. 8169-73.
15. Senanayak, S.P., et al., *Room-temperature bandlike transport and Hall effect in a high-mobility ambipolar polymer.* Physical Review B, 2015. **91**(11).
16. Sosorev, A.Y., *Simple charge transport model for efficient search of high-mobility organic semiconductor crystals.* Materials & Design, 2020. **192**.
17. Kang, K., et al., *2D coherent charge transport in highly ordered conducting polymers doped by solid state diffusion.* Nat Mater, 2016. **15**(8): p. 896-902.
18. Heck, A., J.J. Kranz, and M. Elstner, *Simulation of Temperature-Dependent Charge Transport in Organic Semiconductors with Various Degrees of Disorder.* J Chem Theory Comput, 2016. **12**(7): p. 3087-96.
19. Rammal, H., et al., *Transient Localization from the Interaction with Quantum Bosons.* Phys Rev Lett, 2024. **132**(26): p. 266502.
20. Fratini, S. and S. Ciuchi, *Dynamical localization corrections to band transport.* Physical Review Research, 2020. **2**(1).
21. Fratini, S., D. Mayou, and S. Ciuchi, *The Transient Localization Scenario for Charge Transport in Crystalline Organic Materials.* Advanced Functional Materials, 2016. **26**(14): p. 2292-2315.

22. Fratini, S., et al., *Charge transport in high-mobility conjugated polymers and molecular semiconductors.* Nat Mater, 2020. **19**(5): p. 491-502.
23. Keene, S.T., et al., *Efficient Electronic Tunneling Governs Transport in Conducting Polymer-Insulator Blends.* J Am Chem Soc, 2022. **144**(23): p. 10368-10376.
24. Abdalla, H., K. van de Ruit, and M. Kemerink, *Effective Temperature and Universal Conductivity Scaling in Organic Semiconductors.* Sci Rep, 2015. **5**: p. 16870.
25. Abdalla, H., G. Zuo, and M. Kemerink, *Range and energetics of charge hopping in organic semiconductors.* Physical Review B, 2017. **96**(24).
26. Marianer, S. and B.I. Shklovskii, *Effective temperature of hopping electrons in a strong electric field.* Phys Rev B Condens Matter, 1992. **46**(20): p. 13100-13103.
27. Noriega, R., A. Salleo, and A.J. Spakowitz, *Chain conformations dictate multiscale charge transport phenomena in disordered semiconducting polymers.* Proc Natl Acad Sci U S A, 2013. **110**(41): p. 16315-20.
28. Lemaur, V., et al., *Resilience to Conformational Fluctuations Controls Energetic Disorder in Conjugated Polymer Materials: Insights from Atomistic Simulations.* Chemistry of Materials, 2019. **31**(17): p. 6889-6899.
29. Hoffmann, S.T., H. Bässler, and A. Köhler, *What determines the inhomogeneous broadening of electronic transitions in conjugated polymers?* J. Phys. Chem. B, 2010. **114**(17037).
30. Suga, H. and S. Seki, *Frozen-in States of Orientational and Positional Disorder in Molecular-Solids.* Faraday Discussions, 1980. **69**: p. 221-240.
31. Walzer, K., et al., *Highly efficient organic devices based on electrically doped transport layers,* Chem. Rev. 2007, 107, 4, 1233−1271

32. Rivnay, J., et al., *Organic electrochemical transistors.* Nat Rev Mater, 2018. **3**(17086).

33. Noriega, R., et al., *A general relationship between disorder, aggregation and charge transport in conjugated polymers.* Nat Mater, 2013. **12**(11): p. 1038-44.

34. Meenakshi Upadhyaya, et al., *Raising Dielectric Permittivity Mitigates Dopant-Induced Disorder in Conjugated Polymers.* 2021.

35. Thomas, E.M., et al., *Role of Disorder Induced by Doping on the Thermoelectric Properties of Semiconducting Polymers.* Chemistry of Materials, 2018. **30**(9): p. 2965-2972.

36. Jacobs, I.E., et al., *Comparison of solution-mixed and sequentially processed P3HT:F4TCNQ films: effect of doping-induced aggregation on film morphology.* J. Mater. Chem. C, 2016. **4**(16): p. 3454-3466.

37. Untilova, V., et al., *Intercalation and Ordering of F6TCNNQ and F4TCNQ Dopants in Regioregular Poly(3-hexylthiophene) Crystals: Impact on Anisotropic Thermoelectric Properties of Oriented Thin Films.* Macromolecules, 2021. **54**(13): p. 6073-6084.

38. Scholes, D.T., et al., *The Effects of Crystallinity on Charge Transport and the Structure of Sequentially Processed F4TCNQ-Doped Conjugated Polymer Films.* Advanced Functional Materials, 2017. **27**(44).

39. Duong, D.T., et al., *The chemical and structural origin of efficient p-type doping in P3HT.* Organic Electronics, 2013. **14**(5): p. 1330-1336.

40. Asadi, K., et al., *Polaron hopping mediated by nuclear tunnelling in semiconducting polymers at high carrier density.* Nat Commun, 2013. **4**: p. 1710.

41. Arkhipov, V.I., et al., *Analytic model of carrier mobility in doped disordered organic semiconductors.* Physical Review B, 2005. **72**(23).

42. Neusser, D., et al., *High Conductivities of Disordered P3HT Films by an Electrochemical Doping Strategy.* Chemistry of Materials, 2020. **32**(14): p. 6003-6013.

43. Plyukhin, A.V., *Hitchhiking transport in quasi–one-dimensional systems.* Europhysics Letters (EPL), 2005. **71**(5): p. 716-722.

44. Chew, A.R., et al., *Sequential Doping Reveals the Importance of Amorphous Chain Rigidity in Charge Transport of Semi-Crystalline Polymers.* J Phys Chem Lett, 2017. **8**(20): p. 4974-4980.

45. Dash, A., et al., *Spontaneous Modulation Doping in Semi-Crystalline Conjugated Polymers Leads to High Conductivity at Low Doping Concentration.* Adv Mater, 2024. **36**(13): p. e2311303.

46. Zeng, H., et al., *Optimizing chain alignment and preserving the pristine structure of single-ether based PBTTT helps improve thermoelectric properties in sequentially doped thin films.* Journal of Materials Chemistry C, 2022. **10**(42): p. 15883-15896.

47. Hynynen, J., D. Kiefer, and C. Muller, *Influence of crystallinity on the thermoelectric power factor of P3HT vapour-doped with F4TCNQ.* RSC Adv, 2018. **8**(3): p. 1593-1599.

48. Hofmann, A.I., et al., *Chemical Doping of Conjugated Polymers with the Strong Oxidant Magic Blue.* Advanced Electronic Materials, 2020. **6**(8).

49. Murrey, T.L., et al., *Anion Exchange Doping: Tuning Equilibrium to Increase Doping Efficiency in Semiconducting Polymers.* J Phys Chem Lett, 2021. **12**(4): p. 1284-1289.

50. Scheunemann, D., et al., *Charge transport in doped conjugated polymers for organic thermoelectrics.* Chemical Physics Reviews, 2022. **3**(2).

51. Kim, N.Y., et al., *Enhanced doping efficiency and thermoelectric performance of diketopyrrolopyrrole-based conjugated polymers with*

extended thiophene donors. Journal of Materials Chemistry C, 2021. **9**(1): p. 340-347.

52. Karpov, Y., et al., *High Conductivity in Molecularly p-Doped Diketopyrrolopyrrole-Based Polymer: The Impact of a High Dopant Strength and Good Structural Order.* Adv Mater, 2016. **28**(28): p. 6003-10.
53. Jacobs, I.E. and A.J. Moule, *Controlling Molecular Doping in Organic Semiconductors.* Adv Mater, 2017. **29**(42).
54. Kiefer, D., et al., *Double doping of conjugated polymers with monomer molecular dopants.* Nat Mater, 2019. **18**(2): p. 149-155.
55. Guchait, S., et al., *Phase-Selective Doping of Oriented Regioregular Poly(3-hexylthiophene-2,5-diyl) Controls Stability of Thermoelectric Properties.* Advanced Functional Materials, 2024. **34**(39).
56. Yamashita, Y., et al., *Efficient molecular doping of polymeric semiconductors driven by anion exchange.* Nature, 2019. **572**(7771): p. 634-638.
57. Jacobs, I.E., et al., *High-Efficiency Ion-Exchange Doping of Conducting Polymers.* Adv Mater, 2022. **34**(22): p. e2102988.
58. Xiong, M., et al., *Counterion docking: a general approach to reducing energetic disorder in doped polymeric semiconductors.* Nat Commun, 2024. **15**(1): p. 4972.
59. Lu, K., et al., *Molecular Doping-Driven Modulation of Domain Charge Transport Elevates Thermoelectric Performance in Polar Polythiophene.* ACS Materials Letters, 2024. **6**(9): p. 4351-4359.
60. Moulé, A.J., et al., *Quantifying Polaron Mole Fractions and Interpreting Spectral Changes in Molecularly Doped Conjugated Polymers.* Advanced Electronic Materials, 2021.

61. Wu, E.C., et al., *Counterion Control and the Spectral Signatures of Polarons, Coupled Polarons, and Bipolarons in Doped P3HT Films.* Advanced Functional Materials, 2023. **33**(19).
62. Enengl, C., et al., *Doping-Induced Absorption Bands in P3HT: Polarons and Bipolarons.* Chemphyschem, 2016. **17**(23): p. 3836-3844.
63. Qarai, M.B., R. Ghosh, and F.C. Spano, *Understanding Bipolarons in Conjugated Polymers Using a Multiparticle Holstein Approach.* The Journal of Physical Chemistry C, 2021. **125**(44): p. 24487-24497.
64. Sahalianov, I., et al., *UV-to-IR Absorption of Molecularly p-Doped Polythiophenes with Alkyl and Oligoether Side Chains: Experiment and Interpretation Based on Density Functional Theory.* J Phys Chem B, 2020. **124**(49): p. 11280-11293.
65. Tsokkou, D., et al., *Bipolarons rule the short-range terahertz conductivity in electrochemically doped P3HT.* Mater Horiz, 2022. **9**(1): p. 482-491.
66. Cavassin, P., et al., *Electrochemical Doping in Ordered and Disordered Domains of Organic Mixed Ionic-Electronic Conductors.* Adv Mater, 2023. **35**(35): p. e2300308.
67. Mansour, A.E., et al., *Understanding the evolution of the Raman spectra of molecularly p-doped poly(3-hexylthiophene-2,5-diyl): signatures of polarons and bipolarons.* Phys Chem Chem Phys, 2022. **24**(5): p. 3109-3118.
68. Kroon, R., et al., *Polar Side Chains Enhance Processability, Electrical Conductivity, and Thermal Stability of a Molecularly p-Doped Polythiophene.* Adv Mater, 2017. **29**(24).
69. Hartenstein, B. and H. Bassler, *Transport Energy for Hopping in a Gaussian Density-of-States Distribution.* Journal of Non-Crystalline Solids, 1995. **190**(1-2): p. 112-116.

70. Bässler, H., et al., *Mapping the Density of States Distribution of Organic Semiconductors by Employing Energy Resolved–Electrochemical Impedance Spectroscopy.* Advanced Functional Materials, 2020. **31**(9).
71. Sakanoue, T. and H. Sirringhaus, *Band-like temperature dependence of mobility in a solution-processed organic semiconductor.* Nat Mater, 2010. **9**(9): p. 736-40.
72. Chen, C., et al., *Observation of Weak Counterion Size Dependence of Thermoelectric Transport in Ion Exchange Doped Conducting Polymers Across a Wide Range of Conductivities.* Advanced Energy Materials, 2023. **13**(9).
73. Chen, C., et al., *Single Atom Selenium Substitution-Mediated P-Type Doping in Polythiophenes toward High-Performance Organic Electronics and Thermoelectrics.* Advanced Electronic Materials, 2022. **8**(11).
74. Sheng, P., *Fluctuation-induced tunneling conduction in disordered materials.* Phys. Rev. B, 1980. **21**(2180).
75. Unuma, T., et al., *Direct observation of carrier delocalization in highly conducting polyaniline.* Applied Physics Letters, 2013. **103**(5).
76. Liu, K., et al., *A Quasi-2D Polypyrrole Film with Band-Like Transport Behavior and High Charge-Carrier Mobility.* Adv Mater, 2023. **35**(40): p. e2303288.
77. Cocker, T.L., et al., *Microscopic origin of the Drude-Smith model.* Physical Review B, 2017. **96**(20).
78. Durand, P., et al., *Single Ether-Based Side Chains in Conjugated Polymers: Toward Power Factors of 2.9 mW m−1 K−2.* Advanced Energy Materials, 2021. **12**(2).
79. Murrey, T.L., et al., *Additive solution deposition of multi-layered semiconducting polymer films for design of sophisticated device architectures.* Journal of Materials Chemistry C, 2019. **7**(4): p. 953-960.

80. Liang, Z., et al., *Influence of dopant size and electron affinity on the electrical conductivity and thermoelectric properties of a series of conjugated polymers.* Journal of Materials Chemistry A, 2018.

81. Liang, Z., et al., *n-type charge transport in heavily p-doped polymers.* Nat Mater, 2021. **20**(4): p. 518-524.

82. Zhu, W., et al., *Enhancing the Conductivity and Thermoelectric Performance of Semicrystalline Conducting Polymers through Controlled Tie Chain Incorporation.* Adv Mater, 2024. **36**(28): p. e2310480.

83. Yamashita, Y., et al., *Transition Between Band and Hopping Transport in Polymer Field-Effect Transistors.* Adv. Mater., 2014. **26**.

84. Baranovskii, S.D., et al., *Effective temperature for electrons in band tails.* Journal of Non-Crystalline Solids, 1993. **164-166**.

85. Patel, S.N., et al., *Morphology controls the thermoelectric power factor of a doped semiconducting polymer.* Sci Adv, 2017. **3**(6): p. e1700434.

86. Untilova, V., et al., *High Thermoelectric Power Factor of Poly(3-hexylthiophene) through In-Plane Alignment and Doping with a Molybdenum Dithiolene Complex.* Macromolecules, 2020. **53**(15): p. 6314-6321.

87. Dongmin Kang, S. and G. Jeffrey Snyder, *Charge-transport model for conducting polymers.* Nat Mater, 2017. **16**(2): p. 252-257.

8 THz photoconductivity and hole mobility of an organic–inorganic hybrid bilayer

> *"What we observe is not nature itself, but nature exposed to our method of questioning."*
>
> Werner Heisenberg.

This chapter is based on a communication in preparation for Materials Horizons. Julien Réhault contributed substantially by writing the data acquisition in LabView, by teaching me for the alignment of the pump beam and connection of a second delay stage. Dieter Neher contributed by providing the material and with engaged, deep discussions on the direction of the project. Ultimately, I have the lead of the project, processed the sample in the glovebox, built the telescope and pump–probe overlap in time and space, and undertook the measurements series in Natalie Banerji's laboratories. Moreover, I wrote the script for analysis and the communication.

Eva Röck, Julien Réhault, Dieter Neher, Natalie Banerji.

8.1 THz photoconductivity and hole mobility of an organic–inorganic hybrid bilayer

Abstract

Monolayer transition-metal dichalcogenides (TMDs) have potential for ultrathin, flexible and semi-transparent optoelectronics. TMDs are direct bandgap semiconductors that exhibit high-mobility charge transport in 2 dimensions. This motivates recent efforts to combine TMDs with organic semiconductors to form hybrid materials which feature the advantages of both materials. A strategy for hybrid optoelectronics is stacking a monolayer of TMD and a thin layer (≈ 10 nm) of an organic acceptor small molecule. Particularly, non-fullerene acceptor (NFA) molecules show unbeaten effectiveness in this field of organic optoelectronics. Upon photo-excitation, an exciton is formed and dissociates at the interface between TMD and molecular acceptor. This multi-step process generates mobile holes in the TMD layer. Moreover, signatures from trions, charged excitons, i.e., electron–hole–electron or hole–electron–hole, occur in monolayer TMD. In this chapter, I investigate monolayer tungsten diselenide (WSe_2) with and without a non-fullerene acceptor molecule (IT-4F) layer. Using optical pump-terahertz probe (OPTP) time-domain spectroscopy, I track photo-generated charge carriers, their density, mobility and dynamics. The optical pump at 700 nm excites both, the WSe_2 monolayer and the IT-4F layer. In neat WSe_2, I observe photoconductivity of charged species that are largely immobile, which can be assigned to trions. The presence of an IT-4F layer increases the mobility of charge carriers up to 160 cm2/Vs and up to 47% of incident photons form a mobile charge. Up to 50% of all generated charge carriers are long-lived and remain for more than one nanosecond. This work provides important insights of photo-induced charge generation in TMD–NFA hybrid bilayers for optoelectronic applications.

8.1.1 Introduction

2-dimensional transition-metal dichalcogenides and organic molecules

Following the prominent organic donor–acceptor molecule optoelectronics, hybrid organic–inorganic optoelectronics are investigated intensively[1-6]. Particularly, combining transition-metal dichalcogenides (TMDs) with organic small molecules gained significant attention since Hersam *et al.* reported the photovoltaic effect in such a hybrid material (MoS_2:PTB7) in 2016[7]. Efficiency governing parameters were identified including the molecular orientation at the heterojunction[8, 9] and the potential energy landscape at the organic–TMD interface[10, 11]. Also, major limitations have been identified: defect assisted electron–hole recombination across the hybrid interface being a key limiting factor[12].

Monolayer WSe_2 is an ultrathin, flexible and semi-transparent **transport layer**. It has a direct bandgap in the visible (1.6 eV) and strong Coulomb binding energies (100–500 meV) which allows the effective formation of stable excitons[10, 13, 14]. Exciton dissociation at an interface with matching energy alignment can create highly mobile charge carriers (50–200 cm^2/Vs)[15, 16]. This motivates the combination of monolayer WSe_2 with **electron-accepting small molecules** for optoelectronics with highly mobile charge carriers. WSe_2 has been studied in combination with acceptor molecules such as fullerene (C_{60}), 3,4,9,10-perylenetetracarboxylic dianhydride (PTCDA), and 3,4,9,10-perylenetetracarboxylic diimide (PTCDI)[17, 18]. A famous class of organic small molecules are non-fullerene acceptors (NFAs), which led to major improvements in the organic photovoltaics field[19-21]. Among the high-efficiency NFAs, the ITIC[1] family gained a lot of attraction since its first synthesis in 2015[22]. IT-4F[2] is such a non-fullerene acceptor molecule that has shown efficient charge generation in combination with different donor molecules[23]. IT-4F shows the end-group of 2-(3-oxo-2,3-dihydro-1H-inden-1-ylidene) malononitrile (INCN) which is symmetrically (tetra-)fluorinated. By enhancing the fluorination density, the energy of both the

---

[1] First synthesized in 2015 with the full chemical name: (2,20-[[6,6,12,12-tetrakis(4-hexyl-phenyl)-6,12-dihydrodithieno[2,3-d:20,30-d0]-s-indaceno[1,2-b:5,6-b0]dithiophene-2,8-diyl] bis[methylidyne(3-oxo-1H-indene-2,1(3H)-diylidene)]]bis[propanedinitrile])

[2] Popular non-fullerene acceptor from the ITIC family, also known as ITIC-4F. Full chemical name: 3,9-bis(2-methylene-((3-(1,1-dicyanomethylene)-6,7-difluoro)-indanone))-5,5,11,11-tetrakis(4-hexylphenyl)-dithieno[2,3-d:2',3'-d']-s-indaceno[1,2-b:5,6-b']dithiophene.

highest occupied molecular orbital (HOMO) and the lowest unoccupied molecular orbital (LUMO) levels are decreased. This leads to a contracted optical bandgap. Furthermore, its high crystallinity and energy level alignment with common donor polymers such as PM6 contribute to high power conversion efficiencies (PCEs) in OPVs, often exceeding 15%[23-25]. The combination of WSe_2:IT-4F in a bilayer for optoelectronics is favorable based on simple energy level alignments, but their complex photoconductivity has not been studied experimentally to the best of my knowledge.

Photo-induced charge generation at organic–inorganic interface

In literature the process of photo-induced generation of mobile charges at an interface is described as threefold: (i) exciton formation by photon absorption, (ii) exciton diffusion to the interface followed by (iii) charge transfer (CT) [9, 19, 26-28]. In the case of TMD–NFA, these steps will provide a **hole in the TMD layer**. First, let's introduce the charge generation induced by an optical pump in more detail. Figure 1 (a) shows a simplified sketch of optical pump pulse, THz probe pulse (to the left of a sample) and a transmitted THz pulse with and without a previous optical pump (to the right). Since both monolayer TMD and NFA absorb in the visible one can imagine the processes described in Figure 1 (b) and (c). In (b) the steps are shown upon photo-excitation of the TMD and in (c) the steps upon photo-excitation of the NFA layer. Photo-excitation of the TMD leads to electron transfer from the conduction band of the inorganic to the LUMO of the organic molecule. Photo-excitation of the NFA might lead to hole transfer from the HOMO of the organic molecule to the valence band of the inorganic TMD. This picture of course is vastly simplifying the involved energy levels. It is not depicting band bending at the interface or polarization effects that complicate a full understanding of energy level alignments. In fact, the investigation of energy level alignments in TMD:NFA bilayer systems is a discussed research topic[11, 12]. **Marcus theory of electron transfer**[29] is applied and established to describe electron transfer across organic–organic interfaces[28, 30]. Using Marcus theory to describe charge transfer processes across organic–inorganic interfaces is still relatively rare[31]. According to Markus theory, the electron transfer rate is a function of the transfer integral, the **reorganization energy** and the **Gibbs free energy** between the two states. In the article by Wang *et al.*, the energy offset between the molecule HOMO and the TMD valence band is used as a measure for the Gibbs free energy[31]. The energy offset seen in Figure 1 (c) energetically enables the dissociation of an exciton at the hybrid interface which involves hole transfer from the molecule's HOMO to the photo-generated hole in the TMDs valence band.

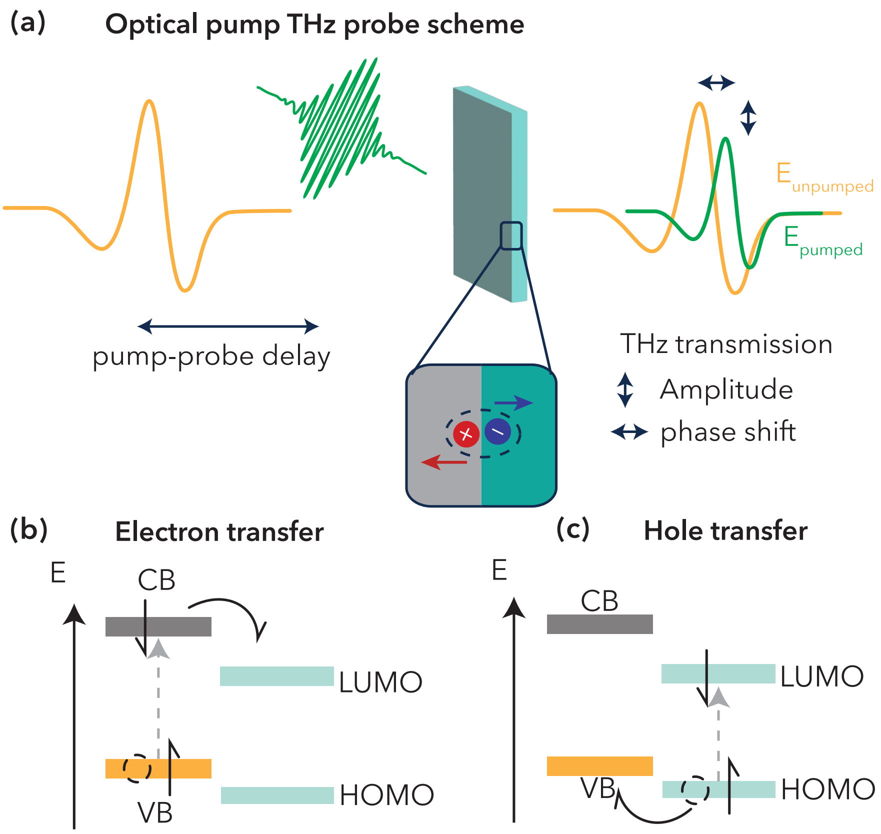

Figure 1. (a) Graphical abstract of the optical pump–THz probe experiment on a hybrid bilayer. Charge generation process upon (b) photo-excitation of the inorganic monolayer TMD leads to electron transfer from the conduction band and (c) photo-excitation of the NFA organic molecule leads to hole transfer from the molecule's HOMO.

The offset between IT-4F HOMO (−5.7 eV)[32] and WSe_2 valence band (−4.8 eV)[33] is 0.9 eV. Note that in this case also the energy offset from the WSe_2 conduction band (−3.2 eV) and the IT-4F LUMO (−4.1 eV) is 0.9 eV, as sketched in Figure 1 (b). Note that in this case the energy offset between IT-4F HOMO (−5.7 eV)[32] and WSe_2 valence band (−4.8 eV)[33] is 0.9 eV as well. At his point, I assume that both processes can occur and contribute to a photoconductivity signal. This type of energy level alignment for organic-inorganic hybrid materials is categorized as **type II: staggered band alignment** and is favorable for photo-transistors, photo-diodes and solar cells[1]. The reorganization energy is a measure of the structural relaxation that occurs in the material upon charge transfer or exciton creation. This energy depends on several factors, such as the electronic environment, interlayer coupling, and lattice dynamics[5, 9, 17, 31, 34]. Literature values for monolayer WSe_2 suggest that the reorganization energy for charge transfer processes typically ranges from 50 meV to 150 meV, depending on the environment and experimental conditions[35, 36]. Apparently, these are **favorable conditions** for efficient charge transfer at the WSe_2:IT-4F interface.

However, considering only the valence/conduction band levels and HOMO/LUMO levels provides a simplistic picture because it ignores the complex interfacial effects, environmental influences, charged excitons like trions and dynamic factors that define the true energy alignment at an interface. A more comprehensive approach would involve analyzing the **interface dipoles**, **polarization effects**, **band bending**, and **charge transfer states** using experimental techniques like UPS (Ultraviolet Photoelectron Spectroscopy) or computational methods like DFT (Density Functional Theory) tailored for interfaces[17, 18]. I hereby mainly aim to extend my expertise to the optical pump–THz probe technique and to hybrid bilayer systems. Nevertheless, this chapter quantifies photoconductivity and the charge transfer efficiency for the WSe_2:IT-4F bilayer as a direct observable. Controlling the fluence of the optical pump allows to calculate the number of incident photons and the fraction thereof that forms a mobile charge. Charged species, such as holes and electrons, move in a changing electric field. Therefore, a THz probe pulse moves charged species in a material. As such, optical pump–THz probe is a sensitive and powerful technique to investigate the photoconductivity in a material by providing a visible pump creating charged species and by probing their interaction with a THz pulse[37, 38]. The photoconductivity is referenced by a THz pulse that is transmitted through the material without a previous optical pump pulse. The THz electric field pulse transmitted through the pumped sample is referred to as E_{pumped} and the THz electric field pulse transmitted through the sample in ground-state as E_{unpumped} or E_0.

Photoconductivity insights from ultrafast THz spectroscopy

Figure 2 shows the OPTP setup with the fundamental laser beam in red (800 nm, around 40 fs pulsed with 1 kHz repetition rate) originating from the laser in the bottom left corner. There are three different colored beams in the scheme: red for the fundamental beam (800 nm), green for the optical pump beam (700 nm) and orange for the THz pulsed beam. The red beam hits the first beam splitter that splits the fundamental into two beams. One part goes into the optical parametric amplifier (OPA) which generates the optical pump beam, in this case a desired optical pump beam at 700 nm. The optical pump beam goes on the delay state D2 and through a chopper before exciting the sample (pump diameter 3.0 mm) and ending after. The second part is split again to fulfill the purpose of THz generation and THz detection respectively. The THz generation occurs in a zinc telluride (ZnTe) nonlinear crystal by optical rectification. The THz beam is focused on the sample (probe diameter 1.5 mm). The transmitted THz beam is then focused on a second ZnTe crystal for detection by electro-optic sampling (EOS). EOS is a technique used to measure the electric field of the transmitted THz pulse with high temporal and spatial resolution. It relies on the electro-optic (Pockels) effect, in which the polarization state of an optical beam (800 nm) is modulated by the electric field of the THz pulse as they interact in the second ZnTe nonlinear crystal. For more details on the pump generation, THz generation or THz detection including the technical specification, please see the supplementary section S.0. Methods. The **pump beam is chopped at half frequency 500 Hz** such that the immediate response of two sub-sequent THz pulses yields the differential THz pulse transmission. The photoconductivity is calculated from the differential signal using equation:

$$\sigma(\omega,t) = -\frac{n_0 + n_{\text{air}}}{Z_0 d} \cdot \frac{E_{\text{pumped}}(\omega,t) - E_0(\omega,t)}{E_0(\omega,t)} \qquad (1)$$

Hereby, $n_0 \approx 3,\ n_{\text{air}} \approx 1$ give the refractive index of the sapphire substrate and air respectively, $Z_0 = 376.7\ \Omega$ is the constant impedance of free space. d is the thickness of the sample, whereby it is important to use the thickness of the charge transport layer. Note that the THz probe is sensitive to mobile charges. Since I expect the WSe_2 monolayer to be the dominant charge transport layer, I use the thickness d=1.5 nm of the WSe_2 also for the measurements of the bilayer. $E_{\text{pump}}(\omega,t),\ E_0(\omega,t)$ is the transmitted THz electric field in the frequency domain of the photoexcited and ground state material respectively.

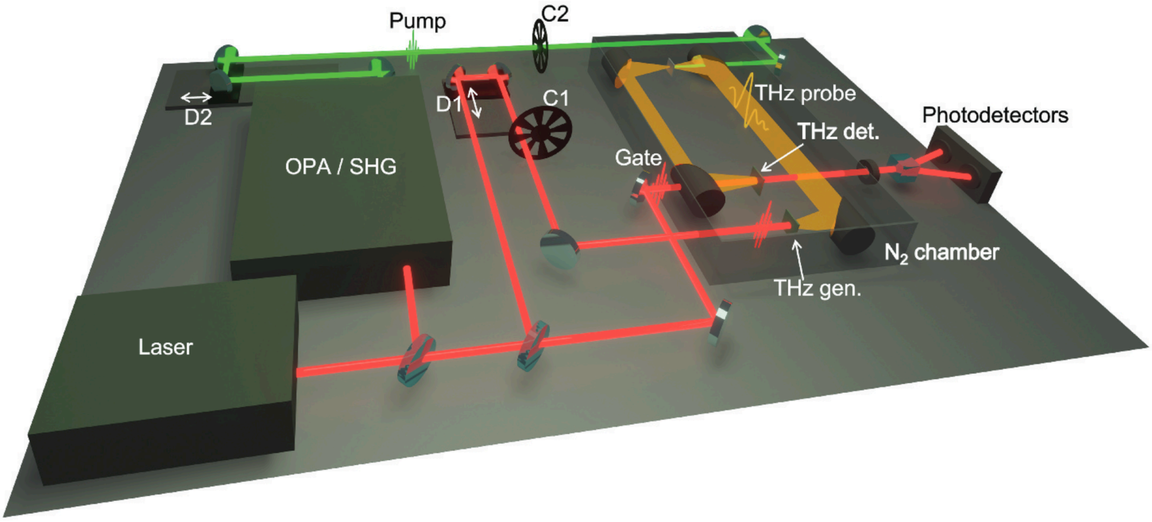

Figure 2: Optical pump–THz probe setup adopted from[39]. The sample is positioned in the focal point of the THz after the second parabolic mirror, where the beam size was determined as 1.5 mm. Guide your eye to the point where the green pump beam in the scheme ends. The sample was always in a chamber with inert atmosphere.

Using the setup shown in Figure 2., I measure photoconductivity spectra or dynamics. To measure the photoconductivity spectra over the entire THz waveform, I set the translation stage D2 of the pump–THz delay at a fixed time after photoexcitation. For example, the translation stage D2 is fixed at a delay of 10 ps after photoexcitation. Having the chopper set at half frequency in the optical pump beam allows me to measure $E_{\mathrm{pump}}(\omega)$ and $E_0(\omega)$ with two subsequent pump pulses. Then, I can scan the entire THz waveform by varying the translation stage D1 of EOS. This is done for all EOS delays and hence angular frequencies ω to obtain the waveform. I use parenthesis, because I am measuring in the time-domain and need to do a Fourier transform to obtain the waveform as a function of angular frequency ω.

To measure the photoconductivity dynamics, I set the translation stage D1 to the maximum of the differential THz waveform. Having the chopper set at half frequency in the optical pump beam allows me to measure $E_{\mathrm{pump}}(t)$ and $\mathrm{E}_0(\mathrm{t})$ with two subsequent pulses. Then, I can vary the time delay between optical pump and THz probe to get the dynamics of the maximum differential THz waveform.

Photoconductivity for the Drude- and Drude-Smith response

Ultrafast optical pump–THz probe spectroscopy is a powerful technique to study the charge carrier dynamics in optoelectronic materials like atomically thin TMDs[38]. The THz electric field pulse strongly **couples to charged particles**[38, 40]. Besides free electrons or holes, there are more charged species that might occur. The Coulomb binding energy in WSe$_2$, as mentioned previously, stabilizes excitons at room temperature[39, 41]. This enables charged excitons such as trions to form. Trions are combinations of an exciton and a charge (electron–hole pair plus another electron or hole). Figure 3 shows a sketch of the energy levels and spins involved in charged excitons. Their presence in WSe$_2$ even at room temperature has been shown repeatedly by spectroscopic techniques[39, 41-43].

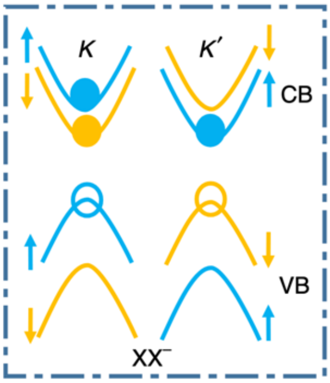

Figure S.1. Trion with solid circles representing electrons and empty circles representing holes. Colors are representing spin-up (blue) and spin-down (orange). X and X^- are two neighboring high symmetry points. Figure adopted from reference[44].

Moreover, it is possible to interpret indirect signatures of electron–hole pairs when they are sufficiently delocalized[40, 45]. Excitons for example can induce a negative imaginary part of the complex conductivity measured by THz spectroscopy, in analogy to what this thesis discussed previously with localization in a Drude–Smith complex conductivity. As such, the exciton dielectric polarization and the related capacitive response is seen as a negative imaginary part in the conductivity. A localized charged exciton and negative imaginary part is an expected response for monolayer WSe$_2$[40]. On the contrary, a Drude-like response of delocalized charge carriers results in a positive real part and a positive imaginary part. For comparison the characteristic Drude-like response and the Drude–Smith response to a THz electric field is shown in Figure S.0.5. in the SI. The complex conductivity spectra of WSe$_2$ and WSe$_2$–IT-4F can be described by the DSM. In this model, the charges are moving in a solid with the effective mass m^* and the unit charge of an electron e. For electrons and holes in monolayer WSe$_2$ the effective mass has been calculated as **$m^* = 0.35$ and 0.45 times the mass of the free electron m_e** respectively[41, 46]. A trion is heavier than a single exciton because it involves an additional charge carrier. The effective mass of a trion is the sum of the effective masses of its constituent particles, making it less mobile than an exciton or a free charge carrier[41].

8.1.2. Results and Discussion

WSe_2 and IT-4F structures

Figure 3 shows the prismatic structure of WSe_2 from three different perspectives. In the side view (a) WSe_2 is depicted together with the molecular structure of IT-4F and (a representation of) the corresponding layer thicknesses 1.5 nm and 11 nm respectively. The line thickness of the representation of the WSe_2 layer is about 0.1 mm, hence the monolayer WSe_2 and IT-4F layer are approximately **100’000 times thinner than the line**. In this study, I use a monolayer of chemical vapor deposition (CVD) grown tungsten diselenide WSe_2 on a sapphire substrate. The selection of the substrate is important since it must be transparent in the THz frequency range. The neat WSe_2 is combined with a thin film of the organic small molecule IT-4F by depositing the organic layer *via* thermal evaporation under vacuum (p=10^{-7} mbar) upon WSe_2. Controlled molecular packing upon vapour deposition ensures efficient charge transport and reduces recombination losses[47]. Later, the IT-4F layer is removed by immersing the bilayer in chloroform for 20 seconds. The WSe_2 monolayer stayed intact as tested by absorbance before and after immersion. The batch specifications are shown in the supplementary section S.0. Methods. Figure 3 (b) shows the isometric view of the tungsten atoms W in grey sandwiched between two Selenium atoms Se in green. Figure 3 (c) shows the top-view forming a honeycomb lattice with the parallelogram representing the unit cell. The inset shows the high symmetry points M, K, and Γ for each hexagon. This is important to interpret the absorbance and band structure presented in the next section.

Based on the described structure, WSe_2 has a high hole mobility and a low hole effective mass, contributing to its capability to support high-frequency electronic and optoelectronic devices[35]. The **effective mass of holes** in WSe_2 has been predicted to be about **0.45** times the mass of the free electron. This leads to hole mobilities ranging from **50 to 200 cm^2/Vs**[15, 16].

A mobility below 50 cm^2/Vs is indicative of trap states caused by defects[15, 16]. IT-4F is a derivative of the ITIC family[21-23]. IT-4F features fluorine atoms incorporated into its end-groups enhancing its electron affinity and intermolecular interactions[21]. This contracts the optical band gap, which can be beneficial for the investigated properties.

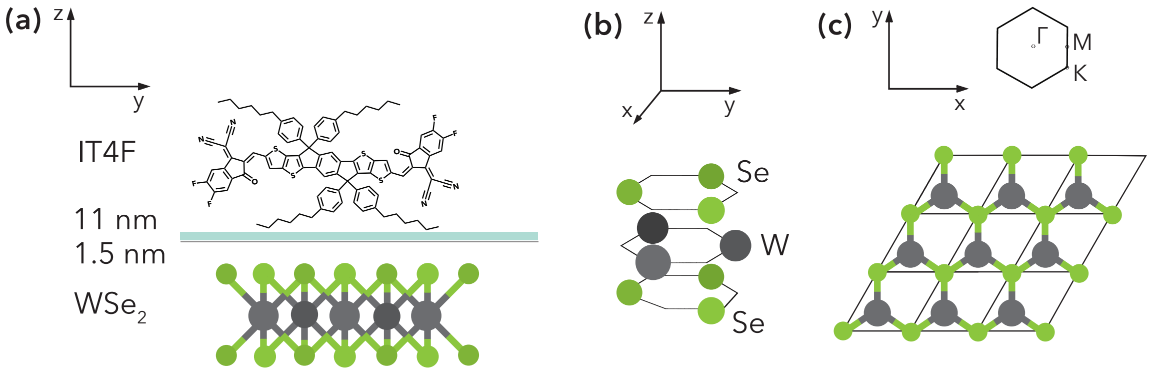

Figure 3: (a) Side-view of bilayer. Tungsten diselenide (WSe$_2$) trigonal prismatic structure together with the non-fullerene acceptor molecule IT-4F (b) WSe$_2$ isometric view and (c) from the top-view.

Absorption of light

In an optical pump experiment it is essential to begin with the steady-state absorbance of the system. Figure 4 (a) shows the steady-state absorbance from the ultraviolet to the near-infrared range. The first observation is that across all visible wavelengths, the bilayer (in turquoise) and the monolayer WSe$_2$ (in black) have an absorbance below 0.125. Hence, **the film is almost transparent and transmits almost 90% of the light** that is visible to the human eye (around 380 nm to 750 nm[48]). Moreover, we see that the WSe$_2$ monolayer has a broad absorbance in the ultraviolet region overlayed with several distinct peaks. To understand the absorbance of this inorganic semiconductors, Figure (a) and (b) show the absorbance and the band structure next to each other. The band structure hereby has the high symmetry points M, K, and Γ on the x-axis and energy on the y-axis. The Fermi energy is thereby set to zero, such that the band below the zero line is the valence band and the band above the zero line is the conduction band. The valence and conduction bands are separated by a band gap of approximately 1.6 eV. The band structure is adopted from reference[33]. The broader absorbance in the ultraviolet region for monolayer WSe$_2$ arises from transitions involving higher-energy electronic states, typically near the Γ point of the Brillouin zone. These transitions typically occur due to the excitation of carriers from the lower-energy valence band to the conduction band, they are labelled C transitions in (a) and (b). In the ultraviolet range, the absorbance is less discrete compared to the visible excitonic peaks labelled A and B. This is attributed to the higher density of states and overlapping transitions in this energy range.

The absorbance arising from the A and B excitonic transitions in monolayer WSe_2 is a hallmark of its direct bandgap and strong excitonic effects[33, 49]. These transitions are associated with electron–hole pairs (excitons) created by light absorption near the high symmetry K points of the Brillouin zone. The **A exciton** corresponds to transitions from the higher-energy valence band maximum to the conduction band, typically resulting in a sharp absorption peak around 760 nm (1.6 eV). The **B exciton**, originating from the lower-energy valence band to the same conduction band, leads to a distinct peak in the range of 600 nm (2.0 eV). The WSe_2 spectrum shows additional **A' and B' features** due to overlap of selenium Se and tungsten W orbitals[49]. Signatures associated with electron–hole–electron or hole–electron–hole particles can be identified using photoluminescence[50]. They occur with a red-shift to the main exciton peaks A and B. Hence, trions are associated with a broadened absorption of an excitonic band with an assymetric red-shifted tail[51]. The full width at half-maximum bandwidth of the A exciton in the WSe_2 monolayer, shown as the black line in (a), is around 50 nm which corresponds to A exciton bandwidths from literature[52]. However, the red-shift between the A exciton and the trion peak can vary between 2 and 20 nm, depending on factors such as doping density, dielectric environment, and temperature, which makes it difficult to draw conclusions on the presence of trions. Nevertheless, the present transitions make monolayer WSe_2 efficient in forming excitons using the visible spectrum, with applications in optoelectronics.

Moreover, also IT-4F absorbs visible light and exhibits the main absorption band between 500 nm and 800 nm. Its absorption spectrum typically peaks around 700–800 nm. The band is extending into the NIR due to the electron-withdrawing fluorine substitutions in its backbone, which lower the energy gap and hence the onset of the absorbance band. A high extinction coefficient of IT-4F further enhances its ability to absorb photons effectively[23]. The chosen excitation wavelength of 700 nm is absorbed by both layers, which poses the question of which layer should face the pump beam. Since both layers are thin, the differences are small. Advantages of having the WSe_2 layer facing the beam could be the lower absorbance of 0.01, the higher mobility of WSe_2 or protection of a sensitive top layer. Disadvantages could be (multiple) reflection losses due to the substrate or beam bending, especially when the quality of the substrate is unknown. After validating that the photoconductivity dynamics are the same in both orientations, here in the main results the IT-4F layer is facing the pump beam.

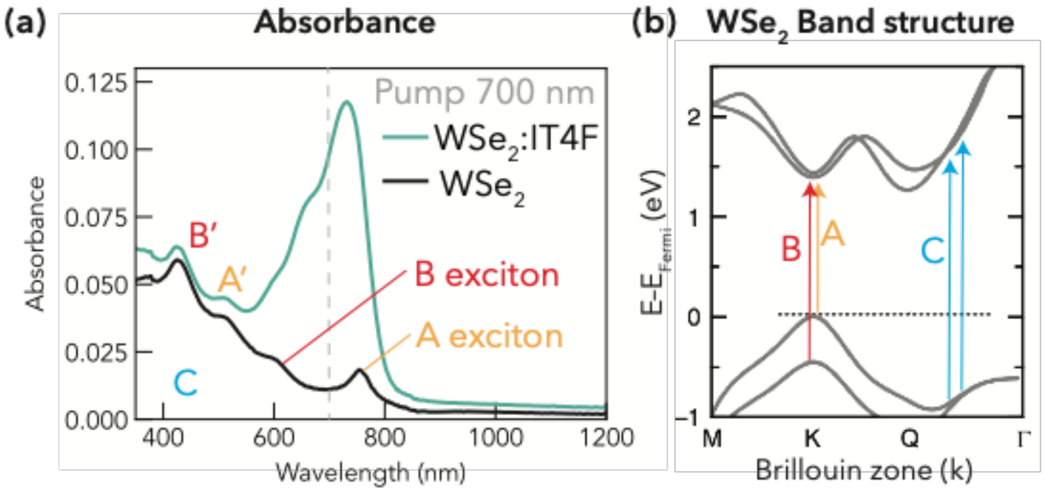

Figure 4. (a) Absorbance of WSe_2:IT-4F bilayer and WSe_2 monolayer. Charge generation process upon (b) photo-excitation of the inorganic monolayer TMD leads to electron transfer from the conduction band.

Transient photoconductivity maximum

Transient photoconductivity, assuming a negligible phase shift with time, can be expressed as:

$$\sigma(t) = n(t) \times \mu(t) \qquad (2)$$

Where both the number of charge carriers $n(t)$ and the mobility $\mu(t)$ are a function of time that has passed after photo-excitation. Intuitively, the number of charge carriers decreases. Less intuitively, the mobility increases with time since usually less mobile species recombine first. The dynamics in Figure 5 show the evolution of the photoconductivity signal as a function of the time after photo-excitation by the pump. Since the photoconductivity signal scales with the number of charged species, the dynamics represent the number of charges as a subject to different possible decay rates. The pump beam fluence determines the number of incident photons and hence the number of excitons. As explained previously, upon photo-excitation, excitons need to diffuse to the interface, where they can separate into charges. The exciton diffusion length is defined as the distance they travel within their lifetime (τ). In organics, when the fluence is high, and hence the density of excitons is high, non-linear effects like exciton–exciton annihilation can occur[53]. In inorganics, when the fluence is high, trap states get filled. This leads to an opposite fluence dependence of the dynamics[3]

---

[3] In this case transient absorption dynamics, but this holds true for photoconductivity dynamics.

between organic and inorganic materials. For organics, the signal from excited species shows shorter lifetimes with high fluence due to exciton-exciton annihilation. For inorganics, the signal from excited species shows longer lifetimes, because the trap states get filled. Moreover, in OPTP the electric field probe is sensitive to charged species only. These two facts guide the decision-making on the fluences used. The used fluence is also based on transient absorption dynamics of WSe_2 from Neher group who have collaborated on this project and provided the sample.

Figure 5 shows dynamics, i.e., the photoconductivity signal intensity as a function of time after photo-excitation. As given by equation (1) the photoconductivity signal is a differential signal, i.e., it is a function of $E_{\text{pumped}} - E_0$. The negative signal shows that the THz pulse that is transmitted through the pumped sample is decreased in amplitude in comparison to the ground-state sample $E_{\text{pumped}} < E_0$, because the conductivity increased. The negative photoconductivity signal reaches a maximum within few picoseconds followed by a slow decay. Figure 5 (a) depicts photoconductivity dynamics of the WSe_2–IT-4F bilayer with increasing fluence. The photoconductivity signal intensity is increasing non-linearly with increasing fluence. The density of absorbed photons (N_{photon}) calculated from the fluences 12, 28 and 56 μJ/cm^2 equals 0.8, 1.8 and 3.6 10^{19} photons cm^{-3}. The dynamics from transient absorption, as well as the calculations for the density of absorbed photons is given in the supplementary S.0. Methods. Figure 5 (b) shows the photoconductivity dynamics of the WSe_2–IT-4F bilayer in comparison to monolayer WSe_2 for the lower fluences. The dynamics between the bilayer and monolayer are similar in intensity and lifetime. That the monolayer WSe_2 has a signal at all has been quite surprising, under the assumption that it forms neutral excitons. This finding is evidence for the presence of charged species in both monolayer and bilayer. Figure 5 (c) shows the normalized photoconductivity dynamics on a logarithmic scale until 1 ns. It shows that the photoconductivity signal persists with a long life-time yielding 27–50% of its initial intensity at 1 ns. To fit the transient decay of the long-lived species I use a monoexponential fit between 50 ps and 1 ns. (d) Shows the corresponding decay lifetimes. Thereby, A represents the signal intensity at a pump-probe delay of 50 ps and τ_c represents the long mono-exponential lifetime between 50 ps and 1 ns. The initial 50 ps are disregarded in the fit. This time-range is based on published optical pump dynamics for similar TMDs like MoS_2[12, 54] to ensure this is the correct assignment for the long-lived lifetime. Before 50 ps fast quenching may occur due to fast surface trapping or surface–substrate interactions[12]. The resulting long-lived lifetimes for the WSe_2–IT-4F bilayer are 400 ps and 600 ps depending on the fluence (28 and 56 μJ/cm^2). The low fluence (12 μJ/cm^2) dynamics were not fitted, because the resolution at long time delays is not high enough to make an accurate assessment. The low fluence bilayer dynamics looks long lived with fewer data points, which is likely an artefact, and therefore excluded. The bilayer WSe_2–IT-4F lifetime of the photoconductivity signal is long-lived, which is a typical observation for free charges. However, the monolayer WSe_2 lifetime is even slightly longer. At high carrier densities, trap states can induce interesting properties. For example, persistent photoconductivity (PPC) has been shown in TMDs when one type of photo-generated charge carriers (positively or negatively charged) are trapped[55, 56]. Then, recombination is delayed and photoconductivity remains for extended periods of time and can last up to days[56]. If PPC is the origin of the photoconductivity signal, the mobility of the trapped charge carrier would be small and the mobility of the untrapped charge carrier would be similar to a free charge. Moreover, in the case of PPC charge carriers would not recombine within a millisecond, so they would not recombine between two laser pulses in the OPTP experiment and the differential signal of pumped and unpumped would be zero. Therefore, the photoconductivity in neat WSe_2 is likely not from PPC.

To sum up the transient photoconductivity, both monolayer and bilayer form a long-lived charged species. The lifetime increases with fluence, indicating that trap assisted recombination decreases. The long-lived decay is likely stemming from trap-assisted recombination. The similarities between mono- and bi-layer could represent several phenomena: First (i) IT-4F does not help nor hurt the overall photoconductivity: the charged species formed in the WSe_2 layer dominate the THz response with and without the IT-4F. Potentially, excitons formed by light absorption in the IT-4F layer do not separate into charges or contribute to the photoconductivity significantly and IT-4F does not act as an electron acceptor. Second (ii) charge transfer at the interface: that this charged species in WSe_2 is transformed into another charged species, such that the number of charges decreases but the mobility of charges increases. The transient photoconductivity dynamics in OPTP only contain information of the combined number and mobility $\sigma(t) = n(t) \times \mu(t)$. To distinguish between phenomenon (i) and (ii) OPTP photoconductivity spectra are utilized.

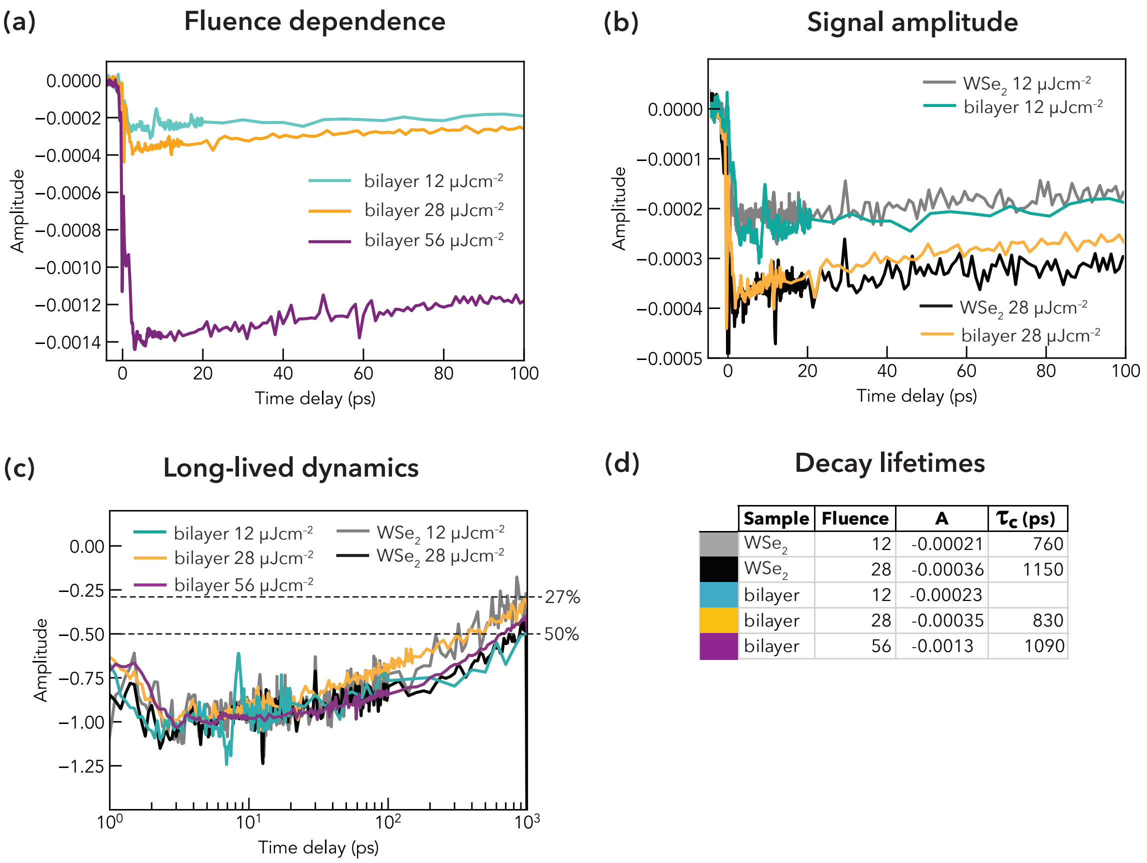

	Sample	Fluence	A	τ_c (ps)
▨	WSe_2	12	-0.00021	760
⬛	WSe_2	28	-0.00036	1150
🟦	bilayer	12	-0.00023	
🟨	bilayer	28	-0.00035	830
🟪	bilayer	56	-0.0013	1090

Figure 5. (a) Fluence dependent dynamics of a WSe_2–IT-4F bilayer. (b) Comparison of signal and dynamics between WSe_2–IT-4F bilayer and neat WSe_2. (c) Normalized dynamics on a log-scale until 1 nanosecond. (d) Table of long-lived lifetime for the curves between 50 ps and 1 ns.

Photoconductivity spectra show CT at WSe_2–IT-4F interface

So far, I have elaborated on the absorption of light and the transient photoconductivity signal as a function of pump–probe delay. Now the presented photoconductivity spectra yield deeper understanding on the nature of charged species, their number and mobility. Figure 6 shows photoconductivity spectra obtained by OPTP at a fixed pump–probe delay. The spectra are calculated by equation (1). Pump–probe delays of 10 ps and 100 ps were chosen. As discussed in the transient photoconductivity section above, neutral excitons typically have a lifetime of <50 ps[57] and the mobility typically increases with time. In Figure 6 the complex photoconductivity is seen with its real part in circular markers and its imaginary part in triangular markers. Evidently, all photoconductivity spectra have a positive real part and a negative imaginary part, showing significant localization effects for photo-generated charges in the materials. The solid lines represent a corresponding Drude–Smith model fit. The **photoconductivity spectra of WSe_2 and the bilayer are very different**, which means that the charged species are different. In panel (a) are the photoconductivity spectra for the bilayer system WSe_2–IT-4F. The real conductivity is around 30 S/cm at 1 THz at 10 ps and decreases to around 15 S/cm at 100 ps. The imaginary part decreases (is closer to zero) as well for 100 ps and the overall frequency-dependent slope appears to be flatter. This indicates more mobile charge carriers at 100 ps, which can be modelled with the DSM. In panel (b) the photoconductivity spectra of the monolayer WSe_2 are shown. While the real conductivity is also around 30 S/cm at 1 THz, the curve has a highly frequency-dependent slope. Similarily, at 100 ps the imaginary part decreased a bit, while it remains steeper than for the bilayer system. This indicates that while the real photoconductivity $\sigma(t) = n(t) \times \mu(t)$ is comparable, the contribution of $n(t)\ versus\ \mu(t)$ does change. This is evidence for phenomenon (ii) charge transfer at the interface: that the charged species in WSe_2 transforms into another charged species in a bilayer with a lower number of charges but a higher mobility. Moreover, Figure (c) and (d) show the fluence dependence of the photoconductivity spectra in the bilayer system WSe_2–IT-4F. In (c) the intermediate fluence of 28 μJ/cm^2 is compared to a lower fluence of 12 μJ/cm^2. In (d) the intermediate fluence of 28 μJ/cm^2 is compared to a higher fluence of 56 μJ/cm^2. As seen by the dynamics the **real conductivity scales non-linearly with increasing fluence**. Additionally, the spectra show how the frequency dependence changes with fluence. The low fluence photoconductivity shows an imaginary curve that is below the zero line over the full frequency range. The high fluence photoconductivity shows crossover at a lower frequency of around 0.7 THz. No crossover indicates that carriers experience significant backscattering or localization, preventing them from contributing fully to conduction. The position of the crossover frequency provides insights into the scattering time (τ) and the degree of disorder in the material. Please note the difference between the lifetime τ_c presented in the dynamics results and the scattering time τ. The lifetime τ_c represents the decay process after which the charge and its signal is vanished, while a scattering event after time τ does not mark the end of a charge's lifetime. A common estimate for the length scale probed by a THz pulse is the distance a carrier diffuses in one period of the probing frequency, roughly approximated as $L = \sqrt{D\omega}$, whereby the diffusion coefficient is denoted $D = \tau\, k_B T / m^*$ and the angular frequency is denoted ω. If scattering in a material occurs on a length scale L then it will influence the THz conductivity at a frequency $f = \omega/2\pi$[58]. The Drude–Smith model captures the features seen in the experimental THz photoconductivity well, as seen in Figure 6.

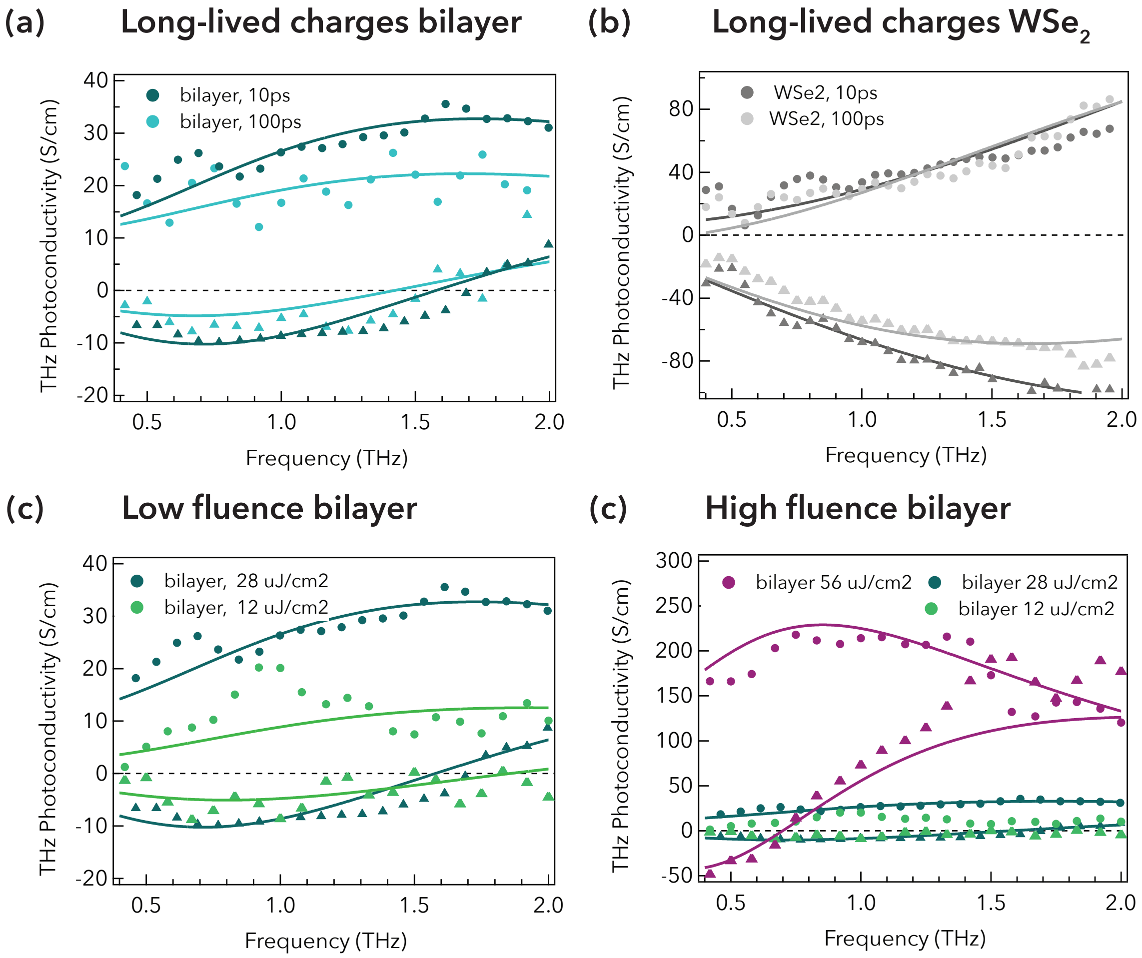

Figure 6. Photoconductivity spectra *versus* THz frequencies. (a) Bilayer spectra from mobile charged species for 10 ps and 100 ps delay after photo-excitation at a fluence of 28 μJ/cm². (b) WSe₂ spectra from immobile charged species for 10 ps and 100 ps delay at a fluence of 28 μJ/cm². (c) Bilayer comparison to spectra for low fluence in light green. (d) Bilayer comparison to spectra from high fluence

Nature of photo-generated charge carriers

The Drude–Smith model is given in Chapter 4 and contains the fitting parameters: number of charge carriers N_{charge}, scattering time τ and localization parameter c_1. Moreover, with the DSM fitting parameters, I calculate the effective mobility of charge carriers μ_{eff} in monolayer WSe_2 and a WSe_2–IT-4F bilayer. So far, the transient and frequency-dependent photoconductivity showed charge transfer at the interface with an increase in charge mobility. However, the nature of the involved charged-species must be clarified. In Table 1. the model parameters for the DSM fits in Figure 6 (a) and (b) are presented for the early pump–probe delay at 10 ps and for the long-lived species at 100 ps (28 μJ/cm^2). The general trends have been discussed with Figure 6. The DSM yields the number of charges N_{charge}. The quotient between N_{charge} and the number of incident photons calculated earlier gives the percentile of photons that generate a charge carrier. When each incident photon reaching monolayer WSe_2 creates a neutral exciton (electron-hole pair) that leads to an upper limit in the number of separate charges of $N_{\mathrm{charge}} = 2 \times N_{\mathrm{photon}}$. Here, the number of charges is 15% higher than that limit, given the incident photons are around 1.3×10^{19} (28 μJ/cm^2). This speaks for a significant contribution of trions, that adopt intrinsic charge carriers that usually get introduced by intrinsic doping, defects, or substrate effects, as reported repeatedly in WSe_2. The nature of the charged exciton trion, is heavier, more prone to scattering event, and immobile. Given the high N_{charge} and the low μ_{eff} in WSe_2, persistent photoconductivity is not the origin of photo-generated charge carriers. The nature of charge carriers in the bilayer is different to the monolayer.

First, their number is smaller with 28% of incident photons becoming charges. The scattering time is doubled yielding 80 fs and the localization parameter c_1 is reduced to −0.84 at 10 ps. The long-lived species measured at 100 ps after the pump is even less localized with a localization parameter c_1 of −0.76. The resulting effective mobility in the WSe_2–IT-4F bilayer is 75 cm^2/Vs and representative for free holes in the transport layer WSe_2[15, 16]. This concludes the nature of charge carriers involved in the CT: **charged excitons in WSe_2 are transferring an electron to IT-4F and dissociate into a free hole in WSe_2.** The differences between positively and negatively charged excitons do need further investigation. While OPTP cannot distinguish between the sign of the charge, in literature usually negative trions are formed[42, 43].

Table 1. DSM parameters with different pump–probe delay time. The values are representing N_{photon} density of absorbed photons, N_{charge} density of mobile charge carriers, τ scattering time and μ_{eff} effective mobility.

Sample **delay**	**bilayer** **10 ps**	**bilayer,** **100 ps**	**WSe$_2$** **10 ps**	**WSe$_2$,** **100 ps**
N_{photon} (10^{19} cm^{-3})	1.8	1.8	1.3	1.3
N_{charge} (10^{19} cm^{-3})	0.5	0.3	3	2.4
τ (fs)	80	80	40	40
c_1	−0.84	−0.76	−1.0	−1.0
μ_{eff} (cm^2/Vs)	50	75	0	0

Without IT-4F the charged excitons do not overcome the binding energy of typically hundreds of meV. Charged excitons and free holes in WSe$_2$ are experiencing a long-lived lifetime with decay rates between 400 ps and 1200 ns depending on the incident fluence. The fluence dependence indicates trap-assisted recombination that is transport layer specific. Comparing the rates with literature values is not very meaningful, since defect and substrate differences are well-known[12, 14, 15]. The possible generation pathway of photo-excitation and exciton generation in the IT-4F layer followed by hole transfer to the WSe$_2$ transport layer is not dominant based on the photoconductivity dynamics. Since for this generation pathway one would expect much improved signal intensity for the bilayer or different dynamics, the second generation pathway is likely dominant. The second generation pathway being photo-excitation and exciton generation in the WSe$_2$ layer followed by electron transfer.

The DSM fit parameters and effective mobility for the WSe$_2$–IT-4F bilayer with increasing fluences are presented in Table 2. The increasing fluence on the bilayer aids charge generation with 26% of photons becoming charges upon a fluence of 12 μJ/cm^2, 28% of photons becoming charges upon 28 μJ/cm^2 and **47% of absorbed photons becoming** mobile charges upon a fluence of 56 μJ/cm^2. Since the electrons remain in the IT-4F layer the optimal percentage of absorbed photons becoming mobile charges would be 50 %. This is under the assumption that the electrons in the IT-4F layer give a negligible in comparison to the holes in the WSe$_2$ layer As seen in the photoconductivity spectra, the fluence effects the number of generated charges non-linearly and it also effects the mobility of the charges. Hence, the higher fluence also comes with an increased scattering time time τ and localization parameter c_1. This yields an effective mobility of 160 cm^2/Vs in the bilayer $\mathrm{WSe_2}$–IT-4F. The value is in accordance with literature values of up to record 200 cm^2/Vs for monolayer $\mathrm{WSe_2}$[15, 16]. In the context of hybrid bilayer materials, the CT rate can increase with fluence under specific conditions. These conditions generally depend on the interplay between charge carrier density, recombination mechanisms, and the energy landscape of the donor-acceptor system. While the mobility alone could be explained by trap-assisted recombination with trap states becoming filled. The increased number of carriers and a higher mobility together suggest more effective charge transfer at the interface between $\mathrm{WSe_2}$–IT-4F with fluence. The bottleneck being diffusion-limited charge transfer is not likely given the ultrathin films. An improved CT with fluence is atypical so further investigations to explain the non-linear positive correlation between fluence and photo-conductivity in the bilayer $\mathrm{WSe_2}$–IT-4F will be interesting. It is possible that as fluence increases, higher carrier densities lead to enhanced intermolecular interactions or electric field effects, which can facilitate charge transfer[15]. Therefore, photoluminescence, EPR and bias-dependent transient absorption experiments are suggested for the bilayer $\mathrm{WSe_2}$–IT-4F system. Further investigations on the type of charged exciton, i.e., electron–hole–electron or hole–electron–hole, and the charge transfer involving charged excitons would be highly interesting and relevant in the field of optoelectronics.

Table 2. DSM parameters with different fluences. The presented values are N_{photon} density of absorbed photons, N_{charge} density of mobile charge carriers, τ scattering time and μ_{eff} effective mobility.

Sample fluence	**bilayer 12 μJ/cm^2**	**bilayer 28 μJ/cm^2**	**bilayer 56 μJ/cm^2**
N_{photon} (10^{19} cm^{-3})	0.8	1.8	3.6
N_{charge} (10^{19} cm^{-3})	0.2	0.5	1.7
τ (fs)	80	80	155
c_1	-0.92	-0.84	-0.73
μ_{eff} (cm^2/Vs)	25	50	160

8.1.3. Conclusion

I use optical pump–THz probe spectroscopy to investigate photo-induced charged species in monolayer WSe_2 and bilayer WSe_2–IT-4F. The main processes upon 700 nm pump are identified in a state-of-the-art hybrid material for optoelectronics. The Drude–Smith model aids the quantification and interpretation of the nature, number and mobilities of charged species. In monolayer WSe_2, charged excitons show a THz electric field response but remain largely immobile. Exciton dissociation at the organic acceptor molecule IT-4F interface yields mobile holes in the transport layer WSe_2. As such, the bilayer WSe_2–IT-4F exhibits free charge carriers with mobilities of up to 160 cm^2/Vs. The photoconductivity scales non-linearly with fluence and is long-lived with lifetimes of up to 1 nanosecond. The limiting decay rate is likely a transport layer specific trap-assisted recombination. This outlook chapter requires complementary experiments in particular EPR and PL, to study the charged excitons in monolayer WSe_2 further. This chapter contributes the THz photoconductivity, efficiency of mobile charge generation and lifetime of mobile charges for a tailor-made organic–inorganic hybrid bilayer.

Supplementary Information

Photoconductivity and hole mobility in an organic–inorganic hybrid bilayer

S.0. Methods

S.0.1. WSe_2–IT-4F fabrication

In this study, I use a monolayer of chemical vapor deposition (CVD) grown tungsten diselenide WSe_2 on a sapphire substrate purchased from 2D materials Inc. The selection of the substrate is important, since it must be transparent in the THz frequency range. The neat ML-WSe_2 is combined with a thin film of the organic small molecule IT-4F by depositing the organic layer *via* thermal evaporation under vacuum ($p=10^{-7}$ mbar) upon ML-WSe_2. IT-4F was purchased from Ossila (CAS-Nr: 2097998-59-7, Purity:99%, Mw: 1499.90 g/mol). To study the neat ML-WSe_2, the organic layer is removed by immersing the sample in anhydrous chloroform for 20 seconds inside the glovebox. The chloroform was purchased from Sigma Aldrich (CAS-Nr: 67-66-3, Purity: >99%, Mw: 119.38 g/mol).

S.0.2. Photon energy and density of absorbed photons

I study the photoconductivity of a bilayer system consisting of a transition metal dichalcogenide WSe_2 and the organic acceptor IT-4F. The photoconductivity experiment involves an optical pump beam that excites the sample, before a THz probe beam modulates the charge movement.
The steady-state absorbance of the bilayer system and of WSe_2 is shown in the main text.

Relevant input values

To calculate the density of absorbed photons for an **optical pump** technique one needs to control the key parameters excitation wavelength, beam diameter and beam energy of the laser.

Excitation wavelength (λ): 700 nm

Pump beam diameter: 3 mm

Probe beam diameter: 1.5 mm

Beam energy: 1 µJ $=1\times10^{-6}$ J

Absorbance of monolayer film at 700 nm: 0.01
Absorbance of bilayer film at 700 nm: 0.08

Then there are also these constants to take into account.
Planck's constant (h): 6.626×10^{-34} Js
Speed of light (c): 3×10^{8} m/s

Apparently, as seen in Figure 4 (a) both materials absorb light at 700 nm. The energy of a single photon is calculated by E = hc/λ and is approximately 1.77 eV (2.84×10^{-19} J). Using the total beam energy and the photon energy, the number of incident photons is determined to be 3.52×10^{12}. Considering the bilayer’s absorbance of 0.1 (10%) of these photons, or 3.5×10^{11}, are absorbed by the sample. The beam area, derived from the probe beam diameter, is 1.8×10^{-2} cm^2, resulting in a film volume of 1.9×10^{-4} cm^3 when multiplied by the film thickness. Dividing the number of absorbed photons by the film volume yields a photon density of 1.8×10^{19} photons cm^{-3}, providing a quantitative measure of the photon population within the absorbing material under these experimental conditions. In the interpretation I use 1.8×10^{19} photons/cm^3 as the upper limit of absorbed photons to calculate the percentile of charges generated from absorbed photons.

Relevant calculated values

Energy of a Single Photon: 2.84×10^{-19} J

Number of Photons Incident: 3.5×10^{12}

Fraction of Photons absorbed: 0.01 (monolayer)

Fraction of Photons Absorbed: 0.1 (bilayer)

Beam Area: 0.018 cm^2

Thickness of the monolayer: 1.5 nm

Thickness of the bilayer: 11 nm + 1.5 nm

Density of Absorbed Photons: 1.8×10^{19} cm^{-3} (monolayer)

Density of Absorbed Photons: 1.3×10^{19} cm^{-3} (bilayer)

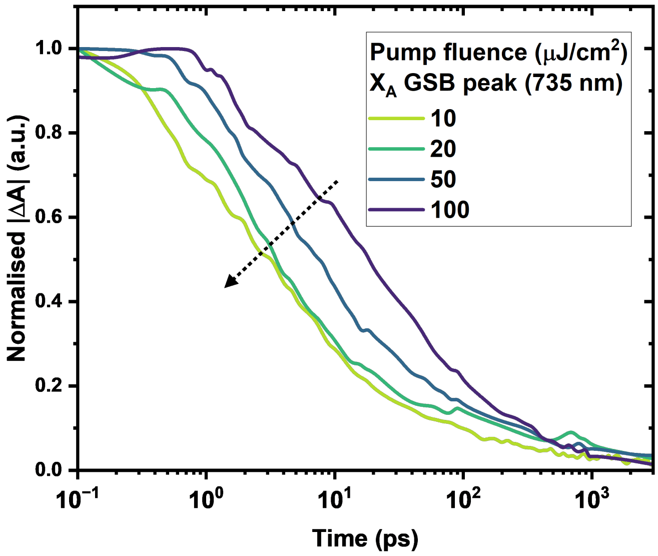

Figure S.0.2. Transient absorption dynamics of monolayer WSe_2.

S.0.3. Photoconductivity by optical pump–THz probe

The THz-TDS setup and the experimental details on the OPTP setup are described in Chapter 5.

Detailed OPA settings

To generate a 700 nm beam from an 800 nm fundamental laser using the TOPAS-PRIME Optical Parametric Amplifier (OPA), you employ the second harmonic generation (SHG) of the signal beam. Here's how it works in more detail than in the introduction.

First, the OPA is configured to produce a signal beam at 1400 nm through optical parametric amplification. The 800 nm pump beam interacts within a nonlinear crystal (such as BBO or LBO) to generate this signal beam at 1400 nm and a corresponding idler beam at a longer wavelength, according to energy conservation: $\lambda_{pump} = \lambda_{signal} + \lambda_{idler}$.

With $\lambda_{pump} = 800\,\text{nm}$ and desired $\lambda_{signal} = 1400\,\text{nm}$, the idler wavelength is determined accordingly. Then, the 1400 nm signal beam is directed into a SHG crystal, where it undergoes frequency doubling. In the SHG process, two photons of the 1400 nm signal beam combine within the nonlinear crystal to produce a single photon at half the wavelength, i.e., 700 nm in this case. The SHG crystal is carefully phase-matched to ensure efficient conversion. This two-step process, i.e. first generating the 1400 nm signal beam and then frequency-doubling it, allows me to efficiently convert the 800 nm fundamental laser output into a 700 nm beam using the SHG of the signal. This is recommended as the most efficient 700 nm output in the manufacturers manual (TOPAS-PRIME).

Photoconductivity dynamics

Set the translation stage of the electrooptic sampling delay stage (D1) at the maximum signal of the THz pulse and scan the optical pump–THz probe translation delay stage (D2). The optical pump delay stage is referred to as D2 in the scheme of the setup in Figure 3. First, I conduct a fluence dependence measurement series of dynamics measurements based with fluences between 12 $\mu J/cm^2$ and 28 $\mu J/cm^2$. These fluences were based on the linear regime seen in transient absorption from preliminary data by a collaborator. The stepsize for the optical pump delay time is 0.1 ps shortly before time zero and at early delays (<10 ps) and then increased when the dynamics become flatter. Based on the dynamics and very small signals I choose a fluence of 28 $\mu J/cm^2$ for the main photoconductivity series.

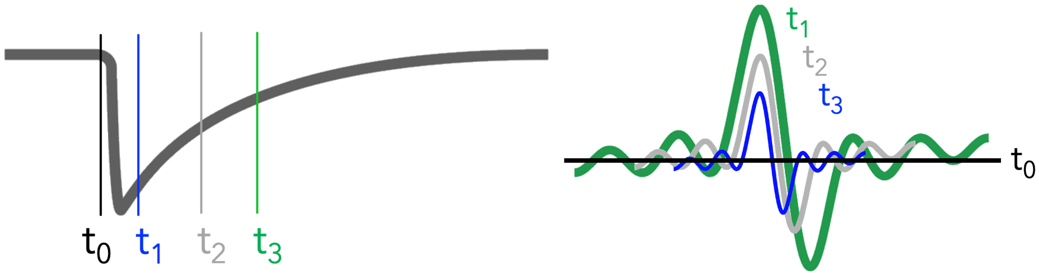

Figure S.0.3. Scheme of photoconductivity dynamics and spectra.

Photoconductivity spectra

Set the translation stage D2 of the pump–THz delay at a fixed time after photoexcitation. Using a chopper at the half-frequency of 500 Hz, I measure pumped and unpumped transmitted THz shot with two subsequent pulses. Then, I scan the THz waveform by moving the translation stage D1 for electrooptic sampling. The signal is calculated from the THz waveform when the sample is unpumped and pumped. For the main results, I chose a time delay of 10 ps and of 100 ps to represent short- and long-lived charges. I was not focusing on studying the photoconductivity when dominantly excitons are present within the first few picoseconds.

S.0.4. Instrument response function and signal processing

I was focusing on photo-induced charge carriers in this chapter and did not discuss the very early times (<5 ps) upon photo-excitation in detail. As given by equation (2) the photoconductivity signal is a differential signal, i.e. it is a function of $E_{\text{pumped}}(\omega, t) - E_0(\omega, t)$. The differential signal of photoconductivity is zero before the pump arrives. The time stamp when the pump beam arrives the sample is defined as time zero. When the pump reaches the sample, I start seeing a photoconductivity signal within around 2 ps. Light absorption and exciton generation happens faster than that, but that does not contribute to the photoconductivity signal. The instrument response function is likely limiting the onset of the signal. In the supplementary information S.0.4. I put a measurement of a classic inoranic semiconductor gallium arsenide (GaAs), because that should have a quick onset, but it also arises within 2 ps. At very early times upon photoexcitation there is presumably a high contribution of excitons. Light absorption and exciton formation happens at ultrafast times, much shorter than our instrument response function. The instrument response for this experiment is estimated to be smaller than 2 ps. I use the photoconductivity dynamics of the inorganic semiconductor GaAs to estimate it.

Low signal in WSe_2 and WSe_2–IT-4F bilayer films are a major difficulty in the experimental part. Here, I show photoconductivity dynamics of the investigated system in comparison to an inorganic semiconductor like GaAs. The Figure S.0.4. shows (a) photoconductivity dynamics of WSe_2 (in orange) in comparison to GaAs (in red and dark orange). The Figure (b) shows photoconductivity spectra of GaAs with a Drude response in line with literature. The Figure (c) shows raw data of photoconductivity spectra for the measurement of bilayer at 56 μJ/cm^2.

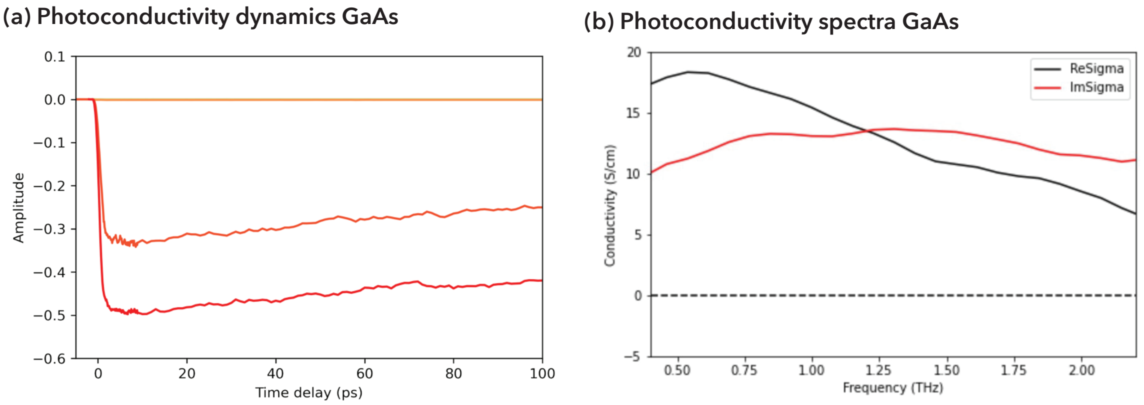
(a) Photoconductivity dynamics GaAs

(b) Photoconductivity spectra GaAs

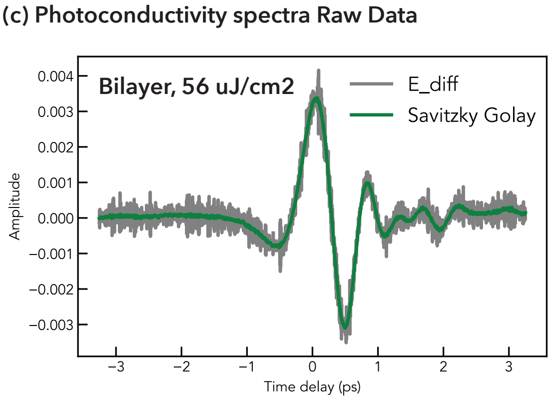
(c) Photoconductivity spectra Raw Data

Figure S.0.4. (a) Photoconductivity dynamics of GaAs in red and dark orange. (b) Drude- like response in GaAs. (c) Raw (exemplary) data of differential THz waveform.

S.0.5. Drude and Drude–Smith response to THz electric field

The differences in the response to an electric field holds so much information about the conductivity of a system. Since in this chapter, I am introducing a monolayer WSe_2, it is worth looking at the Drude and Drude–Smith response again. For the photoconductivity spectra of the bilayer system, I find a characteristic crossover point that is scaling with fluence. The higher the fluence, the smaller the localization effect and hence the crossover happens at lower frequencies.

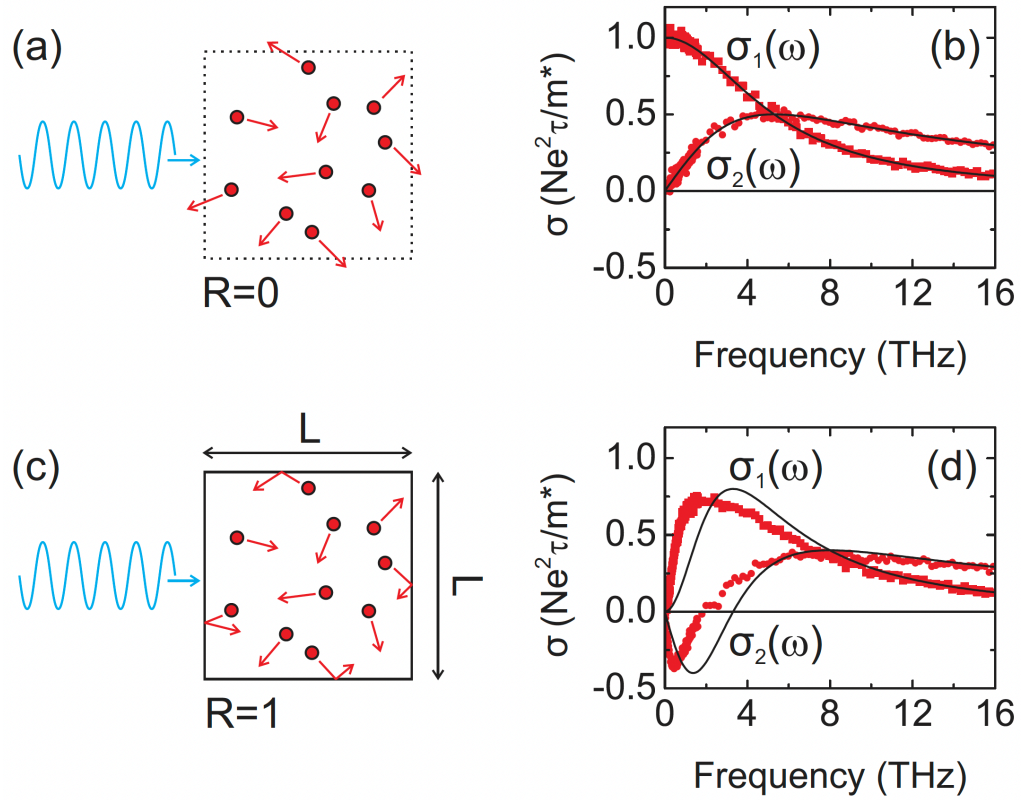

Figure S.0.5. (a) Drude-like ballistic movement of charge carriers without boundaries. (b) Drude-like response to a THz electric field, where σ_1 is the real part and σ_2 is the imaginary part. (c) Introduction of localization in a box of length L. (d) Drude–Smith response to a THz electric field. Figure adopted from reference[58].

References for Chapter 8

1. Zhang, Q., et al., *Recent progress in emerging two-dimensional organic-inorganic van der Waals heterojunctions.* Chem Soc Rev, 2024. **53**(6): p. 3096-3133.
2. Han, J., et al., *Recent Progress in 2D Inorganic/Organic Charge Transfer Heterojunction Photodetectors.* Advanced Functional Materials, 2022. **32**(34).
3. Takada, J., et al., *Organic-Inorganic Hetero Nanosystems as an Approach to Molecular Optoelectronics,* Jpn. J. Appl. Phys., 1995. **34**, 3864..
4. Gobbi, M., E. Orgiu, and P. Samori, *When 2D Materials Meet Molecules: Opportunities and Challenges of Hybrid Organic/Inorganic van der Waals Heterostructures.* Adv Mater, 2018. **30**(18): p. e1706103.
5. Pandey, R.K., et al., *Interface engineering for enhancement in performance of organic/inorganic hybrid heterojunction diode.* Organic Electronics, 2017. **45**: p. 26-32.
6. Azadmanjiri, J., et al., *2D layered organic–inorganic heterostructures for clean energy applications.* Journal of Materials Chemistry A, 2018. **6**(9): p. 3824-3849.
7. Shastry, T.A., et al., *Mutual Photoluminescence Quenching and Photovoltaic Effect in Large-Area Single-Layer MoS(2)-Polymer Heterojunctions.* ACS Nano, 2016. **10**(11): p. 10573-10579.
8. He, D., et al., *A van der Waals pn heterojunction with organic/inorganic semiconductors.* Applied Physics Letters, 2015. **107**(18).
9. Chen, W., et al., *Organic–Organic Heterojunction Interfaces: Effect of Molecular Orientation.* Advanced Functional Materials, 2010. **21**(3): p. 410-424.
10. Obaidulla, S.M., et al., *van der Waals 2D transition metal dichalcogenide/organic hybridized heterostructures: recent breakthroughs and emerging prospects of the device.* Nanoscale Horiz, 2023. **9**(1): p. 44-92.
11. Guo, Y., et al., *Band alignment and interlayer hybridization in monolayer organic/WSe2 heterojunction.* Nano Research, 2021. **15**(2): p. 1276-1281.
12. Wang, H., C. Zhang, and F. Rana, *Ultrafast dynamics of defect-assisted electron-hole recombination in monolayer MoS2.* Nano Lett, 2015. **15**(1): p. 339-45.
13. Park, S., et al., *Direct determination of monolayer MoS2and WSe2exciton binding energies on insulating and metallic substrates.* 2D Materials, 2018. **5**(2).
14. Yang, Y., et al., *Substrate mediated electronic and excitonic reconstruction in a MoS2 monolayer.* Journal of Materials Chemistry C, 2020. **8**(34): p. 11778-11785.

15. Wu, Z., et al., *Defects as a factor limiting carrier mobility in WSe2: A spectroscopic investigation.* Nano Research, 2016. **9**(12): p. 3622-3631.
16. Allain, A. and A. Kis, *Electron and hole mobilities in single-layer WSe2.* ACS Nano, 2014. **8**(7): p. 7180-5.
17. Liu, X., et al., *Photoresponse of an Organic Semiconductor/Two-Dimensional Transition Metal Dichalcogenide Heterojunction.* Nano Lett, 2017. **17**(5): p. 3176-3181.
18. Rijal, K., et al., *Collective Effects of Band Offset and Wave Function Dimensionality on Impeding Electron Transfer from 2D to Organic Crystals.* J Phys Chem Lett, 2020. **11**(18): p. 7495-7501.
19. Lin, Y. and X. Zhan, *Non-fullerene acceptors for organic photovoltaics: an emerging horizon.* Materials Horizons, 2014. **1**(5).
20. Cheng, P., et al., *Next-generation organic photovoltaics based on non-fullerene acceptors.* Nature Photonics, 2018. **12**(3): p. 131-142.
21. Hou, J., et al., *Organic solar cells based on non-fullerene acceptors.* Nat Mater, 2018. **17**(2): p. 119-128.
22. Lin, Y., et al., *An electron acceptor challenging fullerenes for efficient polymer solar cells.* Adv Mater, 2015. **27**(7): p. 1170-4.
23. Forti, G., et al., *Recent Advances in Non-Fullerene Acceptors of the IDIC/ITIC Families for Bulk-Heterojunction Organic Solar Cells.* Int J Mol Sci, 2020. **21**(21).
24. Zhang, X., et al., *Fluorination with an enlarged dielectric constant prompts charge separation and reduces bimolecular recombination in non-fullerene organic solar cells with a high fill factor and efficiency > 13%.* Nano Energy, 2019. **56**: p. 494-501.
25. Quiroz Avalos, Y.A., et al., *Insights into the relationship between molecular and order-dependent photostability of ITIC derivatives for the production of photochemically stable blends.* Journal of Materials Chemistry C, 2024. **12**(11): p. 4130-4141.
26. Zhu, X.Y., Q. Yang, and M. Muntwiler, *Charge-transfer excitons at organic semiconductor surfaces and interfaces.* Acc Chem Res, 2009. **42**(11): p. 1779-87.
27. Kumar, S., K. Ojha, and A.K. Ganguli, *Interfacial Charge Transfer in Photoelectrochemical Processes.* Advanced Materials Interfaces, 2017. **4**(7).
28. Liu, Y., et al., *Managing Challenges in Organic Photovoltaics: Properties and Roles of Donor/Acceptor Interfaces.* Advanced Functional Materials, 2022. **32**(43).

29. Marcus, R.A., *On the Theory of Electron-Transfer Reactions. VI. Unified Treatment for Homogeneous and Electrode Reactions.* The Journal of Chemical Physics, 1965. **43**(2): p. 679-701.
30. Jortner, J., *Temperature dependent activation energy for electron transfer between biological molecules.* The Journal of Chemical Physics, 1976. **64**(12): p. 4860-4867.
31. Wang, J., et al., *Marcus inverted region of charge transfer from low-dimensional semiconductor materials.* Nat Commun, 2021. **12**(1): p. 6333.
32. He, K., et al., *Wide bandgap polymer donors for high efficiency non-fullerene acceptor based organic solar cells.* Materials Advances, 2021. **2**(1): p. 115-145.
33. Hsu, W.T., et al., *Evidence of indirect gap in monolayer WSe(2).* Nat Commun, 2017. **8**(1): p. 929.
34. Mandal, A., *Tuning p-type to n-type semiconductor nature by charge transfer cocrystallization: effect of transfer integral vs. reorganization energy.* CrystEngComm, 2022. **24**(11): p. 2072-2080.
35. Pavoni, E., et al., *First principles study of WSe2 and the effect of V doping on the optical and electronic properties.* Materials Advances, 2024. **5**(6): p. 2230-2237.
36. Nayir, N., et al., *Modeling for Structural Engineering and Synthesis of Two-Dimensional WSe2 Using a Newly Developed ReaxFF Reactive Force Field.* The Journal of Physical Chemistry C, 2020. **124**(51): p. 28285-28297.
37. Nemec, H., F. Kadlec, and P. Kuzel, *Methodology of an optical pump-terahertz probe experiment: An analytical frequency-domain approach.* Journal of Chemical Physics, 2002. **117**(18): p. 8454-8466.
38. Neu, J., *Optical Pump Terahertz Probe (OPTP) and Time Resolved Terahertz Spectroscopy (TRTS) of emerging solar materials.* APL Photonics, 2023. **8**(7).
39. Cinquanta, E., et al., *Charge carrier dynamics in 2D materials probed by ultrafast THzspectroscopy.* Advances in Physics: X, 2022. **8**(1).
40. Docherty, C.J., et al., *Ultrafast transient terahertz conductivity of monolayer MoS(2) and WSe(2) grown by chemical vapor deposition.* ACS Nano, 2014. **8**(11): p. 11147-53.
41. Courtade, E., et al., *Charged excitons in monolayer WSe: Experiment and theory.* Physical Review B, 2017. **96**(8).
42. Mak, K.F., et al., *Tightly bound trions in monolayer MoS2.* Nat Mater, 2013. **12**(3): p. 207-11.
43. Liu, E., et al., *Signatures of moire trions in WSe(2)/MoSe(2) heterobilayers.* Nature, 2021. **594**(7861): p. 46-50.

44. Li, Z., et al., *Revealing the biexciton and trion-exciton complexes in BN encapsulated WSe(2).* Nat Commun, 2018. **9**(1): p. 3719.
45. Docherty, C.J., et al., *Ultrafast transient terahertz conductivity of monolayer MoS(2) and WSe(2) grown by chemical vapor deposition.* ACS Nano, 2014. **8**(11): p. 11147-53.
46. Fallahazad, B., et al., *Shubnikov-de Haas Oscillations of High-Mobility Holes in Monolayer and Bilayer WSe_2: Landau Level Degeneracy, Effective Mass, and Negative Compressibility.* Phys Rev Lett, 2016. **116**(8): p. 086601.
47. Kupgan, G., X.K. Chen, and J.L. Brédas, *Molecular packing of non-fullerene acceptors for organic solar cells: Distinctive local morphology in Y6 vs. ITIC derivatives.* Materials Today Advances, 2021. **11**.
48. Sliney, D.H., *What is light? The visible spectrum and beyond.* Eye (Lond), 2016. **30**(2): p. 222-9.
49. Zhao, W., Z. Ghorannevis, and L. Chu, *Evolution of electronic structure in atomically think sheets of WS2 and WSe2.* ACS Nano, 2023. **7**.
50. Lyons, T.P., et al., *The valley Zeeman effect in inter- and intra-valley trions in monolayer WSe(2).* Nat Commun, 2019. **10**(1): p. 2330.
51. Bae, H., et al., *Light Absorption and Emission Dominated by Trions in the Type-I van der Waals Heterostructures.* ACS Photonics, 2021. **8**(7): p. 1972-1978.
52. Yan, T., et al., *Long valley relaxation time of free carriers in monolayer WSe2.* Physical Review B, 2017. **95**(24).
53. Zhang, K.N. and X.T. Hao, *Multiple-Time Scale Exciton Dynamics in Organic Photovoltaic Devices.* J Phys Chem Lett, 2023. **14**(26): p. 6051-6060.
54. Liu, X., et al., *An ultrafast terahertz probe of the transient evolution of the charged and neutral phase of photo-excited electron-hole gas in a monolayer semiconductor.* 2D Materials, 2016. **3**(1).
55. Wu, Y.C., et al., *Extrinsic Origin of Persistent Photoconductivity in Monolayer MoS2 Field Effect Transistors.* Sci Rep, 2015. **5**: p. 11472.
56. George, A., et al., *Giant persistent photoconductivity in monolayer MoS2 field-effect transistors.* npj 2D Materials and Applications, 2021. **5**(1).
57. Gopalan, P., et al., *Ultrafast THz modulators with WSe2 thin films [Invited].* Optical Materials Express, 2019. **9**(2).
58. Cocker, T.L., et al., *Microscopic origin of the Drude-Smith model.* Physical Review B, 2017. **96**(20).

9 General Conclusions

This doctoral thesis investigates the conductivity of doped organic semiconductors and an organic–inorganic hybrid material and delivers novel insights from THz spectroscopy. Through an integrated approach combining materials science, condensed matter physics, and advanced spectroscopy, the research investigates the origin and limitations of conductivity in this class of materials. Potential applications are versatile and span ultrathin, tuneable, flexible and semi-transparent electronics, thermoelectrics and optoelectronics.

The chapters on materials, charge transport physics, and spectroscopy are foundational for setting the terminology and establishing a background. The described insights emphasise the complexity of charge generation and transport in organic materials and the state-of-the-art in research and development. This understanding frames the originality and relevance of the results discussed thereon. The spectroscopy chapter can also be viewed as a technical methodology to understand the route from data acquisition to results. It directly links to each of the original result chapters, and is essential to read, assess and interpret the findings.

The effectiveness of researching molecular design for enhancing the conductivity of conjugated polymers is evident. The booming research of glycolated side-chains underscores that by better processing and performance, especially with triethylene glycol side-chains. Such glycolated side-chains simultaneously impact the dielectric constant, the energetic disorder, solubility and packing. With a combined experimental and simulated approach this work could clarify the different contributions of those parameters to the overall improved conductivity. The improved conductivity is retained over varied distances from nanometers to millimeters. Innovatively, this work is comparing the conductivity over this short-range and long-range by utilising electrical measurements and ultrafast spectroscopy. Using gycolated side-chains, instead of alkyl side-chains, increases the conductivity 10-fold on short-range distances and 100-fold on long-range distances. This shows that comparing the conductivity over varied distances is highly relevant to understand the differences between materials better. The enhanced conductivity is assigned to the energetic disorder, the dielectric constant and smaller spatial confinement, while the number of total charge carriers, the nature of charge carriers ([+] or [++]), and the number of mobile charge carriers is controlled for and constant. Notably, spatial confinement contributes significantly as well. The research interest in structure-property relationships is rising and particularly machine-learning predictions are found to accelerate this trend further. The chemical versatility of side-chain engineering for example optimising their length, branching, and density is expected to further enhance conductivity.

The charge transport of conjugated polymers and organic semiconductors in general is still under debate. Charge transport models range from pure hopping models to band-like models; the duality of them is questioned. The semi-localized transport model and the transient localization correction to band transport were proposed and separately acknowledged in the research community. This work studies the temperature-dependent complex conductivity and provides direct insights into how doping affects the charge localization. It positions cryogenic THz spectroscopy as a powerful technique to observe the characteristic temperature-dependent conductivity and the complex THz conductivity simultaneously. This informs about the thermal activation to transport and charge localization directly. The findings indicate that there is a crossover from weakly localized transport at low temperatures to transient localized band-like transport at elevated temperatures. Doping affects the overall energetic landscape that a charge carrier trespasses. In this work, high doping levels lead to vanishing small activation energies at room temperature. With cooling transient mechanisms decrease while static disorder remains constant. The static disorder is estimated in the frozen disorder limit, at 10 K, and is only tens of meV at maximum. This leads to an almost temperature-independent conductivity. The observation that some polymers retain up to 90% of their room-temperature conductivity even at 10 K supports the hypothesis of a narrow density of states with a lowered Fermi energy. Thereby, anion exchange doping (AED) almost always leads to improved energetics for charge transport. Particularly, polymers with a thieno[3,2-b]thiophene backbone like PBTTT demonstrate a small temperature dependence (80–95% of conductivity at 10 K in relation to room temperature). This is likely to due to the anisotropic network upon annealing. Simple polythiophenes show a stronger overall localization, i.e., a higher temperature dependence (50–60% of conductivity at 10 K in relation to room temperature). In this case, a lower doping level yields improvement (80% of conductivity at 10K in relation to room temperature), because over doping has been identified to quench the charge transport. This chapter's key take away is that mitigating doping-induced energetic disorder by utilizing AED or resilient backbones reduces charge localization and hence improves conductivity.

The extension of this thesis to photoconductivity in hybrid materials, marks an important outlook into different materials and techniques. Studying the transition-metal dichalcogenide WSe_2 and a bilayer system of WSe_2 with the organic small acceptor molecule IT-4F broadened my expertise significantly. The hybrid bilayer is investigated for optoelectronics, whereby light is absorbed generating an exciton that can dissociate at the hybrid interface by charge transfer. Photoconductivity measurements using optical pump–THz probe reveal that long-lived charges are generated (40% of the exciton density), but they show a high degree of charge localization. Moreover, the comparison of intensity and dynamics of the signal between the bilayer and monolayer suggests that the photoconductivity stems from light absorption by the WSe_2. The findings suggest that photo-induced excitons in the IT-4F layer are not efficiently reaching the interface. This finding has implications for future hybrid designs, suggesting that achieving high mobility and improved transport will likely require modifications to the monolayer material itself or the integration of additional conductive or supportive layers.

This thesis contributes relevant and novel findings to the research field of doped organic semiconductors by utilizing ultrafast spectroscopy. Several avenues for materials with enhanced conductivity emerge from these findings, with potential implications for the applied sciences and organic electronic industry.

First, the optimization of molecular design and side-chain engineering in particular: Functionalized oligo-ethylene glycol side-chains enhance the conductivity by yielding a higher dielectric constant, lower energetic disorder, lower spatial confinement. The spatial confinement in P3HT likely comes from mismatched energy variations across the film, which could be substantially improved using oligo-ethylene glycol side-chains. Further optimization studies, especially large scale screening of side-chain polarity, flexibility, and attachment density by machine learning, would allow for tuning of dielectric and structural properties to meet specific requirements.

Second, the optimization of doping methods: Doping-induced disorder broadens the density of states and limits the conductivity. While the development of novel strong oxidants and doping methods like anion exchange doping unlock higher doping levels and conductivities, achieving a deep understanding of the origin and limits of conductivity remains a challenge. Future work may explore alternative dopants, polymer:dopant combinations and doping duration further.

Third, the development of hybrid materials: The design of organic–inorganic hybrid materials, particularly low dimensional transport materials and organics, allows for combined properties. Photo-induced doping of an organic small molecule IT-4F–WSe_2 transition-metal dichalcogenide bilayer generates long-lived charges. The photo-induced charges are limited by recombination and also their mobility. Future research could explore ways to enhance charge mobility in hybrid systems, perhaps by incorporating layered conductive scaffolds or interfacial materials. Here also porous 3 dimensional structures of hybrid materials, like combinations of polymers and carbon nanomaterials are of interest. Expanding the optical pump–THz probe photoconductivity measurements to different hybrid materials would be one method to identify photo-induced charge mobility and advance the research on hybrid materials for applications like photodetectors or photovoltaics.

In conclusion, this thesis contributes to the understanding and enhancement of conductivity in doped organic and organic–inorganic hybrid systems by utilizing ultrafast spectroscopy.

Appendix One: Contributions

Thesis Chapter 6

Chapter 6 of this thesis is based on an article in preparation for publishing in the Journal of Materials Chemistry C. My contribution has been the experimental lead of steady-state and ultrafast spectroscopy as well as electrical conductivity and the main authorship. The temperature-dependent conductivity results I gathered during a research stay at Chalmers Technical University in Göteborg, Sweden, under the mentorship of Christian Müller. The polymer synthesis, spectroelectrochemistry, grazing-incident wide angle scattering (GIWAXS) and kinetic Monte Carlo simulations were conducted by Emmy Järsfall, Sepideh Zokaei, Jaime Martín and Demetra Tsokkou respectively. The deeper analysis, fitting and interpretation of all results was contributed by me as well.

Eva Röck, Demetra Tsokkou, Emmy Järsfall, Sepideh Zokaei, Jesika Asatryan, Jaime Martín, Christian Müller, Martijn Kemerink, Natalie Banerji.

Thesis Chapter 7

Chapter 7 of this thesis is based on two independent articles in preparation for publishing in Advanced Materials. My contribution includes the experimental implementation of a closed-loop helium cryostat for THz-TDS as well as physical derivation of the semi-transient-localized transport model. Moreover, I was responsible for steady-state and ultrafast spectroscopy as well as electrical conductivity measurements and the main authorship. The Seebeck coefficients I gathered during a research stay at University of California in Los Angeles, USA, together with Diego Garcia Vidales. The eight different investigated polymers and their HOMO energy levels were contributed by collaborators or purchased commercially. First of all, Lize Bynens from Wouter Maes research group contributed the material synthesis of Pg_3BTTT, PBTTT and Pg_32T-T. Badr Jismy from Nicolas Leclerc's research group contributed the material synthesis of $PBTTT^8O$. Samples for GIWAXS and for macroscopic thermal activation, were prepared by Diego Garcia Vidales. GIWAXS results are gathered and analysed by Nesibe Akmanşen-Kalayci from Sarah Tolberts research group.

Eva Röck, Maximilian Horn, Nesibe Akmanşen-Kalayci, Lize Bynens, Wouter Maes, Sarah Tolbert, Natalie Banerji

Eva Röck, Diego Garcia Vidales, Nesibe Akmanşen-Kalayci, Maximilian Horn, Lize Bynens, Badr Jismy, Olivier Bardagot, Nicolas Leclerc, Wouter Maes, Benjamin Schwartz, Sarah Tolbert, Natalie Banerji

Thesis Chapter 8

The topic of Chapter 8 of this thesis is photoconductivity. The chapter is based on a communication in preparation for publishing in the Journal of Physical Chemistry C. Julien Réhault contributed substantially by writing the data acquisition in LabView, by guiding me with the alignment of the pump beam and connection of a second delay stage. Dieter Neher contributed by providing the material and with engaged, deep discussions on the direction of the project. Ultimately, I have the lead of the project, processed the sample in the glovebox, built the telescope and pump probe overlap in time and space, and undertook the measurements series. Moreover, I wrote the script for analysis and the manuscript.

Eva Röck, Dieter Neher, Julien Réhault, Natalie Banerji.

Continued projects

Two independent Master projects that I supervised between September 2022 and August 2023 led to high-impact findings which is subject to two continued projects. Since both Master students: Maximilian Horn and Basil Hunger, have optimized the doping methods, measured steady-state spectroscopy, spectroelectrochemistry and electrical conductivity, and decided to stay in the FemtoMat group and pursue a PhD themselves, they have the lead of the projects. The THz-TDS results gathered during their training period, where measured by me. The materials were provided by Christina Kousseff from Iain McCulloch's research group (Pg_32T-T), and Lize Bynens from Wouter Maes research group (Pg_3BTTT, PBTTT). GIWAXS samples were partly prepared by Maximilian Horn and Diego Garcia Vidales. GIWAXS results are gathered and analysed by Nesibe Akmanşen-Kalayci from Sarah Tolberts research group.

Maximilian Horn, **Eva Röck**, Diego Garcia Vidales, Nesibe Akmanşen-Kalayci, Christina Kousseff, Iain McCulloch, Benjamin Schwartz, Sarah Tolbert, Natalie Banerji.

Basil Hunger, Demetra Tsokkou, Maximilian Horn, **Eva Röck**, Lize Bynens, Iain McCulloch, Wouter Maes, Olivier Bardagot, Natalie Banerji.

There is a continued project led by Isabelle Holzer on high temperature rub aligned $PBTTT^8O$ films. The aim of this work is to characterize the nanoscale conductivity of aligned polymer films in parallel and perpendicular to the rubbing orientation, and comparing spectroelectrochemical doping and molecular doping. I have contributed to this project by adding temperature dependent THz conductivity measurements, training Isabelle in experiment and analysis.

Isabelle Holzer, Demetra Tsokkou, **Eva Röck**, Shubhradip Guchait, Badr Jismy, Martin Brinkmann, Nicolas Leclerc, Natalie Banerji.

There is a continued project on doping of donor–acceptor type copolymers (PDPP3T and PDPP4T) and comparing spectroelectrochemical doping with molecular doping. The data for this project were gathered by Maximilian Horn under my supervision during an exchange semester (Erasmus). Since Maximilian decided to stay in the research group, he will take over the lead of this project. I have contributed the idea, experimental conceptualization and experimental training. I also have conducted some of the absorbance and all of the THz specrtoscopy results.

Maximilian Horn, **Eva Röck**, Natalie Banerji.

Collaborations

The project on the electronic properties of poly(triazine imide), a graphitic carbon nitride, led by David Burmeister is published in Chemical Science. I contributed THz-TDS measurements and analysis on pressed pellets of crystalline. The datasets and the article are published open access in 2023. David Burmeister, Alberto Eljarrat, Michele

Guerrini, **Eva Röck**, Julian Plaickner, Christoph T. Koch, Natalie Banerji, Caterina Cocchi, Emil J. W. List-Kratochvil, Michael J. Bojdys. Chem. Sci., 2023,14, 6269-6277; https://doi.org/10.1039/D3SC00667K .

The project on spiro-OMeTAD led by Feng Gao will eventually be published. I contributed THz-TDS measurements and analysis on films of radical-doped spiro-OMeTAD during two measurement series. The datasets are published open access in 2024.

Eva Röck, Feng Gao, Natalie Banerji.

The project on Coumarin-based dyes for dye sensitized solar cells led by João Sarrato is published in Molecules 2021. The title of the article is: New 3-Ethynylaryl Coumarin-Based Dyes for DSSC Applications: Synthesis, Spectroscopic Properties, and Theoretical Calculations. I contributed the photophysical characterization using steady-state absorbance, fluorescence and phosphoresence measurements of Coumarin dyes in solution and in thin films. I gathered this data as a trainee at the Universidade de Coimbra Portugal, and the article was reviewed and published during my affiliation with the University of Bern.
João Sarrato, Ana Lucia Pinto, Gabriela Malta, **Eva Röck**, João Pina, João Carlos Lima,

A. Jorge Parola, Paula S. Branco. Molecules 2021, 26(10), 2934,
https://doi.org/10.3390/molecules26102934.

Support of young researchers

Being a representative in the committee for the support of young researchers, *Nachwuchsförderungskommission*, I contributed to the visibility and recognition of young researchers with outstanding portfolios. For example, I participated in the award process for the *Haller Medal 2024*, a symbol of excellence in the academic track of young researchers.

Moreover, I have been elected as the ambassador to the Faculty of Sciences in Bern. During 2.5 years I represented the body of PhD students and young researchers from the Department of Chemistry, Biochemistry and Pharmaceutical Sciences (DCBP) at the Faculty meetings. This role provided the chance to stand up for interests of young researchers and PhDs, embody a bi-directional communicator, and find unique insights into the academic system that solidified my understanding of hiring and funding schemes at the University.

Outreach

During my PhD, I also contributed to the field through a variety of outreach activities and oral presentations at international conferences. These experiences allowed me to disseminate my research findings, connect with the scientific community, foster collaborations and present myself professionally.

I presented the work of this thesis at several prestigious international conferences, both in-person and virtually. These conferences provided me with an excellent platform to share my research with leading experts in the field and to receive valuable feedback. My first outreach contribution, was a remote poster talk at the Swiss Chemical Society (SCS) Fall Meeting, presenting my research on organic semiconductors and engaging with the scientific community through a virtual format. (Ultrafast dynamics of doped polymers, SCS Fall Meeting, virtual, 2021.) Shortly after, I presented and defended my PhD project in front of the DCBP, which proved a well-rounded research approach and track for the continuation of my PhD. (Conductivity of doped polythiophenes, First Year Graduate Symposium, Switzerland, 2021.) I extended my outreach activities to a global conference the Materials Research Society (MRS) Spring Meeting in Honolulu, Hawaii, where I actively contributed to the poster session. Thereby, I was showcasing my work on the conductivity of doped organic semiconductors. I am proud that I was nominated for the best poster award with my first poster design. This conference provided an opportunity to portray me and my research project and understand the important component of a professional network. (Short-range conductivity of doped polythiophenes, MRS Spring Meeting, Hawaii, 2022.) My first oral presentation at a high-profile conference happened at the NCCR MUST (Molecular Ultrafast Science and Technology) meeting. There, I presented the glycolated side-chain project of this thesis focusing on the ultrafast spectroscopy techniques and the kinetic Monte Carlo simulations to understand the complex conductivity spectra of doped polymers. The conference facilitated discussions with experts in ultrafast spectroscopy. (Short-range conductivity of doped polymers, NCCR MUST Conference, Switzerland, 2022.) At the SPIE optics + photonics conference, I gave a talk about the insights of terahertz spectroscopy and *in-situ* spectroscopy to the organic electronics community. (Micro- and macroscopic conductivity in doped polythiophenes, SPIE optics + photonics, San Diego, 2023.) Also, in my final year of the PhD, I participated at the MRS Spring Meeting and contributed with a talk, discussing my overall learning in the limits of doped polymers showcasing how side-chain engineering and anion exchange doping improves the conductivity manifold up to tens of S/m. This presentation highlighted the key parameters that are relevant to overcome the limits in conductivity and led to a stimulating discussion. (Overcoming the limits of conductivity in doped polymers, MRS Spring Meeting, Seattle, 2024.)

In addition to conference presentations, I also engaged in outreach projects aimed at sharing my enthusiasm for science with the broader community:

I was an active part of the #NCCRWomen campaign in 2021, which aimed at showcasing the contributions of women in science and inspiring young women to pursue careers in research. This initiative captured the work life of female scientists with a professional videographer team. It was a rewarding opportunity to contribute to improving gender representation in STEM and to connect with a wider audience, including young students and aspiring researchers. (NCCRWomen 2021 Outreach Project, Switzerland, 2021.)

In April 2022, I had the pleasure to work with high school student Liam Jäggi on an outreach project involving the absorbance of light. Together, we conducted experiments to investigate the absorbance of pristine and doped P3HT and PDPP4T films. Liam presented the concepts and results in a poster session at his high school, Gymnasium Lebermatt. I hope this project helped to inspire and educate the next generation to explore the natural sciences. (MINT Poster Praktikum Gymnasium Lebermatt, Switzerland, 2022.)

These outreach activities and conference contributions have played an important role in advancing my research and personal growth. The promotion of exchange within the scientific community and between the scientists and the broader community is utterly important to me. Especially, giving back to the community with transfer of knowledge and the impact of innovation is essential. I hope I could raise awareness for the importance of fundamental research and the potential of organic semiconductors, while fostering connections between people of diverse backgrounds.

Timestamp of projects

The following figure 9.1 visualizes how much time the diverse tasks of my doctorate took in a comprehensive way. The purpose of this graphic is to showcase, how diverse a PhD is on an everyday basis and to give a transparent timestamp. In my opinion, outreach, teaching, and communication actually positively contribute to the scientific output and reach of a PhD project, the tasks transparently documented here may also provide information for future timelines and proposals. The white circles give the number of months it took me to figure out a specific task. The colored textboxes give the beginning month and year of the corresponding task. The accumulated time is the total time between my start at the FemtoMat team and the hand-in of my thesis which were 4 years and 2 months. The first category is technical training in the chemistry laboratory for sample preparation and in the laser laboratory for characterization on sight in Switzerland. I was lucky to have had exposure to optical laboratories before I started at the FemtoMat group, so I was able to get training on transient absorption (TA) and THz-TDS within four months. The second category is Chapter 6 (I), which includes all the experimental time, experimental analysis, visualisation and effective writing time. Since this was my first research project and involved simulations for the first time in this research group, it took a minimum of ten months of total time. Setting up the cryogenic equipment for the temperature dependent THz-TDS, designing a sample holder for THz optical probe, optimizing the cooling efficiency, setting up the electrical connections with ultra high vacuum feedthroughs and limited space, calibrating the

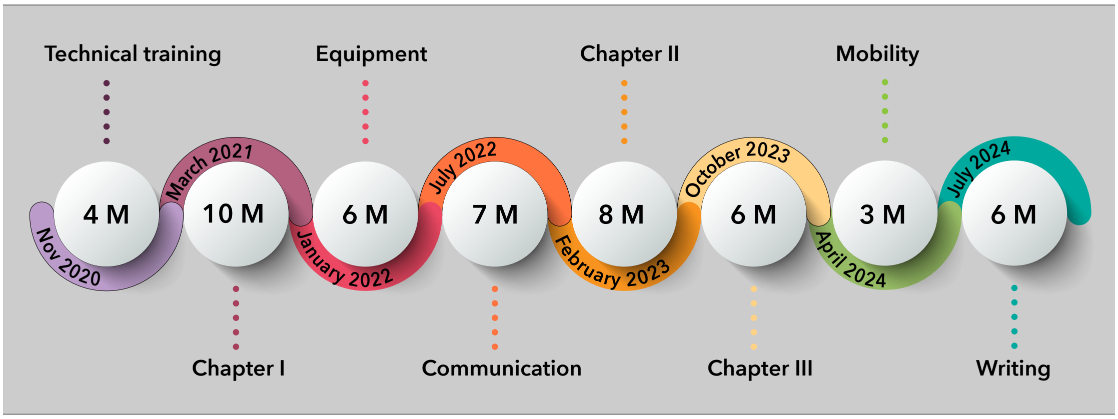

Figure 9.1: Showcasing the timestamp and number of months I roughly spent on the diverse projects and tasks during my PhD.

sensors and testing the equipment required six months of my full attention. The next category is communication. For me that includes the countless discussion I had with my colleagues, teaching, transfer of knowledge, group seminars, as well as the above stated outreach activities. Communication was a fundamental task during my PhD and took an estimated amount of seven months. In February 2023, I was able to start using the cryogenic setup for my temperature-dependent study in the Chapter 7 (II) of this thesis. From that point in time, I have been in the laboratory almost around the clock during eight months. This temperature dependent project and the optical pump–THz probe project from Chapter 8 (III) happened in sequence. The alignment of a second delay stage for the optical pump, the optical pump–THz probe beam size and overlap, the data acquisition of a high-signal reference (gallium arsenide) and the measurements of the hybrid material took at least six months. Just one photoconductivity spectra measurement takes several days or weeks to accumulate for a reasonable signal-to-noise ratio. Next, the tasks involving mobility also took a considerable amount of time during my PhD. I was able to do two experimental research stays in research groups abroad accumulating to three months of mobility. Both times, I was able to learn a key technique in a short amount of time. In July 2024, I was back from my last experimental research stay in California, and ready to wrap up the findings. In summer and fall 2024, during six months, I was busy bringing my learnings and findings on paper. The final interpretation of my findings, modelling, bibliography, visualisations and writing were the ultimate chance to take ownership of my achievements and learnings.

Appendix Two: Zusammenfassung

Organische Halbleiter sind vielversprechende Materialien für die nächste Generation von Elektronik, wie Bildschirme, Beleuchtung, Solarzellen, Transistoren oder Sensoren. Sie sind einfach in Lösung zu verarbeiten, bieten chemische Vielfältigkeit, sind flexibel, leicht, transparent und biokompatibel, was die Tür zu einer neuen Generation von organischer Elektronik mit diesen Eigenschaften öffnet. Wie der Name vermuten lässt, gehören organische Halbleiter zur Klasse der Materialien, die einen gewissen Schub brauchen, um elektrisch leitfähig zu sein. Dotierung ist eine zentrale Methode zur Erhöhung der Leitfähigkeit dieser Materialien, dennoch bleibt ein umfassendes Verständnis der Leitfähigkeit, ihres Ursprungs, Potenzials und ihrer Grenzen nicht fassbar. Diese Dissertation untersucht die Leitfähigkeit in dotierten organischen Halbleitern und liefert innovative und originelle Erkenntnisse durch den Einsatz ultraschneller Spektroskopie. Durch den Einsatz von Terahertz-Spektroskopie untersucht diese Arbeit die frequenzabhängige komplexe Leitfähigkeit von organischen Halbleitern und organisch-anorganischen hybriden Halbleitern. Die Ergebnisse geben Einblick in Anzahl, Mobilität und Natur der Ladungsträger. Darüber hinaus beleuchten sie den Ursprung und die intrinsische Grenze der Leitfähigkeit in organischen Halbleitern. Diese Dissertation hat daher Auswirkungen auf das Design organischer elektronischer Geräte und treibt letztlich das Feld der organischen Halbleitertechnologie voran.

Declaration of originality

This section includes the declaration of consent based on Article 18 of the PromR Phil.-Nat. 2019. It concerns the thesis handed in for the study program PhD in Chemistry and Molecular Sciences (PhD) at the University of Bern.

Author:	**Eva Gabriela Röck**
Title of the thesis:	**Conductivity of doped organic semiconductors: Insights from THz time-domain spectroscopy**
Supervisor:	**Professor Natalie Banerji**

I, Eva Röck, hereby declare that I have written this thesis independently and have not used any sources other than those cited. All passages that have been taken either verbatim or in essence from other sources have been clearly identified as such. All sources used, including literature, data, and ideas from others, have been properly cited and acknowledged. Contributions from AI tools, such as AI-assisted text generation, have been critically reviewed and revised by myself.
I understand the importance of academic integrity and acknowledge that any breach of this declaration may lead to consequences according to the regulations of the institution.
For the purposes of evaluation and verification of compliance with the declaration of independence, I grant the University of Bern the right to process the necessary personal data and to permanently store the thesis in a database.

21 March 2025

Personal statement

Organic semiconductors are relevant for cutting-edge technologies in flexible, tuneable and bio-compatible electronics. The countless applications rely on electrical conductivity in organic films, while there are still many questions concerning the detailed origin, potential and limit of their conductivity. The aim of this thesis is to shed light on the properties and mechanisms that determine the conductivity in doped organic films. Applying ultrafast spectroscopy in innovative ways and on state-of-the-art materials provided many meaningful learnings for me as a scientist and as a person. The investigations span a large variety of organic semiconductor systems and provide an outlook on a organic–inorganic system as well. The conductivity of doped organic semiconductors has seen a steep increase during the four years of my PhD. Discussing novel findings and applying new techniques in every project mentioned in this thesis has been a versatile and enticing task. By investigating novel materials, doping methods, and techniques, it was possible to achieve record high values for conductivity in organic semiconductors; and gain insight into the origin and limitations of it. Completing a PhD is not an easy feat and the experiences from the last years shaped me into a more resilient, confident, and well-rounded scientist. The work of this thesis poses me well to build my career in science and technology.

Before conductive polymers, there were **insulating polymers**. The history of polymers reflects humanity‘s ability to manipulate materials to meet societal and industrial needs. It spans centuries, beginning with ancient civilizations and culminating in the modern boom of plastics in industry. Prehistoric mesoamerican cultures, including the Maya civilization (1600–900 BCE), were among the first to manipulate natural polymers. They mixed the latex sap from rubber trees with juice from morning-glory vines to create elastic and waterproof materials for clothing. Polymers are omni-present in our lives and worth studying.